

NEW

FILE COPY

SC5441.FTR

Copy No. _____

SC5441.FTR

AD-A211154

GROWTH OF TUNGSTEN BRONZE FAMILY CRYSTALS

FINAL TECHNICAL REPORT FOR THE PERIOD
May 06, 1985 through November 30, 1988

MARCH 1989

ARPA Order No.: 4540
Program Code: P2D10
Name of Contractor: Rockwell International Corporation
Effective Date of Contract: 05/06/85
Contract Expiration Date: 11/30/88
Contract No.: N00014-85-C-2443
Principal Investigators: Dr. R.R. Neurgaonkar
(805) 373-4109
Dr. L.E. Cross
Pennsylvania State University
(814) 856-1181

DTIC
ELECTE
FEB 21 1990
S D

Sponsored by:

Defense Advanced Research Projects Agency (DARPA)
DARPA Order No. 4540

Monitored by:

Naval Research Laboratory
Under Contract No. N00014-85-C-2443

Approved for public release; distribution unlimited

The views and conclusions contained in this document are those of the authors and should not be interpreted as necessarily representing the official policies, either expressed or implied, of the Defense Advanced Research Projects Agency or the U.S. Government.



Rockwell International

02

UNCLASSIFIED

SECURITY CLASSIFICATION OF THIS PAGE

REPORT DOCUMENTATION PAGE				FORM APPROVED OMB No. 0704-0188	
1a REPORT SECURITY CLASSIFICATION UNCLASSIFIED			1b. RESTRICTIVE MARKINGS		
2a SECURITY CLASSIFICATION AUTHORITY			3 DISTRIBUTION AVAILABILITY OF REPORT Approved for public release; distribution unlimited		
2b CLASSIFICATION DOWNGRADING SCHEDULE					
4 PERFORMING ORGANIZATION REPORT NUMBER SC5441.FTR			5 MONITORING ORGANIZATION REPORT NUMBER		
6a NAME OF PERFORMING ORGANIZATION ROCKWELL INTERNATIONAL Science Center		6b OFFICE SYMBOL <i>(If Applicable)</i>		7a NAME OF MONITORING ORGANIZATION Naval Research Laboratory	
6c ADDRESS (City, State, and ZIP Code) 1049 Camino Dos Rios Thousand Oaks, CA 91360			7b ADDRESS (City, State and ZIP Code) 4555 Overlook Avenue, S.W. Washington, D.C., 20375		
8a NAME OF FUNDING SPONSORING ORGANIZATION Defense Advanced Research Projects Agency (DARPA)		8c OFFICE SYMBOL <i>(If Applicable)</i>		9 PROCUREMENT INSTRUMENT IDENTIFICATION NUMBER CONTRACT NO. N00014-85-C-2443	
8c ADDRESS (City, State and ZIP Code) 1400 Wilson Blvd. Arlington, VA 22209			10 SOURCE OF FUNDING NOS		
			PROGRAM ELEMENT NO	PROJECT NO ARPA-ORDER No. 4540	WORK UNIT ACCESSION NO
11 TITLE (Include Security Classification) GROWTH OF TUNGSTEN BRONZE FAMILY CRYSTALS					
12 PERSONAL AUTHOR S Neurgaonkar, R.R., Cross, L.E.					
13a TYPE OF REPORT Final Technical Report		13b TIME COVERED FROM 05/06/85 TO 11/30/88		14 DATE OF REPORT (Year, Month, Day) 1988, MARCH	
15 PAGE COUNT					
16 SUPPLEMENTARY NOTATION "The views and conclusions contained in this document are those of the authors and should not be interpreted as necessarily representing the official policies, either expressed or implied, of the Defense Advanced Research Projects Agency or the U.S. Government."					
17 COSATI CODES			18 SUBJECT TERMS (Continue on reverse if necessary and identify by block number)		
FIELD	GROUP	SUB-GROUP	SBN, BSKNN, Czochralski, Tungsten Bronze, Electro-optic, Photorefractive, Phase Conjugation, Optical Computing, Striations, Defects, Coupling, Sensitivity		
19 ABSTRACT (Continue on reverse if necessary and identify by block number) A systematic investigation of tungsten bronze crystals for electro-optic and photorefractive applications has been carried out successfully. The $Sr_{1-x}Ba_xNb_2O_6$ (SBN) and $Ba_{2-x}Sr_xK_{1-y}Na_yNb_5O_{15}$ (BSKNN) system crystals were grown in optical quality with and without specific impurities whose purpose is to enhance photorefractive coupling and speed. Both SBN and BSKNN crystals appear to be excellent hosts for electro-optic applications, e.g., modulators, waveguides, and spatial light modulators (SLM) and photorefractive applications, e.g., phase conjugation, image processing, optical computing and laser hardening. For photorefractive applications cerium and chromium doping show the largest effects on photorefractive coupling and speed.					
20 DISTRIBUTION AVAILABILITY OF ABSTRACT UNCLASSIFIED/UNLIMITED <input type="checkbox"/> SAME AS RPT <input checked="" type="checkbox"/> DTIC USERS <input type="checkbox"/>			21. ABSTRACT SECURITY CLASSIFICATION UNCLASSIFIED		
22a NAME OF RESPONSIBLE INDIVIDUAL Dr. Philipp H. Klein			22b TELEPHONE NUMBER <i>(Include Area Code)</i>		22c OFFICE SYMBOL 6822

DD FORM 1473, JUN 86

Previous editions are obsolete.

UNCLASSIFIED

SECURITY CLASSIFICATION OF THIS PAGE



TABLE OF CONTENTS

	<u>Page</u>
1.0 PROGRESS AND PROSPECTS FOR TUNGSTEN BRONZE MATERIALS .	1
2.0 POTENTIAL OF TUNGSTEN BRONZE FAMILY	2
3.0 ACCOMPLISHMENTS	3
3.1 Tungsten Bronze Host Crystals	3
3.2 Photorefractive Properties of Tungsten Bronze Crystals	6
3.3 Electro-Optic and Pyroelectric Applications of Tungsten Bronze Materials	11
3.4 Growth of Tungsten Bronze Thin Films	12
4.0 PUBLICATIONS AND PRESENTATIONS	14
4.1 Publications	14
4.2 Presentation	14
5.0 CONTRIBUTING LABORATORIES	15
RESEARCH PAPERS	
Progress in Photorefractive Tungsten Bronze Crystals	16
Development and Modification of Photorefractive Properties in the Tungsten Bronze Family Crystals	28
Growth and Ferroelectric Properties of Tungsten Bronze $B_{2-x}Sr_xK_{1-y}Na_yNb_5O_{15}$ (BSKNN) Single Crystals	44
A Review of the State-of-the-Art in the Growth and Ferroelectric Properties of Tungsten Bronze Crystals	56
Ferroelectric Tungsten Bronze BSKNN Crystals for Photorefractive Applications	102
Cr^{3+} -Doped SBN:60 Single Crystals for Photorefractive Applications	110
Self-Starting Passive Phase Conjugate Mirror with Ce-Doped SBN:60	118
Photorefractive Properties of Undoped and Ce-Doped, and Fe-Doped SBN:60 Single Crystals	124
Photorefractive Properties of Strontium Barium Niobate	132
SBN as a Broadband Self-Pumped Phase Conjugate Mirror	142



TABLE OF CONTENTS

	<u>Page</u>
Broadband Photorefractive Properties and Self-Pumped Phase Conjugation in Ce-Doped SBN:60	150
BSKNN as a Self-Pumped Phase Conjugator	164
Time Response of a Ce-Doped SBN:75 Self-Pumped Phase Conjugate Mirror	172
Ferroelectric Properties of La-Modified SBN:60 Single Crystals	178
Vapor Diffused Optical Waveguides in SBN:60	188
Epitaxial Growth of Ferroelectric Tungsten Bronze $\text{Sr}_{1-x}\text{Ba}_x\text{Nb}_2\text{O}_6$ Films for Optoelectronic Applications	194
LPE Growth of Ferroelectric Tungsten Bronze $\text{Sr}_2\text{KNb}_5\text{O}_{15}$ Thin Films	204

LIST OF FIGURES

<u>Figure</u>		<u>Page</u>
1	Classification of tungsten bronze family crystals	4
2	Photorefractive tungsten bronze single crystals	4
3	The $\text{Sr}_2\text{NaNb}_5\text{O}_{15}$ - $\text{Ba}_2\text{KNb}_5\text{O}_{15}$ System (BSKNN)	5
4	Role of dopants for photorefractive applications	10
5	Crystal boule photo	11



Accession For	
NTIS CRA&I	<input checked="" type="checkbox"/>
DTIC TAB	<input type="checkbox"/>
Unannounced	<input type="checkbox"/>
Justification	
By	
Date	
4000 1000 1000	
To 1	
A-1	



LIST OF TABLES

<u>Table</u>		<u>Page</u>
1	Preliminary Photorefractive Result on Different Dopants	8
2	Self-Pumped Phase Conjugate Response Time for Bronze Crystals	9



1.0 PROGRESS AND PROSPECTS FOR TUNGSTEN BRONZE MATERIALS

This report covers work conducted during the last four years of DARPA Contract Nos. N00014-82-C-2446 and N00014-85-C-2443 for the study of the growth processes for tungsten bronze crystals and thin films and their electro-optic, pyroelectric and photorefractive applications. A number of the topics covered represent the development and extension of studies accomplished in our earlier contract "Growth of tungsten bronze family materials for electro-optic and photorefractive applications," and has capitalized on the momentum generated in this study.

Since the work reported covers a rather wide range of materials and device applications, it has been divided, for convenience, into four major sections:

1. Tungsten bronze family crystals and their classification,
2. Photorefractive properties of tungsten bronze crystals and their applications,
3. Electro-optic and pyroelectric applications of tungsten bronze materials,
4. Growth of tungsten bronze thin films,

A brief narrative description is given of current and past work to summarize the progress in each category. Completed topics are included as preprints and reprints of papers published or to be published.



2.0 POTENTIAL OF TUNGSTEN BRONZE FAMILY

The development of tungsten bronze crystals and thin films has reached the point where these materials have clear advantages in electro-optic and photorefractive applications over the presently available LiNbO_3 , BaTiO_3 and KNbO_3 materials. As our understanding of the factors controlling electro-optic properties, crystal quality and size has grown, we have increased the range of applicability of the bronzes through such factors as choice of dopants, control of growth conditions, and establishment of the relation between structure and electro-optic characteristics. Currently, these materials show exceptional promise in photorefractive applications such as phase conjugation, laser hardening and image processing, and in optical display and electro-optic applications such as wave-guides, modulators and spatial light modulators (SLM). To realize this promise, it will be necessary to systematically develop and evaluate members of the tungsten bronze family whose properties have been optimized for specific applications. These include the current best bronzes (SBN, BSKNN, SCNN) along with morphotropic phase boundary bronzes such as PBN, PSKNN, etc. Because of the diversity of electro-optic properties available in this family, and the ability to grow large size crystals, we anticipate these materials will become a major factor in future photorefractive and electro-optic devices, and in some cases, even pyroelectric device applications.



3.0 ACCOMPLISHMENTS

3.1 Tungsten Bronze Host Crystals

The tungsten bronze compositions can be represented by the general formulas $(A_1)_4(A_2)_2C_4B_{10}O_{30}$ and $(A_1)_4(A_2)_2B_{10}O_{30}$, in which A_1 , A_2 , C and B are 15-, 12-, 9- and two 6-fold coordinated sites in the crystal structure. The ferroelectric phases can be divided into two groups: those with tetragonal symmetry (4mm), which are ferroelectric, and those with orthorhombic symmetry (mm2), which are both ferroelectric and ferro-elastic. In the orthorhombic structure, the polar axis can be either along the c-axis, such as in $Sr_{2-x}Ca_xNaNb_5O_{15}$ or $Ba_2NaNb_5O_{15}$, or along the b-axis, such as in $PbNb_2O_6$, $Pb_2KNb_5O_{15}$. These tetragonal and orthorhombic groups can be further classified according to their longitudinal transverse effect as summarized in Fig. 1. These effects can be obtained only in single crystals of each type, as it is very difficult to recognize these differences in polycrystalline materials. Major work has been carried out in three tungsten bronze hosts (Fig. 2) which exemplify the three types electro-optic response available in this family.

SBN Solid Solution Crystals - The $Sr_{1-x}Ba_xNb_2O_6$, $0.25 \leq x \leq 0.75$, solid solution exists on the $SrNb_2O_6$ - $BaNb_2O_6$ binary system and it exhibits strong transverse ferroelectric and optical properties. This system was originally studied at Bell Laboratories where the conclusion was that the $x = 0.50$ (SBN:50) composition was congruently melting. However, later work by Megumi et al indicated that $Sr_{0.6}Ba_{0.4}Nb_2O_6$ (SBN:60) was congruently melting, and they succeeded in growing optical quality crystals. Our crystal growth work on SBN:75, SBN:60 and SBN:50 confirms Megumi's results, and we have been successful in growing all of these compositions in optical quality. Currently, SBN:60 crystals are being

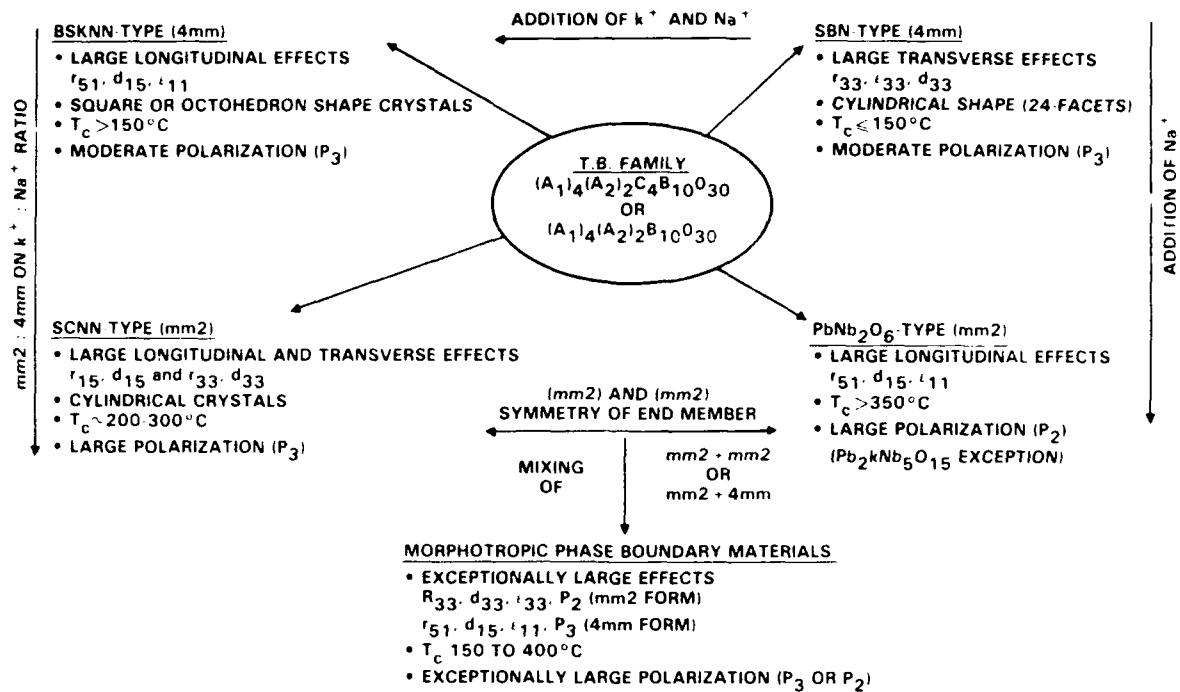


Fig. 1 Classification of tungsten bronze family crystals.

SC44264

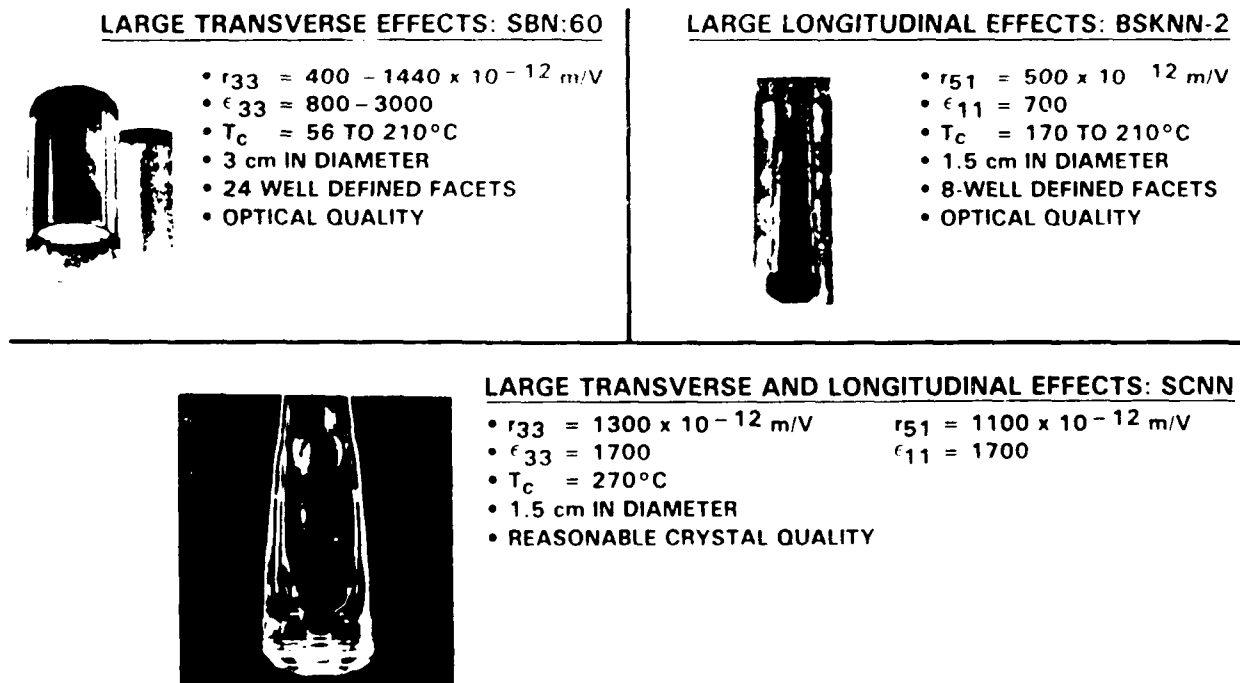


Fig. 2 Photorefractive tungsten bronze single crystals.



grown over 1" in diameter with or without dopants. These crystals have found use in applications such as electro-optic, pyroelectric and millimeter wave devices.

BSKNN Solid Solution Crystals - This solid solution is based on the $\text{Sr}_2\text{NaNb}_5\text{O}_{15}$ - $\text{Ba}_2\text{KNb}_5\text{O}_{15}$ system, and both the tetragonal (4mm) and orthorhombic (mm2) forms have been identified. The BSKNN compositions which are K^+ -rich (e.g., BSKNN-1 and BSKNN-2) which are K^+ -rich, are tetragonal at room temperature and have longitudinal ferroelectric and optical properties similar to perovskite BaTiO_3 . The BSKNN compositions that are Na^+ -rich (e.g., BSKNN-3, BSKNN-5) appear to be weakly orthorhombic at room temperature. As shown in Fig. 3, a morphotropic phase boundary region seems to exist between BSKNN-2 and BSKNN-3, with transverse effects being larger in BSKNN-3. In general, the growth of these crystals is more difficult than to the growth of SBN; however, we have been successful in growing over 1 cm diameter BSKNN-2 and BSKNN-3 crystals.

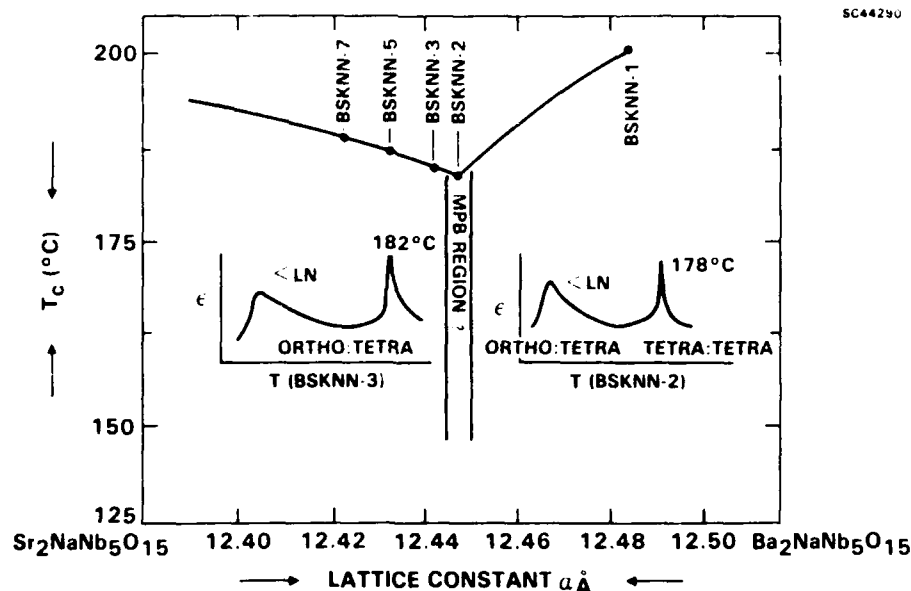


Fig. 3 The $\text{Sr}_2\text{NaNb}_5\text{O}_{15}$ - $\text{Ba}_2\text{KNb}_5\text{O}_{15}$ system (BSKNN).



SCNN Solid Solution Crystals - $\text{Sr}_2\text{NaNb}_5\text{O}_{15}$ is orthorhombic at room temperature, and the addition of Ca^{2+} in the form $\text{Sr}_{2-x}\text{Ca}_x\text{NaNb}_5\text{O}_{15}$ retains the mm2 symmetry. The maximum solid solubility of Ca^{2+} in SCNN is 33 mole%, since Ca^{2+} occupies only the 12-fold coordinated site in the bronze structure. The addition of Ba^{2+} in SCNN has also been studied, and it stabilizes the growth conditions so that crystals as large as 1.5 cm diameter can be grown. The key feature of SCNN and BSCNN crystals is that both transverse and longitudinal dielectric and optical properties are large and nearly equal, with $\text{Sr}_{1.9}\text{Ca}_{0.1}\text{NaNb}_5\text{O}_{15}$ showing electro-optic coefficients $r_{33} = 1350 \times 10^{-12}$ m/V and $r_{51} = 1180 \times 10^{-12}$ m/V. Besides general photorefractive applications, these crystals could have an important impact on three dimensional displays.

3.2 Photorefractive Properties of Tungsten Bronze Crystals

To use tungsten bronze crystals for photorefractive applications, specifically for image processing, laser hardening, optical computing and phase conjugation, the change in the refractive index, n , should be large and should occur rapidly. This change is given by

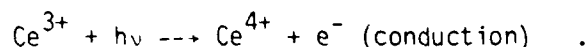
$$\Delta n = -1/2n^3 r_{ij} E_j$$

where r is electro-optic coefficient and E is the space-charge field. Since the electro-optic coefficient is relatively constant for a given crystal composition, Δn can be enhanced by increasing the optically generated space-charge field. Currently, this is an active area of research in large response electro-optic materials such as BaTiO_3 , KNbO_3 and LiNbO_3 . Undoped crystals, including bronzes, BaTiO_3 and others, have sufficiently high sensitivity, but only moderate response speeds of typically 100 ms or higher. If these



crystals are to be of effective use, their response times must be reduced to the order of 1 ms or better, and coupling to 20 cm^{-1} or higher.

It is now established that doping crystals with an impurity that is readily photoionized by incident radiation greatly enhances the susceptibility of crystals to index changes. A variety of different dopants have been tried in SBN, BSKNN and SCNN single crystals, as summarized in Table 1. Ce^{3+} doping of SBN was originally reported by Megumi et al. The addition of Ce^{3+} develops a distinct but wide absorption band around $0.5 \mu\text{m}$, which differs markedly from the band-gap absorption edge. The cerium ion is photoionized by means of the reaction:



Our ongoing research on Ce^{3+} -doped SBN and BSKNN crystals suggests that both Ce^{3+} and Ce^{4+} valence states are present, but this has not yet been conclusively proved. We also suspect that since Nb^{5+} reduces to Nb^{4+} at elevated temperatures, trapping levels due to Nb^{4+} may exist in the present crystals. Doping with Ce^{3+} in the 15- or 12-fold coordinated Ba^{2+} or Sr^{2+} sites of SBN and BSKNN produces pink-colored crystals with spectral response in the visible region. For a 0.1 wt% addition of Ce^{3+} , the coupling coefficient is raised to 45 cm^{-1} in SBN wafers and around 20 cm^{-1} in crystal cubes. This difference in coupling is not presently understood. The speed of response is also significantly faster, being estimated to be 10 - 40 ms depending upon laser intensity. These crystals have proven to be effective in phase conjugate mirror work, and several device concepts are emerging; e.g., bird wing, frog leg, and bridge double-phase conjugators.



Table 1
Preliminary Photorefractive Result on Different Dopants

PROPERTY	Ce ³⁺ -DOPED SBN:60		Cr ³⁺ -DOPED SBN:60	Fe ³⁺ -DOPED SBN:60
	12-FOLD	9-FOLD	6-FOLD	6-FOLD
CRYSTAL COLOR	PINK	GREENISH-YELLOW	GREENISH-YELLOW	YELLOW
QUALITY	EXCELLENT	EXCELLENT	EXCELLENT	REASONABLE*
ELECTRO-OPTIC COEFFICIENT $\times 10^{-12}$ mV	460	460	550	480
BEAM FANNING RESPONSE				
AT 40 mW/cm ²	2.5s	3.0s	0.7s	2.8s
AT 0.2 W/cm ²	0.6s	1.2s	—	—
AT 2 W/cm ²	0.05s	0.09s	0.008s	0.07s
COUPLING COEFFICIENT	~ 19 cm ⁻¹ (CUBE) ~ 45 cm ⁻¹ (PLATE)	~ 5.6 cm ⁻¹	~ 6.7 cm ⁻¹	—
SPECTRAL RESPONSE	0.4-0.7 μ m	0.4-0.9 μ m	0.6-1.0 μ m	0.4-0.9 μ m
SPPCR	EXCELLENT	EXCELLENT	EXPECTED	EXPECTED

*STRIATED AT HIGHER DOPING LEVELS

Table 2 summarizes the self-phase conjugate response time for various photorefractive crystals. Because of such attractive features of Ce-doped crystals, extensive efforts are being made to exploit this dopant for various applications in the visible region. Another interesting feature of Ce³⁺-doped crystals is that when Ce³⁺ is placed in the 9-fold coordinated site, its spectral response shifts from the visible to the near-IR (0.78 μ m) with coupling as high as 6 - 7 cm⁻¹. These results are similar to BaTiO₃ studied under low laser intensity. Since placing Ce³⁺ in a lower coordination extends the spectral response to longer wavelength, efforts are underway to place Ce³⁺ in the 6-fold coordinated Nb⁵⁺ sites. Although Ce³⁺ is known to occupy the 6-fold site in perovskites and other crystal structures, the placement of Ce³⁺ in the bronze 6-fold coordinated site will require the blocking of the 15-, 12- and 9-fold sites.



Table 2
Self-Pumped Phase Conjugate Response Time for Bronze Crystals

Material	Response Time (seconds) @ 0.2 W/cm ²	Wavelength (nm) @ 2 W/cm ²	
Ce-SBN:75	32.0	8.3	457.9
Ce-SBN:75	7.7	1.6	442.0
Ce-SBN:60	5.8	1.1	442.0
BaTiO ₃ 25.0	2.5	514.5	
Ce-BSKNN-2	27.9	8.8	457.9
Ce-BSKNN-3	18.1	3.8	457.9
Cr-SBN:60*	10.2	-	442.0
Ce-SCNN	-	-	-

*Results are inconclusive.

In order to extend the spectral response deeper into the IR region, smaller ions such as Fe²⁺/Fe³⁺, Cr³⁺/Cr⁴⁺, Mn²⁺/Mn³⁺ and Rh³⁺ have been explored in the 6-fold coordinated Nb⁵⁺ sites. These dopants produce yellow to yellowish-brown colored crystals, whereas Cr³⁺-doped crystals are typically greenish-yellow in color. In general, all of these doped crystals can now be produced in optical quality, although initially the growth of optical quality Fe-doped crystals was difficult due to the presence of striations. Currently, the role of iron alone, as well as with other dopants, is being studied in SBN and BSKNN to optimize speed and coupling.

Cr³⁺-doped SBN:60 has been found to have a photorefractive response speed 5-10 times faster than Ce³⁺-doped SBN:60. However, the coupling coefficient for Cr³⁺-doped SBN:60 (6 - 7 cm⁻¹) is lower than in Ce³⁺-doped crystals. The effect of Cr³⁺ concentration on the coupling coefficient is being explored since we suspect that higher concentrations should result in improved coupling.



Figure 4 summarizes the observed relationships between the crystallographic site preference of a dopant and the range of spectral response in bronze hosts. It is clear from these data that longer wavelength response is associated with a lower coordination for the dopants, with response out to 1.0 μm for 6-fold coordinated Cr^{3+} in SBN:60 crystals. This site dependence provides a flexibility rarely seen in other structural families. One can thus use the type of dopant and its site preference to optimize photorefractive properties in a given spectral range for either transverse or longitudinal electro-optic crystals.

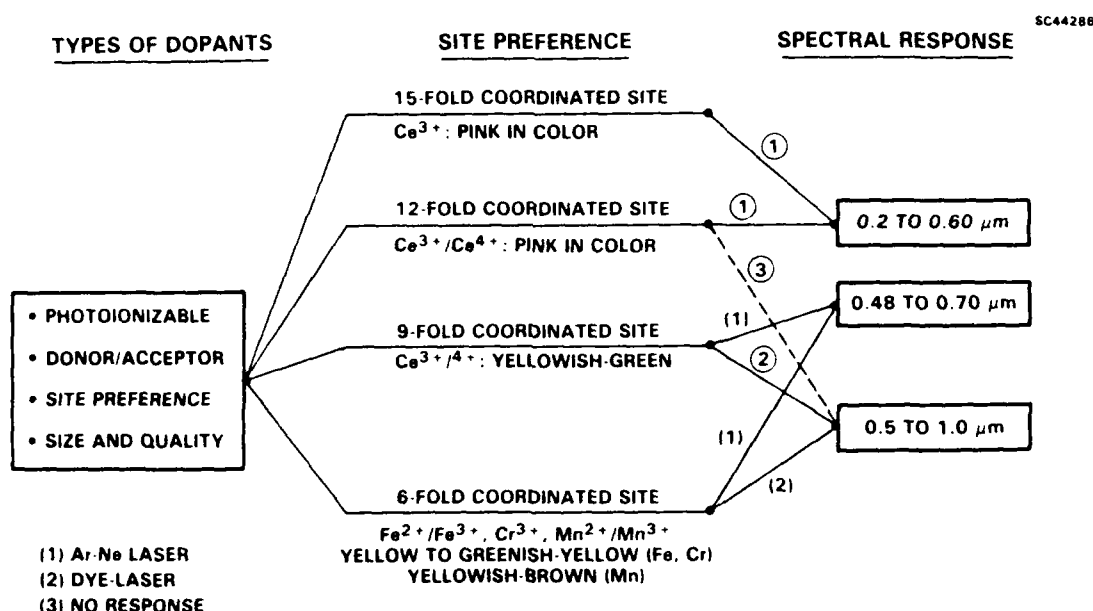


Fig. 4 Role of dopants for photorefractive applications.

Because Ce^{3+} and Cr^{3+} -doped bronze crystals are particularly promising for phase conjugation, laser hardening and optical processing, the growth of these crystals in sizes up to 5 cm diameter is in progress. An example is the growth of Cr^{3+} -doped SBN:60 shown in Fig. 5. This crystal boule is approximately 2.5 cm in diameter and 7 cm in



Fig. 5 Crystal boule photo.

length. BSKNN-2 crystals are also being explored because their ferroelectric and optical properties are similar to BaTiO_3 . Because of the structural flexibility in accommodating dopants and the lack of a second structural phase transition over a range far below room temperature, this material could replace BaTiO_3 for various optical applications.

3.3 Electro-Optic and Pyroelectric Applications of Tungsten Bronze Materials

Single mode planar and channel waveguides have been produced in SBN:60 crystals by sulfur diffusion in a sealed ampule, followed by oxidation in an open tube. Losses in channel waveguides were ~ 15 db/cm for TM polarization and ~ 27 db/cm for TE polarization in z-cut substrates. Electro-optic modulation was observed after poling of the substrate.



The experimentally determined value of the effective electro-optic coefficient was slightly greater than reported earlier for bulk samples of SBN:60, and about 15 times greater than for LiNbO_3 . Based on measurements with the S^{35} radioisotope, the average atomic sulfur concentration was estimated to be about $4 \times 10^{17}/\text{cm}^3$ in the region extending from the surface to a depth of 2.5 μm , and a significant background concentration ($\sim 5 \times 10^{16}/\text{cm}^3$) was present to depths of 20 μm . Currently, efforts are underway to replace sulfur with other suitable diffusing ions in these crystals. However, the current results are very promising and it is expected that with further improvements in crystal quality and diffusing species, this material will have significant value for various electro-optic device applications. In parallel, efforts are also underway to use higher electro-optic coefficient crystals such as SBN:75 and PBN:60, so we can further reduce the voltage requirements for these applications.

La^{3+} -modified SBN:60 single crystals have also been grown in large size and these crystals exhibit excellent response for pyroelectric device applications. The addition of 1 wt% La^{3+} in SBN:60 increases the pyroelectric coefficient by nearly an order of magnitude. Currently, these crystals are being tested as room-temperature pyroelectric detectors. If the performance of these crystals proves to be satisfactory, they may replace HgCdTe-based detectors.

3.4 Growth of Tungsten Bronze Thin Films

In order to include incongruently melting bronzes exhibiting large electro-optic and ferroelectric properties, we also introduced the liquid phase epitaxial (LPE) technique for SBN:50, SKN and PBN:60 compositions with good success. The growth SBN:50 and SKN thin films has opened up new ways to study these materials for SAW and optical applications. Based on our current work, SKN films look more promising for optical applications



Rockwell International
Science Center

SC5441.FTR

since the difference in refractive index between SBN:60 (substrate) and the SKN film is large. Because these films are grown at lower temperatures, their quality appears to be much better for optical applications.



Rockwell International

Science Center

SC5441.FTR

4.0 PUBLICATIONS AND PRESENTATIONS

4.1 Publications

Over 25 technical papers have been prepared and published in refereed journals under this program.

4.2 Presentation

Over 20 technical papers were presented as invited or contributed talks in the USA, England, India, Switzerland, Japan and Australia.



5.0 CONTRIBUTING LABORATORIES

The success of this program was due in large part to the collaboration of many institutions in evaluating these crystals and films allowing us to rapidly improve material characteristics and enhance our overall understanding. The following institutions have played major roles in this research:

<u>Institute</u>	<u>Research Area</u>
Rockwell International Science Center	Photorefractive Electro-Optic Pyroelectric
Naval Research Laboratory	Optical Wave-guides and modulators
Penn State University	Ferroelectric and optical characterization
Caltech	Photorefractive
Army Research Lab. (CNVEO)	Photorefractive Electro-Optic
University of Southern California	Photorefractive
MIT	Spatial Light Modulator (SLM)
Kirtland AFB	Photorefractive
Lawrence Livermore National Lab	Streak Camera (Electro- optic)

The details of the research performed during the past two years are given in the remaining sections of this report in the form of individual research papers. These papers are being submitted to, or have been accepted for publication in, refereed journals.



Rockwell International

Science Center

SC5441.FTR

PROGRESS IN PHOTOREFRACTIVE TUNGSTEN BRONZE CRYSTALS

Progress in photorefractive tungsten bronze crystals

Ratnakar R. Neurgaonkar and Warren K. Cory

Rockwell International Science Center, P.O. Box 1085, Thousand Oaks, California 91360

Received July 23, 1985; accepted October 21, 1985

We review the current status of the photorefractive tungsten bronze family crystals in terms of their growth problems and applications, with special emphasis on the current results for the $\text{Sr}_{1-x}\text{Ba}_x\text{Nb}_2\text{O}_6$ solid-solution system. Ferroelectric morphotropic phase-boundary materials are discussed as an appropriate goal for future development.

INTRODUCTION

The term photorefractive effect has been adopted to refer to optically induced refractive-index changes that occur in many electro-optic materials. This effect has been used recently for optical storage of information, phase conjugation, and nonlinear multiwave mixing applications. These applications require suitable crystals that possess high photorefractive sensitivity, speed, and diffraction efficiency.

Photorefractive effects have been observed in a variety of electro-optic materials, such as $\text{Bi}_{12}\text{SiO}_{20}$, $\text{Bi}_{12}\text{GeO}_{20}$, LiNbO_3 , LiTaO_3 , $(\text{PbLa})(\text{TiZr})\text{O}_3$, KH_2PO_4 , CdS , $\text{Bi}_4\text{Ti}_3\text{O}_{12}$, K_2TaNbO_7 , KNbO_3 , BaTiO_3 , $\text{Ba}_2\text{NaNb}_5\text{O}_{15}$, and $\text{Sr}_{1-x}\text{Ba}_x\text{Nb}_2\text{O}_6$ (SBN).¹⁻¹² and may be considered a general property of electro-optic materials. Depending on the band gap and the electro-optic coefficient of the given crystal, the refractive-index changes may be induced not only by visible light but also by ultraviolet or infrared radiation. The characteristics of a number of currently important electro-optic materials are summarized in Table 1.

At present, a great deal of attention has been focused on two important candidates, namely, perovskite BaTiO_3 and tungsten bronze SBN crystals. BaTiO_3 exhibits several structural transitions, and it has a room-temperature tetragonal structure with very large electro-optic coefficients, e.g., r_{11} and r_{12} . The origin of these anomalously large constants is clearly the phase change below room temperature to an orthorhombic ferroelectric phase. The incipient phase change destabilizes the polar vector in the plane perpendicular to the fourfold axis of the tetragonal form, giving exceedingly high values of ϵ_{11} and thus large electro-optic coefficients, e.g., r_{11} and r_{12} . Unfortunately, however, the normal phase change necessarily carries with it a strong temperature dependence for ϵ_{11} and the electro-optic coefficients. Even worse, if the crystal is accidentally cooled below room temperature, the phase change leads to a catastrophic destruction of the single-domain state essential for device studies. A second major disadvantage of BaTiO_3 crystal is the high paraelectric prototype symmetry ($m3m$), which has three equivalent fourfold axes and thus gives the possibility of 90° twin domains. These ferroelectric twins are difficult to remove by poling and limit strictly the transverse field levels E_\perp that can be tolerated. In spite of these difficulties, small but relatively good-quality BaTiO_3 crystals are available from Sanders Associates for photorefractive device studies.

On the other hand, the tungsten bronze SBN solid-solution-system crystals, in particular $\text{Sr}_{0.6}\text{Ba}_{0.4}\text{Nb}_2\text{O}_6$ (SBN:60), are relatively easier to grow, and crystals as large as 2 to 3 cm in diameter are available.^{13,14} Since this composition exhibits only one paraelectric-ferroelectric phase transition and a unique polar axis, the crystals have no 90° twinning or other problems. In this paper we review the state of the art of this crystal along with that of other tungsten bronze crystals for photorefractive applications.

FERROELECTRIC TUNGSTEN BRONZE FAMILY CRYSTALS

Ferroelectric tungsten bronze oxides have been studied for their electro-optic and pyroelectric^{15,16} properties and have been found to be most useful for these applications. The bronze compositions can be represented by the general formulas as $(A_1)_4(A_2)_2C_4B_{10}O_{30}$ and $(A_1)_4(A_2)_2B_{10}O_{30}$, in which A_1 , A_2 , C , and B are 15-, 12-, 9-, and 6-fold coordinated sites in the structure. The tetragonal bronze prototypic structure is shown in Fig. 1 in projection on the (001) plane.^{17,18} A wide range of solid solutions can be obtained by the substitution of different A_1 , A_2 , and B cations,¹⁹⁻²² and a number of different types of ferroelectric and ferroelastic phases have been identified (more than 100 compounds and numerous solid solutions). The ferroelectric phases can be divided into two groups: those with tetragonal symmetry ($4mm$), which are ferroelectric-paraelectric, and those with orthorhombic symmetry ($mm2$), which are both ferroelectric and ferroelastic.

Crystals that are noncentrosymmetric, i.e., that lack a center of symmetry, may exhibit both linear and quadratic electro-optic and elasto-optic effects. In all the crystals discussed here the linear effects are dominant. Thus a linear change in optical index of refraction can be induced by an electric field (electro-optic effect), or by strain (elasto-optic effect), or under illumination by a laser (photorefractive effect). Strain can be produced by an electric or (piezoelectric) field by a stress (elasticity). The matrices of electro-optic coefficients in the reduced matrix form²³ r_{ij} are given in Table 2.

In the tungsten bronze family in general, the effects (r_{33}) and (r_{31}) are large for the orthorhombic ($mm2$) bronze crystals, while the transverse (r_{13}) effects are large for tetragonal ($4mm$) bronze crystals; but this can change for compositions

Table 1. Photorefractive Characteristics of Electro-Optic Materials

Crystal	Electro-Optic Coefficient (M/V)	Crystal Structure	Photorefractive Sensitivity (cm ² /J)	Response Time (msec)	T (°C)
Bi ₁₂ SiO ₂₀	$r_{11} = 5 \times 10^{-12}$	Cubic	4×10^{-7}	~1-10	-
Bi ₁₂ GeO ₂₀	$r_{11} = 3.2 \times 10^{-12}$	Cubic	-	-	-
LiNbO ₃ :Fe	$r_{33} = 31.8 \times 10^{-12}$	Trigonal	5×10^{-7}	~2000	1150
LiNbO ₃ :Rh	$r_{33} = 31.8 \times 10^{-12}$	Trigonal	7×10^{-7}	~2000	1150
BaTiO ₃ -doped (KTN)	$r_{33} = 802 \times 10^{-12}$ $= 1400 \times 10^{-12}$	Tetragonal Cubic	7×10^{-7}	-	120 10
KNbO ₃ :Mn	$r_{42} = 380 \times 10^{-12}$	Ortho	-	≤100	480
KNbO ₃ :Fe	$r_{42} = 380 \times 10^{-12}$	Ortho	-	~2000	580
Ba _{0.5} NaNbO ₃ (Mo or Fe)	$r_{42} = 57 \times 10^{-12}$	Ortho	$\sim 8 \times 10^{-5}$	-	72
SBN:Ce	$r_{42} = 420 \times 10^{-12}$	Tetragonal	9.5×10^{-7}	~80	75
SBN	$r_{42} = 420 \times 10^{-12}$	Tetragonal	3.2×10^{-5}	-	56
BBN	$r_{42} = 1350 \times 10^{-12}$	Tetragonal	5×10^{-4}	-	-

close to morphotropic phase boundaries. The SBN solid-solution crystals exhibit exceptionally large electro-optic coefficients, which are based on three independent nonzero moduli: $r_{33} = r_{22}$, $r_{42} = r_{51}$, and r_{63} . The largest electro-optic effect is observed for the dc electric field parallel to the single tetrad symmetry axis x_3 , which is also the polar axis, and with light propagation normal to the x_3 direction. The phase retardation in this case is given by

$$\Gamma = (2\pi/\lambda_0)(n_y' - n_x'), \quad (1)$$

where l is the path length, λ_0 is the free-space wavelength, and n_x' and n_y' are the principal indices of refraction normal to the direction of propagation x_3 . In this case

$$n_x' = n_o - n_e r_{42} E / 2, \quad n_y' = n_o + n_e r_{42} E / 2, \quad (2)$$

where n_o and n_e are the ordinary and extraordinary optical indices, respectively.

For light parallel to x_3 and an electric field parallel to x_1 or an axis, Γ is written as above but for n_x' and n_y' , which are

$$n_x' = n_o, \quad n_y' = n_o - n_e \frac{r_{33} E^2}{2(n_o^2 - n_e^2)}. \quad (3)$$

Crystals that have been investigated in the SBN series are those for which $x = 0.25, 0.40, 0.50$, and 0.75 .^{15,24} The half-wave field-distance products $|\mathbf{E} \cdot \mathbf{L}|_{\lambda/2}$ at 632.8 nm for the electric field along x_3 with light normal to x_3 and polarized at 45° with respect to principal axes, are shown in Table 3. In SBN for a one-to-one aspect ratio of electric-field path to optical path length, the half-wave field-distance product $|\mathbf{E} \cdot \mathbf{L}|_{\lambda/2}$ is 48 V at 15 MHz.¹⁴ By way of comparison, this is equivalent to the quadratic effect in $\text{KTa}_{1-x}\text{Nb}_x\text{O}_3$ (KTN) at dc bias fields of 2000 V. The 48 V required is also 60 times smaller than 2800 V obtained previously for LiTaO_3 and LiNbO_3 .²⁵ Because of such excellent electro-optic properties for the SBN solid solution, considerable research has been performed on this composition family as well as on other bronze composition crystals. Table 4 lists a number of orthorhombic and tetragonal tungsten bronze crystals developed at various research laboratories and their important ferroelectric and electro-optic properties. Some of the unique advantages of bronze crystals are as follows:

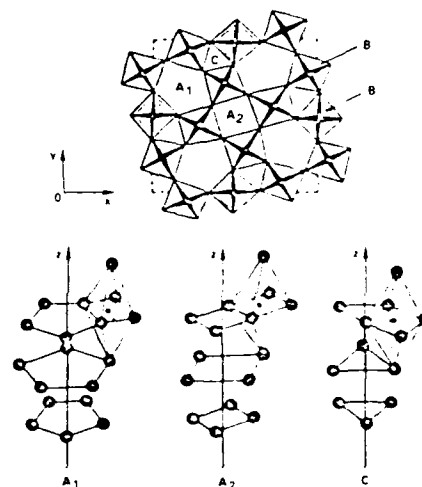


Fig. 1. Projection of structure of tetragonal tungsten bronze parallel to (001).

Table 2. Electro-Optic Matrices r_{ij} for the ($mm2$) and ($4mm$) Bronze Crystals

Orthorhombic ($mm2$)			Tetragonal ($4mm$)		
0	0	r_{13}	0	0	r_{13}
0	0	r_{23}	0	0	r_{13}
0	0	r_{33}	0	0	r_{33}
0	r_{42}	0	0	r_{42}	0
r_{51}	0	0	r_{42}	0	0
0	0	0	0	0	0

Table 3. Half-Wave Field-Distance Products for SBN

f	$ \mathbf{E} \cdot \mathbf{L} _{\lambda/2}^a$			
	$x = 0.75$	$x = 0.40$	$x = 0.50$	$x = 0.25$
dc	37 V dc	150 V dc	250 V dc	-
1 MHz	80 V pp	300 V pp	676 V pp	1340 V pp
15 MHz	48 V pp	200 V pp	580 V pp	1236 V pp

^a pp, peak to peak.

Table 4. List of Important Tungsten Bronze Crystals^a

Composition	T _c (°C)	Dielectric Coefficient		Piezoelectric Coefficient		Electro-Optic Coefficient × 10 ⁻¹² m/V	Unit Cell			Crystal Shape ^b
		ε ₃₃	ε ₁₁	d ₃₃	d ₁₅		a _A	b _A	c _A	
Tetragonal crystals										
SBN:75	56	3400	-	-	-	1400	12.440	-	3.924	C
SBN:60	75	880	470	130	40	420	12.467	-	3.937	C
SBN:50	128	450	300	100	60	180	12.475	-	3.952	C
SKN	150	1000	800	90	30	270	12.470	-	3.939	C
BSKNN	207	200	350	75	84	380	12.560	-	3.973	S
K ₁ (Li ₂ Nb ₃ O ₁₅)	405	115	306	57	68	80	12.580	-	4.015	S
PBN:60	350	310	560	100	300	1000	12.576	-	3.978	S
Ba ₂ Ti ₂ Nb ₂ O ₁₀ ^d	245	209	193	-	-	420	12.589	-	4.020	S
Orthorhombic crystals										
Pb ₂ KNb ₃ O ₁₅	460	129	1550	62	470	r ₄₂ = 100	17.780	17.961	7.784	C
Ba ₂ NaNb ₃ O ₁₅	560	57	242	37	42	r ₄₂ = 92	17.590	17.613	7.982	C
Sr ₂ NaNb ₃ O ₁₅	270	1500	-	-	-	r ₄₂ = 400	17.450	17.493	7.784	C
K ₂ BiNb ₃ O ₁₅	405	500	400	-	-	-	17.851	17.852	7.804	C
K ₂ (Li ₂ Nb ₂ -Ta ₂ O ₁₅)	150	375	300	-	-	-	-	-	-	C

^a Refs. 26-39 (selected references).^b C, cylindrical; S, square.^c All tetragonal crystals have been grown at Rockwell.^d This bigger unit cell has c large.

(1) This family of crystals possesses extraordinarily large transverse and longitudinal electro-optic coefficients, especially near a morphotropic phase boundary (MPB).

(2) Trade-off between sensitivity and speed can be investigated for photorefractive studies because of the structural flexibility. In the tungsten bronze structure, several crystallographic sites are partially empty, which allows the composition to be tailored.

(3) Several ferroelectric MPB compositions have been identified for this family.

(4) The lower prototype symmetry gives a large family of g (quadratic) constants (quadratic and electro-optic) and the possibility of anisotropic conduction. The nonzero values are g_{11} , g_{12} , g_{13} , g_{44} , and g_{56} , as compared to g_{11} , g_{12} , and g_{44} in perovskites.

(5) In the tetragonal bronzes, since the prototype symmetry is $4mm$, only one unique fourfold axis exists, and 90° twins are absent; hence crystals are not likely to crack during poling, as reported for BaTiO₃.

GROWTH OF TUNGSTEN BRONZE CRYSTALS

The growth of orthorhombic ($mm2$) and tetragonal ($4mm$) bronze crystals has been the subject of great interest for many years, and considerable progress has been made toward developing crystals of suitable size and quality. The most important orthorhombic crystals are based on Pb²⁺, e.g., Pb₂KNb₃O₁₅, PbNb₃O₆, Pb₂NaNb₃O₁₅; they are all attractive candidates for surface acoustic waves (SAW's), electro-optic, and piezoelectric transducer applications. These crystals are extremely difficult to grow because of several problems associated with their growth, such as the volatilization of Pb²⁺ at the growth temperature and the cracking of crystals when cycling through the paraelectric-ferroelectric phase-transition temperature. The other orthorhombic bronze crystals, such as Ba₂NaNb₃O₁₅ and K₂Li₂Nb₃O₁₅, are available in small sizes; however, their photorefractive properties are similar to those of LiNbO₃⁴⁰⁻⁴², hence these compositions are not widely studied.

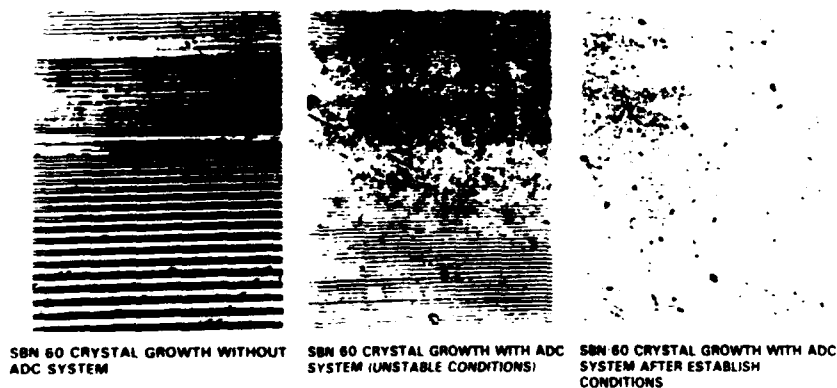


Fig. 2. Growth of striation-free ferroelectric SBN 60 single crystals with ADC, automatic diameter-control system.

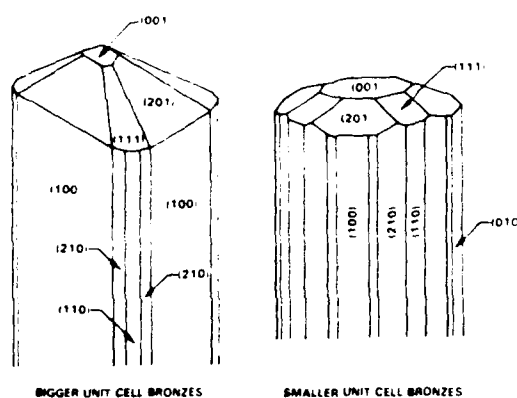


Fig. 3. Idealized forms of the tetragonal tungsten bronze crystals.

Since the tetragonal bronze composition crystals exhibit excellent transverse (r_{12}) electro-optic and pyroelectric properties, Neurgaonkar and co-workers^{13,33,44} have extensively studied the problems associated with these crystals and have successfully established conditions that permit use of the Czochralski technique. The more prominent examples in this category are $\text{Sr}_{0.7}\text{Ba}_{0.3}\text{Nb}_2\text{O}_6$ (SBN:75), (SBN:60), $\text{Pb}_{0.7}\text{Ba}_{0.3}\text{Nb}_2\text{O}_6$ (PBN:60), and $\text{Ba}_{2-x}\text{Sr}_x\text{K}_{1-x}\text{Nb}_2\text{O}_6$ (BSKNN). Although large-sized crystals have been developed for these compositions, the problems associated with these tetragonal bronze crystals are as follows:

- (1) They are multicomponent and solid-solution systems, hence it is difficult to establish true congruent melting compositions for optical applications.
- (2) They possess high melting temperatures (greater than 1500°C); hence volatilization and oxidation-reduction problems ($\text{Nb}^{5+} \rightarrow \text{Nb}^{4+}$) are common.
- (3) Exchange among crystallographic sites, specifically of the 15- and 12-fold coordinated ions such as Ba^{2+} and Sr^{2+} , causes severe striation problems.
- (4) Cracking can occur in crystals when they pass through the paraelectric-ferroelectric phase-transition temperature. For tetragonal crystals this is a less severe problem than for the orthorhombic forms, but it is still of concern, e.g., in PBN:60, BSKNN, and KLN.

Among these crystals, SBN:60 and SBN:50 are much easier to grow than other tetragonal bronzes; crystals as large as 2 to 3 cm in diameter of optical quality are being grown, as shown in Fig. 2 for SBN:60. (SBN:60 is the only congruent melting composition in the SrNb_2O_6 - BaNb_2O_6 system.²⁷) The recent development of optical-quality material is a major step for this family of crystals. In our work we have found that the quality of these crystals depends on the following factors:

- (1) Impurities in starting materials: Ca^{2+} , Fe^{3+} , Mg^{2+} , Na^+ , etc.
- (2) Rotation and pulling rates: faster pulling rates were needed to control temperature instability because of poor thermal conductivity.
- (3) Cooling rate variation: percent of Sr^{2+} and Ba^{2+} distribution changes on 15- and 12-fold coordinated sites for different cooling rates.

A most striking and uncommon feature of these tetragonal bronze crystals is that they all show natural facets. The smaller unit cell bronzes, e.g., SBN:60, SBN:50, and $\text{Sr}_2\text{KNb}_2\text{O}_6$, are cylindrical in shape and exhibit 24 well-defined facets,⁴⁵ whereas the bigger unit cell bronzes, e.g., BSKNN, PBN:60, and BTN, are square in shape and exhibit four well-defined facets. Figure 3 shows the idealized forms for these crystals. This is significant for the study and utilization of this family of crystals, since the task of crystal orientation is otherwise tedious and time consuming.

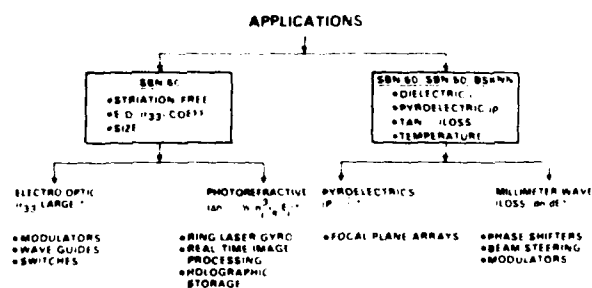
The ferroelectric and piezoelectric properties for these bronze composition crystals have been investigated, and these properties, e.g., ϵ_{33} , ϵ_{11} , d_{33} , and d_{15} , are significantly different from smaller to bigger unit cell bronzes. For example, ϵ_{33} and d_{33} are larger for smaller unit cell bronzes, whereas ϵ_{11} and d_{15} are larger for bigger unit cell bronzes. Since the d_{15} coefficient is equivalent to r_{51} (or to r_{42} in the tetragonal system), it is expected that the bigger unit cell bronzes should have similar electro-optic photorefractive properties to those seen for BaTiO_3 and KNbO_3 crystals. Table 5 summarizes the classification of results obtained for the tetragonal bronzes; the classification has been made on the basis of unit cell dimensions, Curie temperature, and dielectric and piezoelectric properties. The availability of

Table 5. Classification of Tetragonal Tungsten Bronze Family Crystals

Tungsten Bronze Compositions with Smaller Unit Cell Dimensions ^a	Tungsten Bronze Compositions with Bigger Unit Cell Dimensions ^a
Crystal habit is cylindrical with 24 defined facets	Crystal habit is square with 4 facets
Relatively low T_c , below 200°C	Moderately high T_c , above 200°C
Relatively high dielectric constant (ϵ_{33}) and low ϵ_{11}	Moderately high dielectric constant (ϵ_{11}) and low ϵ_{33}
High piezoelectric coefficient d_{33} but low d_{15} at room temperature	High piezoelectric coefficient d_{15} but low d_{33} at room temperature
High electro-optic (r_{12}) and pyroelectric coefficients	Moderately high electro-optic (r_{51}) and pyroelectric coefficients
Large, excellent quality crystals available (2-3-cm diameter)	Moderately large crystals available (1-1.5-cm diameter)

^a e.g., SBN, SKN.

^b e.g., BSKNN, BTN, $\text{Pb}_{1-x}\text{Ba}_x\text{Nb}_2\text{O}_6$, KLiNbO_3 .



--- REPRESENTS THE FIGURE OF MERIT

Fig. 4. Applications of ferroelectric tungsten bronze crystals.

such improved-quality bronze crystals has opened up a variety of new device concepts that includes electro-optic, photorefractive, pyroelectric, SAW millimeter-wave, and transducer applications. Figure 4 shows a number of device concepts being explored at Rockwell International using both bronze crystals and their ceramics. In each case, significant progress has been made.^{16,46-50}

PHOTOREFRACTIVE PROPERTIES

To provide an appropriate context for the discussion of material development, the projected applications of photorefractive materials and the physical basis of the optical effects that make these applications possible should be considered in some detail. These applications include real-time holography, optical data storage, and phase-conjugate wavefront generation. Recently, increasing attention has been focused on using coherent signal beam amplification in two-wave mixing. These new applications include image amplification, vibrational analysis, nonreciprocal transmission, laser-gyro biasing, and optical computing.⁵¹⁻⁵⁶ All these applications share a need for local changes in refractive index produced by illumination. The issues connected with photorefractive effect include the sensitivity of the given material to illumination and the speed which the index can be made to change. In spontaneously polarized ferroelectric crystals, light-induced free carriers excited in an illuminated region of the crystal are displaced along the polar axis to be retrapped. The resulting space charge generates an electric field E , which gives rise to a refractive-index change Δn through the linear electro-optic effect, e.g.,

$$\Delta n = \frac{1}{2} n^3 r E, \quad (4)$$

where r is the electro-optic coefficient.

The space-charge field E generated by the charge displacement and retrapping is given simply by⁵⁷

$$E = \frac{1}{\epsilon} \int p dx = \frac{1}{\epsilon} \int J dt, \quad (5)$$

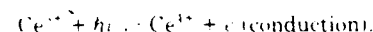
p is the polarization, ϵ is the dielectric constant, and the current density J is a function of both x and t . In general, $J(x)$ is quite complex and is a function of the light intensity $I(x)$

$$J(x) = n(x)(\mu E_x + E_{x0}) + KaI(x) + eD \frac{dn}{dx} + p \frac{dT}{dt} + \Delta \mu \frac{dn}{dt}, \quad (6)$$

The first term in Eq. (6) is the local conduction in a field, which is the sum of space-charge and possible external components. The second term is the volume photovoltaic effect, the third term is due to free-carrier diffusion driven by the concentration gradient (dn/dx), the fourth and fifth terms are transient phenomena that are due to pyroelectric and excited-state polarization, respectively. In view of the complexity of the phenomena contributing to $J(x)$, it is difficult to predict E values in a new crystal. Since the electro-optic coefficient in a given crystal is more or less independent of minor substitutions, the improvement in photorefractive sensitivity and speed within a single composition has to come from the magnitude and speed of the buildup of the electric field E . For this reason, researchers in several

laboratories around the world are concentrating on finding suitable electrically active dopants for those materials having large electro-optic coefficients.

No single material combines all the desired features; hence a large number of ferroelectric crystal compositions have been grown and characterized to determine a possible trade-off between sensitivity and speed. The nonferroelectric $\text{Bi}_{12}\text{SiO}_{20}$ crystal has the desired response time (~ 1 msec), but its photorefractive sensitivity is moderate because r_{33} is low. On the other hand, all ferroelectric crystals summarized in Table 1 have exceedingly high sensitivity but moderate response times. If these ferroelectric crystals are to be used for device applications, their response time must be reduced to the order of 1 msec or better. This is a key issue in ferroelectric crystal development, and efforts are under way to investigate this problem. Figure 5 shows the generic topics that need to be addressed to determine the trade-off between sensitivity and speed in a ferroelectric crystal, for instance in SBN:60. Since the electro-optic coefficient (r_{33}) will be unaffected for given impurities, the space charge can be controlled by adding specific impurity levels. It is now well established that doping crystals with impurities that are readily photoionized by the incident radiation greatly increases the susceptibility of crystals to index changes. Recently Megumi *et al.*⁵⁸ reported that the addition of Ce produces a broad absorption in SBN:60 crystals, which increases the sensitivity considerably. Undoped SBN:60 is transparent in the visible range, with its fundamental absorption edge at about $0.37 \mu\text{m}$. The addition of Ce develops a distinct but wide absorption band around $0.50 \mu\text{m}$, which differs markedly from the electronic absorption edge. The Ce ion photoionizes by means of the reaction



From this work⁵⁸ both the Ce^{3+} and the Ce^{4+} valence states appear to be present, since the sensitivity improves from 10^{-7} to $10^{-5} \text{ cm}^2/\text{J}$. This improvement is 2 orders of magnitude higher than to Fe^{3+} , U^{4+} , and Rh^{3+} -doped LiNbO_3 .^{39,42}

Recently Neurgaonkar *et al.*⁵⁹ successfully demonstrated the growth of Ce- and Fe-doped SBN:60 single crystals as part of an effort to study in detail the role of these ions in photorefractive device applications. As shown in Fig. 6, approximately 1-2-cm-diameter Ce- and Fe-doped SBN:60 crystals have been grown along the (001) direction by using the Czochralski technique. The doping of SBN:60 with Fe, and with Fe and Ce together, has not been done previously; and Fe is expected to produce interesting results, as it has

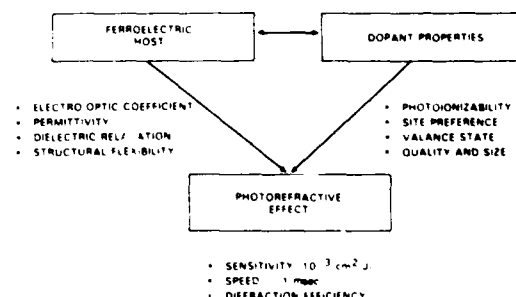


Fig. 5. Factors determining the photorefractive sensitivity and speed in ferroelectric crystals.

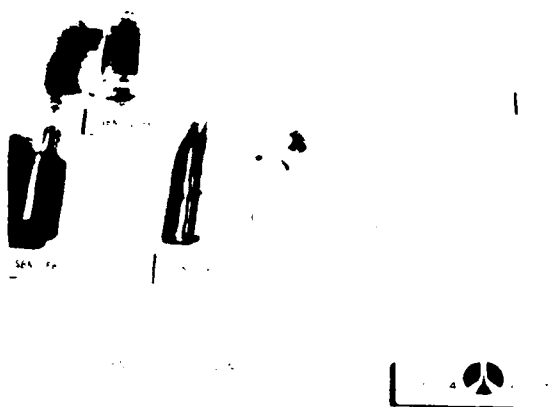


Fig. 6. Doped and undoped SBN:60 single crystals grown along the (100) direction.

Table 6. Goals for Photorefractive Studies and Current Status

Desired Properties	Observed Properties
Response time < 1 msec	Response time achieved ≤ 100 msec
Sensitivity $> 10^{11}$ (ph/cm ²)/J	Sensitivity achieved $> 10^{11}$ (ph/cm ²)/J
Large coupling coefficient > 1 cm ⁻¹	Coupling coefficient achieved > 11 cm ⁻¹
Large sized and optical quality crystals	Large sized (2.5-cm diameter) and striation-free SBN:60 and Ce ³⁺ -doped SBN:60 crystals are available
Large electro-optic coefficient necessary	Electro-optic coefficient enhanced for Fe ³⁺ and Ce ³⁺ doping

been observed to do in other ferroelectric crystals, e.g., LiNbO₃ and KNbO₃.⁴²

Ce-doped SBN:60 crystals show minimum or no striations, and crystals are of optical quality, whereas Fe-doped crystals are highly striated under all growth conditions, and the striations are found difficult to suppress. In the tungsten bronze structure, Ce³⁺ and Ce⁴⁺ are expected to occupy the 12- and 9-fold coordinated sites, while Fe²⁺ and Fe³⁺ ions are expected to occupy 6-fold coordinated sites. Our results suggest that the existence of striations in SBN:60 crystals depends strongly on the type of dopant and its location in the structure. Since Mn²⁺, Mn³⁺, Co²⁺, Co³⁺, Ti³⁺, Ti⁴⁺, etc.

have similar ionic size and site preferences to those of Fe³⁺, it would be interesting to check their influence on striations in SBN:60 crystals.

The development of striation-free Ce-doped SBN:60 crystals makes possible the evaluation of photorefractive properties, specifically sensitivity and speed. Typical 6 mm \times 6 mm \times 6 mm sized cubes have been supplied for the examination, and two- and four-wave mixing techniques are being used. These measurements are being made at California Institute of Technology, Rockwell International, and other laboratories, and these measurements will be reinvestigated as better-quality crystals become available. Table 6 summarizes the proposed goals set and results obtained to date for this material. In agreement with the results reported by Megumi *et al.*,^{5b} the present crystals also show the typical Ce broad absorption band around 0.50 μ m, and this band remained unchanged from one sample to another. Both the photorefractive sensitivity and speed were estimated for these crystals (Table 6), and the results are promising.

A useful evaluation method for photorefractive sensitivity of electro-optic crystal is measured by the sensitivity S as given by Glass *et al.*⁵⁷ The sensitivity is defined as the index change per absorbed energy density, i.e.,

$$S = \frac{\Delta n}{\Delta W_{\text{abs}}} \quad (7)$$

For a 0.1 wt.% Ce-doped crystal, this sensitivity was measured to be 6.5×10^{-7} (cm²/J). This value is in close agreement with value reported by Megumi *et al.*^{5b} and exceeds that of Fe-doped LiNbO₃ (Ref. 41) and Mo⁴⁺- and Fe³⁺-doped Ba₂NaNb₃O₁₅ (Ref. 5) by more than 2 orders of magnitude. For this addition, the response time also changed becoming faster (80–100 msec) compared with that of the undoped crystal (1000 msec). This is considered a significant improvement in ferroelectric crystals, and although details regarding the mechanism are not yet known, both the response time and sensitivity can be improved with a suitable dopant. The Fe-doped crystal also showed similar improvement; however, the estimation of precise values was difficult because of the crystal quality. Efforts are under way to reinvestigate the striation problems associated with Fe-doped SBN:60 crystals.

The improvement in photorefractive characteristics needs to be related to the possible roles of these impurities. In the ideal picture, one needs both a donor of electrons and an acceptor to enhance the space-charge field E_{sc} . These might be Ce³⁺ and Ce⁴⁺, Fe²⁺ and Fe³⁺, Ce³⁺ and Fe³⁺, or combinations of these with Nb⁴⁺ and various vacancies in the SBN:60

Table 7. Valence States of Dopants in SBN:60^a

Dopant	Crystallographic Sites				Donor	Acceptor	Stable States ^b
	12	9	6				
Ce	Ce ³⁺	Ce ⁴⁺		Ce ³⁺	Ce ⁴⁺	Ce ³⁺	Ce ³⁺
Ce and Nb	Ce ³⁺	Ce ⁴⁺	Nb ⁴⁺	Ce ³⁺ , Nb ⁴⁺	Ce ⁴⁺		Ce ³⁺ , Nb ⁵⁺
Ce	Ce ³⁺			Ce ³⁺	Cation vac		Ce ³⁺
Fe			Fe ²⁺ , Fe ³⁺	Fe ²⁺	Fe ³⁺		Fe ³⁺
Fe, Nb			Fe ²⁺ , Nb ⁴⁺	Nb ⁴⁺	Fe ³⁺		Fe ³⁺ , Nb ⁵⁺
Fe			Fe ²⁺	Cation Vac	Fe ³⁺		Fe ³⁺
Ce, Fe	Ce ³⁺		Fe ²⁺	Ce ³⁺	Fe ³⁺		Ce ³⁺ , Fe ³⁺

^avac, Vacant.

^bvac, cation site, growth temperature.

structure. The current results clearly indicate that the addition of Ce and Fe dopant enhances the photorefractive properties; however, the presence of the various charge states of $\text{Ce}^{3+}/\text{Ce}^{4+}$ ($\text{Fe}^{2+}/\text{Fe}^{3+}$) has not yet been established. Because Ce^{3+} (or Fe^{3+}) is stable at the growth temperature, there exist several possibilities for the species that form charge traps, as shown in Table 7.

In the present case, the tendency of Nb^{5+} to reduce to Nb^{4+} provides the possibility of donor states. Since the preferred state of Ce at the growth temperature is Ce^{3+} , a donor, some questions concerning the identity of the acceptor in Ce-doped crystals remain. The observed tendency of Nb^{5+} to reduce the growth temperature may encourage the formation of vacancies, which would act as either donors or acceptors. Currently we are using optical and Mossbauer spectroscopy to identify the donor and acceptor species in these crystals. Once this is accomplished, both sensitivity and speed should be controllable.

The improvement in photorefractive properties obtained by doping SBN:60 crystals presents a unique opportunity to study new device concepts. At the same time, these studies provide the basis for understanding the photorefractive mechanism responsible for these improvements and guide the search for new classes of electro-optic materials.

FUTURE TUNGSTEN BRONZE FAMILY MATERIALS

Another approach to the development of improved photorefractive materials is the use of morphotropic phase boundary (MPB) composition crystals, i.e., investigating photorefractive sensitivity and speed in materials having a large electro-optic effect. The electro-optic properties close to the MPB regions are at least 5 to 10 times better than the current best materials, such as SBN:60 and BaTiO_3 , and offer a unique opportunity to develop superior photorefractive materials. Figure 7 shows a typical ferroelectric tungsten bronze $\text{Pb}_{1-x}\text{Ba}_x\text{Nb}_2\text{O}_6$ system, in which the MPB region is located at $x = 0.37$.⁶¹ In this region, the electro-optic, dielectric, pyroelectric, and piezoelectric properties are exceptionally large, and they are largely temperature independent.

Several of the most useful tungsten bronze and perovskite systems show MPB's near which the polarization is large, giving large electro-optic, dielectric, and other properties. As shown in Fig. 7, on a binary phase diagram a MPB ap-

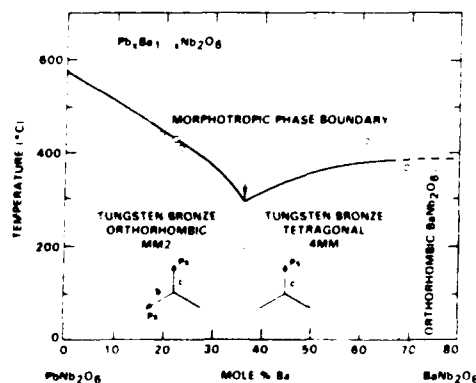


Fig. 7. Phase diagram for the $\text{Pb}_{1-x}\text{Ba}_x\text{Nb}_2\text{O}_6$ solid solution system.

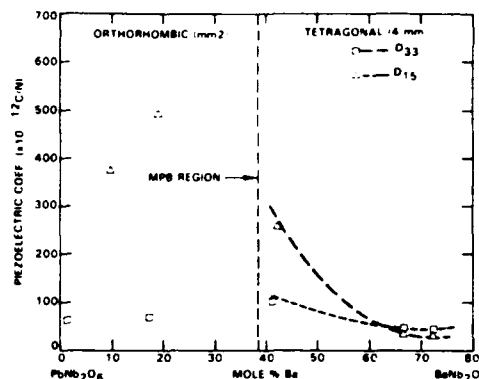


Fig. 8. Piezoelectric (d_{11} and d_{15}) coefficients as a function of composition in the $\text{Pb}_{1-x}\text{Ba}_x\text{Nb}_2\text{O}_6$ system.

pears as a nearly vertical line separating two ferroelectric phases, i.e., the boundary occurs at a nearly constant composition over a wide temperature range up to the Curie temperature. Poled crystals near such boundaries show unique and enhanced electro-optic properties because of the proximity in free energy of an alternate ferroelectric structure. A detailed description of MPB behavior has been provided by Jaffe *et al.*⁶²

For the $\text{Pb}_{1-x}\text{Ba}_x\text{Nb}_2\text{O}_6$ system the coexisting phases at the MPB are tetragonal and orthorhombic. In the tetragonal ($4mm$) symmetry for ferroelectric bronzes, the electro-optic coefficients r_{ij} of single domains are given from the phenomenological model of Cross *et al.*^{63,64} in terms of the g_{ij} quadratic coefficients of the prototype by relations of the form

$$\begin{aligned} r_{11} &= 2g_{11}P/\epsilon_{11}, \\ r_{12} &= 2g_{12}P/\epsilon_{11}, \\ r_{13} &= r_{31} = g_{13}P/\epsilon_{11}, \end{aligned} \quad (8)$$

where r is the electro-optic coefficient, p is polarization, and ϵ is the dielectric constant.

The last relation is of special interest in that for a composition close to the MPB, but a long way from the ferroelectric Curie temperature, both P_1 and ϵ_{11} can be very large and can be largely independent of temperature.

For orthorhombic compositions close to the MPB, the equivalent relations are as follows⁶⁴:

$$\begin{aligned} r_{11} &= r_{22} = 2g_{11}P/\epsilon_{11}, \\ r_{12} &= r_{21} = 2g_{12}P/\epsilon_{11}, \\ r_{31} &= r_{13} = 2g_{13}P/\epsilon_{11}, \\ r_{41} &= r_{14} = g_{14}P/\epsilon_{11}, \\ r_{51} &= r_{15} = g_{15}P/\epsilon_{11}, \end{aligned} \quad (9)$$

Now it is P_2 and ϵ_{33} that will be large, so that the anomalously large and nearly temperature-invariant values of r_{33} and r_{34} are to be expected. A detailed description of the phenomenological model has been given by Cross *et al.*⁶³

In the $\text{Pb}_{1-x}\text{Ba}_x\text{Nb}_2\text{O}_6$ system Cross *et al.*^{63,66} have already demonstrated that it is possible to grow small crystals at compositions close to the PBN:60 boundary phase. For

compositions on both sides of the boundary, as expected, the g_{ij} quadratic coefficients are largely temperature independent as expected, and their quadratic coefficients are bigger than those for SBN. With increasing lead content, they have also demonstrated that the piezoelectric coefficients d_{11} and d_{24} (as shown in Fig. 8), which are equivalent to r_{31} and r_{42} , do in fact escalate dramatically as the composition approaches the MPB and that the values are larger than those for BaTiO₃. Since the Pb²⁺-containing crystals are often difficult to grow, we have identified other MPB systems within the tungsten bronze family, e.g., Ba₂NaNb₅O₁₅-Sr₂NaNb₅O₁₅, Ba₂KNb₅O₁₅-Sr₂NaNb₅O₁₅, and Sr₂NaNb₅O₁₅-Ca₂NaNb₅O₁₅.³⁰ The major advantages of the MPB crystals for photorefractive studies are the following:

- (1) The separation from the phase boundary is a function of composition, not temperatures; i.e., the boundary is morphotropic, so that the very high values of the constants persist over a wide temperature range.
- (2) For compositions close to the boundary, r_{31} and r_{42} values larger than those for BaTiO₃ are possible.
- (3) Since the prototype symmetry is 4 *mm*, only one unique fourfold axis exists and 90° twins are not possible; hence cracking is not so severe a problem as reported for BaTiO₃.
- (4) Very large transverse drift fields could be achieved.

At Rockwell International, we are devoting considerable effort to the development of MPB composition crystals in the expectation that they can provide a real breakthrough for device applications based on the photorefractive effect. These crystals should also be beneficial for other applications, such as electro-optic switches and modulators, transverse pyroelectric focal plane arrays, SAW's, and piezoelectric transducers. The potential benefit in these applications justifies the development of these materials, although the materials may be quite difficult to grow in appropriate size and quality.

ACKNOWLEDGMENTS

This research work on the tungsten bronze family crystals and their applications was supported by the Defense Advanced Research Projects Agency (contract no. N00014-82-C-2466). In this regard, authors wish to thank Richard Reynolds and John Neft for their encouragements and technical support. The authors are also grateful for the discussions on this research with Bill Hall, John Oliver, L. E. Cross, A. Yariv, and Monte Khoshnevisan.

REFERENCES

1. R. L. Townsend and J. T. LaMachia, *J. Appl. Phys.* **41**, 5188 (1976).
2. P. Gunter, U. Fluckiger, J. P. Hugnard, and F. Micheron, *Ferroelectrics* **13**, 297 (1976).
3. F. S. Chen, *J. Appl. Phys.* **38**, 3148 (1967).
4. R. Orlovski, J. A. Boatner, and E. Kratzig, *Opt. Commun.* **35**, 45 (1981).
5. L. C. Anaden, D. L. Stachler, and A. W. Stephens, *Appl. Phys. Lett.* **18**, 607 (1971).
6. J. B. Thaxter, *Appl. Phys. Lett.* **15**, 210 (1969).
7. L. H. Liu, *Proc. IEEE* **57**, 252 (1969).
8. M. P. P. and F. Micheron, *J. Appl. Phys.* **48**, 3683 (1977).
9. A. M. Fridkin, B. N. Popov, and K. A. Verkhovskaya, *Appl. Phys. Lett.* **10**, 17 (1968).
10. A. Ashkin, B. Tell, and J. M. Dziedzic, *IEEE J. Quantum Electron.* **QE-3**, 400 (1967).
11. T. Nakamura, V. Fridkin, R. Magomadov, M. Takashige, and K. Verkhovskaya, *J. Phys. Soc. Jpn.* **48**, 1588 (1980).
12. F. Micheron, A. Hermosin, G. B. Smith, and J. Nicolas, *C. R. Acad. Sci.* **8**, (1971).
13. R. R. Neurgaonkar, W. K. Cory, and J. R. Oliver, *Ferroelectrics* **15**, 3 (1983).
14. R. R. Neurgaonkar, J. R. Oliver and L. E. Cross, *Ferroelectrics* **56**, 31 (1984).
15. P. V. Lenzo, E. G. Spencer, and A. A. Ballman, *Appl. Phys. Lett.* **11**, 23 (1967).
16. S. T. Liu and R. B. Macielek, *J. Electron. Mater.* **4**, 91 (1975); A. M. Glass, *J. Appl. Phys.* **40**, 4699 (1969).
17. P. P. Labbe, M. Frey, B. Raveau, and J. C. Monier, *Acta Crystallog.* **B33**, 2201 (1977).
18. P. B. Jamieson, S. C. Abrahams, and J. L. Bernstein, *J. Chem. Phys.* **48**, 5048 (1968); **50**, 4352 (1969).
19. F. W. Ainger, W. P. Bickley, and G. V. Smith, *Proc. Brit. Ceram. Soc.* **18**, 221 (1970).
20. T. Ikeda, K. Uno, K. Oyama, A. Sagara, J. Kato, S. Takano, and H. Sato, *Jpn. J. Appl. Phys.* **17**, 341 (1978).
21. J. Ravez and P. Hagenmuller, *Mater. Res. Bull.* **12**, 769 (1979).
22. J. Ravez, A. Perron-Simon, and P. Hagenmuller, *Ann. Chim. (Paris)* **268**, 251 (1976).
23. J. F. Nye, *Physical Properties of Crystals* (Oxford U. Press, London, 1960).
24. E. G. Spencer, P. V. Lenzo, and A. A. Ballman, *Proc. IEEE* **52**, 2074 (1967).
25. J. T. Milek and M. Neuberger, *Handbook of Electronic Materials* (IFI/Plenum, New York, 1972), Vol. 8.
26. A. A. Ballman and H. Brown, *J. Cryst. Growth* **1**, 311 (1967).
27. K. Megumi, N. Nagatsuma, K. Kashiwada and Y. Furuhashi, *Mater. Sci.* **11**, 1583 (1976).
28. R. R. Macielek and S. T. Liu, *J. Electron. Mater.* **2**, 191 (1973).
29. R. Clarke and F. W. Ainger, *Ferroelectrics* **7**, 101 (1974).
30. G. Burns, E. A. Geiss, D. F. O'Kane, B. A. Scott, and S. W. Smith, *J. Phys. Soc. Jpn.* **28**, 153 (1970).
31. T. Fukuda, *Jpn. J. Appl. Phys.* **8**, 122 (1968); *J. Cryst. Growth* **6**, 293 (1970).
32. F. W. Ainger, J. A. Beswick, and S. G. Porter, *Ferroelectrics* **3**, 321 (1972).
33. Y. Itoh and H. Iwasaki, *J. Phys. Chem.* **34**, 1639 (1973); *Jpn. J. Appl. Phys.* **9**, 157 (1970).
34. T. Yamada, *Appl. Phys. Lett.* **23**, 213 (1973).
35. J. Nakano and T. Yamada, *J. Appl. Phys.* **46**, 2361 (1975).
36. L. G. Van Uitert, J. J. Rubin, and W. A. Bonner, *IEEE J. Quantum Electron.* **QE-4**, 622 (1968).
37. H. Hirano, T. Takei, and S. Koide, *Jpn. J. Appl. Phys.* **8**, 972 (1969).
38. A. A. Ballman, S. K. Kurtz, and H. Brown, *J. Cryst. Growth* **10**, 185 (1971).
39. T. Sugai and M. Wada, *Jpn. J. Appl. Phys.* **11**, 1863 (1972).
40. A. Ishida, O. Mikami, S. Miyazawa, and M. Sumi, *Appl. Phys. Lett.* **21**, 192 (1972).
41. F. S. Chen, J. T. LaMachia, and D. B. Fraser, *Appl. Phys. Lett.* **13**, 223 (1968).
42. F. Okamoto, H. Ikee, and K. Muto, *Appl. Opt.* **14**, 2453 (1975).
43. R. R. Neurgaonkar, M. H. Kalisher, T. C. Lim, E. J. Staples, and K. K. Keester, *Mater. Res. Bull.* **15**, 1235 (1980).
44. R. R. Neurgaonkar, *Proc. Soc. Photo-Opt. Instrum. Eng.* **465**, 97 (1984).
45. O. F. Dudnik, A. K. Gromov, V. B. Kravchenko, Yu. L. Kopylov, and G. F. Kuznetsov, *Soviet Phys. Crystallogr.* **15**, 330 (1980).
46. R. R. Neurgaonkar, T. C. Lim, E. J. Staples, and L. E. Cross, in *Proceedings of the Ultrasonic Symposium* (1980).
47. O. Eknayan, C. H. Bulmer, H. F. Taylor, and W. K. Burns, Naval Research Laboratory, Washington, D.C. 20375 (personal communication with R. R. Neurgaonkar).
48. W. W. Ho, W. F. Hall, and R. R. Neurgaonkar, *Ferroelectrics* **50**, 325 (1983).
49. W. W. Ho, W. F. Hall, R. R. Neurgaonkar, R. E. DeWames, and T. C. Lim, *Ferroelectrics* **38**, 63 (1981).
50. R. R. Neurgaonkar and L. E. Cross, *Mater. Res. Bull.* (to be published).
51. J. P. Hugnard and A. Marrackchi, *Opt. Commun.* **38**, 249 (1981).

52. J. P. Huignard and A. Marrackchi, *Opt. Lett.* **6**, 622 (1981).
53. P. Yeh, *Opt. Commun.* **45**, 323 (1983).
54. P. Yeh, *J. Opt. Soc. Am.* **73**, 1268 (1983).
55. P. Yeh, *Appl. Opt.* **23**, 2974 (1984).
56. J. O. White, M. Cronin-Golomb, B. Fischer, and A. Yariv, *Appl. Phys. Lett.* **40**, 450 (1982).
57. M. E. Lines and A. M. Glass, *Principles and Applications of Ferroelectrics and Related Materials* (Clarendon, Oxford, 1977).
58. K. Megumi, H. Kozuka, M. Kobayashi, and Y. Furuhashi, *Appl. Phys. Lett.* **30**, 631 (1977).
59. R. R. Neurgaonkar, Semi-Annual Tech. Rep. No. 4, Contract N0014-82-C-2466.
60. P. N. Gunter, *Opt. Lett.* **7**, 10 (1982); *Phys. Rep.* **93**, 199 (1982).
61. E. C. Subbarao, G. Shirane, and F. Jona, *Acta Crystallogr.* **13**, 226 (1960).
62. B. Jaffe, W. R. Cook, and H. Jaffe, *Piezoelectric Ceramics* (Academic, New York, 1971).
63. L. E. Cross, *Materials Research Laboratory*, Pennsylvania State University, University Park, Pa. 19141 (personal communication with R. R. Neurgaonkar).
64. Note that coefficients are given with respect to prototypic tetragonal axes: the usual ... of the matrix can be achieved by a simple 45° rotation in the xy (1, 2) plane.
65. T. R. Shrout, H. Chen, and L. E. Cross, *Ferroelectrics* **56**, 45 (1983).
66. T. R. Shrout, L. E. Cross, and D. A. Hukin, *Ferroelectrics Lett.* **44**, 325 (1983).

Ratnakar R. Neurgaonkar



Ratnakar R. Neurgaonkar is manager of the Ferroelectric Materials Department at the Rockwell International Science Center in Thousand Oaks, California. Dr. Neurgaonkar received the B.Sc. (honors, 1962), M.Sc. (1963), and Ph.D. (1967) degrees in solid-state chemistry from Poona University, India. At Rockwell, Dr. Neurgaonkar has been directing the ferroelectric materials research and development program for various device applications, including electro-optic, photorefractive, pyroelectric

imagers, SAW's, millimeter-wave, and piezoelectric transducer applications. Dr. Neurgaonkar and Warren K. Cory have developed various growth techniques for ferroelectric crystals/films, and recently they successfully demonstrated the growth of optical-quality doped and undoped $\text{Sr}_{1-x}\text{Ba}_x\text{Nb}_2\text{O}_6$ and BSKNN single crystals using the Czochralski technique. Besides ferroelectric materials, Dr. Neurgaonkar has also been interested in magnetics, luminescence, and laser crystal development work. He is a member of various professional societies, including the American Ceramic Society, the Electrochemical Society, and the American Association for Crystal Growth. He is the author or coauthor of more than 70 research publications.

Warren K. Cory



Warren K. Cory is a research specialist in the Ferroelectric Materials Department at Rockwell International Science Center, Thousand Oaks, California. Mr. Cory received the B.A. degree from the University of California at Los Angeles in language (German) in 1965. He has been working in the crystal-growth area for more than 18 years, and he has grown a variety of different crystals by using different techniques. Before joining Rockwell, Mr. Cory worked at Stanford University and the University of Mexico

in Mexico City. At Rockwell, together with Ratnakar Neurgaonkar, he has developed the tungsten bronze $\text{Sr}_{1-x}\text{Ba}_x\text{Nb}_2\text{O}_6$ crystals to a high state of perfection: striation-free and defect-free quality. He is also involved in perfecting the ADC-equipped Czochralski technique for other bronze crystals, such as BSKNN and MPB compositions and perovskite KNbO_3 compositions. Mr. Cory has modified current growth equipment to state-of-art quality and recently introduced computer control of growth. His avocations are mineralogy, astronomy, and computing. He is a member of the American Association for Crystal Growth and is the coauthor of more than 30 publications.



Rockwell International

Science Center

SC5441.FTR

**DEVELOPMENT AND MODIFICATION OF PHOTOREFRACTIVE PROPERTIES
IN THE TUNGSTEN BRONZE FAMILY CRYSTALS**

Development and modification of photorefractive properties in the tungsten bronze family crystals

Ratnakar R. Neurgaonkar

W. K. Cory

J. R. Oliver

M. D. Ewbank

W. F. Hall

Rockwell International Science Center
Thousand Oaks, California 91360

Abstract. The $\text{Sr}_{1-x}\text{Ba}_x\text{Nb}_2\text{O}_6$ (SBN) and $\text{Ba}_{2-x}\text{Sr}_x\text{K}_{1-y}\text{Na}_y\text{Nb}_5\text{O}_{15}$ (BSKNN) tungsten bronze solid-solution systems are shown to be promising photorefractive materials. Because of the versatility of the bronze structure, both the response time and spectral response can be controlled by altering the type of dopant and its crystallographic site preference. This paper reviews the current status of the tungsten bronze crystals SBN and BSKNN for photorefractive applications in terms of their growth, electro-optic character, and the role of cerium dopants. Ferroelectric morphotropic phase boundary (MPB) bronze materials are also discussed as potentially important for future development.

Subject terms: optical information processing; tungsten bronze ferroelectrics; morphotropic phase boundary; electro-optic properties; pyroelectric properties; dielectric properties.

Optical Engineering 26(5), 392-405 (May 1987)

CONTENTS

1. Introduction
2. Ferroelectric tungsten bronze family crystals
3. Tungsten bronze systems for optical applications
 - 3.1. The SBN system
 - 3.2. The BSKNN system
4. Growth of tungsten bronze crystals
5. Ferroelectric and optical properties
6. Photorefractive properties
7. Future tungsten bronze materials
8. Conclusion
9. Acknowledgments
10. References

1. INTRODUCTION

The ability to efficiently interact one light wave with another is the key to a host of applications, including optical computing, image processing, and phase conjugation, which are being developed around the world. This recent upsurge of interest in lightwave technology has focused attention on those materials whose optical properties are sensitive to light and that are therefore known as nonlinear optical materials. An important subset of these are photorefractive materials in which a change in the refractive index is induced by nonuniform illumination via a space-charge field and the electro-optic effect.

Perhaps the best known of the photorefractive materials are perovskite BaTiO_3 and tungsten bronze $\text{Sr}_{1-x}\text{Ba}_x\text{Nb}_2\text{O}_6$ (SBN); significant photorefractive effects also have been observed in a variety of other electro-optic crystals.¹⁻¹⁴ Depending on the crystal structure, the dopant distribution on available crystallographic sites, the band gap, and the electro-optic coefficients of a given

crystal, refractive index changes may be induced not only by visible but also by ultraviolet and infrared radiation.

This paper reports the recent progress at Rockwell International in developing new photorefractive materials based on the ferroelectric tungsten bronzes, principally SBN and $\text{Ba}_{2-x}\text{Sr}_x\text{K}_{1-y}\text{Na}_y\text{Nb}_5\text{O}_{15}$ (BSKNN). Single crystals from these systems exhibit exceptionally large electro-optic properties, making them excellent candidates for development as photorefractive media. From the total group of bronzes studied in our laboratory, SBN and BSKNN crystals were selected because they possess distinctly different electro-optic characters: that is, SBN shows the largest sensitivity with the static and optical fields oriented along the crystal c-axis, whereas BSKNN is most sensitive with the static electric field oriented along the a-axis and the optical field oriented in the a-c plane. The growth of these bronze crystals in optical quality and large size has made possible the systematic investigation of their photorefractive effects at our laboratory and at other institutions, including the U.S. Army Night Vision Laboratory, the California Institute of Technology, and The Pennsylvania State University.

2. FERROELECTRIC TUNGSTEN BRONZE FAMILY CRYSTALS

Ferroelectric tungsten bronze oxides have been studied for their electro-optic and pyroelectric¹⁵⁻¹⁷ properties and are found to be effective in many related applications. The bronze compositions can be represented by the general formulas as $(\text{A}_1)_4(\text{A}_2)_2\text{C}_4\text{B}_{10}\text{O}_{30}$ and $(\text{A}_1)_4(\text{A}_2)_2\text{B}_{10}\text{O}_{30}$, in which A_1 , A_2 , C, and B are 15-, 12-, 9-, and 6-fold coordinated sites in the crystal lattice structure. The tetragonal bronze prototypic structure is shown in Fig. 1 in projection on the (001) plane.^{18,19} A wide range of solid solutions can be obtained by substituting different A_1 , A_2 , and B cations,²⁰⁻²³ and a number of different types of ferroelectric and ferroelastic phases have been identified

Invited Paper IP-110 received Feb. 12, 1987; revised manuscript received March 20, 1987; accepted for publication March 20, 1987; received by Managing Editor March 20, 1987.

© 1987 Society of Photo-Optical Instrumentation Engineers

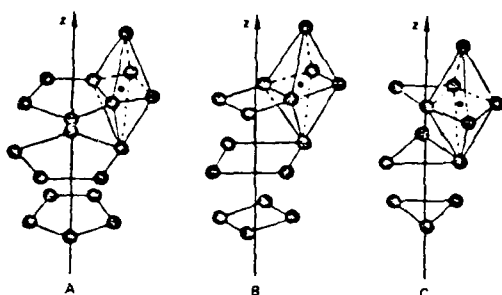
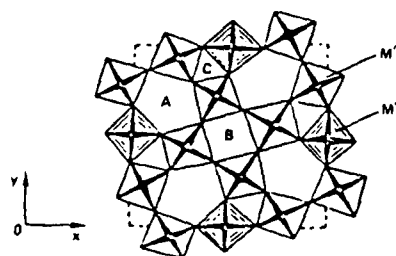


Fig. 1. Projection of the tetragonal tungsten bronze crystal structure on the (001) plane.

(more than 100 compounds and solid solutions). The ferroelectric phases can be divided into two groups: those with tetragonal symmetry (4mm), which are ferroelectric, and those with orthorhombic symmetry (mm2), which are both ferroelectric and ferroelastic.

Crystals that are noncentrosymmetric, i.e., lacking a center of symmetry, may exhibit both linear and quadratic electro-optic and elasto-optic effects. In all of the crystals discussed here, the linear effects are dominant. Thus, a linear change in the optical index of refraction can be induced by either an electric field (electro-optic effect), strain (elasto-optic effect), or nonuniform illumination (photorefractive effect). Strain can be produced by an electric field (piezoelectric) or by stress (elasticity). The matrices of the electro-optic coefficients in the reduced matrix form,²⁴ r_{ij} , are given in Table I.

Generally, for the tungsten bronze family the electro-optic coefficients r_{33} , r_{13} , and r_{51} are large, but they can be substantially larger for compositions close to morphotropic phase boundaries. The SBN solid-solution crystals exhibit exceptionally large electro-optic coefficients that are based on three independent nonzero moduli: $r_{31} = r_{13}$, $r_{42} = r_{51}$, and r_{33} . The largest electro-optic effect is observed for the dc electric field parallel to the single tetrad symmetry axis x_3 , which is also the polar (c) axis, and with light propagation normal to the x_3 direction. The phase retardation δ in this case is given by

$$\delta = \frac{2\pi \ell \lambda_0}{n_2^2 - n_1^2} \quad (1)$$

where ℓ is the path length, λ_0 is the free-space wavelength, and n_2^2 and n_1^2 are the principal indices of refraction normal to the direction of propagation x_1 . In this case,

$$n_2^2 = n_o^2 - \frac{n_o^2 r_{13} E}{2}, \quad n_1^2 = n_e^2 - \frac{n_e^2 r_{13} E}{2} \quad (2)$$

TABLE I. Electro-optic r_{ij} matrices for mm2 and 4mm bronze crystals.

Orthorhombic (mm2)			Tetragonal (4mm)		
0	0	r_{13}	0	0	r_{13}
0	0	r_{23}	0	0	r_{13}
0	0	r_{33}	0	0	r_{33}
0	r_{42}	0	0	r_{51}	0
r_{51}	0	0	r_{51}	0	0
0	0	0	0	0	0

TABLE II. Half-wave field-distance products $[E \cdot L]_{\lambda/2}$ for $\text{Sr}_{1-x}\text{Ba}_x\text{Nb}_2\text{O}_6$.

f	x = 0.25	x = 0.40	x = 0.50	x = 0.75
dc	37 V dc	150 V dc	250 V dc	-
1 MHz	80 V pp	300 V pp	676 V pp	1340 V pp
15 MHz	48 V pp	200 V pp	580 V pp	1236 V pp

where n_o and n_e are the ordinary and extraordinary optical indices, respectively.

For light propagation parallel to x_3 and an electric field parallel to the x_1 (a) axis, δ is written as above, but for n_1^2 and n_2^2 , given by

$$n_2^2 = n_o^2, \quad n_1^2 = n_e^2 - \frac{n_e^2 r_{31}^2 E_1^2}{2(n_o^2 - n_e^2)} \quad (3)$$

Crystals that have been investigated in the SBN system are those for which $x = 0.25, 0.40, 0.50$, and 0.75 .^{15,25} The half-wave field-distance products $[E \cdot L]_{\lambda/2}$ at 632.8 nm for the electric field along x_3 , with light propagation normal to x_3 and polarized at 45° with respect to the principal axes, are shown in Table II. In SBN:75 ($x = 0.25$) for a one-to-one aspect ratio of electric field path to optical path length, the half-wave field-distance product $[E \cdot L]_{\lambda/2}$ is 48 V at 15 MHz.²⁵ By way of comparison, this is equivalent to the quadratic effect in KTN at 2000 V. The 48 V required in SBN:75 is also 60 times smaller than the 2800 V obtained previously for LiTaO_3 and LiNbO_3 .²⁶ Because of such excellent electro-optic properties for the SBN solid solution, considerable research has been performed on this as well as on other bronze systems. Some of the unique advantages of bronze crystals are as follows:

- (1) This family of crystals possesses extraordinarily large transverse and longitudinal electro-optic coefficients, especially near a morphotropic phase boundary (MPB).
- (2) A trade-off between sensitivity and speed can be investigated in photorefractive studies due to the structural flexibility. In the tungsten bronze structure, several crystallographic sites can be partially empty, which allows crystal compositions to be tailored.
- (3) Several ferroelectric MPB compositions have been identified in this family.
- (4) The lower prototype symmetry gives a large family of quadratic electro-optic g coefficients and the possibility of anisotropic conduction. The nonzero values are g_{11} , g_{12} , g_{13} , g_{44} , and g_{66} , as compared to g_{11} , g_{12} , and g_{44} in perovskites.
- (5) In the tetragonal bronzes, since the high-temperature proto-

type symmetry is 4mm, only one unique 4-fold axis exists, and 90° twins are absent; hence, crystals are not likely to crack during poling.

3. TUNGSTEN BRONZE SYSTEMS FOR OPTICAL APPLICATIONS

As discussed in the previous section, the tungsten bronze family offers a wide variety of orthorhombic and tetragonal compositions for optical applications. Since the figures of merit for electro-optic and photorefractive applications are all proportional to the electro-optic coefficients of the materials, respectively, it is important to examine bronzes that exhibit large electro-optic coefficients and at the same time are relatively easy to grow in bulk single-crystal form. From extensive work in this family, we have found the tetragonal (4mm) bronze compositions to be promising, and we have grown a number of tetragonal bronzes for optical studies during the past 10 years. Of the total group of tetragonal bronzes, the SBN and BSKNN solid solutions have been studied in more detail since the transverse and longitudinal electro-optic coefficients are adjustable in these systems. SBN crystals exhibit a strong transverse (r_{33}) electro-optic coefficient,²⁷ whereas a strong longitudinal (r_{51}) electro-optic coefficient is anticipated for BSKNN.²⁷ The phase relation and crystal growth problems associated with each system are discussed in the following sections, together with the potential optical interest in each.

3.1. The SBN system

The solid-solution $Sr_{1-x}Ba_xNb_2O_6$, $0.75 \geq x \geq 0.25$, belongs to the tungsten bronze family, as shown in Fig. 2, even though the end members $SrNb_2O_6$ and $BaNb_2O_6$ do not exhibit a tungsten bronze structure. This system was originally studied by researchers at Bell Laboratories, where SBN:50 crystals were grown using the Czochralski technique,^{28,29} considering SBN:50 to be the congruent melting composition. In the mid-1970s, Honeywell researchers^{30,31} also studied the growth of doped and undoped SBN:50 for pyroelectric applications with considerable success. Subsequently, Japanese researchers³² reexamined the phase relation in the $SrNb_2O_6$ - $BaNb_2O_6$ system and reported that $Sr_{0.6}Ba_{0.4}Nb_2O_6$ (SBN:60) is the only congruent melting composition in this system. The work at Rockwell International also confirmed that SBN:60 is very close to congruent melting and therefore is much easier to grow than SBN:50 or SBN:75.

The tetragonal tungsten bronze SBN solid solution is represented by the formula $(A_1)_{14}(A_2)_{12}B_{10}O_{30}$, in which both Ba^{2+} and Sr^{2+} are in the 15-fold (A_1) and 12-fold (A_2) coordinated lattice sites. Since the 15- and 12-fold coordinated sites are partially empty in this system, SBN is referred to as an unfilled bronze. Furthermore, because of these partially empty crystallographic sites, both Ba^{2+} and Sr^{2+} have a considerable tendency to exchange sites, often creating crystal strain and optical striations. However, these problems have been successfully overcome, and optical-quality crystals are now available.³³⁻³⁸

3.2. The BSKNN system

The $Ba_{2-x}Sr_xK_{1-x}NaNb_5O_{15}$ compositions considered here exist on the $SrNb_2O_6$ - $BaNb_2O_6$ - $KNbO_3$ - $NaNbO_3$ quaternary system shown in Fig. 3. Although the end members in this system do not belong to the tungsten bronze family, extensive tungsten bronze regions have been established. The compositions exhibiting a tungsten bronze structure can be either tetragonal (4mm) or orthorhombic (mm2), the latter occurring basically for

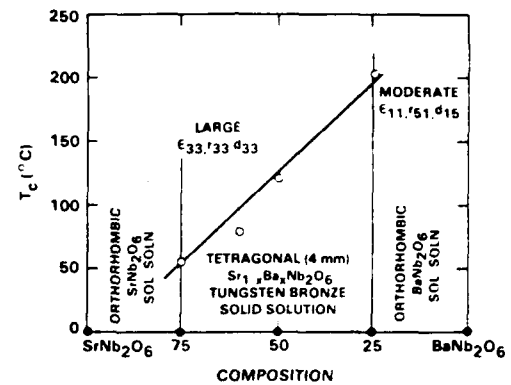


Fig. 2. Curie temperature versus composition for the $SrNb_2O_6$ - $BaNb_2O_6$ binary system.

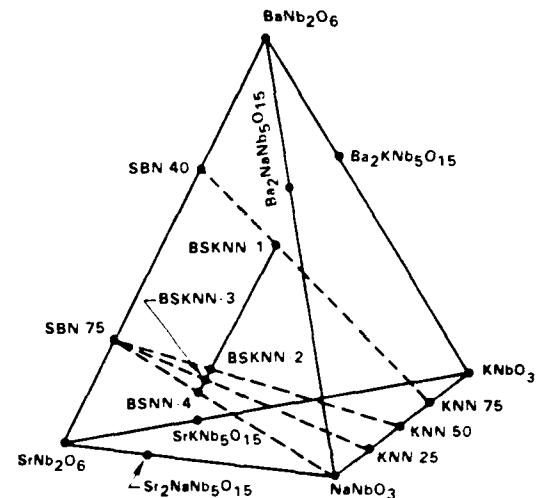


Fig. 3. The phase relation in the $SrNb_2O_6$ - $BaNb_2O_6$ - $KNbO_3$ - $NaNbO_3$ quaternary system.

Na^+ -containing compositions such as $Sr_2NaNb_5O_{15}$ and $Ba_2NaNb_5O_{15}$. On the other hand, K^+ -containing bronzes are typically tetragonal at room temperature, except for a few materials such as $Pb_2KNb_5O_{15}$ and $K_3Li_2Ta_5O_{15}$.³⁷⁻⁴¹

In the tetragonal BSKNN system, the relative magnitudes of the transverse (r_{33}) and longitudinal (r_{51}) electro-optic coefficients are strong functions of both the Ba:Sr and K:Na ratios. Since these properties are important for optical studies, our work has concentrated on the binary join between BSKNN-1 and BSNN-4, shown in Fig. 3. Although Yuhuan and Cross* successfully grew a few BSKNN compositions, they did not fully establish the phase diagram for this system. We have expanded on this early work and have systematically studied this system; part of this work is published elsewhere.²⁷ In the binary join between BSKNN-1 and BSNN-4 in Fig. 3, BSNN-4 is orthorhombic at room temperature and is a part of the $Sr_2NaNb_5O_{15}$ - $Ba_2NaNb_5O_{15}$ system. This system was studied by Oliver et al.,⁴² and a possible morphotropic phase boundary was found at $x = 1.2$ ($Sr_{1.2}Ba_{0.8}NaNb_5O_{15}$). Because of the MPB region in this system, BSKNN compositions that lie close to this boundary also should exhibit enhanced electro-optic and ferroelectric properties.

*Xu Yuhuan and L. E. Cross, private communication (1981)

TABLE III. Growth conditions for tungsten bronze SBN and BSKNN crystals.

Growth Condition	SBN:75	SBN:60	BSKNN-1	BSKNN-2	BSKNN-3
Growth Temperature ($^{\circ}\text{C}$)	- 1500	- 1510	1480	1475	1475
Growth Atmosphere	Air or O_2	Air or O_2	Air	Air	Air
Size Cubes Available	- 6 to 8 mm	10 to 25 mm	5 to 6 mm	6 to 8 mm	10 mm
Crystal Size	- 2.0 cm	- 3.0 cm	- 1.0 cm	- 1.5 cm	- 1.5 cm
Crystal Shape	Cylindrical	Cylindrical	Square	Octahedron	Octahedron
Facets ([001] growth)	24	24	4	8	8
Crystal Color [without Ce]	Pale Cream	Pale Cream	Colorless	Colorless	Colorless
Ce $^{3+}$ in 15- or 12-Fold	Pink	Pink	Pink	Pink	Pink
Ce $^{3+}$ in 9-Fold	Green-Yellow	Green-Yellow	Green-Yellow	Green-Yellow	Green-Yellow

In contrast to SBN crystals, BSKNN has all of the 15- and 12-fold coordinated sites filled. For this reason, BSKNN compositions show quasi first-order ferroelectric phase transition behavior with reduced relaxor (frequency-dependent) effects compared to SBN. The results of our investigations suggest that relaxor behavior may depend on the distribution of Ba^{2+} and Sr^{2+} over the 15- and 12-fold coordinated sites, as well as on crystal annealing conditions.

4. GROWTH OF TUNGSTEN BRONZE CRYSTALS

The growth of orthorhombic (mm2) and tetragonal (4mm) bronze crystals has been a subject of great interest for many years, and considerable progress has been made in the growth of crystals of suitable size and quality. Future goals involve the development of large-scale SBN and BSKNN growth facilities to routinely grow 4 to 5 cm diameter crystal boules. Based on current work, the development of such large high-quality crystals should now be feasible.

The tetragonal SBN and BSKNN solid solutions are comparatively easier to grow than orthorhombic crystals. Neurgaonkar et al.³³⁻³⁶ extensively studied the problems associated with these crystals and successfully established the necessary conditions for Czochralski crystal growth. Table III lists the growth conditions for a number of key tungsten bronze materials. Although large crystals have been developed from these compositions, several problems are associated with their growth:

- (1) Multicomponent solid-solution systems: it is difficult to establish the true congruently melting compositions.
- (2) High material melting temperatures (above 1450°C): volatilization and oxidation-reduction problems ($\text{Nb}^{5+} \rightleftharpoons \text{Nb}^{4+}$) are common.
- (3) Exchange among crystallographic sites, specifically of the 15- and 12-fold coordinated ions such as Ba^{2+} , Sr^{2+} , K^{+} , and Na^{+} , which causes severe striation problems.
- (4) Cracking of crystals when passing through the paraelectric/ferroelectric phase transition temperature. For tetragonal crystals, this is less severe than for the orthorhombic forms, but it is still a concern for BSKNN, $\text{K}_3\text{Li}_2\text{Nb}_5\text{O}_{15}$ (KLN), etc.

The congruent melting composition SBN:60 is the easiest to grow in large sizes up to 2 to 3 cm in diameter, as shown in Fig. 4. Two other compositions, SBN:75 and SBN:50, also have been grown in optical quality by carefully controlling the melt temperature during growth. Since these latter compositions are far from true congruent melting, it is noteworthy that optical-quality crystals of sizes up to 1.5 cm in diameter have been achieved in both doped and undoped forms (Fig. 4).

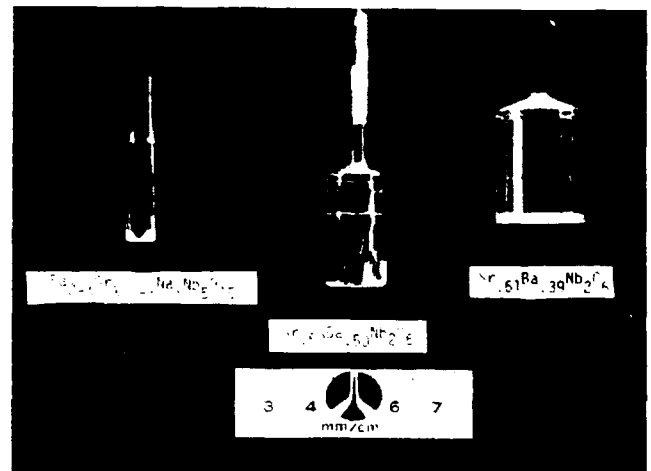


Fig. 4. Typical SBN and BSKNN single crystals grown along the (001) direction.



Fig. 5. Typical BSKNN single crystals grown along the (001) direction.

The congruent melting composition for the BSKNN system has not been conclusively established; however, the ease of growth of BSKNN-2 (Table III) suggests that the congruent melting composition lies near this composition. Notwithstanding this uncertainty, optical-quality crystal growths have been obtained for BSKNN-1, BSKNN-2, and BSKNN-3, as shown in Fig. 5.

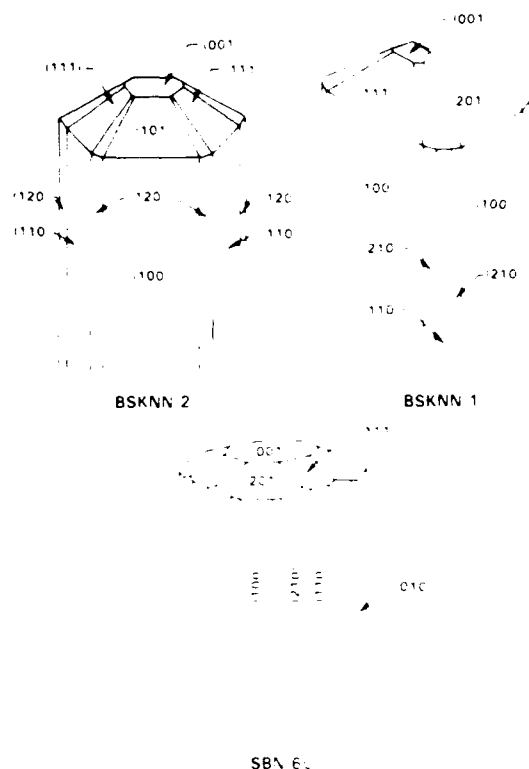


Fig. 6. Idealized forms of tungsten bronze crystals. Top—large longitudinal effects; bottom—large transverse effects.

for BSKNN-1 and BSKNN-2. The results indicate that factors of major concern in obtaining optical-quality tungsten bronze crystals are

- (1) Impurities in starting materials: Ca^{2+} , Fe^{3+} , Mg^{2+} , etc.
- (2) Rotation and pulling rates: Optimum rates are needed to control temperature instability arising from poor thermal conductivity.
- (3) Cooling rate variation: Sr^{2+} and Ba^{2+} distribution changes on the 15- and 12-fold coordinated sites for different cooling rates.

A most striking and uncommon feature of these tetragonal bronze crystals is that they all show natural facets. The bronzes exhibiting large transverse effects, e.g., SBN:60, SBN:75, and $\text{Sr}_2\text{KNb}_5\text{O}_{15}$ (SKN), are cylindrical in shape and exhibit 24 well-defined facets,^{43,44} whereas bronzes exhibiting large longitudinal effects, e.g., BSKNN, $\text{Pb}_{0.6}\text{Ba}_{0.4}\text{Nb}_2\text{O}_6$ (PBN:60), and KLN, have a square or octahedral shape, depending on the size of the crystal unit cell. For BSKNN compositions, the larger unit cell BSKNN-2 and BSKNN-3 grow in an octahedral shape, with eight well-defined facets.²⁷ Figure 6 shows the idealized forms of bronze crystals. The results of our investigation of the BSKNN system indicate that as one moves toward the BSNN-4 end member composition, transverse optical effects become large; hence, we expect that beyond the BSKNN-3 composition, the crystal habit should be nearly cylindrical, as is the case for bronze SBN:60.

5. FERROELECTRIC AND OPTICAL PROPERTIES

The dielectric properties at 10 kHz for bronze SBN:60 are shown in Fig. 7 as a function of temperature for a- and c-axis (polar)

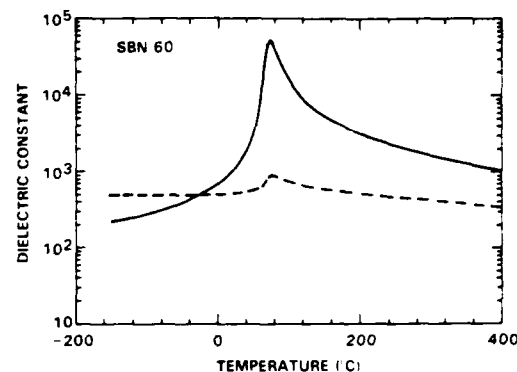


Fig. 7. Temperature dependence of the dielectric constant for SBN:60. Solid line—c-axis (polar); dashed line—a-axis.

crystals. Similar to other ferroelectric materials, the polar axis dielectric constant shows a very large anomaly at the Curie phase transition temperature T_c , which for SBN:60 occurs nominally at 75°C. Below T_c , the dielectric constant decreases monotonically to a value of 900 to 950 at room temperature. Along the nonpolar a-axis, only a small discontinuity is seen at T_c , below which the dielectric constant remains relatively flat with temperature, with a value of 450 to 500 at room temperature. Other SBN compositions show similar behavior but with differing values for T_c (120°C for SBN:50, 56°C for SBN:75).

SBN crystals that have been poled to a single ferroelectric domain, achieved by applying electric fields of 6 to 10 kV/cm during slow cooldown from above the phase transition (90°C), show minimal frequency dependence of the low-frequency dielectric properties at or below room temperature (2% dispersion over 100 Hz to 100 kHz). However, as T_c is approached, a strong dielectric relaxation behavior is observed,¹⁷ and therefore SBN crystals are referred to as relaxor ferroelectrics. This behavior results from the distribution of phase transition temperatures in the bulk of the crystal arising from the lattice site uncertainty of the Sr and Ba ions in the partially filled lattice structure. In SBN:60, this transition temperature distribution is estimated to be 3 to 7°C in width.

The effects of a distribution in phase transition temperatures are especially evident in the behavior of the spontaneous polarization P_s derived from measurement of the pyroelectric coefficient p as a function of temperature, both of which are shown in Fig. 8 for SBN:60. The notable feature in this figure is that P_s has a nonzero value well above T_c as a result of the distribution of phase transition temperatures in the crystal. Below T_c , P_s rises smoothly to a value of 33 $\mu\text{C}/\text{cm}^2$ at room temperature. The large pyroelectric coefficient at room temperature (0.10 $\mu\text{C}/\text{cm}^2\cdot\text{K}^{-1}$) is the reason that SBN also has been found interesting for uncooled pyroelectric thermal imaging investigations.

Crystals in the BSKNN solid-solution system are characterized by significantly higher T_c values than found for SBN compositions. The 10 kHz dielectric properties for BSKNN-1, our original BSKNN composition grown in bulk single-crystal form, are shown in Fig. 9 for the a- and c-axis (polar) crystallographic orientations. Like SBN, the polar axis dielectric constant is characterized by a sharp dielectric anomaly at the ferroelectric phase transition temperature T_c , which for BSKNN-1 occurs at 203 to 208°C. Below T_c , the c-axis dielectric constant decreases monotonically to approximately 100 at room temperature. Along the

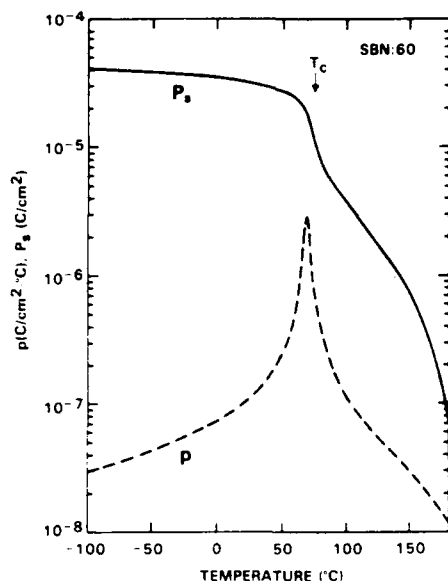


Fig. 8. Spontaneous polarization P_s and pyroelectric coefficient p as a function of temperature for SBN:60.

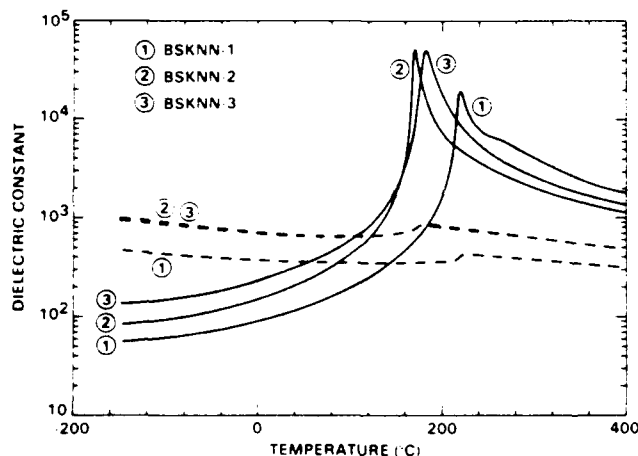


Fig. 9. Temperature dependence of the dielectric constant for BSKNN crystals. Solid line—c-axis (polar); dashed line— a-axis.

a-axis, only a slight dielectric anomaly is observed at the Curie point, with a value nearly two orders of magnitude smaller than for the c-axis. However, the a-axis dielectric constant remains relatively flat below T_c , so at room temperature it is nearly four times larger than the c-axis constant. Below room temperature, it then rises gradually to a value of 470 at -150°C .

The low-frequency dielectric properties of BSKNN-2, also shown in Fig. 9, are similar in overall behavior to those for BSKNN-1. However, BSKNN-2 has a lower Curie point (170 to 178°C), which contributes in part to its higher c-axis dielectric constant of 170 (poled) at room temperature. The a-axis dielectric properties for BSKNN-2 are also considerably larger, with a dielectric constant of 750 at room temperature, rising to above 1000 at -150°C , values that are a factor of 2 or more greater than for tungsten bronze SBN:60 single crystals.

The most recently developed BSKNN crystal composition, BSKNN-3, has dielectric behavior strikingly similar to that shown for BSKNN-2, with a T_c only 3 to 5°C higher (Fig. 9). The

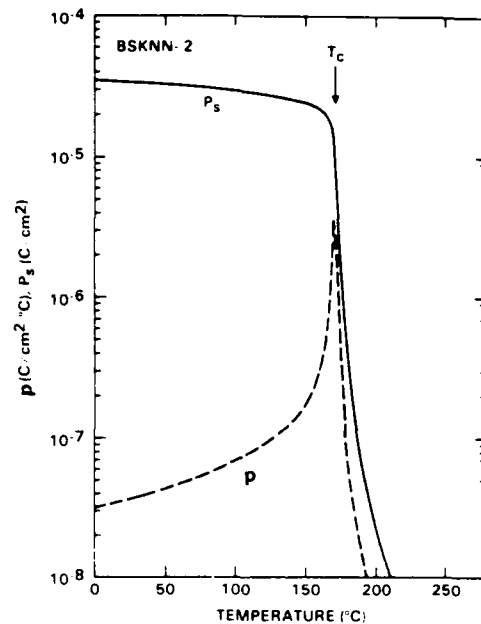


Fig. 10. Spontaneous polarization P_s and pyroelectric coefficient p as function of temperature for BSKNN-2.

major difference observed is a more gradual decline in the c-axis dielectric constant below T_c , resulting in a room-temperature value of 270. The a-axis behavior of BSKNN-3, on the other hand, is virtually unchanged from that of BSKNN-2.

The spontaneous polarization and pyroelectric coefficient as a function of temperature for BSKNN-2 are shown in Fig. 10. Like SBN, the spontaneous polarization has a nonzero value above the mean Curie point T_c ; however, both the polarization and dielectric data indicate that BSKNN compositions have a much narrower distribution of phase transition temperatures (2 to 3°C) than does SBN:60. This is a reflection of the fact that in BSKNN compositions, all of the A_1 and A_2 lattice sites are filled, unlike in SBN, where up to 20% of these sites can be vacant. Below T_c , the polarization of BSKNN-2 rises sharply and attains a value of $34 \mu\text{C}/\text{cm}^2$ at room temperature, a value roughly equal to that for SBN:60. This high spontaneous polarization, combined with the high a-axis dielectric constant, implies that BSKNN-2 (and BSKNN-3) should have a very large r_{51} electro-optic coefficient.

The ferroelectric and electro-optic properties of these bronze compositions are summarized in Table IV. All of the quantities shown have been measured except r_{51} , which is presently under evaluation. In the table, r_{51} is estimated from the phenomenological relation

$$r_{51} = 2g_{44}P_3\epsilon_{11}\epsilon_0 \quad (4)$$

where g_{44} is the quadratic electro-optic coefficient of the high-temperature (paraelectric) prototype, P_3 is the c-axis polarization, ϵ_{11} is the a-axis dielectric constant, and ϵ_0 is the permittivity of vacuum. The value of g_{44} is estimated to be $0.09 \text{ m}^4/\text{C}^2$ from measurements on SBN crystals; however, there is evidence that the quadratic electro-optic g coefficients may not be constant across the family of tungsten bronze compositions. In particular, the r_{51} values estimated for the BSKNN compositions in Table IV may, in fact, significantly underestimate the true values.

TABLE IV. Ferroelectric and optical properties of bronze crystals.

Property	Sr _{1-x} Ba _x Nb ₂ O ₆ (SBN)		Ba _{2-x} Sr _x K _{1-y} Na _y Nb ₅ O ₁₅ (BSKNN)		
	SBN:75	SBN:60	BSKNN-1	BSKNN-2	BSKNN-3
T _c (°C)	56	78	209	175	180
Dielectric Constant (23°C)	$\epsilon_{33} = 3000$ $\epsilon_{11} = 500$	$\epsilon_{33} = 900$ $\epsilon_{11} = 450$	$\epsilon_{33} = 120$ $\epsilon_{11} = 360$	$\epsilon_{33} = 170$ $\epsilon_{11} = 750$	$\epsilon_{33} = 270$ $\epsilon_{11} = 780$
Piezoelectric Coefficient ($\times 10^{-12}$ C/N)		$d_{33} = 130$ $d_{15} = 40$	$d_{33} = 60$ $d_{15} = 80$	$d_{33} = 70$ $d_{15} = 200$	
Electro-optic Coefficient ($\times 10^{-12}$ m/V)	$r_{33} = 1400$ $r_{51} = 42$	$r_{33} = 470$ $r_{51} = 42$	$r_{33} = 150$ $r_{51} = 200$	$r_{33} = 170$ $r_{51} = 350$	$r_{33} = 270$ $r_{51} = 400$

TABLE V. Electro-optic figure of merit for leading ferroelectric crystals.

Crystal	Dielectric Constant		Electro-Optic Coefficient 10^{-12} m/V			
	ϵ_{11}	ϵ_{33}	r_{33}	r_{51}	r_{ij}/ϵ	$n^3 r_{ij}/\epsilon$
Sr _{0.75} Ba _{0.25} Nb ₂ O ₆ (SBN:75)	500	3000	1400	42	0.467	5.60
Sr _{0.6} Ba _{0.4} Nb ₂ O ₆ (SBN:60)	450	900	420	42	0.522	6.26
Sr _{2-x} Ca _x NaNb ₅ O ₁₅ (SKNN)	1700	1700	> 1800	-	0.470	5.65
Pb _{0.6} Ba _{0.4} Nb ₂ O ₆ (PBN:60)	1900	500	-	> 1600	0.840	10.10
BSKNN-1	360	120	150	> 200	0.550	6.67
BSKNN-2	700	170	170	350	0.590	6.00
BSKNN-3	780	270	> 270	> 400	0.510	6.15
BaTiO ₃	4100	1500	80	1600	0.390	4.01
KNbO ₃	950	200	67	380	0.4	4.20

TABLE VI. Comparison between leading photorefractive crystals.

TUNGSTEN BRONZE BSKNN	PEROVSKITE BaTiO ₃
* Large longitudinal r_{51} , d_{15} , ϵ_{11} available	* Large longitudinal r_{51} , d_{15} , ϵ_{11} available
* Excellent host for photorefractive and electro-optic applications	* Excellent host for photorefractive and electro-optic applications
* Large square and octahedron crystals (> 1.5 cm) with optical quality can be grown	* Pure BaTiO ₃ crystals are available up to $1 \times 1 \times 1$ cm ³
* Absence of twinning (4/mm \rightarrow 4mm)	* 90° twins are present (m3m \rightarrow 4mm)
* Absorption and response controlled in the desired spectral range using proper crystallographic site/sites for a given dopant	* Controlled spectral response with dopants possible, but difficult
* No tetragonal to orthorhombic transition observed down to 1n temperature	* Tetragonal to orthorhombic transition occurs at 10°C
* Open structure - structural flexibility to alter crystal composition	* Close-packed structure: limited compositional flexibility

based on the observed discrepancies between theoretical and experimental values for r_{33} . However, this awaits further experimental confirmation.

Table V summarizes the optical figures of merit $n^3 r_{ij}/\epsilon$ and r_{ij}/ϵ for a number of tungsten bronze and perovskite crystals, including SBN and BSKNN. For phase conjugation (self-pumped), image processing, and optical computing applications, the relevant figure of merit can be taken as $n^3 r_{ij}/\epsilon$, which has been found to be larger for many tungsten bronze crystals than for

perovskites. In the case of bronze crystals exhibiting large longitudinal electro-optic effects, there is a possibility of raising this merit further simply by cooling below room temperature. For example, in BSKNN crystals, both ϵ_{11} (and therefore r_{51}) and the spontaneous polarization increase upon cooling to liquid nitrogen temperature.

Table VI summarizes the comparison between tungsten bronze BSKNN and perovskite BaTiO₃ crystals. Both crystals are excellent for electro-optic and photorefractive applications. BaTiO₃

crystals are commercially available, and as a consequence they are extensively studied for optical applications. However, BaTiO_3 is relatively difficult to grow as compared to BSKNN solid-solution crystals. The two major advantages of BSKNN crystals over BaTiO_3 are that (1) no twinning or poling problems exist due to the simple tetragonal-tetragonal phase transition (4/mm to 4mm), and (2) cooling can enhance the figure of merit (decrease in polar-axis ϵ_{33} and increase in r_{51}) because the tetragonal-orthorhombic phase transition, if any, lies at or below liquid nitrogen temperature, as opposed to ~ 5 to 10°C in BaTiO_3 .

The availability of large size, optical-quality SBN and BSKNN crystals opens up a variety of new optical device concepts, including phase conjugation, image processing, and optical computing. Because of the versatility of this family, either r_{33} or r_{51} can be made large for specific device needs by changing the composition in either the SBN or BSKNN system.

6. PHOTOREFRACTIVE PROPERTIES

To provide an appropriate context for the discussion of material development, the projected applications of photorefractive materials and the physical basis for the optical effects that make these applications possible should be considered in some detail. These applications include real-time holography, optical data storage, and phase-conjugate wavefront generation. Recently, increasing attention has been focused on using coherent signal beam amplification in two-wave mixing. These new applications include image amplification, vibrational analysis, nonreciprocal transmission, laser gyro biasing, and optical computing.⁴⁵⁻⁵⁰ All of these applications share a need for local changes in the optical refractive index produced by nonuniform illumination. The issues connected with the photorefractive effect include the material sensitivity to illumination and the speed with which the index can be made to change.

In photorefractive crystals, light-induced free carriers excited in an illuminated region of the crystal migrate to the dark regions, where they are trapped. The resulting space charge generates an electric field E_s , which gives rise to a refractive index change Δn through the linear electro-optic effect:

$$\Delta n = \frac{1}{2} n^3 r E_s \quad (5)$$

where r_{ij} is the electro-optic coefficient. The space-charge field E_s generated by charge displacement and re trapping is given by⁵¹

$$E_s = \frac{1}{\epsilon \epsilon_0} \int \rho dx = \frac{1}{\epsilon \epsilon_0} \int J(t) dt \quad (6)$$

where ρ is the charge density and ϵ is the dielectric constant. The current density J is a function of both the distance x and time t . In general, $J(x)$ is quite complex and is a function of the light intensity $I(x)$:

$$J(x) = \sigma(x)E_s + K I(x) + eD \frac{dn}{dx} + p \frac{dT}{dt} + \Delta \mu \frac{dn}{dt} \quad (7)$$

The first term is the local conduction in a field, which is the sum of the space-charge and possible external components, and the second term is the volume photovoltaic effect. The third term is due to free-carrier diffusion (D) driven by the concen-

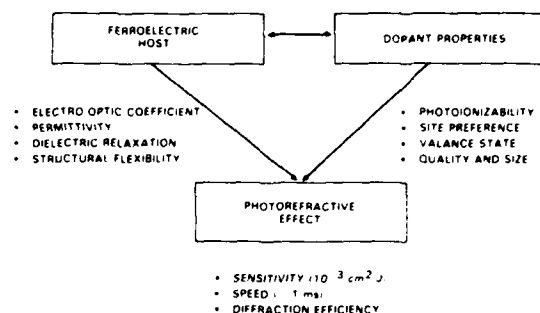
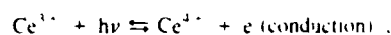


Fig. 11. Factors determining the photorefractive sensitivity and speed in ferroelectric crystals.

tration gradient (dn/dx), while the fourth and fifth terms are transient phenomena due to pyroelectric (p) and excited-state polarization, respectively. In view of the complexity of the phenomena contributing to $J(x)$, it is difficult to predict E_s values in a new crystal. Since the electro-optic coefficient in a given crystal is more or less independent of minor substitutions, the improvement in photorefractive sensitivity, efficiency, and speed within a single composition has to come from the magnitude and speed of the buildup of the electric field E_s . For this reason, researchers in several laboratories around the world are concentrating on finding suitable electrically active dopants for those materials having large electro-optic coefficients.

No single material combines all of the desired photorefractive features; hence, a large number of ferroelectric crystal compositions have been grown and characterized to determine possible trade-offs between sensitivity and speed. The nonferroelectric $\text{Bi}_{12}\text{SiO}_{20}$ crystal has the desired response time (~ 1 ms), but its photorefractive sensitivity (change in refractive index per absorbed energy density, Ref. 51) is moderate because r_{ij} is low. On the other hand, all ferroelectric crystals have exceedingly high sensitivity but moderate response speeds. To use these ferroelectric crystals for device applications, their response times must be reduced to the order of 1 ms or better; this is a key issue in ferroelectric crystal development. Figure 11 shows the generic topics that need to be addressed to determine the trade-off between sensitivity and speed in a ferroelectric crystal, such as SBN:60.

Since the electro-optic coefficient is largely unaffected by most impurities, space charge can be controlled by adding specific impurity levels to the crystal. It is now well established that doping crystals with impurities readily photoionized by incident optical radiation greatly increases the susceptibility of the crystals to index changes. Megumi et al.⁵² reported that the addition of Ce^{3+} produces a broad absorption in SBN:60 crystals, thereby increasing the sensitivity considerably. Undoped SBN:60 is transparent in the visible range, with its fundamental absorption edge at about $0.37 \mu\text{m}$; the addition of Ce develops a distinct but broad absorption edge around $0.50 \mu\text{m}$ that differs markedly from the intrinsic absorption edge. Ce photoionizes via the reaction



and from work on SBN:60,⁵³ it appears that both the Ce^{3+} and Ce^{4+} valence states are present. The photorefractive sensitivity improves from 10^{-5} to $10^{-3} \text{ cm}^2/\text{J}$ with Ce doping. This is two orders of magnitude higher than for LiNbO_3 doped with Fe^{3+} , U^{6+} , and Rh^{3+} .^{54,55}

TABLE VII. Influence of dopants on spectral response.

DOPANTS	VALANCE STATES	COLOR	CRYSTALLOGRAPHIC SITES				SPECTRAL RESPONSE
			15-FOLD	12-FOLD	9-FOLD	6-FOLD	
CERIUM (Ce)	Ce ³⁺ /Ce ⁴⁺	PINK	Ce ³⁺	Ce ³⁺	Ce ⁴⁺ *	—	0.45 TO 0.50 μm
IRON (Fe)	Fe ²⁺ /Fe ³⁺	YELLOW	—	—	—	Fe ²⁺ /Fe ³⁺	0.62 TO 0.67 μm
IRON (Fe)*	Fe ²⁺ /Fe ³⁺	GREEN	—	—	—	Fe ²⁺ /Fe ³⁺	0.68 μm
Ce + Fe	Ce ³⁺ /Fe ³⁺	PALE PINK	Ce ³⁺	Ce ³⁺	—	Ce ³⁺ /Fe ³⁺	0.45 TO 0.65 μm
MANGANESE (Mn)	Mn ²⁺ /Mn ³⁺	—	—	—	—	Mn ²⁺ /Mn ³⁺	—
Ce + M**	Ce ³⁺	GREENISH-YELLOW	M	M	Ce ³⁺	—	0.62 TO 0.75 μm

*HEAVY CONCENTRATION OF Fe

**BIGGER CONCENTRATIONS IN 15- AND 12-FOLD COORDINATED SITES

TABLE VIII. Goals for photorefractive studies and current status of Ce-doped tungsten bronze crystals.

Desired Properties	Observed Properties*		
	Ce-Doped SBN:60	Ce-Doped SBN:75	Ce-Doped BSKNN
1) Sensitivity, $\sim 10^{-4}$ - 10^{-5} cm ² /J	$\sim 10^{-2}$ cm ² /J	$\sim 10^{-2}$ cm ² /J	$\sim 10^{-3}$ cm ² /J
2) Large Coupling Coefficient ~ 1 cm ⁻¹	~ 13 cm ⁻¹	~ 11 cm ⁻¹	~ 10 cm ⁻¹
3) Large Size and Optical Quality	≥ 2.5 cm dia.	~ 2.0 cm dia.	~ 1.5 cm dia.
4) Large Electro-Optic Coefficient	$r_{33} = 420 \pm 10^{-12}$ m/V	$r_{33} = 1400 \pm 10^{-12}$ m/V	$r_{31} \geq 400 \pm 10^{-12}$ m/V
5) 2- and 4-wave Mixing Response Time ~ 1 ms	≥ 50 ms at 6 W/cm ²	≥ 120 ms at 6 W/cm ²	≥ 100 ms at 6 W/cm ²
6) Fast Self-Pumped Response Time	-----	1.6 s at 2 W/cm ²	6.6 s at 2 W/cm ²
7) Fast Beam Fanning Response Time	0.05 s at 2 W/cm ²	0.25 s at 2 W/cm ²	0.6 s at 2 W/cm ²
8) Spectral Response (0.4 to 2.0 μm)	0.48 to 1.0 μm	0.48 to 1.0 μm	0.48 to 1.0 μm

*Photorefractive properties may improve further with optimized Ce concentration.
References 36, 58, 64.

Recently, Neurgaonkar et al.⁵⁵ successfully demonstrated the growth of Ce- and Fe-doped SBN:60 single crystals as part of an effort to study the role of these ions in photorefractive device applications. This work was extended to BSKNN, and approximately 1 to 2 cm diameter Ce- and Fe-doped SBN:60 and BSKNN-2 crystals have now been grown using the Czochralski technique. The doping of SBN:60 and BSKNN-2 with Fe and with Fe and Ce together has not been done previously. Fe is expected to produce interesting results, as it has done in other ferroelectric crystals, e.g., LiNbO₃ and KNbO₃^{3,53-57}; however, Fe-doped bronze crystals are highly striated under all growth conditions, with the striations very difficult to suppress.

On the other hand, Ce-doped bronze crystals, e.g., SBN:60, SBN:75, and BSKNN-2, show minimal or no striations and are of optical quality. In the tungsten bronze structure, Ce³⁺ and Ce⁴⁺ are expected to occupy the 12- and 9-fold coordinated sites, while Fe²⁺ and Fe³⁺ are expected to occupy the 6-fold coordinated sites. Our results suggest that the existence of striations in these crystals depends strongly on the type of dopant and its location in the structure. Since Mn²⁺/Mn³⁺, Cr³⁺/Cr⁴⁺, Co²⁺/Co³⁺, Ti³⁺/Ti⁴⁺, etc., have ionic sizes and site preferences similar to Fe³⁺, it would be interesting to also check their influence on striations. The spectral responses for a few transition metal ion dopants have been evaluated from ceramics and solidified melts and are summarized in Table VII.

The development of striation-free Ce-doped SBN:60, SBN:75, and BSKNN-2 crystals makes possible the evaluation of photorefractive properties, specifically sensitivity, speed, and coupling coefficient. Typical 6 \times 6 \times 6 mm cubes were used in two- and four-wave mixing experiments for these studies. More recently, larger SBN:60 and SBN:75 cubes up to 20 \times 20 \times 20 mm were produced for this work, as shown in Fig. 12. Measurements of the photorefractive properties of these bronze crystals have been made at the California Institute of Technology, Rockwell International, and the U.S. Army Night Vision and Electro-Optics Laboratory (NVEOL) and are continuing as still better-quality crystals with various doping concentrations become available. Table VIII summarizes the goals set and the results obtained to date for these crystals.

In agreement with Megumi et al.,⁵² the results for the present crystals show the typical broad Ce absorption band, as shown in Fig. 13. An interesting feature is that the spectral response can be extended from the visible to the IR region by changing the site preference of the Ce ion. For example, when cerium is placed in the 15- and 12-fold coordinated sites, the optical absorption is observed in the visible, whereas the absorption extends to the near-IR region when Ce is located in the 9-fold coordinated site. This site flexibility is a unique advantage for tungsten bronze crystals, including BSKNN, whose spectral behavior is similar to that shown for SBN.

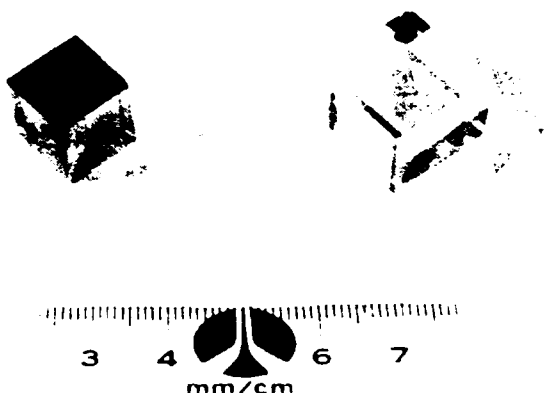


Fig. 12. Large size (12 × 12 × 12 and 20 × 20 × 20 mm), Ce-doped SBN:60 cubes.

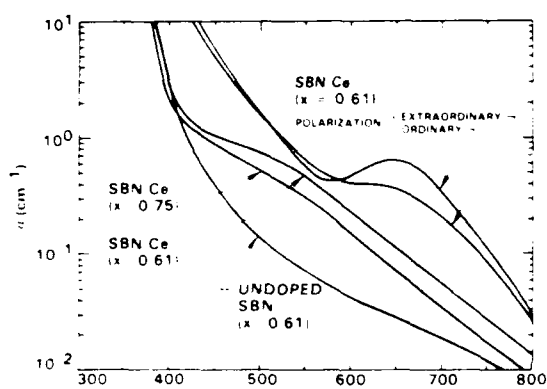


Fig. 13. Absorption spectra for undoped and Ce-doped SBN.

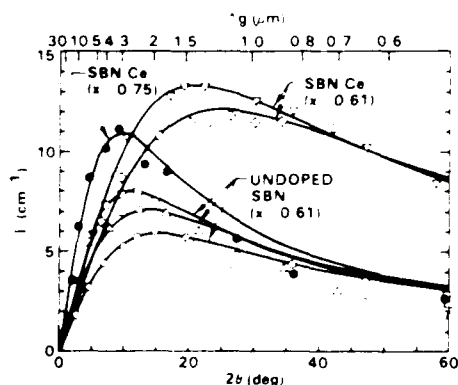


Fig. 14. Dependence of the two-wave mixing gain coefficient Γ' on grating spacing Λ_g or full external crossing angle 2θ in undoped and cerium-doped SBN at $\lambda = 514.5$ nm. The photorefractive grating was aligned along $\langle 100 \rangle$, and the optical beams were polarized extraordinary. The solid curves are best fits to the data using simple photorefractive theory (Ref. 58).

The photorefractive coupling efficiencies for Ce-doped and undoped SBN crystals are shown in Fig. 14. We found that Ce doping increases the photorefractive coupling coefficient by a factor of 2 to 3 at large crossing angles, while at the same time the photorefractive grating formation rate per unit inten-

TABLE IX. Beam fanning response time.

Material	Response Time (sec)		Wavelength (nm)	Point of Measurement
	0.2 W/cm ²	2 W/cm ²		
Ce-SBN:75	7.2	0.6	442	90%
Ce-SBN:75	2.0	0.25	442	e ⁻¹
Ce-SBN:60	0.6	0.05	442	e ⁻¹
BaTiO ₃	4.8	0.6	488	90%
Ce-BSKNN-2	5.8	0.6	457.9	e ⁻¹

TABLE X. Response time of self-pumped photorefractive materials.

Material	Response Time (sec)		Wavelength (nm)	Point of Measurement
	0.2 W/cm ²	2 W/cm ²		
Ce-SBN:75	32	8.3	442	90%
Ce-SBN:75	7.7	1.6	442	e ⁻¹
BaTiO ₃	25	2.5	514.5	90%
Ce-BSKNN-2	27.9	8.8	457.9	e ⁻¹

sity is larger by a factor of 4 to 6 compared to undoped material.⁵⁸⁻⁶¹ Although Ce doping is being evaluated to obtain optimum photorefractive properties, the grating formation rate in the visible spectrum for SBN:60 crystals is the largest among the bronze crystals studied so far (~ 50 to 100 ms at 6 W/cm²). As in the case of perovskite BaTiO₃, the response time is much slower in the IR region; however, the results of our work on the bronzes indicate that there is room for improvement in the IR response time (currently 5 to 10 s at 0.9 μ m) through the optimization of the shallow trap concentration and the crystallographic location of dopants in the bronze structure.

SBN:75 crystals are similar to SBN:60 in their electro-optic character, but with a much higher transverse electro-optic coefficient ($r_{33} = 1400 \times 10^{-14}$ m/V). On the other hand, BSKNN-2 has a strong longitudinal electro-optic coefficient ($r_{31} \approx 400 \times 10^{-12}$ m/V), and its general features such as fanning, coupling coefficient, and self-pumped phase-conjugate behavior are similar to those observed for perovskite BaTiO₃. Although the photorefractive properties of SBN:75 and BSKNN-2 appear to be promising, further improvements are needed to decrease their response time. Tables IX and X summarize the beam fanning and self-pumped phase-conjugate response times for these bronzes and for BaTiO₃ as determined by Sharp et al.⁶²⁻⁶⁴ Based on their investigations, it appears that the Ce-doped tungsten bronze crystals studied are comparable to BaTiO₃. More experimental data on these crystals are being obtained at the U.S. Army NVEOL and will be published elsewhere.

Improvements in photorefractive characteristics need to be related to the possible roles of dopant impurities. In the ideal picture, one needs both a donor of electrons and an acceptor to enhance the space-charge field E_s . These might be Ce³⁺ and Ce⁴⁺, Fe²⁺ and Fe³⁺, Ce³⁺ and Fe³⁺, or combinations of these with Nb⁴⁺ and various vacancies in the SBN:60 structure. The current results clearly indicate that the additions of Ce and Fe enhance photorefractive properties; however, the distribution of the various charge states, such as Ce³⁺, Ce⁴⁺, has not yet been established. Because Ce³⁺ (or Fe³⁺) is stable at growth temperatures, several possibilities exist for the species forming charge traps; these are shown in Table XI.

In the present case of tungsten bronze crystals, the tendency of Nb⁵⁺ to reduce to Nb⁴⁺ provides the possibility of donor

TABLE XI. Valence states of dopants in bronze crystals.

Dopant	Crystallographic Sites				Donor	Acceptor	Stable* States
	15-	12-	9-	6-			
Ce	-	Ce ³⁺	Ce ⁴⁺	-	Ce ³⁺	Ce ⁴⁺	Ce ³⁺
Ce and Nb	-	Ce ³⁺	Ce ⁴⁺	Nb ⁴⁺	Ce ³⁺ , Nb ⁴⁺	Ce ⁴⁺	Ce ³⁺ , Nb ⁵⁺
Ce	-	Ce ³⁺	-	-	Ce ³⁺	Cation Vac	Ce ³⁺
Fe	-	-	-	Fe ²⁺ , Fe ³⁺	Fe ²⁺	Fe ³⁺	Fe ³⁺
Fe, Nb	-	-	-	Fe ³⁺ , Nb ⁴⁺	Nb ⁴⁺	Fe ³⁺	Fe ³⁺ , Nb ⁵⁺
Fe	-	-	-	Fe ³⁺	Cation Vac	Fe ³⁺	Fe ³⁺
Ce, Fe	-	Ce ³⁺	-	Fe ³⁺	Ce ³⁺	Fe ³⁺	Ce ³⁺ , Fe ³⁺

*Valence state at growth temperature, vac - vacancy

states. Since the preferred state of Ce at growth temperatures is Ce³⁺, a donor, some questions remain concerning the identity of the acceptor in Ce-doped crystals. The observed tendency of Nb⁵⁺ to reduce during growth may encourage the formation of vacancies that could act as either donors or acceptors. Currently, we are using optical and Mossbauer spectroscopy in an attempt to positively identify the donor and acceptor species in these crystals.

7. FUTURE TUNGSTEN BRONZE MATERIALS

Another alternative approach to the development of improved photorefractive materials is the use of morphotropic phase boundary (MPB) crystals that have very large electro-optic effects. The electro-optic properties for crystal compositions close to MPB regions can be at least 5 to 10 times better than the current best materials and offer a unique opportunity to develop superior photorefractive materials.

Figure 15 shows a typical ferroelectric tungsten bronze system, Pb_{1-x}Ba_xNb₂O₆, in which the MPB region is located at $x = 0.37$.⁶⁵ In this region, the electro-optic, dielectric, pyroelectric, and piezoelectric properties are exceptionally large and are largely temperature independent. Several of the more useful tungsten bronze and perovskite systems show MPBs near which the polarization is large, giving large electro-optic and dielectric properties. As shown in Fig. 15, on a binary phase diagram an MPB appears as a nearly vertical line separating two ferroelectric phases; i.e., the boundary occurs at a nearly constant composition over a wide temperature range up to the Curie temperature. Poled crystals near such boundaries show unique and enhanced electro-optic properties because of the proximity in free energy of an alternative ferroelectric structure. A detailed description of MPB behavior has been provided by Jaffe et al.⁶⁶

For the Pb_{1-x}Ba_xNb₂O₆ system, the coexisting phases at the MPB are tetragonal and orthorhombic. In the tetragonal (4mm) symmetry for ferroelectric bronzes, the electro-optic coefficients r_{ij} of single domains are given from the phenomenological model of Cross et al.⁶⁷⁻⁶⁹ in terms of the g_{ij} quadratic coefficients of the paraelectric prototype by relations of the form

$$\begin{aligned} r_{11} &= 2g_{11}P_1\epsilon_{11}\epsilon_{00} \\ r_{33} &= 2g_{33}P_1\epsilon_{11}\epsilon_{00} \\ r_{42} &= r_{51} = 2g_{44}P_1\epsilon_{11}\epsilon_{00} \end{aligned} \quad (8)$$

The last relation is of special interest in that for a composition

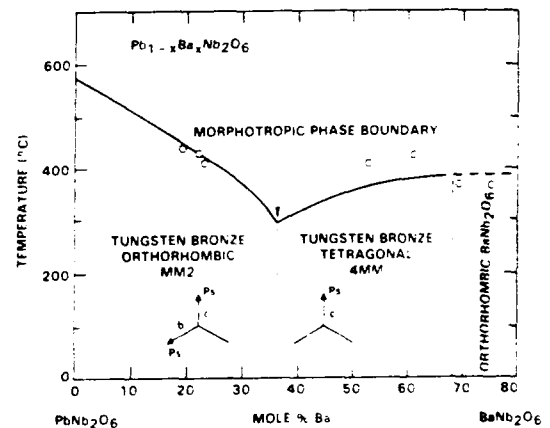


Fig. 15. Curie temperature versus composition for the Pb_{1-x}Ba_xNb₂O₆ system (Ref. 65).

close to the MPB but a long way from the ferroelectric Curie temperature, both P_3 and ϵ_{11} can be very large and nearly temperature independent.

For orthorhombic compositions close to the MPB, the equivalent relations are, with respect to the prototypic tetragonal axes,

$$\begin{aligned} r_{11} &= r_{22} = 2g_{11}P_1\epsilon_{11}\epsilon_{00} \\ r_{12} &= r_{21} = 2g_{21}P_1\epsilon_{11}\epsilon_{00} \\ r_{31} &= r_{32} = 2g_{31}P_1\epsilon_{11}\epsilon_{00} \\ r_{43} &= r_{53} = g_{44}P_1\epsilon_{11}\epsilon_{00} \\ r_{61} &= r_{62} = g_{44}P_1\epsilon_{11}\epsilon_{00} \end{aligned} \quad (9)$$

Now it is P_1 and ϵ_{33} that will be large, so large and nearly temperature invariant values of r_{31} and r_{43} are to be expected.

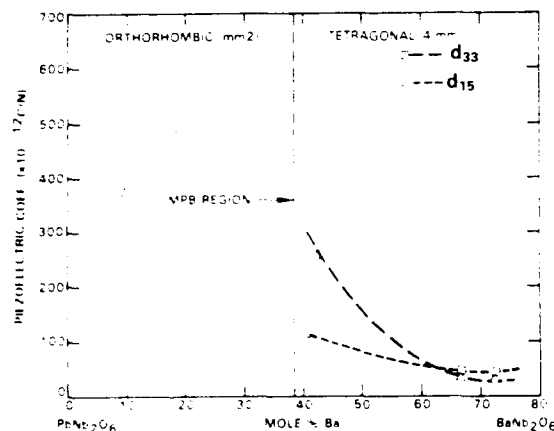
In the Pb_{1-x}Ba_xNb₂O₆ system, Shrout et al.^{70,71} demonstrated that it is possible to grow small crystals with compositions close to the MPB. For compositions on both sides of the boundary, the g_{ij} quadratic coefficients are largely temperature independent, as expected, and are bigger than those for SBN. With increasing Pb content, the piezoelectric coefficients d_{15} and d_{33} , shown in Fig. 16, escalate dramatically as the composition approaches the MPB, with values larger than those found for BaTiO₃. We have also identified other MPB systems within the tungsten bronze family, e.g., Ba₂NaNb₅O₁₅-Sr₂NaNb₅O₁₅, Pb₂KNb₅O₁₅-

TABLE XII. Ferroelectric properties at MPB for tungsten bronze systems.

System	x at MPB	T _c (°C)	Dielectric Constant at R.T.	Electro-Optic Coefficient $\times 10^{-12}$ m/V
(1-x) PbNb ₂ O ₆ - (x) BaNb ₂ O ₆	0.3*	300	1900	$\geq 1600^*$
+ La ³⁺ (2%)		230	1700	420**
+ La ³⁺ (6%)		115	3500	780**
(1-x) Pb _{2.5} Nb ₅ O ₁₅ - (x) Sr ₂ NaNb ₅ O ₁₅	0.75	135	2200	Large
(1-x) Pb ₂ KNb ₅ O ₁₅ - (x) Ba ₂ NaNb ₅ O ₁₅	0.25	255	1340	Large
(1-x) Ba ₂ NaNb ₅ O ₁₅ - (x) Sr ₂ NaNb ₅ O ₁₅	0.60	170	> 500	Low
(1-x) Pb ₂ KNb ₅ O ₁₅ - (x) Sr ₂ NaNb ₅ O ₁₅	0.70	155	930	Medium

* Single crystal samples

** Ceramic samples

Fig. 16. Piezoelectric d_{33} and d_{15} coefficients as a function of composition in the $\text{Pb}_{1-x}\text{Ba}_x\text{Nb}_2\text{O}_6$ system (Ref. 68).

$\text{Sr}_2\text{NaNb}_5\text{O}_{15}$, and $\text{Pb}_2\text{KNb}_5\text{O}_{15}$ - $\text{Ba}_2\text{NaNb}_5\text{O}_{15}$,⁴² summarized in Table XII. The major advantages of MPB materials for photorefractive applications are

- (1) The separation from the phase boundary is a function of composition, not temperature; i.e., the boundary is morphotropic, so very high values of the dielectric and electro-optic constants can persist over a wide temperature range.
- (2) For compositions close to the boundary, r_{51} and r_{42} values larger than those for BaTiO_3 are possible.
- (3) Since the prototype symmetry is 4-mm, only one unique 4-fold axis exists, and 90° twins are not possible; hence, cracking is not as severe a problem as reported for BaTiO_3 .^{70,71}
- (4) Very large transverse drift fields could be achieved.

We are devoting a considerable effort to the development of MPB crystals in the expectation that they can provide a real breakthrough for device applications based on the photorefractive effect. These crystals should also be beneficial for other applications such as electro-optic switches and modulators, transverse pyroelectric focal plane arrays, SAW devices, and piezoelectric transducers. The potential benefit in these applications justifies the further development of these materials, al-

though they may prove quite difficult to grow in appropriate size and quality.

8. CONCLUSION

The prospects are bright for further development of SBN and BSKNN solid-solution crystals to larger sizes, and efforts in that direction are progressing. By selecting the proper dopant concentration and its site preference in the tungsten bronze structure, it is possible to control not only the photorefractive time of response but also the spectral response in both the visible and IR regions. Such opportunities are rarely seen in other ferroelectric materials. Applications to optical computing, image processing, and phase conjugation will follow the development of still larger crystals.

Better photorefractive effects may be achievable in morphotropic phase boundary materials if suitable growth techniques become available. The current problems associated with the growth of MPB PBN:60 may be overcome by developing thin films of reasonable size and quality. Recently, we demonstrated the growth of ferroelectric PBN:60 films on SBN:60 substrates of various orientations with good success. Although considerable further development is required, the current success of achieving crystalline films of this morphotropic composition suggest that devices based on MPB thin films may soon emerge. Substrates are key to obtaining single-crystal films of the desired orientation with good ferroelectric properties. Currently, ferroelectric thin-film growth is being pursued in Japan and the USSR on nonferroelectric substrates such as sapphire, glass, and MgO. On such substrates, however, crystallinity and good ferroelectric properties are often difficult to obtain. The use of ferroelectric paraelectric single-crystal substrates from the same crystal family should help to minimize many film growth problems; for this reason, we are now actively engaged in developing MPB films for optical applications using SBN and BSKNN substrate materials.

9. ACKNOWLEDGMENTS

This research work on tungsten bronze crystals and their applications was supported by the Defense Advanced Research Products Agency (contract No. N00014-82-C-2466). In this regard, the authors wish to thank Richard Reynolds and John Neff for their encouragement and technical support. The authors are also

grateful for the discussions on this research with L. E. Cross, A. Yariv, P. Yeh, M. Khoshnevisan, and E. Sharp.

10. REFERENCES

1. R. L. Townsend and J. T. LaMacchia, "Optically induced refractive index in BaO," *J. Appl. Phys.* 41, 5188 (1970).
2. P. Gunter, I. Flückiger, J. P. Huignard, and F. Micheron, *Ferroelectrics* 13, 297 (1976).
3. F. S. Chen, *J. Appl. Phys.* 38, 3148 (1967).
4. R. Orlowski, L. A. Boatner, and E. Krutzig, "Photorefractive effects in the cubic phase of KTN," *Opt. Commun.* 35, 45 (1980).
5. J. J. Amodio, D. L. Staebler, and A. W. Stephens, "Holographic storage in doped barium sodium niobate ($\text{Ba}_{1-x}\text{Na}_x\text{Nb}_2\text{O}_6$)," *Appl. Phys. Lett.* 18, 507 (1971).
6. J. B. Thaxter, "Electrical control of holographic storage in SBN," *Appl. Phys. Lett.* 15, 210 (1969).
7. L. H. Lin, *Proc. IEEE* 57, 252 (1969).
8. M. Peltier and F. Micheron, "Volume hologram recording and charge transfer process in BSO and BGO," *J. Appl. Phys.* 48, 3683 (1977).
9. V. M. Fridkin, B. N. Popov, and K. A. Verkhovskaya, *Appl. Phys.* 16, 313 (1978).
10. A. Ashkin, B. Tell, and J. M. Dziedzic, "Laser induced refractive index inhomogeneities and absorption saturation in CdS," *IEEE J. Quantum Electron.* QE-3, 400 (1967).
11. T. Nakamura, V. Fridkin, R. Magomadov, M. Takashige, and K. Verkhovskaya, "Photovoltaic and photorefractive phenomena in ferroelectric Rb_2ZnBr_4 ," *J. Phys. Soc. Jpn.* 48, 1588 (1980).
12. F. Micheron, A. Hermosin, G. B. Smith, and J. Nicolas, *C. R. Acad. Sci.* 8 (Dec. 1971).
13. R. R. Neurgaonkar, W. K. Cory, and J. R. Oliver, "Growth and applications of tungsten bronze family crystals," *Ferroelectrics* 51, 3 (1983).
14. R. R. Neurgaonkar, J. R. Oliver, and L. E. Cross, "Ferroelectric properties of tetragonal tungsten bronze single crystals," *Ferroelectrics* 56, 31 (1984).
15. P. V. Lenzo, E. G. Spencer, and A. A. Ballman, "Electro-optic coefficients of ferroelectric SBN," *Appl. Phys. Lett.* 11, 23 (1967).
16. S. T. Liu and R. B. Maciulek, "Rare earth modified $\text{Sr}_{1-x}\text{Ba}_x\text{Nb}_2\text{O}_6$ ferroelectric crystals and their applications as infrared detectors," *J. Electron. Mater.* 4, 91 (1975).
17. A. M. Glass, "Investigation of the electrical properties of SBN with special reference to pyroelectric detection," *J. Appl. Phys.* 40, 4699 (1969).
18. P. P. Labbe, M. Frey, B. Ravcau, and J. C. Monier, "Structure cristalline de la phase ferroelectrique du niobate de plomb PbNb_2O_6 , remplacement des atomes metalliques et interpretation de la structure," *Acta Crystallogr. B* 33, 2201 (1977).
19. P. B. Jamieson, S. C. Abrahams, and J. L. Bernstein, "Ferroelectric tungsten bronze type crystal structure. I. barium strontium niobate $\text{Ba}_{1-x}\text{Sr}_x\text{Nb}_2\text{O}_6$," *J. Chem. Phys.* 48, 5048 (1968) and 50, 4352 (1969).
20. F. W. Ainger, W. P. Bickley, and G. V. Smith, "The search for new ferroelectrics with the tungsten bronze structure," *Proc. Brit. Ceram. Soc.* 18, 221 (1970).
21. T. Ikeda, K. Uno, K. Oyama, A. Sagara, J. Kato, S. Takano, and H. Sato, "Some solid solution of the $\text{A}(\text{B}_2\text{O}_6)_2$ and $\text{A}_2\text{B}_2\text{O}_6$ type tungsten bronze ferroelectrics," *Jpn. J. Appl. Phys.* 17, 341 (1978).
22. J. Ravez and P. Hagenmuller, "Sequence de transitions des phases de structure bronzes de tungsten quadratiques," *Mater. Res. Bull.* 12, 769 (1979).
23. J. Ravez, A. Perron-Simon, and P. Hagenmuller, "The tetragonal tungsten bronze like phases crystallochemical rules, relations between ferroelectric properties and structural distortions," *Ann. Chim. (France)* 268, 251 (1976).
24. J. F. Nye, *Physical Properties of Crystals*, Oxford Univ. Press, London (1966).
25. E. G. Spencer, P. V. Lenzo, and A. A. Ballman, *Proc. IEEE* 52, 2074 (1967).
26. J. T. Mielek and M. Neuberger, *Handbook of Electronic Materials*, Vol. 8,IFI Plenum, New York (1972).
27. J. Rodriguez, A. Siahmakoun, G. Salamo, M. J. Miller, W. W. Clark III, G. L. Wood, E. J. Sharp, and R. R. Neurgaonkar, "BSKNN as broadband self-pumped conjugate mirror," accepted for publication in *Opt. Lett.*
28. J. R. Carruthers and H. Grosso, "Phase equilibrium relations in the ternary system $\text{BaO}-\text{SrO}-\text{Nb}_2\text{O}_5$," *J. Electrochem. Soc.* 117, 1426 (1970).
29. A. A. Ballman and H. Brown, "The growth and properties of $\text{Sr}_{1-x}\text{Ba}_x\text{Nb}_2\text{O}_6$ a tungsten bronze ferroelectric," *J. Cryst. Growth* 1, 311 (1967).
30. S. T. Liu and R. B. Maciulek, *J. Electron. Mater.* 4, 91 (1975).
31. R. B. Maciulek and S. T. Liu, "Preparation and properties of low loss SBN ferroelectric single crystals," *J. Electron. Mater.* 2, 191 (1973).
32. K. Megumi, N. Nagatsuma, K. Kashiwada, and Y. Furuhashi, "The congruent melting composition of SBN," *Mater. Sciences* 11, 1583 (1976).
33. R. R. Neurgaonkar, M. H. Kalisher, T. C. Lim, E. J. Staples, and K. L. Keester, "Czochralski single crystal growth of $\text{Sr}_{0.6}\text{Ba}_{0.4}\text{Nb}_2\text{O}_6$ for surface acoustic wave devices," *Mater. Res. Bull.* 15, 1235 (1980).
34. R. R. Neurgaonkar, W. K. Cory, and J. R. Oliver, "Growth and applications of tungsten bronze family crystals for optical applications," *Ferroelectrics* 53, 301 (1985).
35. R. R. Neurgaonkar, "Tungsten bronze family crystals for optical device applications," in *Spatial Light Modulators and Applications*, U. Efron, ed., Proc. SPIE 465, 97-101 (1984).
36. R. R. Neurgaonkar and W. K. Cory, "Progress in photorefractive tungsten bronze crystal," *J. Opt. Soc. Am. B* 3, 274 (1986).
37. T. Fukuda, "Growth and properties of ferroelectric $\text{K}_3\text{Li}_2(\text{Ta}_2\text{Nb}_{1-x}\text{O}_{15})$," *Jpn. J. Appl. Phys.* 8, 122 (1968) and *J. Cryst. Growth* 6, 293 (1970).
38. F. W. Ainger, J. A. Beswick, and S. G. Porter, "Ferroelectrics in the $\text{K}_2\text{O}-\text{SrO}-\text{Nb}_2\text{O}_5$ system," *Ferroelectrics* 3, 321 (1972).
39. Y. Itoh and H. Iwasaki, "Ferroelectric and optical properties of $\text{Ba}_2\text{Ti}_2\text{Nb}_2\text{O}_{10}$ single crystals," *J. Phys. Chem.* 34, 1639 (1973) and *Jpn. J. Appl. Phys.* 9, 157 (1970).
40. T. Yamada, "Single crystal growth and piezoelectric properties of $\text{Pb}_2\text{KNb}_2\text{O}_8$," *Appl. Phys. Lett.* 23, 213 (1973).
41. J. Nakano and T. Yamada, "Ferroelectric and optical properties of $\text{Pb}_2\text{KNb}_2\text{O}_8$," *J. Appl. Phys.* 46, 2361 (1975).
42. J. R. Oliver, R. R. Neurgaonkar, and G. L. Shoop, "Structural and ferroelectric properties of morphotropic phase boundary systems in tungsten bronze family," in *Proc. 6th IEEE Int. Symp. on Applications of Ferroelectrics*, p. 485 (1986).
43. O. F. Dudnik, A. K. Gromov, V. B. Kravchenko, Yu. L. Kopylov, and G. F. Kuznetsov, *Soviet Phys. Crystallogr.* 15(2), 330 (1980).
44. R. R. Neurgaonkar, W. K. Cory, W. W. Ho, W. F. Hall, and L. E. Cross, "Low and high frequency dielectric properties of ferroelectric tungsten bronze $\text{Sr}_2\text{KNb}_2\text{O}_8$ crystals," *Ferroelectrics* 38, 857 (1981).
45. J. P. Huignard and A. Marrackchi, *Opt. Commun.* 38, 249 (1981).
46. J. P. Huignard and A. Marrackchi, *Opt. Lett.* 6, 622 (1981).
47. P. Yeh, *Opt. Commun.* 45, 323 (1983).
48. P. Yeh, *J. Opt. Soc. Am.* 73, 1268 (1983).
49. P. Yeh, *Appl. Opt.* 23, 2974 (1984).
50. J. O. White, M. Cronin-Golomb, B. Fischer, and A. Yariv, *Appl. Phys. Lett.* 40, 450 (1982).
51. M. E. Lines and A. M. Glass, *Principles and Applications of Ferroelectrics and Related Materials*, Clarendon Press, Oxford (1977).
52. K. Megumi, H. Kozuka, M. Kobayashi, and Y. Furuhashi, *Appl. Phys. Lett.* 30, 631 (1977).
53. R. R. Neurgaonkar and J. R. Oliver, Semi-Annual Technical Report No. 4, DARPA Contract N0014-82-C-2466 (1985).
54. A. Ishida, O. Mikami, S. Miyazawa, and M. Sumi, *Appl. Phys. Lett.* 21, 192 (1972).
55. E. Okamoto, H. Ikeo, and K. Muto, *Appl. Opt.* 14, 2453 (1975).
56. P. N. Gunter, "Electric-field dependence of phase conjugate wave front reflectivity in reduced KNbO_3 and BSO," *Opt. Lett.* 7, 10 (1982).
57. P. N. Gunter, *Phys. Reports*, 93, 199 (1982).
58. M. D. Ewbank, R. R. Neurgaonkar, W. K. Cory, and J. Feinberg, "Optical characterization of photorefractive strontium barium niobate," submitted to *J. Appl. Phys.*
59. G. Rakuljic, A. Yariv, and R. R. Neurgaonkar, "Photorefractive properties of undoped, cerium-doped, and iron-doped single-crystal strontium barium niobate," *Opt. Eng.* 25(11), 1212-1216 (1986).
60. G. Rakuljic, A. Yariv, and R. R. Neurgaonkar, "Photorefractive properties of ferroelectric BaTiO_3 and SBN:60," in *Nonlinear Optics and Applications*, P. Yeh, ed., Proc. SPIE 613, 110-118 (1986).
61. G. Rakuljic, K. Sayano, A. Yariv, and R. R. Neurgaonkar, "Self-starting passive phase conjugate mirror with Ce-doped $\text{Sr}_{0.5}\text{Ba}_{0.5}\text{Nb}_2\text{O}_6$," *Appl. Phys. Lett.* 50(1), 10 (1987).
62. E. J. Sharp, M. J. Miller, G. L. Wood, W. W. Clark III, G. Salamo, and R. R. Neurgaonkar, "Photorefractive properties of tungsten bronze SBN single crystals," in *Proc. 6th IEEE Int. Symp. on Applications of Ferroelectrics*, p. 51 (1986).
63. G. Salamo, M. J. Miller, W. W. Clark III, G. L. Wood, and E. J. Sharp, "SBN:60 as broadband self-pumped conjugate mirror," accepted for publication in *Opt. Lett.*
64. M. J. Miller, E. J. Sharp, G. L. Wood, W. W. Clark III, G. Salamo, and R. R. Neurgaonkar, "Time response of a Ce-doped $\text{Sr}_{0.5}\text{Ba}_{0.5}\text{Nb}_2\text{O}_6$ self-pumped phase-conjugate mirror," accepted for publication in *Opt. Commun.*
65. E. C. Subbarao, G. Shirane, and F. Jona, "X-ray, piezoelectric and optical studies of ferroelectric PbNb_2O_6 and related compounds," *Acta Crystallogr.* 13, 226 (1960).
66. B. Jaffe, W. R. Cook, and H. Jaffe, *Piezoelectric Ceramics*, Academic Press, New York (1971).
67. R. R. Neurgaonkar, J. R. Oliver, and L. E. Cross, Final Technical Report, DARPA Contract N0014-82-C-2466 (1986).
68. M. DiDomenico and S. H. Wemple, "Oxygen octahedra ferroelectrics. I. theory of electro-optical and nonlinear optical effects," *J. Appl. Phys.* 40, 720 (1969).
69. S. H. Wemple, "Electro-optical and nonlinear optical properties of crystals," in *Applied Solid-State Sciences*, Vol. 3, R. Wolfe, ed., p. 263, (1972).
70. T. R. Shrout, H. Chen, and L. E. Cross, "Dielectric, piezoelectric properties of $\text{Pb}_{1-x}\text{Ba}_x\text{Nb}_2\text{O}_6$ ferroelectric tungsten bronze crystals," *Ferroelectrics* 56, 45 (1983).
71. T. R. Shrout, L. E. Cross, and D. A. Hukin, "Ferroelectric properties of tungsten bronze lead barium niobate (PBN) single crystals," *Ferroelectrics Lett.* 44, 325 (1983).



Ratnakar R. Neurgaonkar is manager of the Ferroelectric Materials Department at the Rockwell International Science Center. He received the B.Sc. (1962), M.Sc. (1963), and Ph.D. (1967) degrees in solid-state chemistry from Poona University, India. At Rockwell, Dr. Neurgaonkar has been directing the ferroelectric materials research and development program for various device applications, including electro-optic, photorefractive, and pyroelectric imagers, SAWs, millimeter wave,

and piezoelectric transducer applications. With Warren K. Cory he has developed various growth techniques for ferroelectric crystals: films and has successfully demonstrated the growth of optical-quality doped and undoped $\text{Sr}_{1-x}\text{Ba}_x\text{Nb}_2\text{O}_6$ and BSKNN single crystals using the Czochralski technique. Besides ferroelectric materials, Dr. Neurgaonkar has also been interested in magnetics, luminescence, and laser crystal development work. He is a member of the American Ceramic Society, the Electrochemical Society, and the American Association for Crystal Growth. He is the author or coauthor of more than 90 research publications.



Warren K. Cory is a research specialist in the Ferroelectric Materials Department at Rockwell International Science Center. He received the BA degree from the University of California at Los Angeles in language (German) in 1965. He has been working in the crystal-growth area for more than 18 years and has grown a variety of different crystals using different techniques. Before joining Rockwell, Mr. Cory worked at Stanford University and the University of Mexico in Mexico City.

At Rockwell, together with Ratnakar Neurgaonkar, he has developed striation-free and defect-free quality tungsten bronze $\text{Sr}_{1-x}\text{Ba}_x\text{Nb}_2\text{O}_6$ crystals. He is also involved in perfecting the ADC-equipped Czochralski technique for other bronze crystals such as BSKNN and MPB compositions and perovskite KNbO_3 compositions. Mr. Cory has modified current growth equipment to state-of-the-art quality and recently introduced computer control of growth. He is a member of the American Association for Crystal Growth and is a coauthor of more than 40 publications.



John R. Oliver received his BS degree in 1967 and MS degree in 1969 in electrical engineering from the University of Colorado. From 1969 to 1972 he was an instructor and a graduate research assistant in high speed optical switching at the University of Colorado. In 1972 he joined the Rockwell International Science Center, where he has been involved in the study of dielectric, electronic, and ionic transport properties of semiconducting and insulating materials. His work includes the

study of thermally stimulated conductivity in perovskites and semi-insulating GaAs, ionic diffusion in wide-bandgap insulators, the ionic and electronic properties of interfaces, the electrical and optical properties of AlGaAs/GaAs solar photovoltaics, and electrical transport phenomena in semiconducting and semi-insulating materials. Mr. Oliver is a codeveloper of the photoinduced current transient spectroscopy (PITS) technique for the characterization of electronic trapping levels in semi-insulating materials, particularly GaAs crystals and epilayers. He is currently engaged in the growth, ferroelectric characterization, and phenomenological theory of tungsten bronze materials. Mr. Oliver has 35 publications and is a member of Sigma Xi and the American Ceramic Society.

Mark D. Ewbank is a member of the technical staff in the Applied Optics Department at the Rockwell International Science Center, where he has been involved in infrared focal plane development, optical thin film structures, and materials characterization measurements (including refractive index, photoelastic, electro-optic, and thermoelectric properties). Presently, his research interests are in the areas of optical phase conjugation, nonlinear optics, and photorefractive effects. He has coauthored more than 30 scientific publications and is a member of the American Physical Society and the OSA.



W. F. Hall received his Ph.D. in physics from the University of California in 1964. From 1965 to the present, he has worked as a research physicist, member of the technical staff, and currently as principal scientist at the Rockwell International Science Center. He has made significant scientific contributions in the following areas: charged-particle scattering in crystals, properties of magnetic systems, viscoelastic effects in polymer solutions, and characteristics of compound semiconductor

interfaces. In addition to his research in the above areas, he has collaborated in the investigation of distributed-feedback lasers, magnetic suspension viscosity, dielectric properties of condensed matter, and various applications of electromagnetic theory. Dr. Hall is a member of the American Physical Society, Pi Mu Epsilon, and Sigma Pi Sigma, and has over 40 publications.



Rockwell International

Science Center

SC5441.FTR

GROWTH AND FERROELECTRIC PROPERTIES OF TUNGSTEN BRONZE

$B_{2-x}Sr_xK_{1-y}Na_yNb_5O_{15}$ (BSKNN) SINGLE CRYSTALS

GROWTH AND FERROELECTRIC PROPERTIES OF TUNGSTEN BRONZE $\text{Ba}_{2-x}\text{Sr}_x\text{K}_{1-y}\text{Na}_y\text{Nb}_5\text{O}_{15}$ (BSKNN) SINGLE CRYSTALS

R.R. NEURGAONKAR, W.K. CORY and J.R. OLIVER

Rockwell International Science Center, P.O. Box 1085, Thousand Oaks, California 91360, USA

and

W.W. CLARK III, G.L. WOOD, M.J. MILLER and E.J. SHARP

Center for Night Vision and Electro-Optics, Ft. Belvoir, Virginia 22060-5677, USA

Received 9 March 1987; manuscript received in final form 1 July 1987

The undoped and Ce-doped ferroelectric tungsten bronze crystals, specifically $\text{Ba}_{1.5}\text{Sr}_{0.5}\text{K}_{0.75}\text{Na}_{0.25}\text{Nb}_5\text{O}_{15}$ (BSKNN-1) and $\text{Ba}_{0.5}\text{Sr}_{1.5}\text{K}_{0.5}\text{Na}_{0.5}\text{Nb}_5\text{O}_{15}$ (BSKNN-2), have been grown in optical quality using the Czochralski technique. Although both of these crystals are tetragonal with point group 4mm, their growth habit along the [001] direction differs: BSKNN-1 crystals grow in a square shape with four well-defined facets, while BSKNN-2 crystals have an octahedral growth habit with eight well-defined facets. The longitudinal dielectric (ϵ_{11}) and linear electro-optic (r_{31}) constants show strong enhancement when expanding from BSKNN-1 and BSKNN-2 crystals, indicating that the latter could be of major interest for electro-optic, photorefractive and pyroelectric applications.

1. Introduction

Tungsten bronze crystals exhibit excellent electro-optic [1,2], photorefractive [4-7], and pyroelectric [8,9] properties, and these attractive features make them potential important for applications in optoelectronics. Bronze solid-solution crystals such as $\text{Sr}_{1-x}\text{Ba}_x\text{Nb}_2\text{O}_6$ (SBN), either doped or undoped, have proven to be excellent materials for various applications such as guided-wave optics [10], photorefractive [3-7] and millimeter-wave [11-14] device studies. These crystals are also being used in pyroelectric detector studies because of their large pyroelectric coefficients.

Tetragonal (4mm) SBN solid-solution crystals exhibit excellent transverse ferroelectric and optical properties in contrast to perovskite BaTiO_3 crystals, which show strong longitudinal ferroelectric and optical properties. Currently, both SBN and BaTiO_3 are leading candidates for various applications; however, the use of BaTiO_3 is limited due to extreme difficulty in growing large size,

optical-quality doped crystals. For this reason, we have investigated the $\text{Ba}_{2-x}\text{Sr}_x\text{K}_{1-y}\text{Na}_y\text{Nb}_5\text{O}_{15}$ (BSKNN) solid-solution system which resembles BaTiO_3 in many respects, particularly in its ferroelectric properties [15,16]. The present paper reports on the growth and characterization of $\text{Ba}_{1.5}\text{Sr}_{0.5}\text{K}_{0.75}\text{Na}_{0.25}\text{Nb}_5\text{O}_{15}$ (BSKNN-1) and $\text{Ba}_{0.5}\text{Sr}_{1.5}\text{K}_{0.5}\text{Na}_{0.5}\text{Nb}_5\text{O}_{15}$ (BSKNN-2) crystals for optical and pyroelectric applications.

2. Experimental

The undoped and doped BSKNN solid-solution system was studied using reagent grade chemicals, specifically BaCO_3 , SrCO_3 , K_2CO_3 , NaCO_3 , CeO_2 and Nb_2O_5 . The appropriately weighed materials were thoroughly mixed and calcined at 900°C and then sintered at 1350°C. The structure identification and solid solubility range for each phase were checked using X-ray diffraction measurements. The compositions BSKNN-1 and

BSKNN-2 were then studied in more detail using DTA techniques to ascertain melting temperatures and supercooling behavior.

For single crystal growth experiments, high-purity starting materials (Johnson Matthey, Ltd.) were used. To maintain a high degree of homogeneity in the crystals, the starting materials were thoroughly ball-milled before they were melted in a platinum crucible (chemical analysis did not show the presence of Al_2O_3 due to alumina ball milling). The crucible was 2 in. in both diameter and height, and was supported in a fibrous alumina insulating jacket (table 1). The furnace used was RF induction heated to 370 kHz. All of the crystals were cooled through their paraelectric/ferroelectric phase transition (170–210 °C) in an after-heater furnace.

A variety of techniques were used to evaluate the ferroelectric, pyroelectric and electro-optic properties of these crystals. Crystals belonging to the tetragonal point group 4mm have three piezoelectric and electro-optical coefficients and two dielectric constant, thus requiring various samples of differing orientation. Bar and plate-shaped specimens, as shown in fig. 1, oriented along (001) and (100) were cut with a diamond saw from the crystal boule with the orientation determined by Laue X-ray back reflection. Samples were then lapped and polished to achieve optical quality.

Prior to most measurements, the crystals were poled by the field-cooling method (T_c to room temperature in O_2) under a DC field of 8–10 kV/cm along the polar (001) axis using either Au or Pt electrodes. Unlike BaTiO_3 , no special precautions are required to pole these tungsten bronze crystals. The completeness of poling was checked

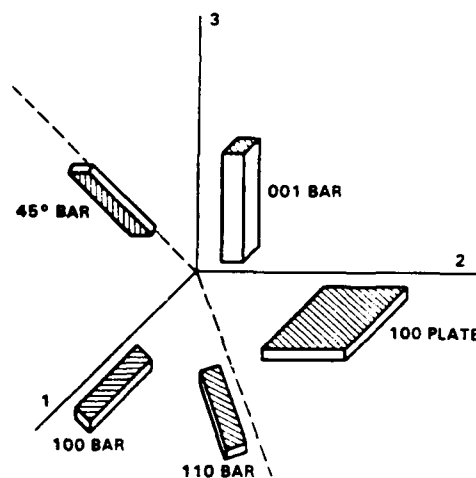


Fig. 1. Bar- and plate-shape BSKNN single crystal specimens

by measuring the dielectric constant before and after poling.

3. Results and discussion

The BSKNN-1 and BSKNN-2 compositions exist on a SrNb_2O_6 – BaNb_2O_6 – KNbO_3 – NaNbO_3 quaternary system, as shown in fig. 2. Compositions exhibiting the tungsten bronze structure in this system can possess either tetragonal (4mm) or orthorhombic (mm2) structures, the latter occurring basically for Na^+ -containing compositions such as $\text{Sr}_2\text{NaNb}_5\text{O}_{15}$, $\text{Ba}_2\text{NaNb}_5\text{O}_{15}$ and $(\text{Sr,Ba})_2\text{NaNb}_5\text{O}_{15}$. For this reason, the relative magnitudes of the transverse (r_{33}) and longitudinal (r_{31}) electro-optic coefficients in these crystals

Table 1
Growth conditions for the BSKNN solid-solution crystals

Composition	Growth temperature (°C)	Pulling rate (mm/h)	Color	Size (cm)	Growth habit	Lattice constant (Å)
BSKNN-1	1480	8–10	Colorless	0.5–1.0	Square	$a = 12.506$, $c = 3.982$
BSKNN-1:Ce	1480	6–10	Pink	0.5–1.0	Square	$a = 12.506$, $c = 3.982$
BSKNN-2	1490	6–8	Colorless	0.8–1.2	Octahedron	$a = 12.449$, $c = 3.938$
BSKNN-2:Ce	1490	6–8	Pink	0.8–1.2	Octahedron	$a = 12.449$, $c = 3.938$

All crystals were grown in oxygen along the (001) direction. Loss of K due to volatilization was sometimes a problem in BSKNN-1 crystals

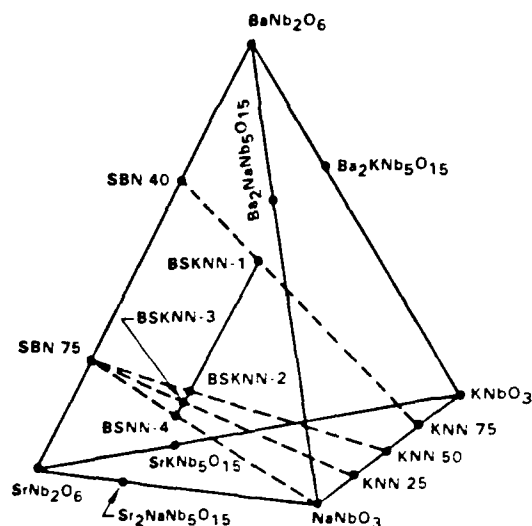


Fig. 2 The phase relation in the SrNb_2O_6 - BaNb_2O_6 - KNbO_3 - NaNbO_3 quaternary system

are strong functions of both the Ba : Sr and K : Na ratios. Since these coefficients are adjustable, our work has concentrated on the binary join between BSKNN-1 and BSNN-4, as shown in fig. 2. The end-member composition BSNN-4 is orthorhombic at room temperature and is a part of the $\text{Sr}_2\text{NaNb}_5\text{O}_{15}$ - $\text{Ba}_2\text{NaNb}_5\text{O}_{15}$ system [17]. The latter system was recently studied by Oliver et al. [17] and exhibits an apparent morphotropic phase boundary at the composition $\text{Sr}_{1.2}\text{Ba}_{0.8}\text{NaNb}_5\text{O}_{15}$.

Both BSKNN-1 and BSKNN-2 are considered to be filled bronze structures because the 15- and 12-fold coordinated sites are completely occupied. The tetragonal tungsten bronze compositions can be represented by the chemical formulae $(A_1)_4(A_2)_2C_4B_{10}O_{30}$ and $(A_1)_4(A_2)_2B_{10}O_{30}$, where A_1 , A_2 , C and B are 15-, 12-, 9- and 6-fold coordinated sites, respectively. The BSKNN compositions are based on the $(A_1)_4(A_2)_2B_{10}O_{30}$ formulation and in this arrangement both the A_1 and A_2 sites are completely occupied by Ba^{2+} , Sr^{2+} , K^+ and Na^+ . In contrast, other important bronze compositions based on the $\text{Sr}_{1-x}\text{Ba}_x\text{Nb}_2\text{O}_6$ solid-solution system have partially empty 15- and 12-fold coordinated sites with a vacancy of up to 20%.

3.1. Growth of BSKNN Crystals

Both BSKNN-1 and BSKNN-2 crystal were grown using an automatic diameter-controlled Czochralski growth technique used for other tungsten bronze crystals, e.g., SBN : 60, SBN : 75, SKN and KLN [3,18-20]. The growth of these BSKNN crystals was successful; however, growing BSKNN-1 was found to be more difficult than for BSKNN-2. Since these crystal compositions contain six components, it is very difficult to establish precisely the true congruent melting composition. However, apparent BSKNN-2 is closer to the true congruent melting composition than BSKNN-1.

The growth conditions for these crystals are given in table 1. Initially, bronze SBN : 60 crystals were used as seed material, but as small BSKNN crystals became available, these were used in subsequent crystal growths. Because these components are multicomponent and have several crystallographic sites available for Ba^{2+} , Sr^{2+} , K^+ and Na^+ , the following problems were encountered:

- (1) Exchange of crystallographic sites, specifically of the 15- and 12-fold coordinated ions such as Ba^{2+} , Sr^{2+} , K^+ and Na^+ , can cause severe optical striations and cracking problems.
- (2) Crystals cracked when cycled through the paraelectric/ferroelectric phase transitions. This was less severe for BSKNN-2.
- (3) High solid-solution melting temperatures were in excess of 1480°C ; hence, volatilization of K^+ and oxidation-reduction ($\text{Nb}^{5+} \rightleftharpoons \text{Nb}^{4+}$) problems were observed.

These growth problems have also been reported [3,18] for other solid-solution tungsten bronze crystals such as SBN : 60, SBN : 75, SKN, KLN and PBN, and were sufficiently minimized in BSKNN crystal growths to obtain optical quality crystals as large as 1 to 1.2 cm square. Fig. 3 shows typical BSKNN-1 and BSKNN-2 crystal boules grown along the (001) direction. The crystal growth of these compositions along other directions such as (100) and (110) was also attempted, but was found to be very difficult because of poor control over the neck-out from the crystal seed.

The use of an automatic diameter control system in these growths helped to maintain the necessary growth temperature stability. We have found

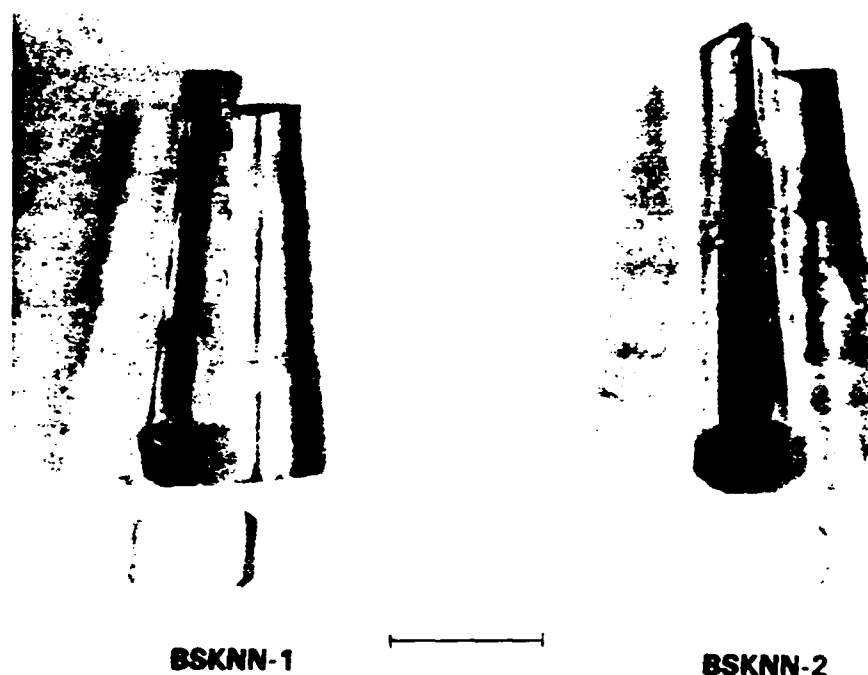


Fig. 3. Typical BSKNN-1 and BSKNN-2 crystals grown along the (001) direction. Marker represents 1 cm.

in this work, as well as in our work on SBN:60 and SBN:75 that crystal quality also depends strongly on the following factors:

- (1) Impurities in the starting materials: Ca^{2+} , Fe^{3+} , Mg^{2+} , etc. The presence of Fe^{3+} seems to be a major cause of optical striations in these crystals.
- (2) Rotation and pulling rates: Faster pulling rates are needed at lower rotation rates to control temperature stability since crystal thermal conductivity is low.
- (3) Cooling rate variations: the Ba: Sr and K: Na distribution on the 15- and 12-fold coordinated sites change for different cooling rates, causing strain, as well as striations, in the crystals.

As reported for Ce-doped SBN:60 crystals [3], the addition of 0.05 wt% Ce in both BSKNN compositions did not change the growth conditions or degrade the optical quality. However, the addition of Fe^{3+} in the 6-fold coordinated site causes severe striation problems in tungsten bronze BSKNN-1, BSKNN-2 and SBN:60. For photore-

fractive applications, one needs Ce in two valence states, Ce^{3+} and Ce^{4+} . Since photorefractive properties are enhanced significantly for Ce-doped BSKNN-2 crystals, we believe that Ce exists in both states. However, further work is necessary to establish the actual valence state distribution.

As shown in fig. 4, both BSKNN-1 and BSKNN-2 crystal boules exhibit natural facets: however, BSKNN-1 grows in a square shape with four well-defined faces, while BSKNN-2 crystals have an octahedral shape with eight well-defined facets or faces. The wider facets in both crystals are (100), thus facilitating the process of orienting the crystal axes. SBN solid-solution crystals are also faceted, but they are cylindrical in shape with 24 well-defined facets [3,21]. We have found that the differences observed in crystal shape with composition also reflect insignificant differences in the respective ferroelectric and optical properties. Fig. 4 shows the idealized forms of bronze crystals.

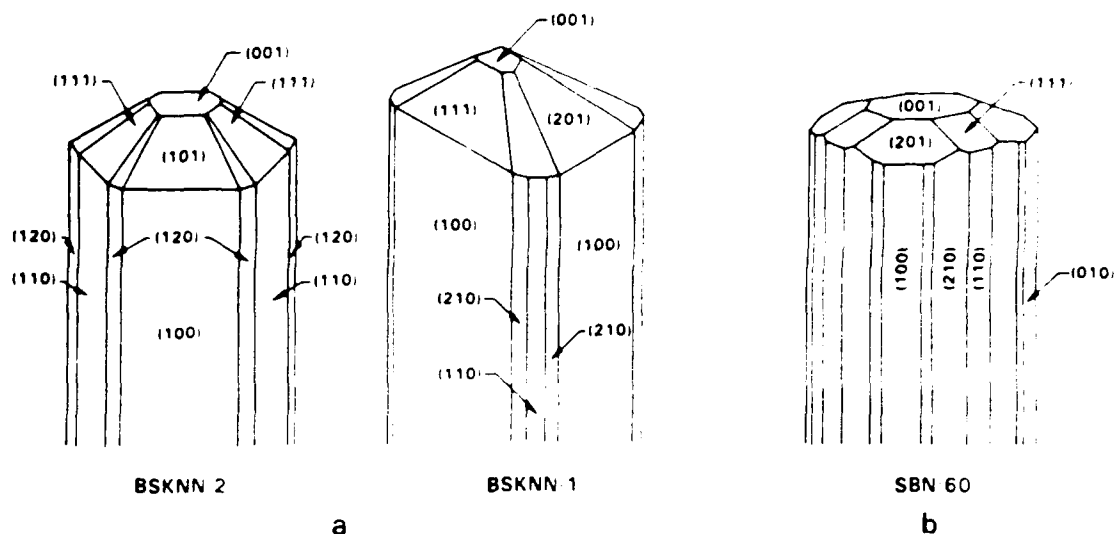


Fig. 4. Idealized forms of tungsten bronze crystals. (a) large longitudinal effects. (b) large transverse effects.

3.2. Ferroelectric and optical properties

The temperature-dependent dielectric properties of BSKNN crystals were measured from -150°C to above 400°C using a Hewlett-Packard capacitance bridge. The dielectric properties at 10 kHz for BSKNN-1 are shown in fig. 5 for the a - and c -axis (polar) crystallographic orientations. Like other tungsten bronze ferroelectrics, the polar axis dielectric constant is characterized by a sharp dielectric anomaly at the ferroelectric phase transition temperature, T_c , which occurs at $205\text{--}210^{\circ}\text{C}$ for BSKNN-1. Below T_c , the c -axis dielectric constant decreases monotonically to approximately 100 at room temperature, and to 55 at -150°C . For crystals poled to a single ferroelectric domain, the dielectric dispersion has been found to be minimal over the range 100 Hz to 100 kHz, except near T_c . Along the a -axis, only a slight dielectric anomaly is observed at the Curie point, with a value nearly two orders of magnitude smaller than for the c -axis. Since the a -axis dielectric constant remains relatively flat below T_c , it is nearly four times larger than the c -axis constant at room temperature. Below room temperature, the a -axis dielectric constant rises gradually to a value of 470 at -150°C .

The low-frequency dielectric properties of BSKNN-2, shown in fig. 6, are similar in overall behavior to those for BSKNN-1. However, BSKNN-2 has a lower Curie point ($170\text{--}178^{\circ}\text{C}$) which contributes in part to this higher c -axis dielectric constant of 170 (poled) at room temperature. The a -axis dielectric constant for BSKNN-2 is also considerably larger, with a value of 750 at room temperature and rising to above 1000 at -150°C . These values are roughly a factor of two or more greater than for a -axis tungsten bronze SBN:60 single crystals [22].

The dielectric constants for both BSKNN compositions exhibit Curie-Weiss behavior above T_c , that is,

$$\epsilon_{ij} = C_c / (T - \theta),$$

where θ is the Curie temperature and C_c the Curie-Weiss constant. BSKNN-1 deviates somewhat from this relationship because of an unexplained "kink" near 270°C , evident in fig. 5. For temperatures just above T_c , $C_{c3} = 2.6 \times 10^5^{\circ}\text{C}$ and $\theta_3 = 203\text{--}208^{\circ}\text{C}$ for BSKNN-1, whereas for BSKNN-2, $C_{c3} = 3.2 \times 10^5^{\circ}\text{C}$ and $\theta_3 = 168\text{--}175^{\circ}\text{C}$. In both cases, T_c is $2\text{--}5^{\circ}\text{C}$ higher than θ , indicating a quasi-first-order ferroelectric transition behaviour. Curiously, BSKNN-1 and

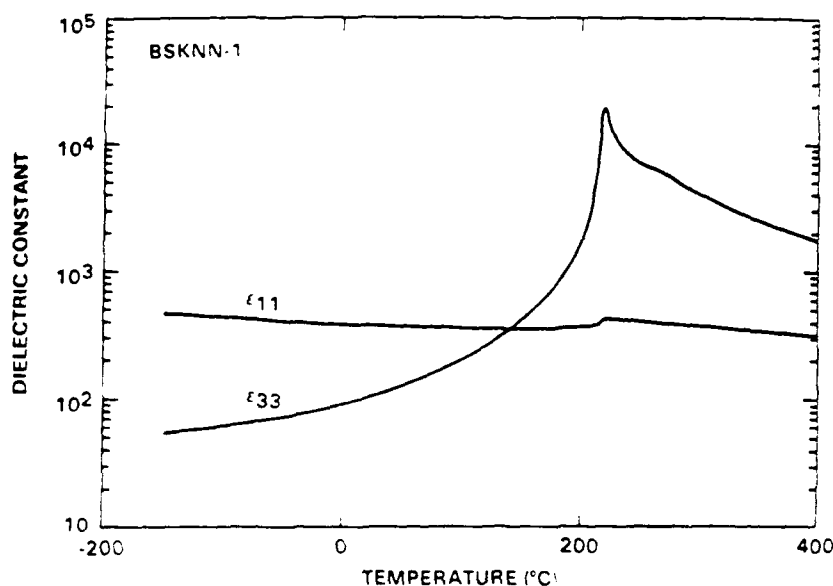


Fig. 5. Temperature dependence of dielectric constant for BSKNN-1 at 10 kHz.

BSKNN-2 also show strict Curie-Weiss behavior over a 300°C range below T_c , with Curie-Weiss constants C , a factor of 7–8 smaller than the respective high-temperature (paraelectric) values. This observation suggests that the Devonshire polarization coefficients in the free-energy expansion for BSKNN may be strongly temperature-dependent. A more detailed examination of the ferroelectric phenomenology for BSKNN crystals will be presented in a subsequent paper upon the completion of additional measurements.

The polar axis pyroelectric coefficient, p , obtained from the zero bias current density measured at a constant temperature rate, and the spontaneous polarization, P_s , obtained by integration of p over temperature, are shown in fig. 7 for a BSKNN-2 crystal with $T_c = 170^\circ\text{C}$. Although BSKNN is a quasi-first-order phase transition ferroelectric, fluctuations in ionic site preference results in a moderate distribution of transition temperatures in the crystal. Hence, the spontaneous polarization P_s has a nonzero value above the mean Curie point, T_c , as seen in fig. 7. Below T_c , the polarization rises sharply and attains a value

of $34 \mu\text{C}/\text{cm}^2$ at room temperature, a value similar to that of SBN:60.

The room-temperature pyroelectric coefficient of BSKNN-2 is $0.036 \mu\text{C}/\text{cm}^2 \text{K}$, nearly a factor of three lower than for bronze SBN:60 ($0.10 \mu\text{C}/\text{cm}^2 \text{K}$). However, the lower room-temperature polar-axis dielectric constant of BSKNN-2 (170 versus 920 for SBN:60) results in a much higher pyroelectric figure-of-merit, p/ϵ (2.1×10^{-4} versus 1.1×10^{-4} for SBN:60); furthermore, this figure-of-merit is much less temperature-sensitive because of the higher transition temperature for BSKNN.

A transverse modulation technique was used to determine the optical half-wave voltage (V_π) and the value of $n_e^3 r_c = n_e^3 r_{33} - n_o^3 r_{13}$ for BSKNN-2. The crystal was placed between crossed polarizers set at 45° to the c -axis and a modulation field was applied along the c -axis. A low-frequency ($\sim 400 \text{ Hz}$) AC modulation field was used to avoid space-charge effects. All measurements were made at room temperature (300 K). At 442 nm, V_π was found to be 220 V and $n_e^3 r_c = 2.0 \times 10^{-9} \text{ m/V}$. At 633 nm, V_π was 425 V and $n_e^3 r_c$ was

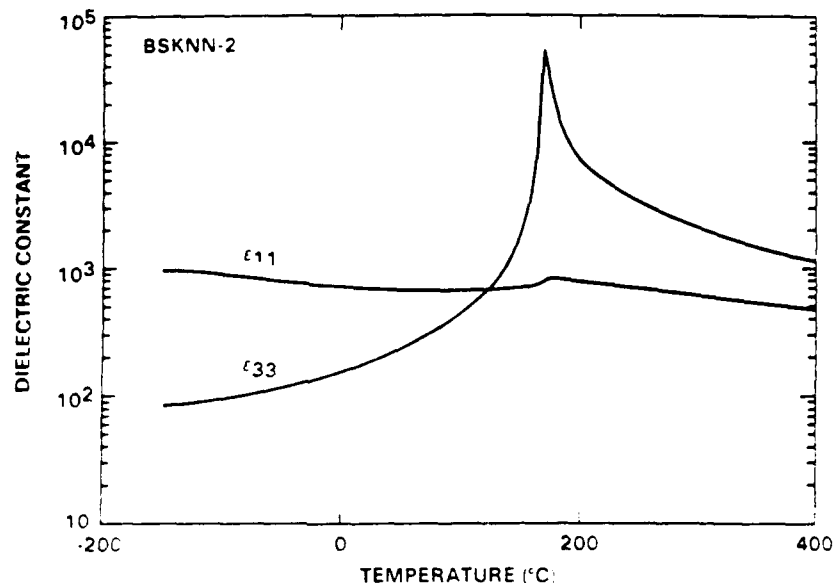
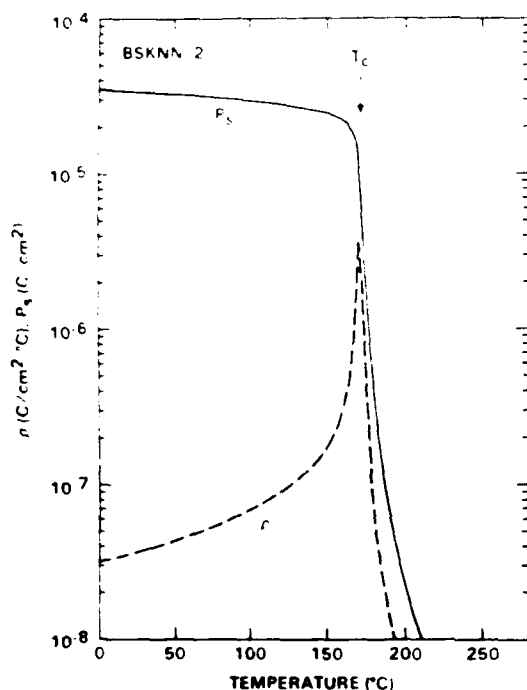


Fig. 6. Temperature dependence of dielectric constant for BSKNN-2 at 10 kHz.

Fig. 7. Spontaneous polarization, P_2 , and pyroelectric coefficient, p , as function of temperature for a BSKNN-2 c -axis crystal.

1.5×10^{-9} m/V. Since r_{13} is generally small and n_e is about 2.3, r_{33} is therefore expected to be about $(150-200) \times 10^{12}$ m/V for BSKNN-2. This figure may be compared with the value computed from the relation $r_{33} = 2g_{33}P_3\epsilon_0\epsilon_{33}$, where g is the quadratic electro-optic coefficient [23]. For $g_{33} = 0.11$ m⁴/C², r_{33} is estimated to be 112×10^{12} m/V, significantly smaller than the measured values. Similarly, r_{31} may be estimated from the relation $r_{31} = 2g_{44}P_3\epsilon_0\epsilon_{11}$; using $g_{44} = 0.09$ m⁴/C² and $\epsilon_{11} = 750$, r_{31} is estimated to be 400×10^{12} m/V.

Because of the large discrepancy between the computed and measured values for r_{33} (which, curiously, does not occur for SBN:60), the actual value for r_{31} may be 300×10^{12} or greater in BSKNN-2. The apparent variation of the quadratic electro-optic g coefficients in BSKNN compared to bronze SBN indicates that the g coefficients may not be constant throughout the tungsten bronze family, as previously assumed. Clearly, this subject deserves renewed attention in experimental and theoretical work.

Table 2 summarizes the ferroelectric and optical properties of tungsten bronze BSKNN-1 and

Table 2
Ferroelectric and optical properties of BSKNN-1 and BSKNN-2 crystals

Property	BSKNN-1	BSKNN-2
Symmetry	4mm	4mm
T_c ($^{\circ}\text{C}$)	205–210	170–178
$T_c - \theta$ ($^{\circ}\text{C}$)	2–5	3–5
Curie-Weiss coefficient ($^{\circ}\text{C}$)	2.6×10^5	3.2×10^5
Dielectric constant	$\epsilon_{11} = 380$ $\epsilon_{33} = 120$	$\epsilon_{11} = 750$ $\epsilon_{33} = 170$
Piezoelectric coefficient ($\times 10^{-12}$)	$d_{15} = 70$ $d_{33} = 60$	$d_{15} = 200$ $d_{33} = 60$
Electro-optic coefficient: ($\times 10^{-12}$ m/V)	$r_{31} \geq 250$ $r_{33} = 110$	$r_{31} \geq 300$ $r_{33} = 180$
Pyroelectric coefficient: ($\mu\text{C}/\text{cm}^2 \cdot \text{K}$)	$p = 0.030$	$p = 0.036$
Spontaneous polarization ($\mu\text{C}/\text{cm}^2$)	$P_s = 35$	$P_s = 34$

BSKNN-2. In table 3, the optical figures-of-merit $n^3 r_{ij}/\epsilon$ and r_{ij}/ϵ are given for BSKNN, SBN and BaTiO₃. For phase conjugation (self-pumped), image processing and optical computing applications, the relevant figure-of-merit can be calculated as $n^3 r_{ij}/\epsilon$, which is found to be two to three times larger in the BSKNN system than for any other material. This difference is due to the high dielectric anisotropy found in the BSKNN system which results, for example, in a high r_{31} with a simultaneously low ϵ_{33} .

Table 3
Electro-optic figure-of-merit for tungsten bronze crystals

Crystal	Dielectric constant		Electro-optic coefficient (10^{-12} m/V)			
	ϵ_{11}	ϵ_{33}	r_{33}	r_{31}	r_{ij}/ϵ	$n^3 r_{ij}/\epsilon$
$\text{Sr}_{0.75}\text{Ba}_{0.25}\text{Nb}_2\text{O}_6$ (SBN:75)	450	3000	1400	42	0.467	5.60
$\text{Sr}_{0.6}\text{Ba}_{0.4}\text{Nb}_2\text{O}_6$ (SBN:60)	450	900	470	42	0.522	6.25
$\text{Sr}_{2-x}\text{Ca}_x\text{NaNb}_3\text{O}_{15}$ (SCNN)	1700	1700	≥ 800	—	0.470	5.65
$\text{Pb}_{0.6}\text{Ba}_{0.4}\text{Nb}_2\text{O}_6$	1900	500	—	≥ 1600	0.840	10.10
BSKNN-1	360	120	150	≥ 200	0.550	6.67
BSKNN-2	700	170	170	350	0.500	6.00
BSKNN-3	780	270	200	~ 400	0.510	6.15
BaTiO ₃	4100	1500	80	1600	0.390	4.01
KNbO ₃	950	201	67	380	0.400	4.20

Table 4
Comparison between leading photorefractive crystals

Tungsten bronze BSKNN	Perovskite BaTiO ₃
Large longitudinal r_{31} , d_{15} , ϵ_{11} available	Large longitudinal r_{31} , d_{15} , ϵ_{11} available
Excellent host for photorefractive and electro-optic applications	Excellent host for photorefractive and electro-optic applications
Large square and octahedron crystals (≥ 1.15 cm) with optical quality are available	Pure BaTiO ₃ crystals and difficult to grow
Absence of twinning (4/mm \rightarrow 4mm)	90° twins are present (3m \rightarrow 4mm)
Absorption and response controlled in the desired spectral range using proper crystallographic site/sites for a given dopant	Controlled spectral response with dopant possible, but difficult
No tetragonal to orthorhombic transition observed down to LN temperature	Tetragonal to orthorhombic transition occurs at 10° C
Open structure – structural flexibility to alter crystal decomposition	Closed-packed structure limited compositional flexibility

Recent photorefractive work by Rodriguez et al. [24] on BSKNN-2 crystals doped with Ce has shown this material to have excellent self-pumped phase-conjugated behavior. These crystals also exhibit large photorefractive coupling coefficients

and fast response times [25]. As summarized in table 4, in many respects BSKNN-2 resembles perovskite BaTiO_3 in its photorefractive properties, but with the advantages of high optical quality, absence of twinning, and relative ease of poling to a single ferroelectric domain. As such, it can be anticipated that with further development and optimization of compositions in the BSKNN system, and with further optimization of the dopant concentration and ionic site preference in photorefractive crystals, this tungsten bronze ferroelectric may ultimately surpass BaTiO_3 and SBN:60 in many photorefractive and electro-optic device application.

Acknowledgements

This research work was supported by DARPA contract Nos. DAAK20-84-C-0129 and N00014-82-C-2446, and U.S. Army Contract No. DAAK70-83-C-0016. The authors are grateful for the discussions on this research by Professor L.E. Cross of Penn State University.

References

- [1] S. Sakamoto and T. Yazaki, *Appl. Phys. Letters* 22 (1973) 429.
- [2] P.B. Lenz, E.G. Spencer and A.A. Balman, *Appl. Phys. Letters* 11 (1967) 23.
- [3] R.R. Neurgaonkar and W.K. Cory, *J. Opt. Soc. Am.* 3 (1986) 274.
- [4] G.J. Salamo, M.J. Miller, E.J. Sharp, G.L. Wood and W.W. Clark III, *Opt. Commun.* 59 (1986) 417.
- [5] E.J. Sharp, M.J. Miller, G.L. Wood, W.W. Clark III, G.J. Salamo, and R.R. Neurgaonkar, in: *Proc. 6th IEEE (ISAF-Ferroelectrics)* 1986, p. 51.
- [6] R.R. Neurgaonkar, *Proc. SPIE* 465 (1984) 97.
- [7] G.E. Rakuljic, A. Yaniv and R.R. Neurgaonkar, *Appl. Phys. Letters* 50 (1987) 10.
- [8] S.T. Liu and R.B. Maclellan, *J. Electron. Mater.* 4 (1975) 91.
- [9] A.M. Glass, *J. Appl. Phys.* 40 (1969) 4699.
- [10] O. Eknayan, C.H. Bulmer, H.F. Taylor, W.K. Burns, A.S. Greenblatt, L.A. Beach and R.R. Neurgaonkar, *Appl. Phys. Letters* 48 (1986) 13.
- [11] B. Bobbs, M. Matloubian, H.R. Fetterman, R.R. Neurgaonkar and W.K. Cory, *Appl. Phys. Letters* 48 (1986) 1642.
- [12] W.W. Ho, W.F. Hall and R.R. Neurgaonkar, *Ferroelectrics* 56 (1984) 230.
- [13] R.R. Neurgaonkar, W.W. Ho, W.K. Cory, W.F. Hall and L.E. Cross, *Ferroelectrics* 51 (1984) 185.
- [14] B. Bobbs, M. Matloubian, H.R. Fetterman, R.R. Neurgaonkar and W.K. Cory, *Proc. SPIE* 545 (1985) 25.
- [15] Landolt-Bornstein, *New Series (Crystal and Solid State Physics)*, Vol. 11 (Springer, Berlin, 1978).
- [16] A.T. Johnson, *Appl. Phys. Letters* 7 (1965) 195, *J. Opt. Soc. Am.* 55 (1965) 828.
- [17] J.R. Oliver, R.R. Neurgaonkar and G.L. Sharp, in: *Proc. 6th IEEE (ISAF)*, 1986, p. 485.
- [18] R.R. Neurgaonkar, M.H. Kalisher, T.C. Lim, E.J. Staples and K.K. Keester, *Mater. Res. Bull.* 15 (1980) 1305.
- [19] R.R. Neurgaonkar, W.K. Cory and J.R. Oliver, *Ferroelectrics* 35 (1983) 301.
- [20] R.R. Neurgaonkar, W.K. Cory and J.R. Oliver, *Proc. SPIE* 540 (1985) 146.
- [21] O.F. Dudnik, A.K. Gromov, V.B. Kravchenkov, Y.L. Kopylov and G.F. Kunznetsov, *Soviet Phys.-Cryst.* 15 (1979) 330.
- [22] R.R. Neurgaonkar, W.K. Cory, W.W. Ho, W.F. Hall and L.E. Cross, *Ferroelectric* 38 (1981) 857.
- [23] L.E. Cross and R.R. Neurgaonkar, *J. Mater. Sci.*, submitted.
- [24] J. Rodriguez, A. Siahmakoun, G.J. Salamo, M.J. Miller, W.W. Clark III, G.L. Wood, E.J. Sharp and R.R. Neurgaonkar, *Appl. Opt.* 26 (1987) 1732.
- [25] G.A. Rakuljic, A. Yaniv et al., R.R. Neurgaonkar, *Appl. Phys. Letters* 50 (1987) 10.



Rockwell International

Science Center

SC5441.FTR

**A REVIEW OF THE STATE-OF-THE-ART IN THE GROWTH AND FERROELECTRIC
PROPERTIES OF TUNGSTEN BRONZE CRYSTALS**

A REVIEW OF THE STATE-OF-THE-ART IN THE GROWTH AND FERROELECTRIC PROPERTIES OF TUNGSTEN BRONZE CRYSTALS

R.R. Neurgaonkar, W.K. Cory and J.R. Oliver
Rockwell International Science Center
Thousand Oaks, CA 91360, USA

and

L.E. Cross
Materials Research Laboratory
The Pennsylvania State University
University Park, PA 16802, USA

ABSTRACT

The state-of-the-art in the Czochralski growth of various optical-quality ferroelectric tungsten bronze single crystals is reviewed. This growth work, undertaken with specific optoelectronic applications in view, has succeeded in providing large crystals of bronze $\text{Sr}_{1-x}\text{Ba}_x\text{Nb}_2\text{O}_6$ (SBN), $\text{Ba}_{2-x}\text{Sr}_x\text{K}_{1-y}\text{Na}_y\text{Nb}_5\text{O}_{15}$ (BSKNN) and $\text{Sr}_{2-x}\text{Ca}_x\text{NaNb}_5\text{O}_{15}$ (SCNN) suitable for electro-optic, pyroelectric and photorefractive applications.

INTRODUCTION

Tungsten bronze ferroelectrics are found to be very useful for surface acoustic wave, electro-optic, pyroelectric, and millimeter wave applications, and more recently for photorefractive applications.¹⁻¹⁵ A considerable amount of work has been published on the development of this family of materials; however, it did not formerly find wide application due to lack of availability of crystals of adequate size and suitable quality. At Rockwell International, we have systematically studied and classified the major growth problems, crystal habits and ferroelectric properties of various bronzes, tailoring

compositions according to particular device applications.¹⁶⁻²⁰ In this paper, we report our major findings on the growth of these crystals and discuss the mechanisms which give rise to their unusual ferroelectric and optical properties.

BACKGROUND: FUNDAMENTAL PROPERTIES

The tungsten bronze compositions can be represented by the general formulae $(A_1)_4(A_2)_2C_4B_{10}O_{30}$ and $(A_1)_4(A_2)_2B_{10}O_{30}$, in which A_1 , A_2 , C and B are 15-, 12-, 9- and 6-fold coordinated sites in the crystal lattice structure. The tetragonal bronze prototypic structure is shown in Fig. 1 in projection on the (001) plane.^{21,22} A wide range of solid solutions can be obtained by substituting different A_1 , A_2 , C and B cations,²³⁻²⁶ and a number of different ferroelectric and ferroelastic phases have been identified (more than 150 compounds and solid solutions). The ferroelectric phases can be divided into two groups: those with tetragonal symmetry (4mm), which are ferroelectric, and those with orthorhombic symmetry (mm2), which are both ferroelectric and ferroelastic.

The origin of ferroelectric properties in these materials is best understood in terms of their high symmetry prototype phase, which in this case is 4mm. A Gibbs free energy function can be derived for this phase which incorporates the effects of polarization and temperature. The excess Gibbs energy in the ferroelectric phase due to nonzero polarization, P_i , along the three principal crystallographic axes may be written as a Taylor series expansion in powers of the P_i given by

$$\begin{aligned} \Delta G_1 = & \alpha_1(P_1^2 + P_2^2) + \alpha_3P_3^2 + \alpha_{11}(P_1^4 + P_2^4) + \alpha_{33}P_3^4 \\ & + \alpha_{13}(P_1^2 + P_2^2)P_3^2 + \alpha_{12}P_1^2P_2^2 + \dots - E_1P_1 - E_2P_2 - E_3P_3 \end{aligned} \quad (1)$$

where the E_i are the corresponding electric field components. Setting the first partial derivatives of ΔG with respect to the polarization equal to zero gives the field components:

$$E_1 = 2\alpha_1 P_1 + 4\alpha_{11} P_1^3 + 2\alpha_{12} P_1 P_2^2 + 2\alpha_{13} P_1 P_3^2 + \dots \quad (2)$$

$$E_2 = 2\alpha_1 P_2 + 4\alpha_{11} P_2^3 + 2\alpha_{12} P_1^2 P_2 + 2\alpha_{13} P_2 P_3^2 + \dots$$

$$E_3 = 2\alpha_3 P_3 + 4\alpha_{33} P_3^4 + 2\alpha_{13} (P_1^2 + P_2^2) P_3 + \dots$$

Finally, the dielectric stiffnesses $\partial E_i / \partial P_i = \chi_{ii} = (\epsilon_{ii} \epsilon_0)^{-1}$ are:

$$\chi_{11} = 2\alpha_1 + 12\alpha_{11} P_1^2 + 2\alpha_{12} P_2^2 + 2\alpha_{13} P_3^2 + \dots \quad (3)$$

$$\chi_{22} = 2\alpha_1 + 12\alpha_{11} P_2^2 + 2\alpha_{12} P_1^2 + 2\alpha_{13} P_3^2 + \dots$$

$$\chi_{33} = 2\alpha_3 + 12\alpha_{33} P_3^2 + 2\alpha_{13} (P_1^2 + P_2^2) + \dots$$

In the paraelectric phase ($P_1 = P_2 = P_3 = 0$), the stiffnesses follow a Curie-Weiss law with

$$\begin{aligned} \chi_{11} = \chi_{22} = 2\alpha_1 &= (T - \theta_1) / C_1 \\ \chi_{33} = 2\alpha_3 &= (T - \theta_3) / C_3 \end{aligned} \quad (4)$$

If $\theta_3 > \theta_1$, the material will go into the tetragonal ($4mm$) state ($P_3^2 \neq 0$) below the ferroelectric transition temperature, T_c . Hence, since P_3 increases at much less than a

linear rate below T_C , $\epsilon_{33} = (\epsilon_0 \chi_{33})^{-1}$ will decrease with decreasing temperature, whereas ϵ_{11} will increase below T_C . Conversely, if $\theta_1 > \theta_3$, the material will go into an orthorhombic (mm2) state ($P_1^2 \approx P_2^2 \neq 0$) in the ferroelectric phase. In this case, ϵ_{11} will decrease with decreasing temperature, whereas ϵ_{33} will increase.

The consequences of the two types of ferroelectric states on the electro-optic behavior may be found in the phenomenological expressions for the linear electro-optic coefficients, r_{ij} . For tetragonal (4mm) bronzes, these are given by

$$\begin{aligned} r_{31} &= 2g_{31}P_3\epsilon_0\epsilon_{33} \\ r_{33} &= 2g_{33}P_3\epsilon_0\epsilon_{33} \end{aligned} \tag{5}$$

$$r_{42} = r_{51} = g_{44}P_3\epsilon_0\epsilon_{11},$$

where the g 's are the quadratic electro-optic coefficients of the paraelectric phase; generally g_{33} is much greater than either g_{13} or g_{44} . As a consequence, room temperature values for r_{33} are usually large for tetragonal ferroelectric bronzes (e.g., SBN:60), although r_{31} can also become large as a consequence of the increasing ϵ_{11} below T_C .

For orthorhombic (mm2) bronzes, the corresponding linear electro-optic coefficients are

$$r_{11} = 2g_{11}P_3\epsilon_0\epsilon_{11}$$

$$r_{21} = 2g_{21}P_1\epsilon_0\epsilon_{11}$$

$$r_{31} = 2g_{31}P_1\epsilon_0\epsilon_{33} \quad (6)$$

$$r_{43} = r_{53} = 8g_{44}P_1\epsilon_0\epsilon_{33}$$

$$r_{61} = r_{62} = 8g_{44}P_1\epsilon_0\epsilon_{11}.$$

Hence, r_{11} can be large for orthorhombic bronzes, but the increasing ϵ_{33} below T_C can also make r_{31} and r_{43} large.

SELECTED TUNGSTEN BRONZE SYSTEMS

Table I lists key properties of the more important tungsten bronzes grown to date. We have selected four different types for growth studies, namely, $\text{Sr}_{1-x}\text{Ba}_x\text{Nb}_2\text{O}_6$, $\text{Ba}_{2-x}\text{Sr}_x\text{K}_{1-y}\text{Na}_y\text{Nb}_5\text{O}_{15}$, $\text{Sr}_{2-x}\text{Ca}_x\text{NaNb}_5\text{O}_{15}$ and $\text{Pb}_{1-x}\text{Ba}_x\text{Nb}_2\text{O}_6$, because of their distinctly different ferroelectric and optical characteristics. These are:

- | | | |
|----|-------------|---|
| 1. | SBN System: | Exhibits strong transverse optical effects
largely independent of the Ba:Sr ratios |
|----|-------------|---|

- | | | |
|----|--------------------------------|--|
| 2. | BSKNN System: | <p>*Exhibits strong longitudinal optical effects for K-rich BSKNN crystals.</p> <p>*Exhibits large longitudinal and transverse effects large for Na⁺-rich BSKNN crystals.</p> |
| 3. | SCNN System: | <p>*Exhibits longitudinal and transverse optical effects which are large and nearly equal for most compositions.</p> |
| 4. | PBN System:
MPB at x = 0.37 | <p>*Exhibits strong transverse effects for x ≤ 0.37 (mm²).</p> <p>*Exhibits strong longitudinal effects for x ≥ 0.37 (4mm).</p> |

A brief description of each of these bronze crystals is given below.

SBN System

The solid solution system $\text{Sr}_{1-x}\text{Ba}_x\text{Nb}_2\text{O}_6$, $0.75 \leq x \leq 0.25$, belongs to the tungsten bronze family even though the end members, SrNb_2O_6 and BaNb_2O_6 , do not exhibit a bronze structure. This solid solution is based on the formula $(\text{A}_1)_4(\text{A}_2)_2\text{B}_{10}\text{O}_{30}$ in which both Sr^{2+} and Ba^{2+} are in the 15- and 12-fold coordinated sites; since these sites are partially empty, the SBN solid solution is referred to as an unfilled bronze. Japanese work reports that $\text{Sr}_{0.6}\text{Ba}_{0.4}\text{Nb}_2\text{O}_6$ (SBN:60) is close to the congruent melting region,²⁷

and not $\text{Sr}_{0.5}\text{Ba}_{0.5}\text{Nb}_2\text{O}_6$ (SBN:50) reported by Carruthers et al²⁸ in the early 1960s. More detailed information on this system can be found in earlier papers.^{29,30}

BSKNN System

The $\text{Ba}_{2-x}\text{Sr}_x\text{K}_{1-y}\text{Na}_y\text{Nb}_5\text{O}_{15}$ compositions exist on the SrNb_2O_6 - BaNb_2O_6 - KNbO_3 - NaNbO_3 quaternary system as shown in Fig. 2.¹⁹ The BSKNN crystals listed in Table 1 exist on the BSKNN-1 - BSNN-4 binary joint, and we currently believe that there exists a morphotropic phase boundary (MPB) region between BSKNN-2 and BSKNN-3. In this system, BSKNN-1 is tetragonal at room temperature, whereas BSNN-4 is orthorhombic and hence permits MPB regions. The BSKNN solid solution is also based on the formula $(\text{A}_1)_4(\text{A}_2)_2\text{B}_{10}\text{O}_{30}$ in which the larger Ba^{2+} , Sr^{2+} , K^+ and Na^+ ions are in the 15 and 12-fold coordinated sites. In this case, both of these sites are completely filled; hence this solid solution is referred to as a filled bronze.

SCNN System

The solid solution $\text{Sr}_{2-x}\text{Ca}_x\text{NaNb}_5\text{O}_{15}$, $0.0 \leq x \leq 0.33$, belongs to the orthorhombic bronze structure for all Ca^{2+} additions,³¹ and as shown in Fig. 2, the dielectric properties increase with increasing Ca^{2+} up to 20 mole%. The main feature of this system is that it exhibits transverse and longitudinal optical effects which are large and nearly equal. This is the first system where we have found both properties to be potentially large. Like BSKNN, SCNN crystals have a filled lattice structure.

PBN System

The $\text{Pb}_{1-x}\text{Ba}_x\text{Nb}_2\text{O}_6$ solid solution exhibits an MPB region^{32,33} at $x = 0.37$ (Fig. 2). For $x \leq 0.37$, the compositions are orthorhombic at room temperature with large transverse optical effects, whereas for $x \geq 0.37$, the compositions are tetragonal and exhibit large longitudinal effects. Although we have recently reported various other bronze MPB systems,^{34,35} the PBN solid solution remains as the best studied MPB bronze and is potentially very useful for a number of optoelectronic applications.

CRYSTAL DEVELOPMENT

Table 2 lists a number of tungsten bronze single crystals grown in our work and their associated growth conditions. The Czochralski pulling technique was used for these growths, with the crystals pulled from 2×2 " platinum crucibles in an oxygen atmosphere to minimize the reduction of Nb^{5+} to Nb^{4+} . Initially, spattering during growth was a severe problem due to the incomplete decomposition of BaCO_3 ; this problem was subsequently eliminated by sintering the starting materials above 1350°C (the decomposition temperature of BaCO_3). The crystals were grown along the $\langle 001 \rangle$ direction using suitable seed material, and after growth was completed they were held in a post-annealing furnace and then slowly cooled to room temperature. Crystal cracking during cooldown through the paraelectric/ferroelectric phase transition was initially a problem, but this has now been minimized for tetragonal bronze crystals. However, this problem is still a concern for orthorhombic crystals.

We initially developed our growth technique for $\text{Sr}_{1-x}\text{Ba}_x\text{Nb}_2\text{O}_6$, $x = 0.25, 0.40$ and 0.50 , because of its excellent electro-optic and pyroelectric properties. Early work at Bell Laboratories^{28,29} indicated that SBN:50 was the congruent melting composition

within this system, and SBN:50 growth was performed at various laboratories.³⁶⁻⁴¹ Subsequently in 1976, Megumi et al²⁷ reported SBN:60 to be closer to the congruent melting region. Our crystal growth work has confirmed these results by achieving optical quality SBN:60 growths of up to 3 cm diameter,^{16,17} while the growth of SBN:75 and SBN:50 has been comparatively more difficult, with maximum crystal diameters of 2 cm.

Figure 3 shows optical quality SBN single crystals grown along $\langle 001 \rangle$. These crystals grow in a cylindrical shape with 24 prominent facets, with these features unchanged for different Ba:Sr ratios. Although the growth of SBN:75 and SBN:50 has been widely studied,⁴² their growth has been confined to smaller sizes to maintain moderate optical quality. Based on our extensive crystal growth experiments in this system, we believe that SBN:60 is close to the congruent melting region, with a solidus-liquidus gap substantially narrower than for either SBN:75 or SBN:50. In general, the optical quality of these crystals depends not only on this factor, but also on factors such as temperature stability during growth and the purity of the starting materials.

Doping of SBN crystals with Ce^{3+} , Cr^{3+} and La^{3+} does not degrade optical quality, with doped crystals being successfully used in photorefractive and pyroelectric studies.¹⁸ However, the addition of Fe^{3+} introduces optical striations which have proven difficult to suppress under the current growth conditions. La^{3+} -doping was basically studied for pyroelectric applications and it was found that although the quality of these crystals remains generally good, La^{3+} doping in excess of 1 mole% changes the crystal shape from cylindrical to squarish, as shown in Fig. 4.¹⁸ Liu et al⁹ also investigated the growth of La^{3+} -doped SBN:50 crystals, but they did not report such changes in the shape of their crystals.

Three distinctly different BSKNN compositions, listed in Table 2, have been grown in optical quality up to 1.5 cm diameter. Since the BSKNN system contains five components, it is very difficult to precisely determine the true congruent melting composition on the BSKNN-1 and BSKNN-4 binary joint. This system was originally introduced by Cross and co-workers,⁴³ and later studied in China⁴⁴ without mention of the existence of a congruent melting composition. However, the growth of BSKNN-2 and BSKNN-3 is relatively easier than BSKNN-1 and show superior optical quality, suggesting that the congruent melting region may be in the vicinity of BSKNN-2 and BSKNN-3.

Figure 5 shows BSKNN-1 and BSKNN-2 crystals grown along $\langle 001 \rangle$, with BSKNN-3 having a growth habit similar to BSKNN-2. Note that BSKNN-1 grows in a square shape with four well-defined facets, whereas the relatively smaller unit cell BSKNN-2 and BSKNN-3 grow in an octohedron shape with eight facets. Another bronze composition, $K_3Li_2Nb_5O_{15}$ (KLN)³¹ grows in a square shape similar to BSKNN-1, suggesting that this growth habit is common for larger unit cell bronzes containing alkaline ions. As listed in Table 2, the dielectric and optical properties for these larger unit cell crystals (BSKNN-1, KLN) are generally smaller than for the smaller unit cell BSKNN-2 and BSKNN-3 crystals. Another interesting feature of the BSKNN system is that as one moves from BSKNN-2 to BSKNN-3, the transverse effects (ϵ_{33}, r_{33}) become larger, suggesting the possible existence of a morphotropic phase boundary region between BSKNN-2 and BSKNN-3 (Fig. 6). Further work is in progress to establish the existence of an MPB region, if any, within this binary join.

The growth of orthorhombic $Sr_{1.9}Ca_{0.1}NaNb_5O_{15}$ (SCNN-2) and $Sr_{1.8}Ca_{0.2}NaNb_5O_{15}$ (SCNN-1) was found to be more difficult than BSKNN and SBN due to a lower crystal symmetry and the lack of information on the congruent melting compositions within this system. Initially, these crystals were grown using SBN:60

crystal seeds and as better SCNN crystals became available, they were subsequently used as seeds. Currently, SCNN crystals have been grown up to 0.7 cm diameter with reasonable quality; Fig. 7 shows an SCNN-2 crystal grown along $\langle 001 \rangle$. SCNN grows in a cylindrical shape and exhibits certain facet formation, although the actual number of facets has not been conclusively established. Ce^{3+} -doped SCNN-2 was recently examined in photorefractive measurements,³¹ and although the crystal quality needs improvement, strong photorefractive effects were evident. Further work is underway on these SCNN compositions to improve their size and quality for various device studies.

The Pb^{2+} -containing bronze composition, $\text{Pb}_{0.6}\text{Ba}_{0.4}\text{Nb}_2\text{O}_6$ (PBN:60), has proven even more difficult to grow due to the continuous loss of lead during growth. Although we have succeeded in growing approximately 1 cm diameter crystals at Penn State,³⁵ homogeneity has been poor due to lead loss. This composition is important primarily because it has the highest potential figures-of-merit (FOM) for optical and nonlinear optical applications. To better realize the benefits of such high FOM materials and to better understand their basic properties, we are currently developing single crystal films of PBN:60 on SBN:60 substrates.⁴⁵ We believe that the growth of these materials in the form of thin films will ultimately prove more beneficial to device applications than the poorer quality bulk single crystals.

Figure 8 shows idealized forms of the growth habits for bronze ferroelectric crystals. Since only a few orthorhombic bronzes, such as $\text{Ba}_2\text{NaNb}_5\text{O}_{15}$, $\text{Pb}_2\text{KNb}_5\text{O}_{15}$, $\text{K}_2\text{BiNb}_5\text{O}_{15}$ and $\text{K}_3\text{Li}_2(\text{Ta}_{1-x}\text{Nb}_x)_5\text{O}_{15}$ (KLTN) have been grown in decent size, the basic growth habits of these crystals are not yet well established, except for KLTN which grows as square crystals. Based on our work, it is clear that heat flow and other growth factors are important in developing facets in all of these crystals.

PROBLEMS ASSOCIATED WITH ATTAINING OPTICAL QUALITY

Tetragonal SBN and BSKNN single crystals have proven comparatively easier to grow than orthorhombic SCNN crystals. However, the quality of SCNN crystals has been adequate for the measurement of ferroelectric properties such as the dielectric constant, polarization and pyroelectricity. Nevertheless, the crystal quality for optical measurements has not been adequate.

As shown in Fig. 9, we have encountered numerous problems in all bronze crystal growths, particularly for BSKNN and SCNN. Although moderate to large size crystals have been developed in all of these compositions, the following problems have been of greatest concern:

1. Multicomponent solid-solution systems, making it difficult to establish true congruent melting regions.
2. High material melting temperatures ($\geq 1450^{\circ}\text{C}$), resulting in volatilization and oxidation-reduction ($\text{Nb}^{5+} : \text{Nb}^{4+}$) problems.
3. Exchange among crystallographic sites, specifically of the 15- and 12-fold coordinated ions such as Ba^{2+} , Sr^{2+} , K^{+} , Na^{+} , causing severe striations.
4. Cracking of crystals when passing through the paraelectric/ferroelectric phase transition temperature. This problem is more severe for orthorhombic SCNN crystals because they undergo two phase transitions, i.e., paraelectric/ferroelectric (at high temperature) and ferroelectric/ferroelastic (at lower temperature).

Because these bronze systems are multicomponent, often incorporating four or more elements, compositional fluctuations on a large scale were routine in our early growth experiments, producing defects such as coring, banding, bubble formation and striations, as summarized in Fig. 10. These defects were partly related to the poor heat flow through the growth interface resulting from oxygen loss at elevated temperatures. These crystals also twinned easily, probably due to the above plus the complicated unit cell and a poor choice of growth temperature gradients. We quickly realized that sharp temperature gradients were not appropriate for growing these bronze materials, as they tended to produce crystals with high dislocation densities along the c-axis with massive strain fields, twinning, and the cracking of boules when cooling to room temperature or, in the worst cases, even while the crystals were growing. These experimental results led us to the development of lower temperature gradients near the melt interface and, as a result, boule quality has gradually improved with the successful suppression of coring and compositional fluctuations responsible for banding.

Although coring and compositional fluctuations (banding) were finally eliminated to a large extent, the crystals were still found inadequate for optical studies due to the presence of striations. At this stage, effort shifted towards investigating the problems associated with optical striations, and it was found that the following factors were important contributors:

1. Impurities in starting materials, particularly Fe^{3+} .
2. Temperature instability near the solid-liquid interface.

3. Cooling rate variation: Under different cooling rates, the distribution of Sr^{2+} and Ba^{2+} on the 15- and 12-fold coordinated sites varies (for example, T_c increases with faster cooling rates), and striations result due to nonuniform distributions of these ions.

Since $\text{Fe}^{2+}/\text{Fe}^{3+}$ is an active dopant in producing favorable photorefractive effects in $\text{Ba}_2\text{NaNb}_5\text{O}_{15}$, KNbO_3 and LiNbO_3 ,⁴⁶⁻⁵⁰ its role has been studied in SBN and BSKNN in some detail. In the tungsten bronze structure, Fe^{3+} occupies the 6-fold coordinated Nb^{5+} site and it gives a beautiful golden yellow color for low doping levels.⁵¹ Although these Fe-doped bronze crystals also exhibit large photorefractive effects, their quality is degraded by the occurrence of striations. Based on our investigations, these striations exist unless ultra-pure starting materials are used with iron concentrations less than 2 to 3 ppm.

In order to understand more fully the role of 6-fold coordinated cations, we have also introduced Cr^{3+} and Mn^{3+} in the 6-fold site and have found that the crystals grown are of optical quality with excellent photorefractive effects up to 0.20 wt% Cr^{3+} or Mn^{3+} .⁵² Similar attempts to replace Sr^{2+} by Ce^{3+} or La^{3+} in the 12-fold coordinated site have also been successful, and these crystals also have excellent quality for several applications. In particular, Ce-doped SBN and BSKNN crystals have been extensively used in photorefractive experiments,¹⁰⁻¹¹ while La^{3+} -doped SBN crystals are found to be particularly suitable for pyroelectric detector studies.¹⁸ Table 3 summarizes the various dopants investigated and their site preference in the bronze structure. The unusual role of Fe^{3+} in introducing striations is still a mystery in bronze crystals and we believe that effort should be continued to distinguish its character from other trivalent dopants such as Cr^{3+} and Mn^{3+} .

Another important parameter for achieving high crystal quality is the maintenance of a flat solid-liquid interface during growth. This strongly depends on strict temperature stability and controlled pulling conditions which have been achieved by the use of an automatic diameter control (ADC) system in our growth facilities. Currently, two different types of ADC systems are being used: one weighs the boule during growth (Crystar), and the other weighs the crucible (Technical Specialties and Services (TSS)). Both systems are adequate for our needs, but the TSS system is designed for larger crystals of 80 to 100 gms total weight. Using larger crucibles and other necessary modifications, one can use this system for even bigger crystals in excess of 300 to 500 gms. The use of these ADC systems has improved heat flow conditions and helped to maintain temperature stability of $\pm 1/2^\circ\text{C}$ or better. To make these systems more reliable and versatile, they are now interfaced to a computer to maintain a constant crystal diameter through the control of the pulling rate and the melt temperature. Although further improvements are being investigated, the present crystal quality and diameter control are sufficient for routine large production.

Thin polished sections of numerous crystals have been examined under a transmission microscope, examples of which are shown in Fig. 11. When bronze crystals have been pulled without the use of an ADC system, they are invariably striated. On the other hand, when an ADC system is used and is well tuned to the optimum growth conditions, the crystal quality dramatically improves and can be maintained throughout the boule. However, as shown in Fig. 11, the system needs a certain amount of time to adjust (1 to 2 h), and once the heat flow and pulling rates are optimized, high crystal quality can be maintained throughout the growth.

The development of striation-free SBN:60 crystals was found to be easier than other bronze crystals, because this composition exists close to, or at, the congruent

melting region. The growth of optical quality BSKNN-1 crystals was difficult since it exists far away from the so-called congruent melting region, which appears to lie between BSKNN-2 and BSKNN-3. The present successful growth of doped and undoped bronze crystals in optical quality is considered to be an essential step in their ultimate application in optoelectronic devices.

FERROELECTRIC PROPERTIES

Figure 12 shows the polar axis dielectric properties for three bronze ferroelectrics in which good crystal quality has been attainable, specifically SBN:60, BSKNN-2 and $\text{Sr}_{1.90}\text{Ca}_{0.10}\text{NaNb}_5\text{O}_{15}$ (SCNN(190/10)). Both SBN:60 and BSKNN show very large dielectric maxima at the phase transition temperature, T_C , reflecting the essentially second order phase transition behavior ($T_C \approx \theta_3$) of these materials. SBN compositions, in general, have a somewhat broadened transition region due to their unfilled lattice structure compared to the sharper transition of filled bronzes such as BSKNN, as illustrated in Fig. 12. On the other hand, SCNN crystals are somewhat unique in that the dielectric maximum at T_C is an order of magnitude lower than that found in either SBN or BSKNN, with a broad secondary maximum occurring well below T_C due to a ferroelastic transition. The behavior of the ferroelectric transition in SCNN may be understood by an examination of the normalized dielectric stiffness $\chi_{33} = \epsilon_{33}^{-1}$, as shown in Fig. 13. In SCNN, the transition temperature, T_C ($P_3 \neq 0$), occurs above the Curie temperature, θ_3 , determined from the extrapolation of the high temperature slope to $\chi_{33} = 0$. Hence, unlike SBN and BSKNN, SCNN is a first order phase transition ferroelectric with $T_C = 268^\circ\text{C}$ and $\theta_3 = 242^\circ\text{C}$. The broad secondary transition occurring near 90°C is ferroelastic, causing SCNN crystals to be weakly orthorhombic at room

temperature. However, unlike more classic orthorhombic bronzes such as PBN, the 3- or \underline{c} -axis is the unique polar axis, similar to tetragonal bronze ferroelectrics. Hence, SCNN is referred to as a Type II orthorhombic, or pseudo-tetragonal, ferroelectric similar to bronze $\text{Ba}_2\text{NaNb}_5\text{O}_{15}$ (BNN).

Figure 14 shows the a- and c-axis dielectric stiffness properties of Cr-doped (0.01 wt%) SBN:60, showing the large difference between the Curie temperatures θ_1 and θ_3 typical of tetragonal or pseudo-tetragonal bronze ferroelectrics. An interesting feature is the nearly linear variation of χ_{33} with temperature in the ferroelectric phase; from the standpoint of the phenomenology (Eqs. (3) and (4)), this reflects strong temperature dependencies for the higher order Devonshire coefficients α_{33} , α_{333} , etc.⁵³ This behavior is also observed in BSKNN compositions and in SCNN for temperatures below the ferroelastic transition (Fig. 13). Note also that in SBN:60, χ_{11} (and therefore, ϵ_{11}) varies only weakly with temperature below T_C . Hence, the linear electro-optic coefficient r_{51} (Eq. (5)) is expected to be only weakly temperature-dependent.

Doping with Ce, Cr and Mn does not appreciably affect the ferroelectric properties of these crystals for dopant concentrations of 0.02 wt% or more, depending on the dopant. Lanthanum doping, however, appreciably broadens the dielectric character near the phase transition,¹⁸ and significantly lowers the phase transition temperature. This is important for pyroelectric applications, since the pyroelectric coefficient,

$$p = - \frac{\partial P_s}{\partial T} \quad (7)$$

achieves a maximum near T_C where the spontaneous polarization, P_s , varies rapidly with temperature. Hence, La-doped SBN:60, with T_C close to room temperature, is particularly suited to high sensitivity pyroelectric detector applications.

Figure 15 shows the variation of the spontaneous polarization and the pyroelectric coefficient as a function of temperature for undoped SBN:60; La-doped material shows the same characteristics, with the curves shifted downward in temperature according to the level of doping. It is seen that P_s is only a weak function of temperature, varying as $(\theta_3 - T)^{1/6}$ over much of the temperature range below the transition temperature for SBN and BSKNN compositions, and likewise for temperatures below the 90°C ferroelastic transition in SCNN.

In general, these bronze crystals show very low dielectric dispersion and dielectric losses after poling to a single domain condition. Room temperature values of the dielectric loss tangent (100 Hz-100 kHz) have been measured as low as 0.0005 in SBN and BSKNN crystals, with dc conductivities of $5 \times 10^{-15} \text{ ohm}^{-1}\text{-cm}^{-1}$ or less. Poling is relatively easy to accomplish by applying a moderate dc field of 5-10 kV/cm during slow cooldown from the transition temperature. However, the field must be brought up gradually when close to, but below, T_C to avoid the formation of a thin fracture region underneath the positive electrode. Aside from this consideration, these crystals have proven to be mechanically very rugged, and can withstand repeated thermal cycling without damage.

DISCUSSION

Table 4 lists the optical figures-of-merit r_{ij}/ϵ and $n^3 r_{ij}/\epsilon$ for several of the more important bronze ferroelectrics in comparison with BaTiO_3 and KNbO_3 . With the

exception of PBN:60 bulk crystals, which presently suffer from inhomogeneity and a lack of optical quality, all of these materials possess high FOMs and good optical quality for serious consideration in several optical device applications. Perhaps the most important of these applications is in the area of photorefractive devices¹⁰⁻¹⁷ (optical phase conjugation, optical computing, etc.), in part because of the relative ease with which these crystals can be doped and tailored for specific spectral regions from 0.4 μm to the near-IR.

One of the more encouraging aspects of these bronze crystals is the excellent uniformity of their ferroelectric properties from growth to growth. Considering that all of these materials are solid solutions of varying complexity and high melting temperatures, this is something we could only hope for when this work was initiated eleven years ago. Although each new material system presents its own unique set of growth problems and considerations, all of these materials -- and in particular, SBN -- have contributed to a better overall understanding of the requirements for the growth of homogeneous, optical quality crystals of moderate to large size.

SBN:60 remains as the material of choice at the present time because of the maturity of its development and its particular suitability for investigating new dopants for photorefractive applications. However, other bronze crystals, such as BSKNN and SCNN, may ultimately prove more advantageous in certain applications, depending on the specific device requirements. Aside from bulk crystal applications, bronzes such as SBN and BSKNN are being investigated for guided wave optical applications^{3,6} and are also being effectively used in our work as substrate material for ferroelectric and superconducting thin film growths. With the diversity of potential applications for these crystals, and the possibilities for developing new solid solutions within the tungsten bronze crystal family, it is evident that ferroelectric bronze crystals will continue to play an important and growing role in optoelectronics.

ACKNOWLEDGMENTS

This work has been made possible by the support of DARPA, ONR, AFOSR and the U.S. Army Night Vision Laboratory. The authors are especially grateful to Bob Pohanka (ONR) and Ed Sharp (NVL) for their discussions, support and encouragement during the course of this work.

REFERENCES

1. P.V. Lenzo, E.G. Spencer and A.A. Ballman, Appl. Phys. Lett. 11 (1967), 23.
2. E.G. Spencer, P.V. Lenzo and A.A. Ballman, Proc. IEEE 52 (1967), 1074.
3. O. Eknayan, C.H. Bulmer, H.F. Taylor, W.K. Burns, A.S. Greenblatt, L.A. Beach and R.R. Neurgaonkar, Appl. Phys. Lett. 48 (1986), 13.
4. A.A. Ballman, S.K. Kurtz and H. Brown, J. Cryst. Growth 10 (1971), 185.
5. W.W. Ho, W.F. Hall and R.R. Neurgaonkar, Ferroelectrics 50 (1983), 325.
6. S. Nomura and H. Kojima, Jpn. J. Appl. Phys. 13 (1974), 1185.
7. B. Bobbs, M. Matloubian, H.R. Fetterman, R.R. Neurgaonkar and W.K. Cory, Appl. Phys. Lett. 48 (1986), 1642.
8. A. Glass, J. Appl. Phys. 40 (1969), 4699.
9. S.T. Liu and R.B. Maciolek, Proc. SPIE (1975), 259.
10. G.L. Wood, W.W. Clark, III, M.J. Miller, E.J. Sharp, G.J. Salamo and R.R. Neurgaonkar, IEEE, J. Quant. Electron. QE23 (1987), 2126.
11. G. Rakuljic, A. Yariv and R.R. Neurgaonkar, J. Opt. Engi. 25 (1986), 1212.

12. M.J. Miller, E.J. Sharp, G.L. Wood, W.W. Clark, III, G.J. Salamo and R.R. Neurgaonkar, *Opt. Lett.* 12 (1987), 340.
13. K. Megumi, H. Kozuka, M. Kobayashi and Y. Furunata, *Appl. Phys. Lett.* 30 (1977), 631.
14. J. Rodriquez, A. Siahmakoun, G.J. Salamo, M.J. Miller, W.W. Clark, III, G.L. Wood, E.J. Sharp and R.R. Neurgaonkar, *Appl. Opt.* 26(6) (1987), 1732.
15. G.A. Rakuljic, K. Sayano, A. Yariv and R.R. Neurgaonkar, *Appl. Phys. Lett.* 50(1) (1987), 10.
16. R.R. Neurgaonkar and W.K. Cory, *J. Opt. Soc. Am.* B(3) (1986), 274.
17. R.R. Neurgaonkar, W.K. Cory, J.R. Oliver, M.D. Ewbank and W.F. Hall, *Opt. Eng.* 26(5) (1987), 392.
18. R.R. Neurgaonkar, W.K. Cory, J.R. Oliver and L.E. Cross, to appear in *J. Cryst. Growth* - June 1988.
19. R.R. Neurgaonkar, W.K. Cory, J.R. Oliver, M.J. Miller, W.W. Clark, III, G.L. Wood and E.J. Sharp, *J. Cryst. Growth* (1987).
20. R.R. Neurgaonkar, W.W. Ho, W.K. Cory, W.F. Hall and L.E. Cross, *Ferroelectrics* 51 (1984), 185.
21. P.P. Labbe, M. Frey, B. Raveau and J.C. Monier, *Acta. Crystallogr.* B33 (1977), 2201.
22. P.B. Jamieson, S.C. Abrahams and J.L. Bernstein, *J. Chem. Phys.* 48 (1968), 5048, and 50 (1969), 4352.
23. F.W. Ainger, W.P. Bickley and G.V. Smith, *Proc. Brit. Ceram. Soc.* 18 (1970), 221.
24. T. Ikeda, K. Uno, K. Oyamada, A. Sagara, J. Kato, S. Takano and H. Sato, *Jpn. Appl. Phys.* 17 (1978), 341.
25. J. Ravez and P. Hagenmuller, *Mater. Res. Bull.* 12 (1979), 769.

26. J. Ravez, A. Perron-Simon and P. Hagenmuller, *Ann. Chim.* (1976), 251.
27. K. Megumi, N. Nagatsuma, K. Kashiwada and Y. Furuhashi, *Mat. Sciences* 11 (1976), 1583.
28. J.R. Carruthers and H. Grosso, *J. Electrochem. Soc.* 117 (1970), 1426.
29. A.A. Ballman and H. Brown, *J. Cryst. Growth* 1 (1967), 321.
30. M.H. Francombe, *Acta. Cryst.* 13 (1960), 131.
31. R.R. Neurgaonkar, W.K. Cory, J.R. Oliver, E.J. Sharp, M.J. Miller, G.L. Wood, W.W. Clark, III and G.J. Salamo, to appear in *Appl. Phys. Lett.*
32. E.C. Subbarao, G. Shirane and F. Jona, *Acta. Crystallogr.* 13 (1960), 226.
33. B. Jaffe, W.R. Cook and H. Jaffe, *Piezoelectric Ceramics*, Academic Press, New York (1971).
34. T.R. Shrout, H. Chen and L.E. Cross, *Ferroelectrics* 56 (1983), 45.
35. T.R. Shrout, L.E. Cross and D.A. Hukin, *Ferroelectrics* 44 (1983), 325.
36. W.R. Bekebrede, M. Kestigian, A.B. Smith and R.M. Joseph, *J. Appl. Phys.* 50(3) (1979), 2167.
37. R.B. Macilek and S.T. Liu, *J. Elect. Mater.* 2 (1973), 191, and 4 (1975), 517.
38. J.C. Brice, O.F. Hill, P.A.C. Whiffin and J.A. Wilkinson, *J. Cryst. Growth* 10 (1971), 133.
39. Y. Boniort, C. Brehm, G. Desplanches, J-Y Barraud and P. Margotin, *J. Cryst. Growth* 30 (1975), 357, and 18 (1973), 191.
40. Y. Ito, H. Kozuka and Y. Kashiwada, *Jpn. J. Appl. Phys.* 14 (1975), 1443.
41. M. Kestigian and W.R. Bekebrede, *Mat. Res. Bull.* 8 (1973), 319.
42. R.R. Neurgaonkar, W.F. Hall, J.R. Oliver, W.W. Ho and W.K. Cory, submitted to *Ferroelectrics*.
43. X. Yukuan, H. Chen and L.E. Cross, *Ferroelectrics* 54 (1984), 123.

44. Y. Xu and H. Chen, Wuli Xuebao 32 (1983), 705, Zhongshan Daxue Xuedao 2 (1982), 52.
45. R.R. Neurgaonkar, I. Santha and J.R. Oliver, submitted to J. Mat. Science.
46. J.J. Amodei, D.L. Staebler and A.W. Stephens, Appl. Phys. Lett. 18 (1971), 507.
47. L.H. Lin, Proc. IEEE 57 (1969), 210.
48. F.S. Chen, J. Appl. Phys. 38 (1967), 3148.
49. E. Okamoto, H. Ikeo and K. Muto, Appl. Opt. 14 (1975), 2453.
50. P.N. Gunter, Opt. Lett. 7 (1982), 10.
51. R.R. Neurgaonkar and J.R. Oliver, Semi-Annual Report No. 4, DARPA Contract N00015-82-C-2466 (1985).
52. R.R. Neurgaonkar, W.K. Cory, J.R. Oliver, E.J. Sharp, M.J. Miller, G.L. Wood, W.D. Clark III, G.J. Salamo, submitted to Appl. Phys. Lett.
53. J.R. Oliver, R.R. Neurgaonkar and L.E. Cross, to be published in J. Appl. Phys. (1988).

List of Figures

1. Tungsten bronze crystal structure.
2. Tungsten bronze crystal systems of primary interest. (a) BSKNN quaternary system; (b) SBN phase diagram; (c) BNN-SNN-CNN dielectric properties (ceramic samples); (d) PBN phase diagram.
3. Optical-quality SBN single crystals grown by the Czochralski technique.
4. La^{3+} -doped and undoped SBN:60 crystals.
5. BSKNN-1 and BSKNN-2 single crystals. BSKNN-3 has a boule cross-section similar to that of BSKNN-2.
6. Ferroelectric phase transition temperature, T_C , vs a-axis lattice constant for compositions in the BSKNN system.
7. SCNN-2 crystal grown along $\langle 001 \rangle$.
8. Idealized growth habits of BSKNN and SBN:60 single crystals.
9. Potential defects in tungsten bronze crystals.
10. Schematic representations of defects in tungsten bronze crystal boules.

11. Transmission microscope photographs of SBN:60 crystals grown with and without automatic diameter control (ADC).
12. Polar axis dielectric constant vs temperature for SBN:60, BSKNN-2 and SCNN(190/10) crystals. $F = 10$ kHz.
13. Reciprocal dielectric constant (stiffness) along the polar c-axis for SCNN(190/10). $F = 10$ kHz.
14. Normalized dielectric stiffnesses $\chi_{11} = \epsilon_{11}^{-1}$ and χ_{33} (polar) for Cr-doped SBN:60. The data shown are essentially identical to those of undoped SBN:60.
15. Spontaneous polarization, P_S , and pyroelectric coefficient, p , for undoped SBN:60.

Table I
List of Important Tungsten Bronze Single Crystals

Crystal Composition	T _c (°C)	Dielectric Constant: ε ₃₃	ε ₁₁	Electro-Optic Coefficient (· 10 ⁻¹² m/V)	r ₃₃	r ₅₁
<u>Tetragonal Crystals (θ₃ > θ₁)</u>						
Sr _{0.75} Ba _{0.25} Nb ₂ O ₆ (SBN:75)	56	3000			1400	42
Sr _{0.6} Ba _{0.4} Nb ₂ O ₆ (SBN:60)	78	900	470		470	60
Sr _{0.5} Ba _{0.5} Nb ₂ O ₆ (SBN:50)	128	450	300		180	80
Sr ₂ KNb ₅ O ₁₅ (SKN)	156	1000	800		270	---
Ba _{1.2} Sr _{0.8} K _{0.75} Na _{0.25} Nb ₅ O ₁₅ (BSKNN-1)	209	170	550		---	---
Ba _{0.5} Sr _{1.5} K _{0.5} Na _{0.5} Nb ₅ O ₁₅ (BSKNN-2)	178	180	700		100	~ 350
Ba _{0.5} Sr _{1.5} K _{0.25} Na _{0.75} Nb ₅ O ₁₅ (BSKNN-3)	182	270	780		180	> 300
K ₃ Li ₂ Nb ₅ O ₁₅ (KLN)	405	115	306		---	80
Ba ₆ Ti ₂ Nb ₈ O ₃₀ (BTN)	245	200	193		420	---
Sr ₆ Ti ₂ Nb ₈ O ₃₀ (STN)	100					
<u>Orthorhombic Crystals (θ₃ < θ₁)</u>						
Pb ₂ KNb ₅ O ₁₅ (PKN)	460	129	1500		---	100
Ba ₂ NaNb ₅ O ₁₅ (BNN)	560	57	242		---	92
Sr ₂ NaNb ₅ O ₁₅ (SNN)	270	1500	---		---	400
Sr _{2-x} Ca _x NaNb ₅ O ₁₅ (SCNN)	270	1700	1740		1320	1100
Sr _{1.85} Ba _{0.05} Ca _{0.1} NaNb ₅ O ₁₅ (BSCNN)	270	750	800		520	480
K ₂ RiNb ₅ O ₁₅ (KBN)	405	500	460		---	---
K ₃ Li ₂ Ta _{5-x} Nb _x Nb ₅ O ₁₅ (KLTN)	---	375	390		---	---
Ba ₂ Ag _{0.5} Nb ₅ O ₁₅ (BAN)	---	---	---		---	---
<u>MPB Crystals</u>						
Pb _{0.9} Ba _{0.1} Nb ₂ O ₆	350					

Table 2
Growth Conditions for Tungsten Bronze Crystals

Cryst. Composition*	Growth Temp. (°C)	Pulling Rate (mm/hr)	Crystal Diameter	Quality
$\text{Sr}_{0.75}\text{Ba}_{0.25}\text{Nb}_2\text{O}_6$ (SRN:5)	1500	6-7	1.5 to 2 cm 24 facets	Optical quality
$\text{Sr}_{0.6}\text{Ba}_{0.4}\text{Nb}_2\text{O}_6$ (SRN:60)	1510	7-10	2.5 to 3.2 cm 24 facets	Optical quality
$\text{Sr}_{0.5}\text{Ba}_{0.5}\text{Nb}_2\text{O}_6$ (SRN:50)	1515	7-10	1.5 to 2 cm 24 facets	Optical quality
$\text{Ba}_{1.2}\text{Sr}_{0.8}\text{K}_{0.75}\text{Na}_{0.25}\text{Nb}_5\text{O}_{15}$ (BSKNN-1)	1480	8-10	0.5 to 1.0 cm 4 facets	Optical quality, but needs improvement
$\text{Ba}_{0.5}\text{Sr}_{1.5}\text{K}_{0.5}\text{Na}_{0.5}\text{Nb}_5\text{O}_{15}$ (BSKNN-2)	1480	5-7	1 to 1.2 cm 8 facets	Optical quality
$\text{Ba}_{0.5}\text{Sr}_{1.5}\text{K}_{0.25}\text{Na}_{0.75}\text{Nb}_5\text{O}_{15}$ (BSKNN-3)	1485	6-10	1 to 1.5 cm 8 facets	Optical quality
$\text{Sr}_{1.9}\text{Ca}_{0.1}\text{NaNb}_5\text{O}_{15}$ (SCNN-1)	1480	5-7	0.5 to 0.8 cm	Reasonable quality, striated
$\text{Pb}_{0.6}\text{Ba}_{0.5}\text{Nb}_2\text{O}_6$ (PBN:60)**	1350	5-9	1 cm	Compositional inhomogeneity

*All compositions were grown along <001>.

**Grown at Penn State.

Table 3
The Role of Various Impurities in Bronze Crystals

Dopant*	Crystallographic Site					Remarks
	15-fold	12-fold	9-fold	6-fold	Crystal Color	
SiN (Undoped)	Ba ²⁺	Sr ²⁺	---	Nb ⁵⁺	Pale Cream	Optical quality (3 cm diameter)
Cerium (Ce ³⁺ /Ce ⁴⁺)	Ce ³⁺	Ce ³⁺	---	---	Pink	Optical quality (2.5 cm diameter)
Iron (Fe ²⁺ /Fe ³⁺)	---	---	Ce ³⁺	---	Greenish Yellow	Optical quality (2.5 cm diameter)
Chromium (Cr ³⁺)	---	---	---	Fe ²⁺ /Fe ³⁺	Yellow	Striated crystals (2 cm diameter)
Manganese (Mn ²⁺ /Mn ³⁺)	---	---	---	Cr ³⁺	Greenish	Optical quality (1.5 to 1.8 cm diameter)
Lanthanum (La ³⁺)	La ³⁺	La ³⁺	---	Mn ²⁺ /Mn ³⁺	Pale Brown	Optical quality (2 cm diameter)
Magnesium (Mg ²⁺)	---	---	---	---	Pale Cream	Optical quality (2 cm diameter)
					Pale Cream	Striated crystals

*Doping levels are less than 0.2 wt% except for La³⁺ (up to 1.5 wt%).

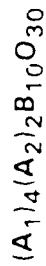
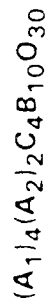
Table 4
Electro-Optic Figure-of-Merit
for Tungsten Bronze Single Crystals

Crystal	r_{ij}/ϵ	$n^3 r_{ij}/\epsilon$
• $\text{Sr}_{0.75}\text{Ba}_{0.25}\text{Nb}_2\text{O}_6$ (SBN:75)	0.475	5.01
• $\text{Sr}_{0.6}\text{Ba}_{0.4}\text{Nb}_2\text{O}_6$ (SBN:60)	0.530	5.90
• $\text{Sr}_{1.9}\text{Ca}_{0.1}\text{NaNb}_5\text{O}_{15}$ (SCNN-1)	0.740 - T 0.660 - L	8.690 - T 7.512 - L
• $\text{Pb}_{0.6}\text{Ba}_{0.4}\text{Nb}_2\text{O}_6$ (PRN:60)	1.200	14.520
• BSKNN-2	0.500 - L 1.000 - T	6.000 - L 11.000 - T
• BSKNN-3	0.512 - L 0.740 - T	6.150 - L 9.110 - T
• BaTiO_3	0.390 - L	4.010 - L
• KNbO_3	0.400 - L	4.200 - L

T = transverse
L = longitudinal

TUNGSTEN BRONZE CRYSTAL STRUCTURE

CHEMICAL FORMULAE



A_1 = 15-FOLD COORDINATED SITE

A_2 = 12-FOLD COORDINATED SITE

C = 9-FOLD COORDINATED SITE

B = 6-FOLD COORDINATED SITE (TWO SITES)

CRYSTAL STRUCTURE

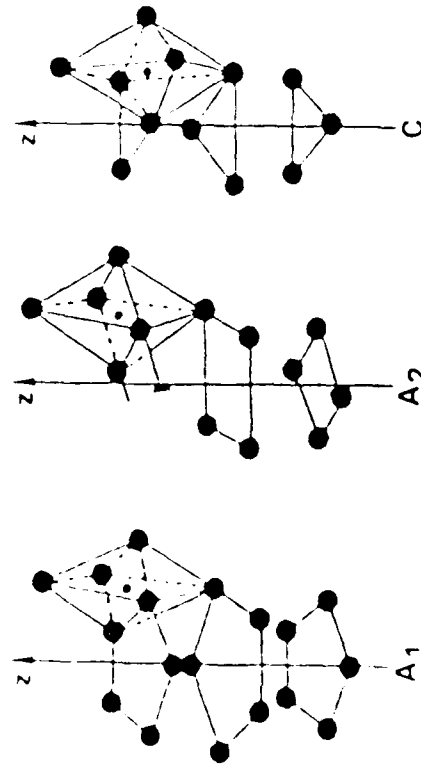
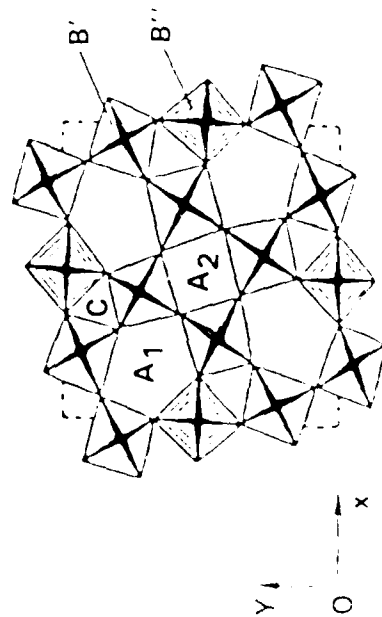
4/mm TO 4mm (TETRAGONAL-TETRAGONAL)

4mm TO mm2 (TETRAGONAL-ORTHORHOMBIC)

KNOWN SYSTEMS

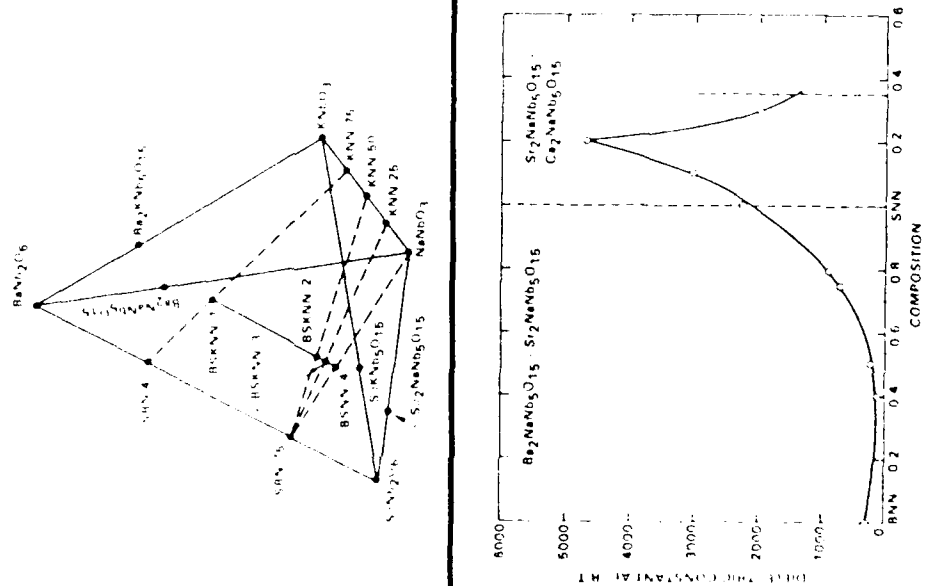
150 COMPOUNDS OR

SOLID SOLUTIONS BETWEEN END MEMBERS
SEVERAL MORPHOTROPIC PHASE BOUNDARY
SYSTEMS

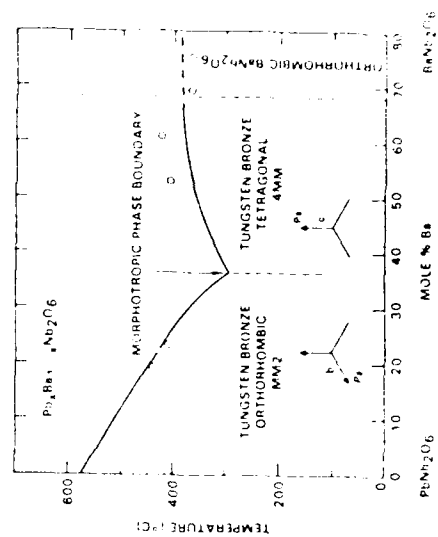
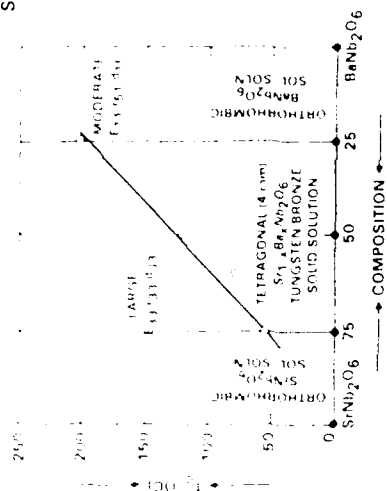


Rockwell International
Science Center

CURRENT TUNGSTEN BRONZE SYSTEMS OF PRIME INTEREST

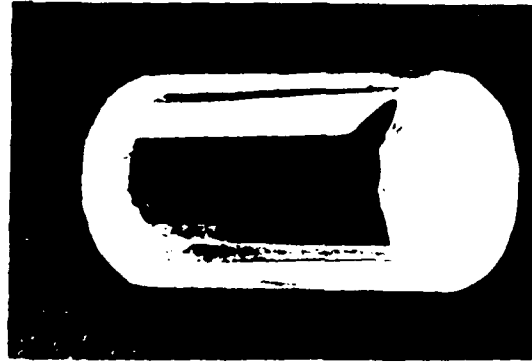


SC42622

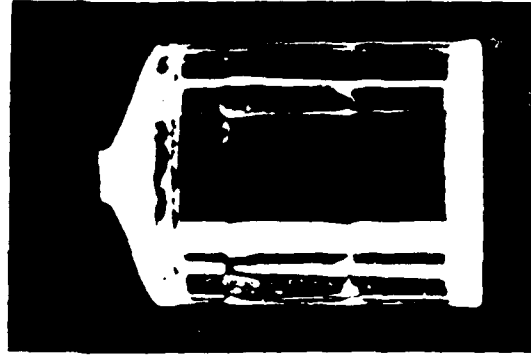


FERROELECTRIC TUNGSTEN BRONZE
 $\text{Sr}_{1-x}\text{Ba}_x\text{Nb}_2\text{O}_6$ SOLID SOLUTION CRYSTALS

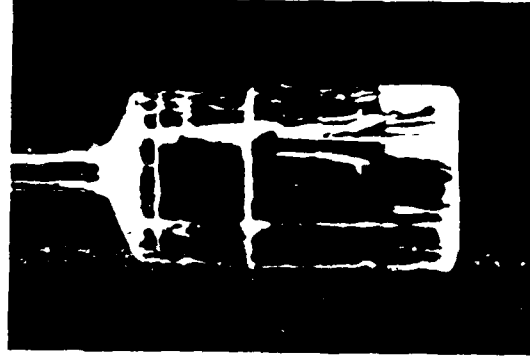
SC44256



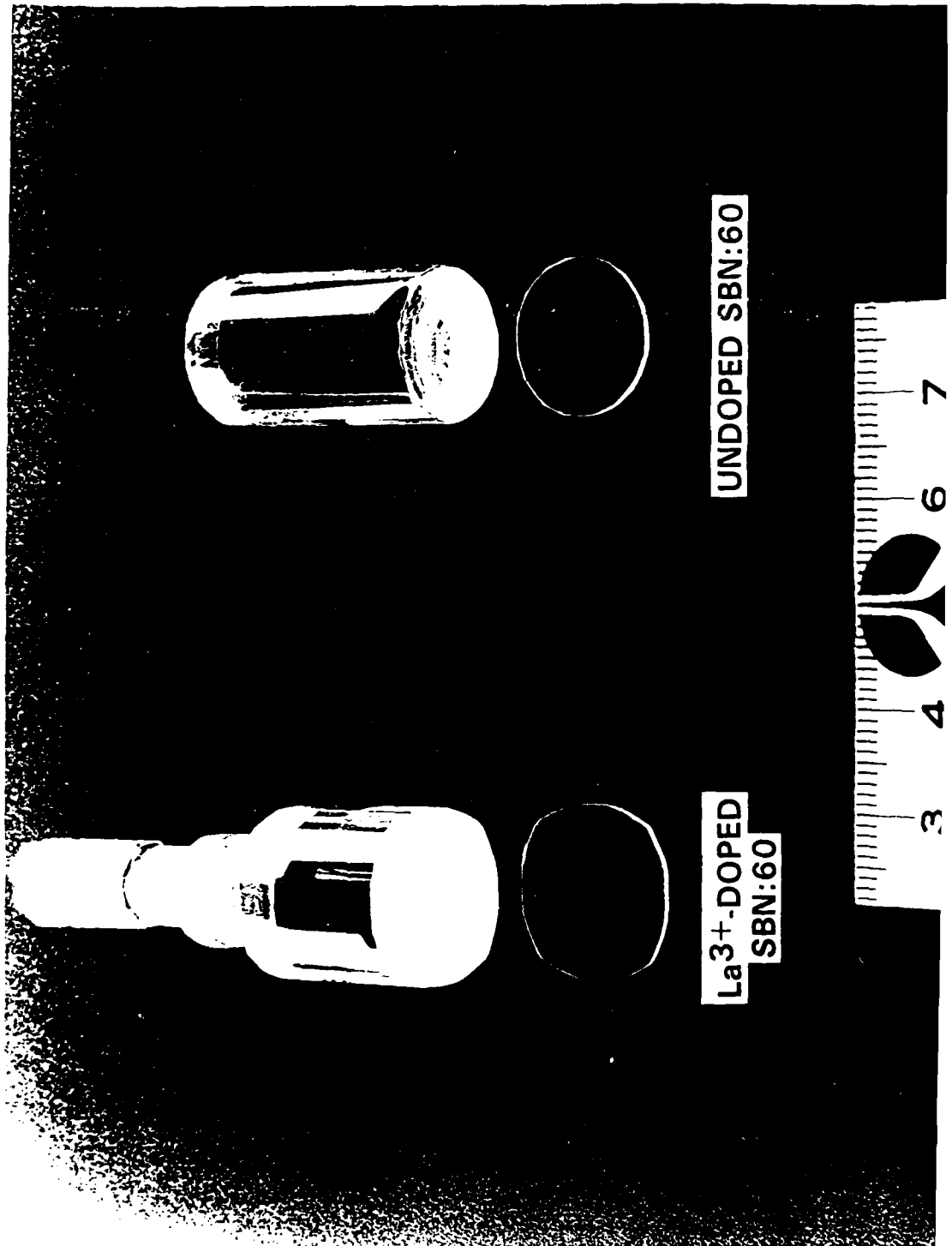
SBN:75



SBN:60

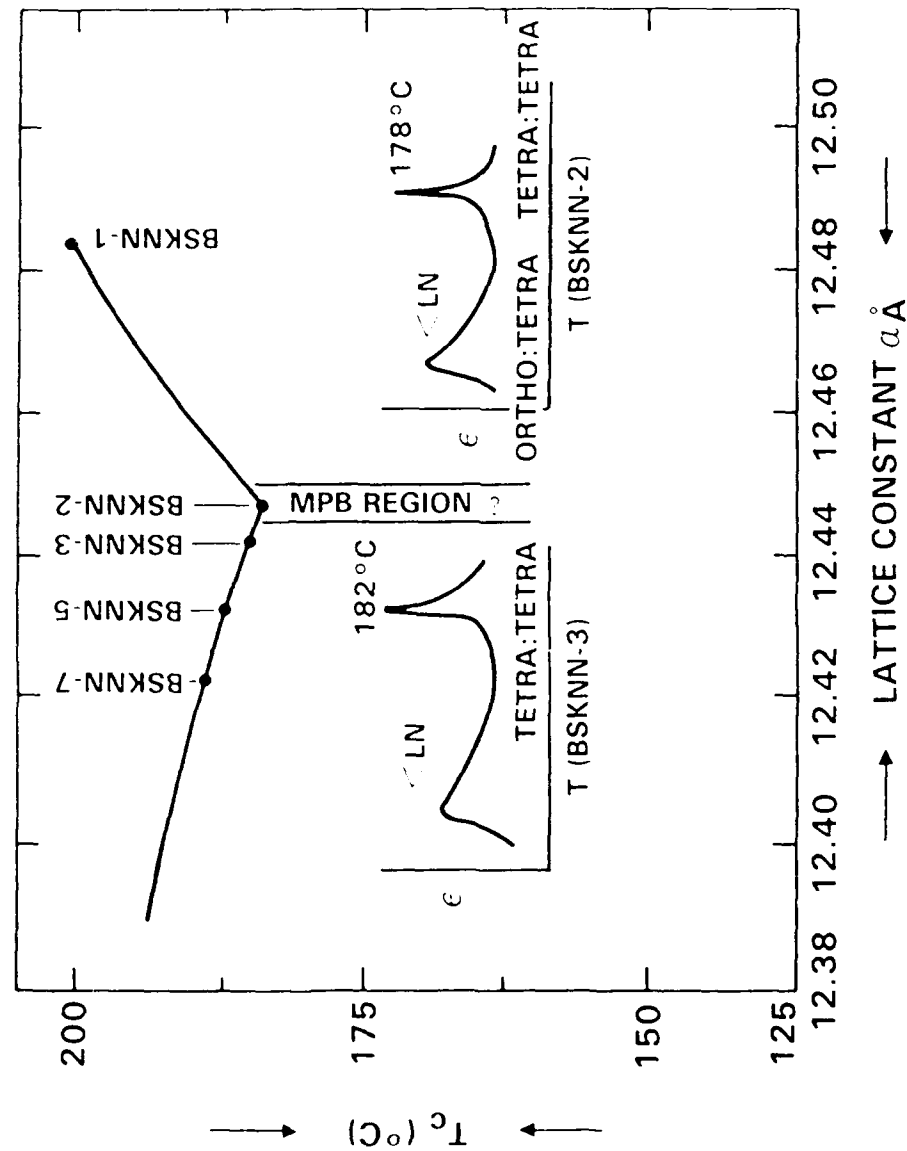


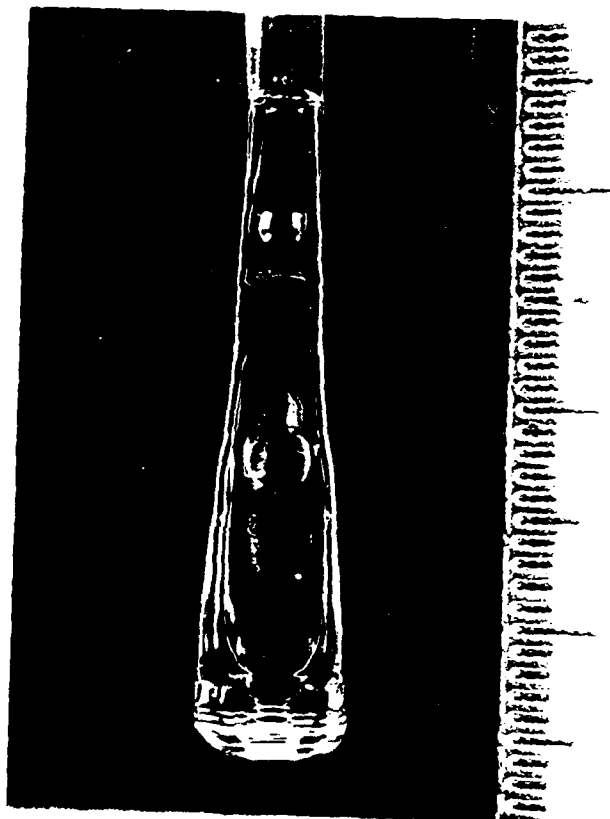
SBN:50

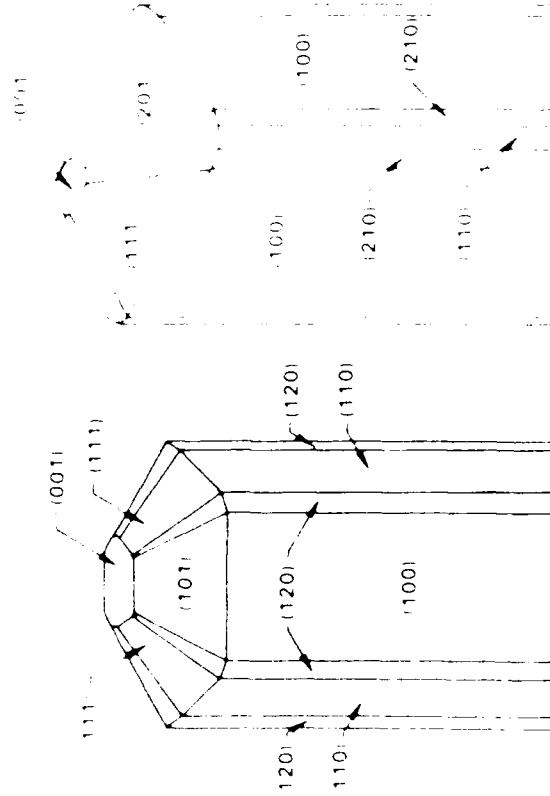


THE $\text{Sr}_2\text{NaNb}_5\text{O}_{15}\text{-Ba}_2\text{KNb}_5\text{O}_{15}$ SYSTEM (BSKNN)

SC44290



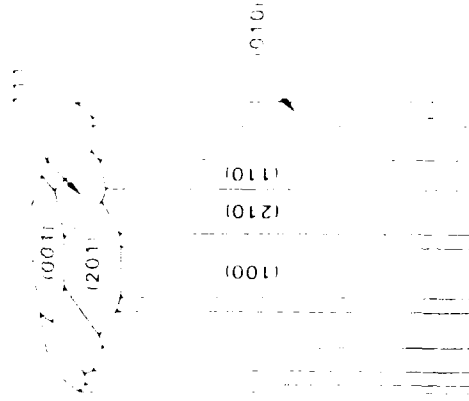




BSKNN.2

BSKNN.1

LARGE LONGITUDINAL EFFECTS

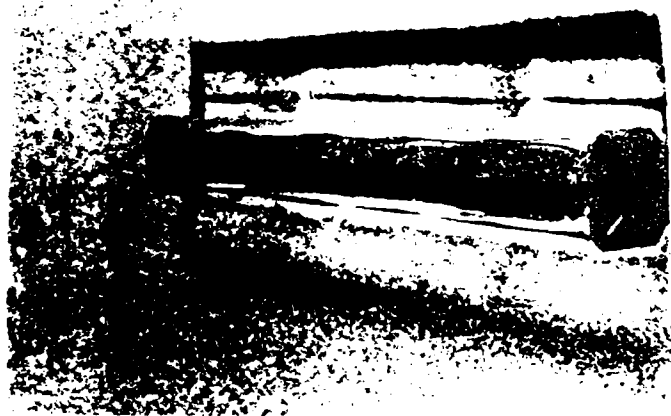


SBN.60

LARGE TRANSVERSE EFFECTS

TUNGSTEN BRONZE BSKNN SINGLE CRYSTALS

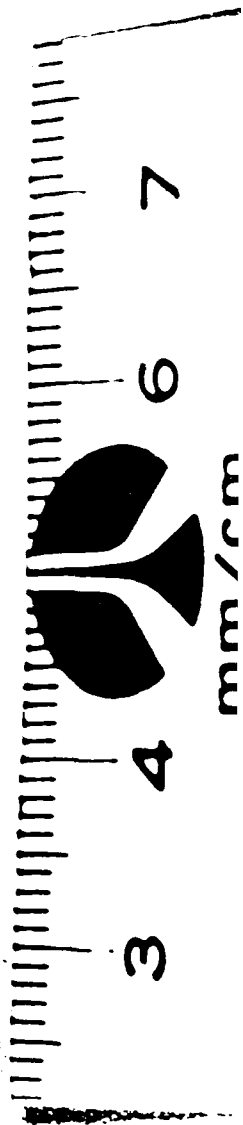
SC39143

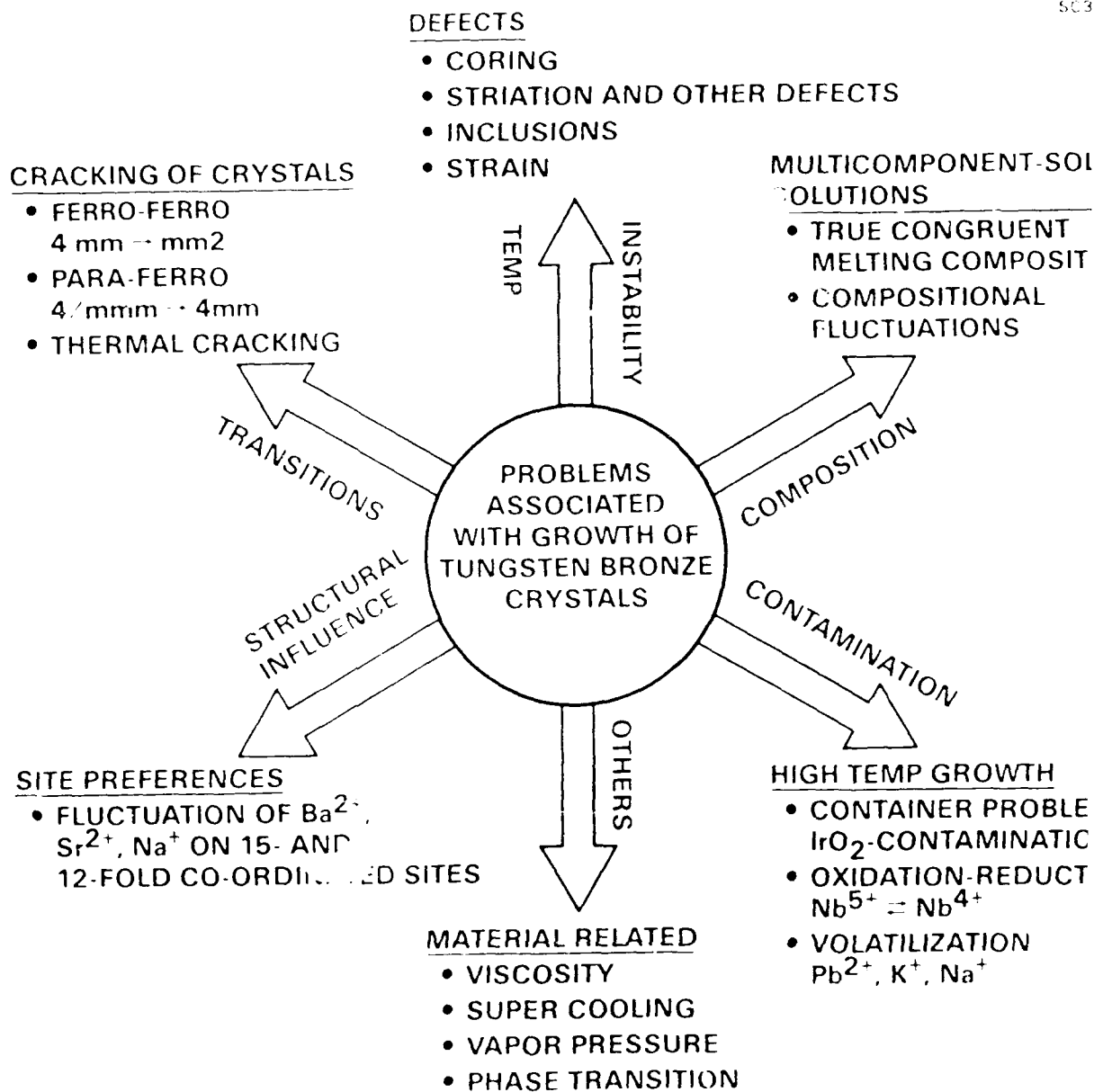


BSKNN-1



BSKNN-2

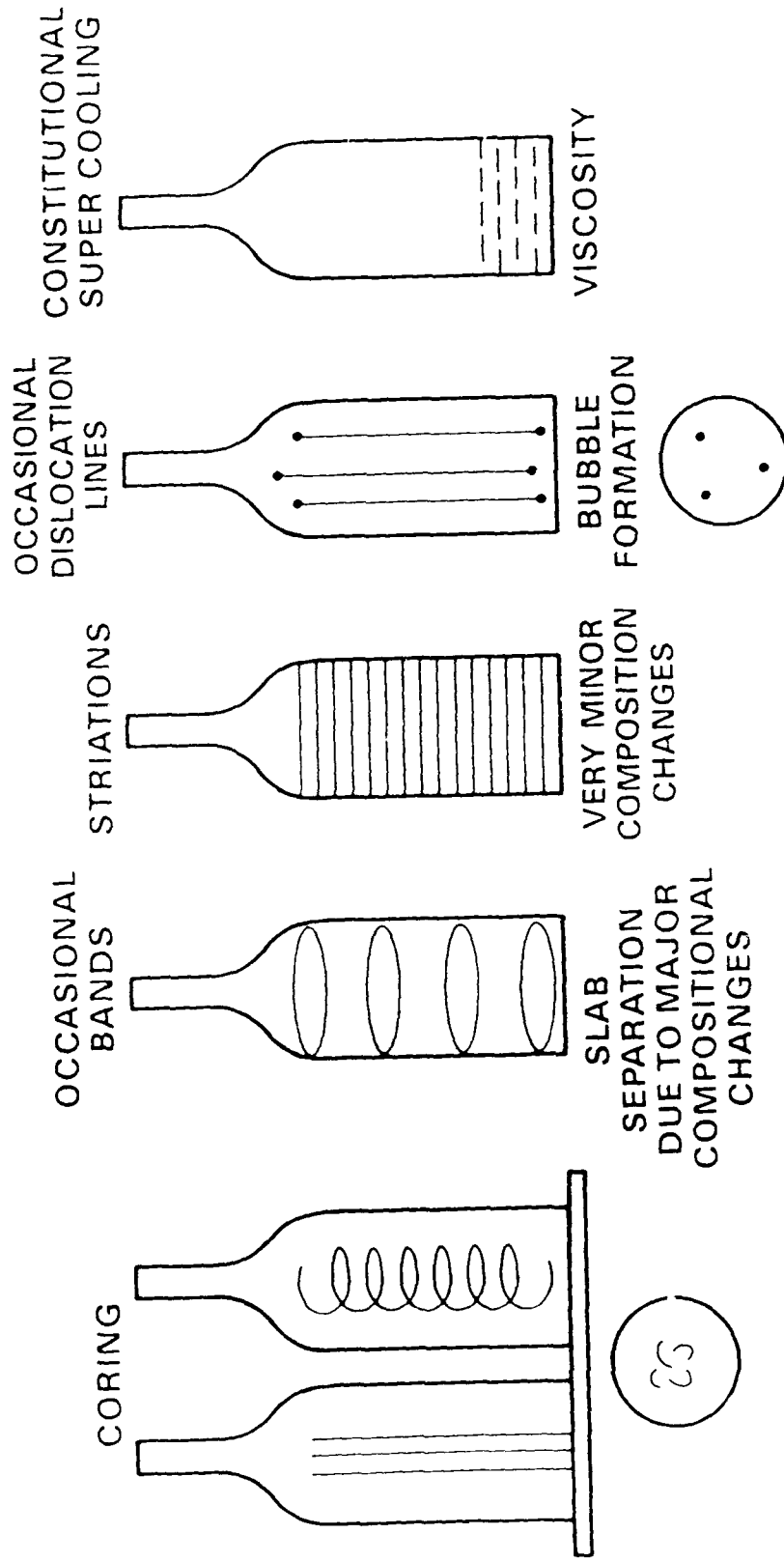




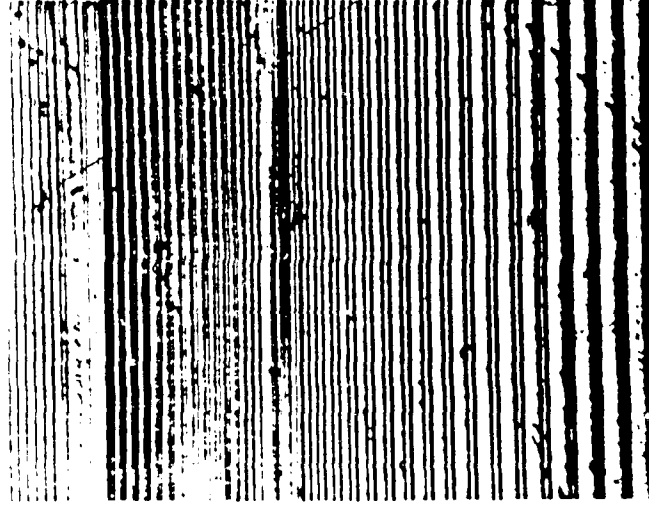
Rockwell International
Science Center

DEFECTS IN TUNGSTEN BRONZE CRYSTALS

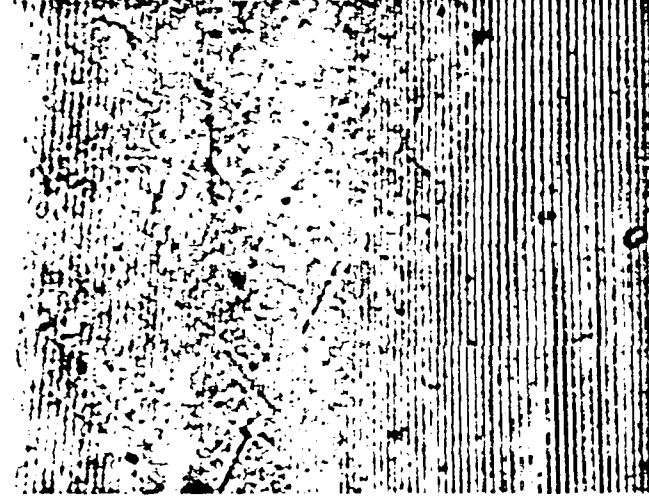
SC3703H



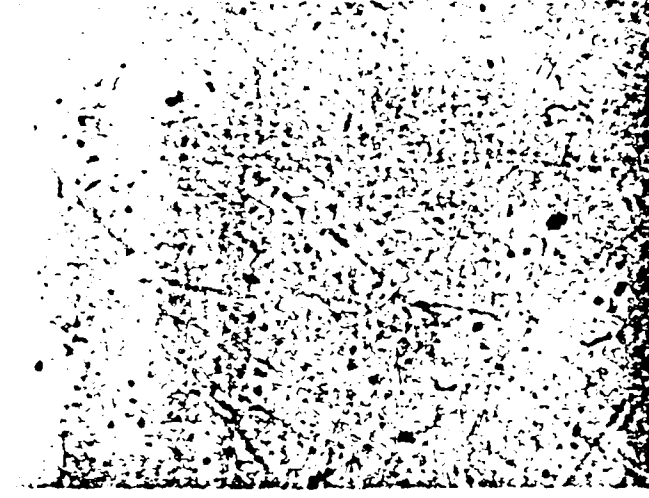
SCB3 24485



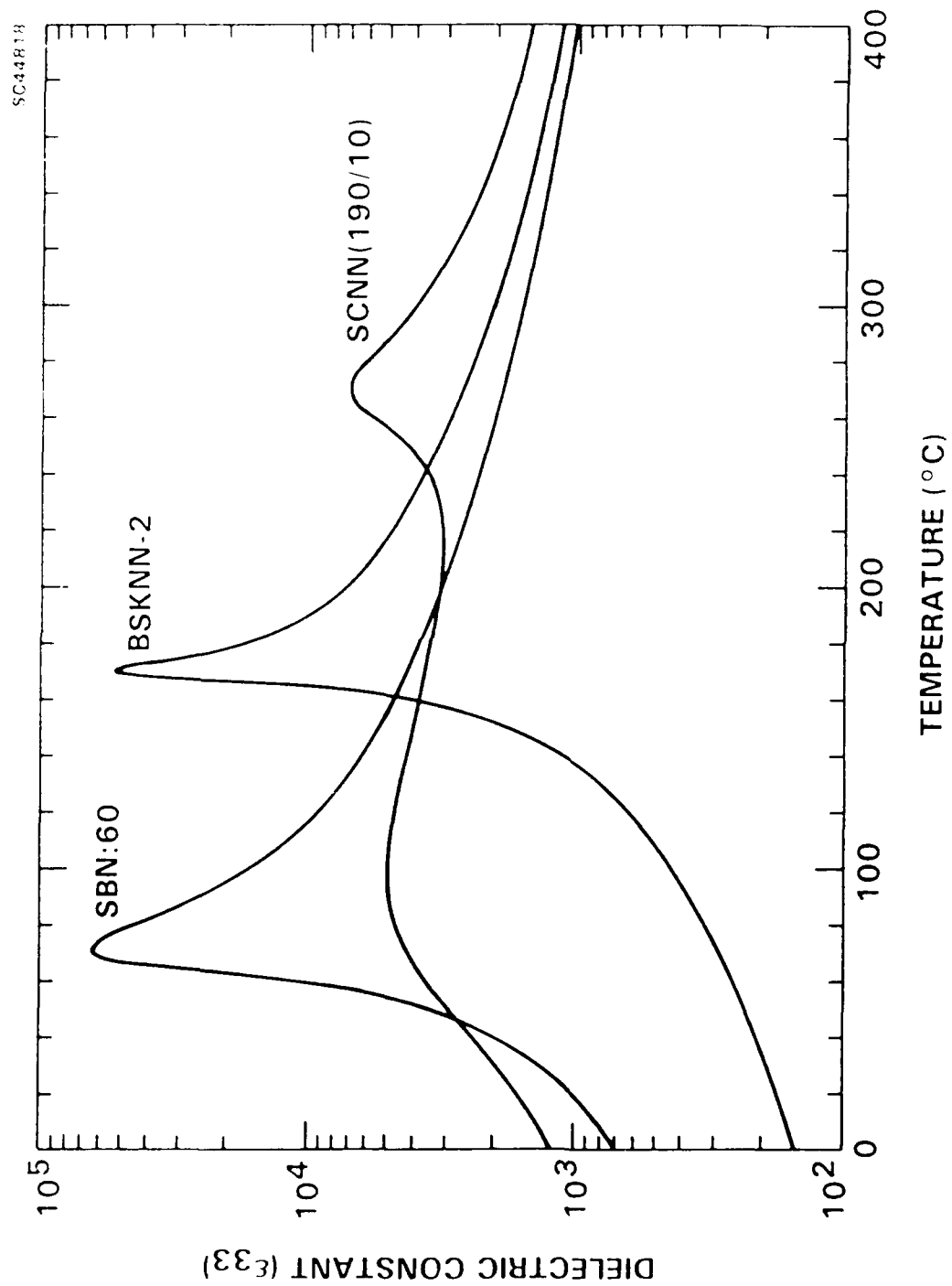
SBN:60 CRYSTAL GROWTH WITHOUT
ADC SYSTEM

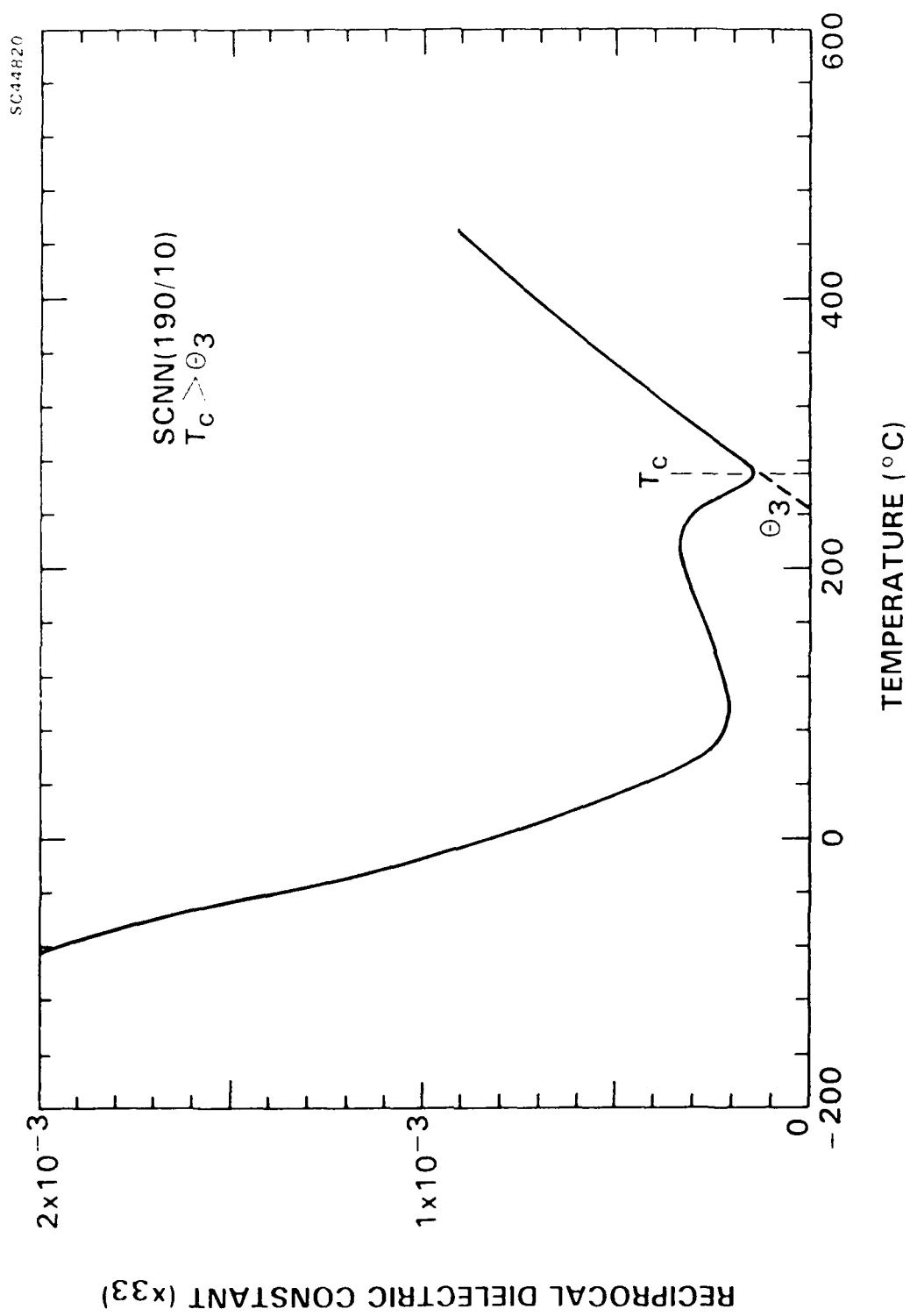


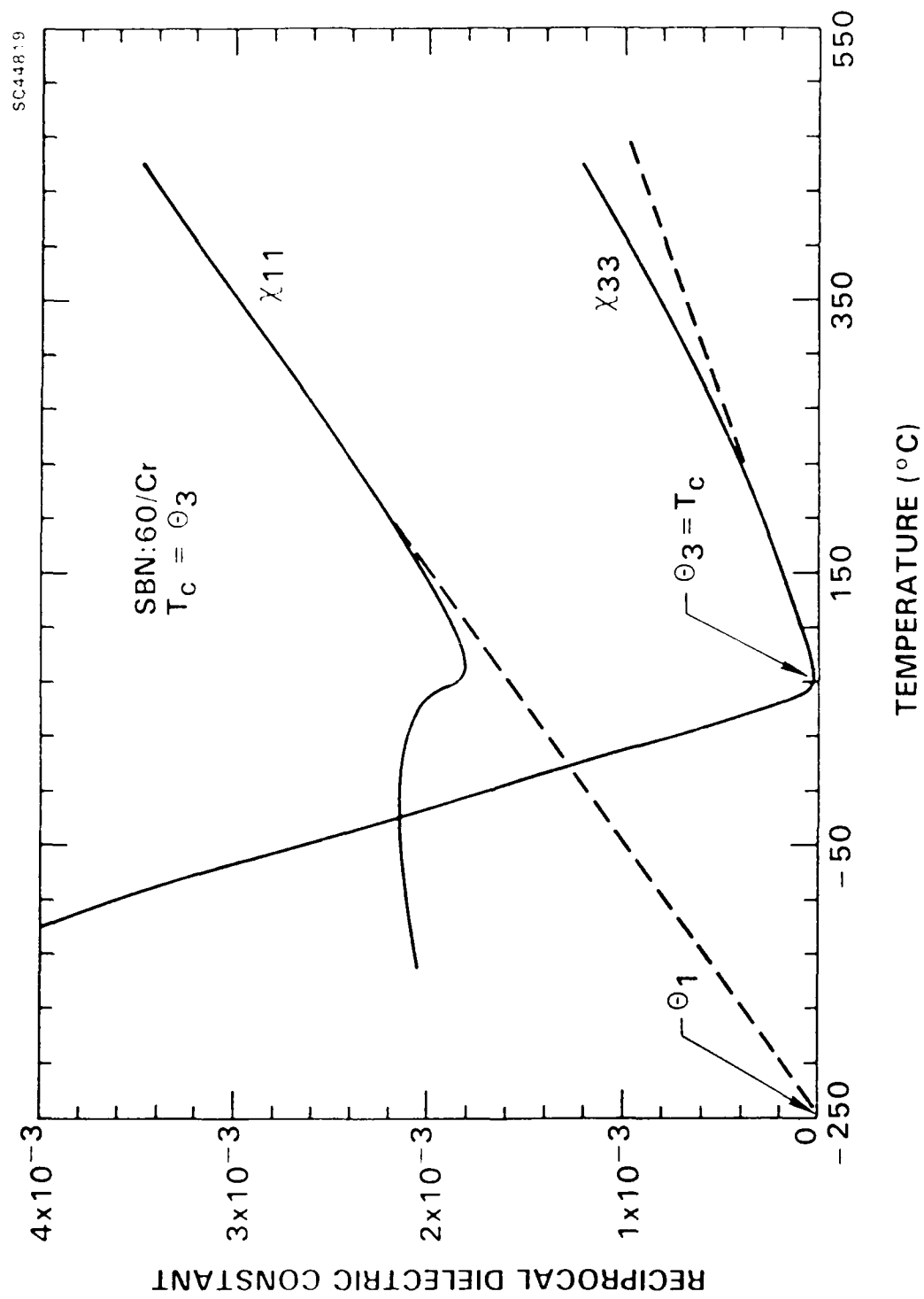
SBN:60 CRYSTAL GROWTH WITH ADC
SYSTEM (UNSTABLE CONDITIONS)

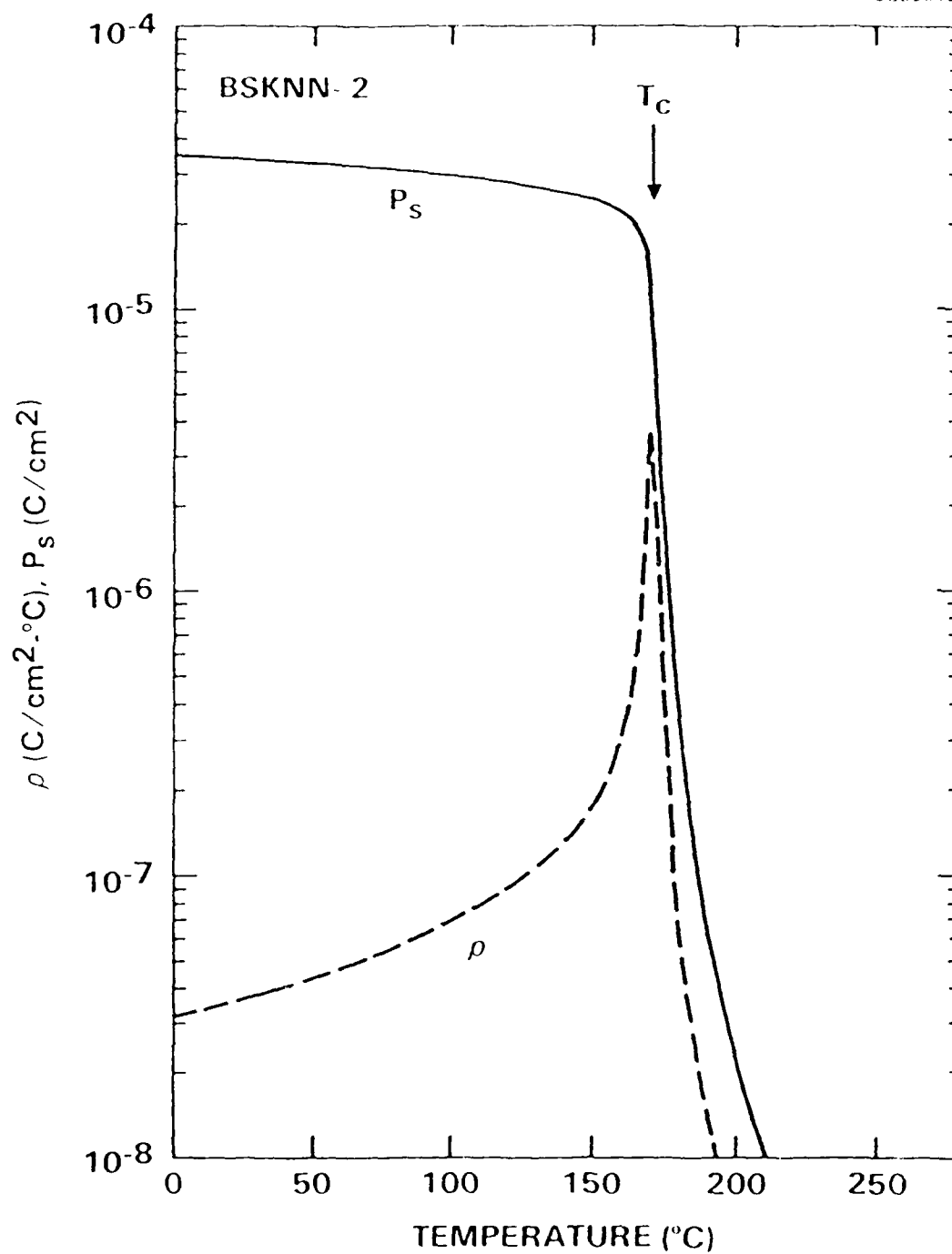


SBN:60 CRYSTAL GROWTH WITH ADC
SYSTEM AFTER ESTABLISHING
CONDITIONS











Rockwell International

Science Center

SC5441.FTR

**FERROELECTRIC TUNGSTEN BRONZE BSKNN CRYSTALS FOR
PHOTOREFRACTIVE APPLICATIONS**

Ferroelectric tungsten bronze BSKNN crystals for photorefractive applications

R.K. Neurgaonkar, W.K. Cory and J.K. Cliver

Rockwell International Science Center, Thousand Oaks, CA 91361

Abstract

Ce-doped tungsten bronze $\text{Ba}_{2-x}\text{Sr}_x\text{K}_{1-y}\text{Na}_y\text{Nb}_5\text{O}_{16}$ (BSKNN) ferroelectric crystals have been grown by the Czochralski technique, and are found to be of optical quality with excellent photorefractive properties. Although the BSKNN crystals studied have a tetragonal bronze structure at room temperature, their growth habits are different: BSKNN-1 grows in a square shape with four well-defined facets, while BSKNN-2 crystals have an octahedron shape with eight well-defined facets. Ferroelectric and optical measurements show these crystals to have strong longitudinal effects similar to perovskite BaTiO_3 and excellent self-pumped phase-conjugate behavior.

Introduction

Tetragonal tungsten bronze BSKNN is a ferroelectric material with properties similar to BaTiO_3 , but with a ferroelectric/paraelectric transition occurring at relatively high temperatures.¹ According to the recent work by Rodriguez et al.,² $\text{Ba}_{1.5}\text{Sr}_{1.5}\text{K}_{1.5}\text{Na}_{1.5}\text{Nb}_5\text{O}_{16}$ (BSKNN-2) crystals have an excellent potential for photorefractive and phase-conjugation applications because of the following features:

1. Exhibits large longitudinal effects, e.g., electro-optic coefficient r_{33} is $\sim 400 \times 10^{-12} \text{ m/V}$.
2. Exhibits large dielectric anisotropy with $\epsilon_{11} > \epsilon_{33}$, thus with a large photorefractive figure-of-merit $n^2 r_{33}^2 / \epsilon_{33}$.
3. Most BSKNN compositions melt nearly congruently and also at relatively lower temperatures ($< 1400^\circ\text{C}$) than other photorefractive crystals such as BaTiO_3 ($\sim 1630^\circ\text{C}$) and SBN ($> 1510^\circ\text{C}$).
4. Growth of large size ($\sim 1.5 \text{ cm}$ in diameter), optical-quality crystals has now been demonstrated.

We have grown a number of crystal compositions in the BSKNN system^{1,3} and have found that these crystals, particularly BSKNN-2, have excellent potential for electro-optic and photorefractive applications. This paper reports preliminary data on the growth of Ce-doped $\text{Ba}_{1.2}\text{Sr}_{1.8}\text{K}_{0.5}\text{Na}_{1.75}\text{Nb}_5\text{O}_{16}$ (BSKNN-1) and BSKNN-2 crystals and data on phase-conjugate effects.

Experimental

The tungsten bronze BSKNN-1 and BSKNN-2 compositions exist on the SrNb_2O_6 - BaNb_2O_6 - KNbO_3 - NaNbO_3 system, even though the end-member materials do not belong to the tungsten bronze structural family. The discussion of the tungsten bronze solid solution range and the types of bronze structures has been published elsewhere.¹ Tungsten bronze compositions are represented by the chemical formulae $(\text{A}_1)_4(\text{A}_2)_2\text{C}_4\text{B}_{10}\text{O}_{30}$ and $(\text{A}_1)_4(\text{A}_2)_2\text{B}_{10}\text{O}_{30}$, where A_1 , A_2 , C and B are the 15-, 12-, 9- and 6-fold coordinated lattice sites. Since the C sites are empty in the BSKNN solid solution, BSKNN is represented by the second chemical formula with all of the 15- and 12-fold coordinated sites completely filled. It is interesting to note that although the bronze $\text{Sr}_{1-x}\text{Ba}_x\text{Nb}_2\text{O}_6$ (SBN) solid-solution system is also represented by the latter formula, the 15- and 12-fold coordinated sites in this case are partially empty.

Single crystals of BSKNN were grown using ultra-pure BaCO_3 , SrCO_3 , K_2CO_3 , Na_2CO_3 , Nb_2O_5 and CeO_2 powders. The Czochralski crystal growth furnace used was rf induction-heated at 370 kHz, and the crystals were cooled through their paraelectric/ferroelectric phase transition in an after-heater furnace.

A variety of techniques were used to evaluate the ferroelectric, optical and photorefractive properties of these crystals. Crystals belonging to the tetragonal point group $4mm$ have three electro-optic (r_{33} , r_{51} and r_{13}), the piezoelectric (d_{33} , d_{15} and d_{13}) and two dielectric constants (ϵ_{33} and ϵ_{11}), thus requiring samples of different orientations. Bar and plate samples oriented along (001) and (100) were cut with a

diamond saw from the boules, and then were lapped and polished to an optical finish. Prior to most measurements, the crystals were poled by the field-cooling method under a dc field of 8-10 kV/cm along the polar axis (001).

Growth of Ce-doped BSKNN crystals

To use BSKNN crystals for photorefractive applications, specifically for image processing, optical computing and phase conjugation, it is important that the change in the photorefractive index, n , should be large and should occur rapidly. The change in n is given by

$$\Delta n = -\frac{1}{2} n^3 r_{ij} E_i$$

where r is the electro-optic coefficient and E is the space-charge field. Since the electro-optic coefficient is relatively constant for a given crystal composition, Δn can be enhanced by increasing the optically generated space-charge field. Currently, this is an active area of research in ferroelectric optical materials exhibiting large electro-optic effects, such as SBN, $x = 0.25$ and 0.40 , and perovskite BaTiO_3 .

In our laboratory, we have found that both the photorefractive speed and spectral response can be controlled using $\text{Ce}^{3+}/\text{Ce}^{4+}$ in various crystallographic sites in SBN:60 and SBN:75 crystals.⁴ These Ce-doped SBN crystals have shown excellent photorefractive properties with optical phase-conjugate behavior comparable or better than BaTiO_3 . For this reason, Ce-doped BSKNN-1 and BSKNN-2 crystals were grown by the Czochralski growth technique established for other tungsten bronze crystals such as SBN:60, SBN:75, SKN and PBN.^{7,8} Initially, undoped BSKNN crystals were used as seed material, and as small doped crystals become available, the latter were used as seeds in subsequent growths. Typical growth conditions are as follows:

1. Growth Temperature: 1480-1485°C
2. Pulling Rate: 6-10 mm/h
3. Growth Direction: (001)
4. Ce Concentration: 0.05 wt%

As encountered in the growth of SBN and other tungsten bronze crystals, the Czochralski growth of high-quality BSKNN crystals can be adversely affected by a number of factors, leading to bulk crystal fracture, composition nonuniformity and optical striations. Of these factors, the most significant are:

1. Impurities in the starting materials, particularly Fe^{3+} .
2. Rotation and pulling rates. In particular, the rotation rate has a strong influence on the dopant uniformity in the crystal.
3. Cooling rate variation. The Ba:Sr and K:Na distribution on the 15- and 12-fold coordinated sites change with the cooling rate, and can cause severe striation problems.

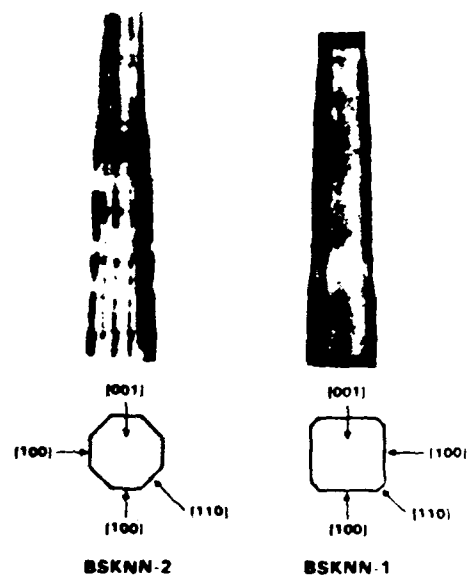
In addition, the very complexity of the BSKNN solid-solution system makes successful crystal growth a more difficult task in comparison with simpler systems such as SBN. Nevertheless, we have been able to grow optical-quality BSKNN-1 crystals up to 1.2 cm diameter and BSKNN-2 crystals up to 1.5 cm diameter using automatic diameter-controlled Czochralski crystal growth. Figure 1 shows typical BSKNN crystals grown along the (001) axis.

The small addition of Ce (0.05 wt%) did not significantly alter the growth conditions or the ferroelectric phase transition temperature for either BSKNN-1 or BSKNN-2. The doped crystals are pink in color and show differing natural growth habits: BSKNN-1 grows in a square shape with four well-defined facets, while BSKNN-2 has an octahedron growth habit with eight well-defined facets. These growth habits differ from other bronze crystals such as SBN:60 and SBN:75, which are cylindrical with 24 well-defined facets.^{7,8}

Characterization

The grown BSKNN crystals were characterized by various ferroelectric and optical techniques. Both BSKNN-1 and BSKNN-2 exhibit strong longitudinal effects, e.g., large ϵ_{11} , d_{15} and r_{31} , which differ from other tungsten bronze crystals such as SBN:60, SBN:75, etc., in which transverse effects such as ϵ_{33} and r_{33} , are stronger. A more

Figure 1 BSKNN crystals grown along (001) axis.



detailed description of comparative crystal properties is presented in another paper.² Table 1 summarizes the photorefractive properties of BSKNN crystals doped with Ce.

Table 1. Role of Ce^{3+} in Tungsten Bronze BSKNN Crystals

15- or 12-Fold Coordinated Sites	9-Fold Coordinated Sites
<ul style="list-style-type: none"> • Pink in color crystals with absorption at 0.48 μm • Fanning in green region • Response time ~ 100 ms • Coupling coefficient ~ 10 cm^{-1} • Sensitivity $\sim 10^{-3}$ J/cm^2 • Optical-quality crystals 	<ul style="list-style-type: none"> • Greenish-yellow in color crystals with absorption at 0.72 to 0.8 μm • Fanning in red region • Response time $\sim 5-6s^*$ • Coupling $> 0.9^*$ • Sensitivity $\sim 10^{-3}$ J/cm^2 • Optical-quality crystals

* Predicted values

Table 2 summarizes the optical figures-of-merit $n^3 r_{11}/\epsilon$ and r_{11}/ϵ for a number of tungsten bronze and perovskite crystals, including SBN and BSKNN. For photorefractive applications, the relevant figure-of-merit can be taken as $n^3 r_{11}/\epsilon$, which can be substantially larger in bronze crystals than in perovskites. In the case of BSKNN crystals exhibiting large longitudinal electro-optic effects similar to $BaTiO_3$, the figure-of-merit can be raised further by simply cooling below room temperature, since ϵ_{11} , and therefore r_{11} , increases below room temperature, whereas ϵ_{33} decreases, as shown in Fig. 2.

Fig. 2 Temperature dependence dielectric properties for BSKNN-crystal.

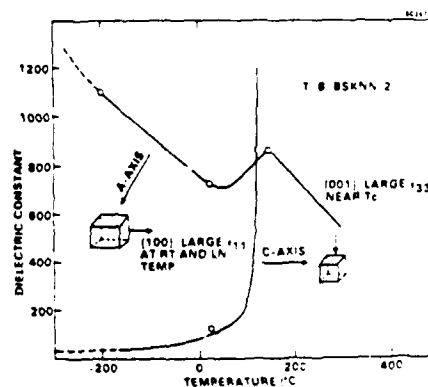


Table 1 compares the major properties of tungsten bronze BSKNN and perovskite BaTiO₃ crystals. Both crystals are excellent hosts for electro-optic and photorefractive applications. BaTiO₃ crystals are commercially available and, as a consequence, are being studied extensively for optical applications. However, BaTiO₃ is extremely difficult to grow in the large sizes possible for SBN and BSKNN solid-solution crystals. In the case of BSKNN, its additional advantages over BaTiO₃ are: 1) no twinning or poling problems due to the simple tetragonal-to-orthorhombic phase transition (4/mm to 4mm); and 2) cooling enhances the electro-optic figures-of-merit rather than destroying the ferroelectric state, because the tetragonal-orthorhombic phase transition, if any, lies at or below liquid nitrogen temperature.

Table 2. Electro-Optic Figure-of-Merit for Tungsten Bronze Crystals

Crystal	Dielectric Constant		Electro-Optic Coeff. 10^{-12} m/V		r_{13}/c	$n^3 r_{13}/c$
	ϵ_{11}	ϵ_{33}	r_{33}	r_{51}		
$\text{Sr}_{0.75}\text{Ba}_{0.25}\text{Nb}_2\text{O}_6$ (SBN:75)	450	3000	1400	42	0.467	5.60
$\text{Sr}_{0.6}\text{Ba}_{0.4}\text{Nb}_2\text{O}_6$ (SBN:60)	450	900	470	42	0.522	6.26
$\text{Sr}_{1-x}\text{Ca}_x\text{Nb}_2\text{O}_6$ (SCNN)	1700	1700	> 800	---	0.470	5.65
$\text{Pb}_{0.6}\text{Ba}_{0.4}\text{Nb}_2\text{O}_6$ (PBN:60)	1900	500	---	> 1600	0.840	10.10
BSKNN-1	360	120	150	> 200	0.550	6.67
BSKNN-2	700	170	170	350	0.500	6.00
BSKNN-3	780	270	---	~ 400	0.510	6.15
BaTiO ₃	4100	1500	80	1600	0.390	4.71
LiNbO ₃	950	201	67	380	0.400	4.20

Table 3. Comparison Between Leading Photorefractive Crystals

Tungsten Bronze BSKNN	Perovskite BaTiO ₃
<ul style="list-style-type: none"> • Large longitudinal r_{33}, d_{33}, c_{11} available • Excellent host for photorefractive and electro-optic applications • Large square and octahedron crystals (> 1.5 cm) with optical quality are available • Absence of twinning (4/mm → 4mm) • Absorption and response controlled in the desired spectral range using proper crystallographic site(s) for a given dopant • No tetragonal to orthorhombic transition observed down to 4K temperature • Open structure - structural flexibility to alter crystal composition 	<ul style="list-style-type: none"> • Large longitudinal r_{51}, d_{51}, c_{11} available • Excellent host for photorefractive and electro-optic applications • Pure BaTiO₃ crystals are difficult to grow • 90° twins are present (4/m → 4mm) • Controlled spectral response with dopants possible, but difficult • Tetragonal to orthorhombic transition occurs at 10°C • Close-packed structure: limited compositional flexibility

Codoped BSKNN-2 crystals, in particular, show excellent photorefractive properties with a response time of around 100 ns light intensities. We expect that the response

time could ultimately be better than for Ce-doped SBN:60, since BSKNN has a much smaller polar axis dielectric constant. Another interesting feature noted is that the spectral response region can be extended from the visible to the infrared by changing the site preference of the Ce ion. For example, when Ce is placed in the 15- or 12-fold coordinated sites, photorefractive absorption is observed in the visible, whereas the absorption is shifted out to the near-IR when Ce is located in the 9-fold coordinated sites. As also reported for BaTiO₃, the response of Ce-doped BSKNN-1 is presently slow in the IR region; however, there may be room for further improvement through the optimization of the shallow trap concentration and the dopant crystallographic site distribution in the tungsten bronze structure.

Tables 4 and 5 summarize the beam fanning and self-pumped phase-conjugate response times for BSKNN and other leading photorefractive materials as determined by Rodriguez et al.² Based on their investigations, Ce-doped BSKNN-1, SBN:60 and SBN:75 bronze crystals are presently comparable to BaTiO₃ in their performance. More experimental data on these crystals are being obtained at the U.S. Army Night Vision and Electro-Optics Laboratory, and will be published elsewhere.

Table 4. Beam-Fanning Response Time

Material	Response Time For 0.1 W/cm ² 1 W/cm ²		Wavelength (nm)	Point of Measurements
Ce-SBN:75	7.1	0.6	441	90%
Ce-SBN:75	2.0	0.3	441	67%
Ce-SBN:60	0.6	0.0	441	67%
BaTiO ₃	4.5	0.6	485	90%
Ce-BSKNN*	5.1	0.6	487.4	67%

* Nonfluorine doped crystals

Table 5. Self-Pumped Phase-Conjugate Response Time

Material	Response Time For 0.1 W/cm ² 1 W/cm ²		Wavelength (nm)	Point of Measurements
Ce-SBN:75	4.1	8.3	441	90%
Ce-SBN:75	7.7	1.6	441	67%
BaTiO ₃	25	2.5	514.5	90%
Ce-BSKNN	27.4	8.8	487.4	67%

Conclusions

The prospect for the further development of optical-quality BSKNN solid-solution crystals to larger sizes (up to 2 cm in diameter) are bright, and efforts toward that direction are in progress. It is expected that with further refinement of dopant concentrations and site preference distributions in the tungsten bronze structure, it should be possible to optimize the photorefractive response time, and additionally control the spectral response in the visible or IR regions. Since BSKNN crystals resemble BaTiO₃ in many respects, a number of potential optical device applications can be anticipated for this interesting bronze material.

Acknowledgements

This work was supported by DARPA under Contract No. N00014-C-82-2466, and the U.S. Army under Contract No. DAAK20-83-C-0016. The authors are grateful for the discussions on this work with L.E. Cross, P. Yeh, M. Khoshnevisan and E. Sharp.

References

1. Neurgaonkar, R.R., Cory, W.K., Oliver, J.R., Clark III, W.W., Miller, M.J., Wood, G.L. and Sharp, E.J., submitted to Mat. Res. Bull.
2. Rodriguez, J., Siamakoun, A., Salamo, G., Miller, M.J., Clark III, W.W., Wood, E.J. Sharp and Neurgaonkar, R.R., accepted for publication in Appl. Phys. Lett.,
3. Neurgaonkar, R.R., Cory, W.K. and Oliver, J.R., Ferroelectrics, Vol. 35, p. 301. 1983.
4. Jarieson, P.B., Abrahams, S.C., and Bernstein, J.L., J. Chem. Phys., Vol. 48, p. 1048. 1968; Vol. 50, p. 4352. 1969.
5. Neurgaonkar, R.R. and Cory, W.K., Opt. Soc. Am., Vol. B/3, p. 274. 1986.
6. Neurgaonkar, R.R., Ho, W.W., Cory, W.K., Hall, W.F. and Cross, L.E., Ferroelectrics, Vol. 51, p. 185. 1984.
7. Neurgaonkar, R.R., Kalisher, M.H., Lim, T.C., Staples, E.J. and Keester, K.L., Mat. Res. Bull., Vol. 15, p. 1305. 1980.
8. Dudnik, O.F., Gromov, A.F., Kravchenko, V.B., Kipylov, Y.L. and Kuznetsov, G.F. Sov. Phys. Crystal., Vol. 15 (2), p. 330. 1980.
9. Neurgaonkar, R.R., Cory, W.K., Ho, W.W., Hall, W.F. and Cross, L.E., Ferroelectrics, Vol. 38, p. 857. 1981.



Rockwell International
Science Center

SC5441.FTR

Cr^{3+} -DOPED SGN:60 SINGLE CRYSTALS FOR PHOTOREFRACTIVE APPLICATIONS

**Cr^{3+} - $\text{Sr}_{0.6}\text{Ba}_{0.4}\text{Nb}_2\text{O}_6$ SINGLE CRYSTALS FOR
PHOTOREFRACTIVE APPLICATIONS**

R.R. Neurgaonkar, W.K. Cory and J.R. Oliver
Rockwell International Science Center
1049 Camino Dos Rios
Thousand Oaks, CA 91360

and

E.J. Sharp, M.J. Miller, W.W. Clark, III, G.L. Wood and G.J. Salamo
Center for Night Vision and Electro-Optics
Fort Belvoir, VA 22060-5677

(Received November 10, 1988; Communicated by W.B. White)

ABSTRACT: Optical quality Cr^{3+} -doped $\text{Sr}_{0.6}\text{Ba}_{0.4}\text{Nb}_2\text{O}_6$ (SBN:60) single crystals have been grown by the Czochralski technique with boules as large as 2 cm in diameter and 5 cm long being grown. The doping of 0.01 wt% Cr^{3+} on the 6-fold coordinated Nb^{5+} site increases the dielectric constant approximately 15% and reduces the phase transition temperature from 75° to 72°C. Photorefractive faning measurements show a response time of 0.9 s at 40 mW/cm², a value nearly three times faster than found in Ce^{3+} -doped SBN:60 crystals.

MATERIALS INDEX: tungsten bronze ferroelectrics, strontium barium niobate, chromium doping

INTRODUCTION

The photorefractive properties of ferroelectric single crystals such as BaTiO_3 and tungsten bronze SBN:60 are of great interest because of their potential for applica-

tions in optical computing, image processing, phase conjugation and laser hardening. Recent studies indicate that Ce^{3+} -doped SBN:60 has a photorefractive gain and time of response comparable to BaTiO_3 (1-8). In our recent work, we have measured gains as high as 45 cm^{-1} and response times as fast as 10-40 ms, depending upon the laser intensity, for Ce^{3+} -doped SBN:60 single crystals. Further improvements, specifically in the speed of response, are still desirable in most applications, and for this reason we have recently undertaken the study of other dopants such as $\text{Fe}^{2+}/\text{Fe}^{3+}$, Cr^{3+} and $\text{Cr}^{3+} + \text{Ce}^{3+}$ in SBN:60. This paper reports the growth of Cr^{3+} -doped SBN:60 single crystals and their major ferroelectric and photorefractive properties:

EXPERIMENTAL

The selected $\text{Sr}_{0.6}\text{Ba}_{0.4}\text{Nb}_2\text{O}_6$ (SBN:60) composition exists on the SrNb_2O_6 - BaNb_2O_6 system in which a complete solid solution has been reported between these two end members (10). However, the ferroelectric tungsten bronze (4mm) solid solution, $\text{Sr}_{1-x}\text{Ba}_x\text{Nb}_2\text{O}_6$, occurs for $0.25 \leq x \leq 0.75$, with SBN:60 being the congruent melting composition (11). For this reason, we selected this composition for this work, with crystals being grown using ultrapure BaCO_3 , SrCO_3 , Nb_2O_5 and Cr_2O_3 starting materials. These materials were batched in the appropriate ratios and thoroughly mixed before sintering at 1350°C . The sintered powders were then melted in a platinum crucible (2 in. in both diameter and height) supported by a fibrous alumina insulating jacket. The Czochralski furnace was rf induction-heated at 370 KHz, and utilized automatic crystal diameter control. All crystals were cooled through their paraelectric/ferroelectric phase transition in an after-heater furnace. Further information on SBN crystal growths can be found in earlier papers (1,2,12-14).

A variety of techniques were used to evaluate the ferroelectric and optical properties of these crystals. Prior to measurement, the crystals were poled by a field-cooling method (T_c to room temperature) under a dc field of 5-10 kV/cm along the polar (001) axis using either Au or Pt electrodes. The completeness of poling was checked by measuring the dielectric constant before and after poling.

RESULTS AND DISCUSSION

SBN:60 single crystals were doped with chromium at concentrations of 0.011 and 0.016 wt%. For these additions, we did not notice any major changes in the growth conditions adopted for undoped SBN:60 single crystals (12,13). The growth of Cr^{3+} -doped crystals proceeded without undue difficulties under the following conditions:

- | | |
|---------------------------|----------------------|
| 1. Melting Temperature: | 1485°C |
| 2. Pulling Direction: | (001) axis |
| 3. Crystal Rotation Rate: | 10-25 rpm |
| 4. Crystal Pulling Rate: | 6-10 mm/h |
| 5. Growth Atmosphere: | Oxygen |

Initially, undoped SBN:60 crystal seeds of optical quality were used for these growths. As Cr^{3+} -doped crystal seeds became available, they were used in subsequent experiments to maintain a uniform Cr^{3+} concentration in both the crystals and the melt. As shown in Fig. 1, crystals as large as 2 cm diameter and 5 cm long have now



FIG. 1 Cr^{3+} -doped $\text{Sr}_{0.6}\text{Ba}_{0.4}\text{Nb}_2\text{O}_6$ (SBN:60) crystal.

been grown along the (001) direction. Growths along other orientations, e.g., (100) and (110), were also attempted, but these did not yield crystals of sufficient size or quality. For this reason, all succeeding growths were performed only along the (001) direction (3,4).

Cr^{3+} -doped SBN:60 single crystal boules show a yellowish-green color with 24 well-defined facets, a unique feature of these solid solution crystals (1,2,15). The color becomes more greenish as the Cr^{3+} concentration is increased. SBN solid solution crystals are represented by the chemical formula $(\text{A}_1)_4(\text{A}_2)_2\text{B}_{10}\text{O}_{30}$, where A_1 , A_2 and B are in 15-, 12- and 6-fold coordinated lattice sites, respectively. Cr^{3+} occupies the 6-fold coordinated Nb^{5+} site. Based on work on ceramic samples, we have found that Cr solid solubility is surprisingly high (15 mole% or more) even though the charge difference between Nb^{5+} and Cr^{3+} is not balanced.

The quality of these Cr-doped crystals is generally excellent for photorefractive applications. Prior to this work, we also investigated the growth of SBN:60 single crystals doped with Fe^{3+} , with crystals as large as 2 cm diameter being grown without any problems (1,2). The $\text{Fe}^{2+}/\text{Fe}^{3+}$ ions are known to be active photorefractive species in other ferroelectric hosts such as BaTiO_3 , KNbO_3 , LiNbO_3 and $\text{Ba}_2\text{NaNb}_5\text{O}_{15}$ (16-19); however, the addition of Fe^{3+} in SBN:60 resulted in degraded optical quality due to severe striations. Since both Cr^{3+} and Fe^{3+} have similar ionic size, valence states and site occupancy in the tungsten bronze structure, one would expect to achieve similar results in crystal optical quality for these two dopants. Efforts are underway to distinguish the differences arising from these ions, so that the origin of striations in Fe-doped crystals can be better understood.

Cr^{3+} -doped SBN:60 single crystals possess ferroelectric properties similar to undoped crystals, but with slightly lower phase transition (Curie) temperature. A reduction in T_c of approximately 3°C has been observed for a 0.011 wt% addition of Cr^{3+} . A similar trend has also been observed for Fe^{3+} , Ti^{4+} and $(\text{Ti}^{4+} + \text{W}^{6+})$ -doped SBN:60 compositions. All of these dopants prefer the 6-fold coordinated Nb^{5+} site in the bronze structure. However, their effects on photorefractive properties depend upon

the electronic structure of each dopant. Since the addition of ($\text{Ti}^{4+} + \text{W}^{6+}$) in orthorhombic tungsten bronze PbNb_2O_6 raises T_C and increases the piezoelectric coefficients, we had expected that T_C would rise for Ti^{4+} -doped SBN:60, something which was not observed. A more detailed investigation on this dopant is in progress and will be discussed in a future publications.

The room temperature c-axis dielectric constant of Cr-doped SBN:60 is around 1100. This is 10-15% higher than in undoped SBN:60 crystals and is due to a slight drop in T_C and a somewhat shallower slope of the dielectric constant below T_C . In contrast, the a-axis dielectric constant of 485 is virtually unchanged from that found in undoped SBN:60. The spontaneous polarization, P_S , was determined using P vs E hysteresis loop measurements and integrated pyroelectric current measurements as a function of temperature. Both methods yielded a value of $P_S = 29 \pm 0.5$ coul/cm² at 20°C, comparable to that found in undoped crystals. The static coercive (switching) field is 2.1 kV/cm; this value can be expected to increase at nonzero frequencies due to the long time constant for domain reversal (approximately 1 min) at this applied field.

The room-temperature dielectric losses in poled Cr^{3+} -doped SBN:60 crystals are $\tan \delta \leq 0.01$ from 100 Hz - 100 KHz, with vanishingly low dc conductivities of $10^{-14} \Omega^{-1}\text{-cm}^{-1}$ or less. At high temperatures ($\geq 350^\circ\text{C}$), the dc conductivity has a thermal activation energy of approximately 1.6 eV, indicating that the equilibrium Fermi level is pinned near mid-gap as in the case of undoped SBN:60. The similarity in the dc conductivities of undoped and Cr^{3+} -doped SBN:60 suggests that electron donor levels introduced by doping are closely compensated by additional acceptor levels, so that the overall donor/acceptor ratio, N_D/N_A , remains essentially unchanged.

We have carried out preliminary experiments on the photorefractive behavior of an optically polished Cr^{3+} -doped SBN:60 crystal. The transmission spectrum of this crystal, along with that of Ce^{3+} -doped SBN:60 crystals, is given in Fig. 2. As can be seen from the transmission spectra, Cr^{3+} -doped SBN:60 has an increased red response compared to either the undoped or Ce^{3+} -doped crystals. Based on this difference in spectral behavior, Cr^{3+} -doped SBN:60 thus has potential for use as a photorefractive material at laser diode wavelengths. In general, the photorefractive response of these materials shifts toward the near infrared as the coordination site of the dopant is lowered from the 12-fold site. For example, the spectrum of the Ce^{3+} -doped sample in Fig. 2 is typically observed when Ce^{3+} occupies the 12-fold coordinated site. When Ce^{3+} is placed in the 9-fold coordinated site, the spectral response extends to longer wavelengths (3,20), as in the case here for 6-fold coordinated Cr^{3+} .

We have measured the e^{-1} response time for beam fanning (21) using a HeCd laser operating at 440 nm with a beam diameter of 1.4 mm. These results are given in Table I along with a summary of the ferroelectric properties for undoped, Ce^{3+} -doped, and Cr^{3+} -doped SBN:60. For similar dopant concentrations, the Cr^{3+} -doped SBN:60 crystal was substantially faster than either the undoped or the Ce^{3+} -doped crystals. In addition, the Cr^{3+} -doped crystal was also found to be faster than a BaTiO_3 crystal measured under the same experimental conditions. However, neither the dopant species nor concentration was known for the BaTiO_3 sample, although it displayed a behavior typical to reports in the literature.

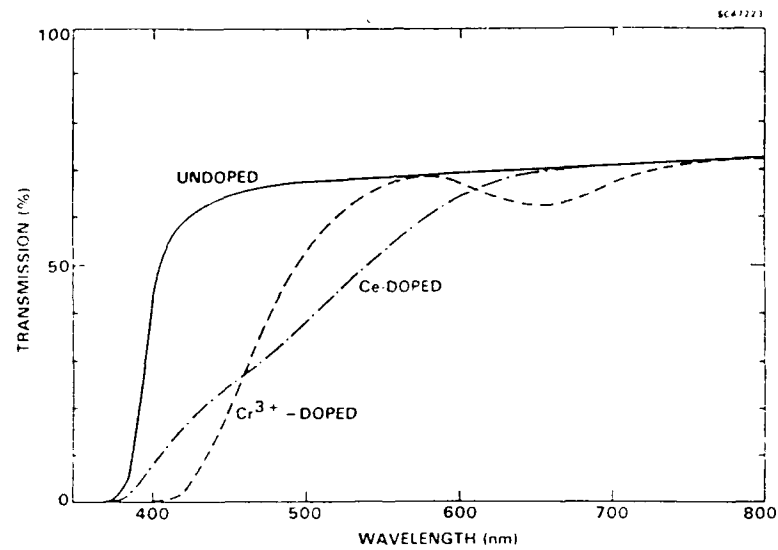


FIG. 2 Transmission spectra for undoped and doped SBN:60 crystals.

TABLE I
Ferroelectric and Optical Properties of SBN:60 Crystals

Property	Undoped SBN:60	Ce ³⁺ -Doped (0.013 wt%)	Cr ³⁺ -Doped (0.011 wt%)
Crystal Size (Diameter)	3 cm	2.5 cm	2 cm
Crystal Color	Pale Cream	Pink	Yellowish-Green
Crystal Quality	Optical	Optical	Optical
Dielectric Constant:	$\epsilon_{33} = 920$ $\epsilon_{11} = 485$	$\epsilon_{33} = 950$ $\epsilon_{11} = 485$	$\epsilon_{33} = 1100$ $\epsilon_{11} = 485$
Phase Transition Temp.	75°C	74°C	72°C
Electro-Optic Coeff., $r_{33} (\times 10^{-12} \text{ m/V})$	465	470	560*
Polarization ($\mu\text{Coul/cm}^2$)	28.5	28	29
Beam Fanning Response:			
At 40 mW/cm ²	----	2.5 s	0.90 s
At 0.2 W/cm ²	----	0.6 s	0.30 s
At 2.0 W/cm ²	----	0.05 s	0.018 s
Spectral Response (μm)	0.35 to 0.6	0.4 to 0.6	0.4 to 0.8**

* Estimated value using $r_{33} = 2g_{33}P_3/\epsilon_{33}\epsilon_0$, $g = 0.10 \text{ m}^2/\text{C}^2$.

** Based on absorption spectra.

CONCLUSIONS

Our initial studies indicate that Cr^{3+} -doped SBN:60 has the potential to be a new photorefractive material that is competitive with, or superior to, both Ce^{3+} -doped SBN:60 and BaTiO_3 . Further experiments are needed, however, to determine the photorefractive coupling coefficient and the crystal behavior as a self-pumped phase conjugator (22).

ACKNOWLEDGEMENT

This research work was supported by DARPA (Contract Nos. N00014-82-C-2466 and DAAB07-88-C-243). The authors are grateful to Professor L.E. Cross and Dr. W.F. Hall for their discussions on this work.

REFERENCES

1. Neurgaonkar, R.R., and Cory, W.K., J. Opt. Soc. Am. 3(B), 276 (1986).
2. Neurgaonkar, R.R., Cory, W.K., Oliver, J.R., Ewbank, M.D., and Hall, W.F., J. Opt. Eng. 26(5), 392 (1987).
3. Ewbank, M.D., Neurgaonkar, R.R., Cory, W.K., and Feinberg, J., J. Appl. Phys. 62(2), 374 (1987).
4. Rakuljic, G.A., Yariv, A., and Neurgaonkar, R.R., J. Opt. Eng. 25, 1212 (1986).
5. Rakuljic, G.A., Sayano, K., Yariv, A., and Neurgaonkar, R.R., Appl. Phys. Lett. 50(1), 10 (1987).
6. Wood, G.L., Clark, III, W.W., Miller, M.J., Sharp, E.J., Salamo, G.J., and Neurgaonkar, R.R., IEEE J. Quant. Electron. QE-23, 2126 (1987).
7. Miller, M.J., Sharp, E.J., Wood, G.L., Clark, III, W.W., Salamo, G.J., and Neurgaonkar, R.R., Opt. Lett. 12, 349 (1987).
8. Megumi, K., Kozuka, H., Kobayashi, M. and Furuhashi, Y., Appl. Phys. Lett. 30, 631 (1977).
9. Ewbank, M.D., and Neurgaonkar, R.R., private communication.
10. Ballman, A.A., and Brown, H., J. Cryst. Growth 1, 311 (1967).
11. Megumi, K., Nagatsuma, N., Kashiwada, K., and Furuhashi, Y., Mater. Sci. 11, 1583 (1976).
12. Neurgaonkar, R.R., Cory, W.K., and Oliver, J.R., Ferroelectrics 15, 3 (1983).
13. Neurgaonkar, R.R., Kalisher, M.H., Lim, T.C., Staples, E.J., and Keester, K.L., Mat. Res. Bull. 15, 1305 (1980).
14. Neurgaonkar, R.R., Cory, W.K., Oliver, J.R., Miller, M.J., Clark, III, W.W., Wood, G.L. and Sharp, E.J., J. Cryst. Growth 84, 629 (1987).
15. Dudnik, O.F., Gromov, A.K., Kravchenko, V.B., Kopylov, Yu. L., and Kunzetsov, G.F., Soviet Phys. Crystallgr. 15, 330 (1980).
16. Gunter, P., Fluckiger, U., Huignard, J.P., and Micheron, F., Ferroelectrics 13, 297 (1976).
17. Gunter, P.N., Opt. Lett. 7, 10 (1982); Phys. Rev. 93, 199 (1982).
18. Amodei, J.J., Staebler, D.L., and Stephens, A.W., Appl. Phys. Lett. 18, 507 (1971).
19. Ashykin, A., Tell, B., and Dziedzic, J. IEEE J. Quant. Electron. QE-3, 400 (1967).
20. Montgomery, S.R., Yarrison-Rice, J., Pederson, D.O., Salamo, G.J., Miller, M.J., Clark, III, W.W., Wood, G.L., Sharp, E.J., and Neurgaonkar, R.R., to appear in J. Opt. Soc. Am. B.
21. Feinberg, J., Opt. Lett. 7, 486 (1982).
22. Feinberg, J., J. Opt. Soc. Am. 72, 46 (1981).



Rockwell International
Science Center

SC5441.FTR

SELF-STARTING PASSIVE PHASE CONJUGATE MIRROR WITH Ce-DOPED SBN:60

Self-starting passive phase conjugate mirror with Ce-doped strontium barium niobate

George A. Rakuljic, Koichi Sayano, and Amnon Yariv
California Institute of Technology, Pasadena, California 91125

Ratnakar R. Neurgaonkar
Rockwell International, Thousand Oaks, California 91360

(Received 15 September 1986; accepted for publication 4 November 1986)

We report the use of Ce-doped $\text{Sr}_x\text{Ba}_{1-x}\text{Nb}_2\text{O}_6$, $x = 0.60$ and 0.75 , as the holographic four-wave mixing medium in the construction of a self-starting passive phase conjugate mirror using internal reflection. Without correcting for Fresnel reflections, a steady-state phase conjugate reflectivity of 25% was measured with $\text{Sr}_{0.75}\text{Ba}_{0.25}\text{Nb}_2\text{O}_6\text{:Ce}$. The distortion correcting property of such a mirror was demonstrated using an imaging experiment.

Two-beam coupling in photorefractive crystals has been used to demonstrate passive phase conjugate mirrors (PPCM's) which do not require external pump beams.¹⁻³ A more recent version of such a device⁴⁻⁶ introduces an important simplification by using total internal reflection in the photorefractive crystal instead of external mirrors. Such a mirror, however, requires a higher coupling threshold than that of the earlier devices. In this letter we report on the construction of this phase conjugate mirror using cerium-doped strontium barium niobate photorefractive crystals as the holographic four-wave mixing media.

Strontium barium niobate (SBN) belongs to a class of tungsten bronze ferroelectrics that are pulled from a solid solution of alkaline earth niobates. The crystal is transparent and can be grown with a variety of ferroelectric and electro-optic properties depending on the specific cation ratios introduced into the structure. In SBN the unit cell contains ten NbO_6 octahedra with only five alkaline earth cations to fill ten interstitial sites.⁷ The structure is thus incompletely filled, which permits the addition of a wide range of dopants into the host crystal. The general formula for SBN is $\text{Sr}_x\text{Ba}_{1-x}\text{Nb}_2\text{O}_6$, so SBN:60 and SBN:75 represent $\text{Sr}_{0.60}\text{Ba}_{0.40}\text{Nb}_2\text{O}_6$ and $\text{Sr}_{0.75}\text{Ba}_{0.25}\text{Nb}_2\text{O}_6$, respectively.

The point group symmetry of SBN is 4 mm, which implies that its electro-optic tensor is nonzero. The dominant electro-optic coefficient is r_{33} , which at room temperature ranges from 100 pm/V in SBN:25 to 1400 pm/V in SBN:75. In order to realize the large values of electro-optic coefficients in SBN crystals, they must, in practice, be poled by first heating them above their Curie points and then allowing

them to cool to room temperature with an applied dc electric field of 5–8 kV/cm.

Single crystals of cerium-doped SBN:60 and SBN:75 were grown along the [001] direction by the Czochralski technique. The resulting samples are high optical quality, striation-free cubes 0.5 cm on a side. Cerium doping was chosen since it dramatically enhances the photorefractive properties of SBN.⁸⁻¹⁰ In fact, the resultant crystals have been shown to be just as photorefractive as BaTiO_3 .⁹

The experimental setup for studying phase conjugation with SBN is shown in Fig. 1. Initially the lenses and transparency were removed so that the response of the phase conjugate mirror could be studied with a simple Gaussian beam. The reflectivity of two mirrors, one with Ce-doped SBN:60 and the other with Ce-doped SBN:75, is given in Fig. 2 as a function of time. Not only does the data of Fig. 2 show that phase conjugation using internal reflection is possible with SBN, but also that the steady-state phase conjugate reflectivity measured with Ce-doped SBN:75 is comparable to the 30% reflectivity obtained with BaTiO_3 .⁴ A photograph of the SBN:75 phase conjugate mirror in operation is shown in Fig. 3.

The imaging characteristics of the SBN phase conjugator were also determined with the arrangement shown in Fig. 1, but now with the transparency and lenses in place. The transparency, an Air Force resolution chart, was illuminated by the argon ion laser and focused onto the crystal by the lenses. The phase conjugate reflection was picked off by the beamsplitter and projected onto the screen. Figures 4(a) and 4(b) show the resolution chart and the phase conjugate

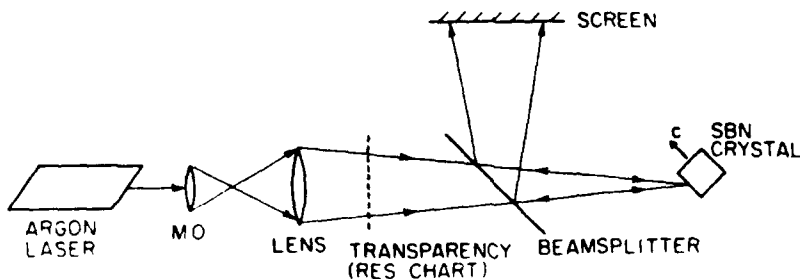


FIG. 1. Experimental setup for studying phase conjugation with SBN.

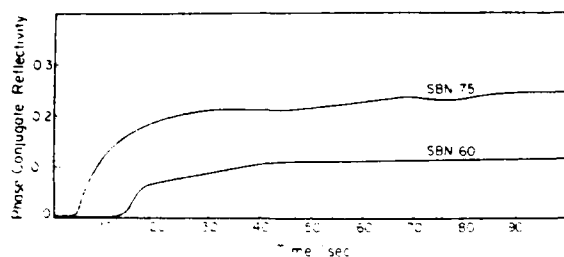


FIG. 2. Phase conjugate reflectivities of the SBN phase conjugators as a function of time. Pump beam power density was approximately 1.5 W/cm^2 .

image of the chart. Next, a phase distortion was placed between the transparency and the crystal, which, as shown in Fig. 4(c), rendered the chart indiscernible, and the phase conjugate image was once again viewed as it was projected onto the screen. Since the phase conjugate wave front at the crystal surface is that of the resolution chart after passing through the distortion, but with time reversal, the beam emerging from the distortion is the original undistorted image of the chart. This distortion correcting property of the SBN phase conjugator is shown in Fig. 4(d).

In summary, we have shown that the self-starting passive phase conjugate mirror using internal reflection can be

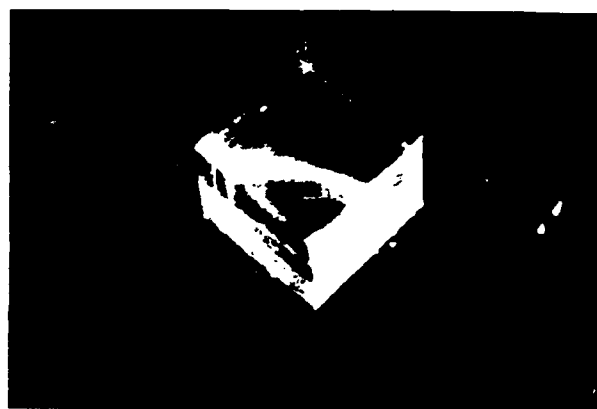
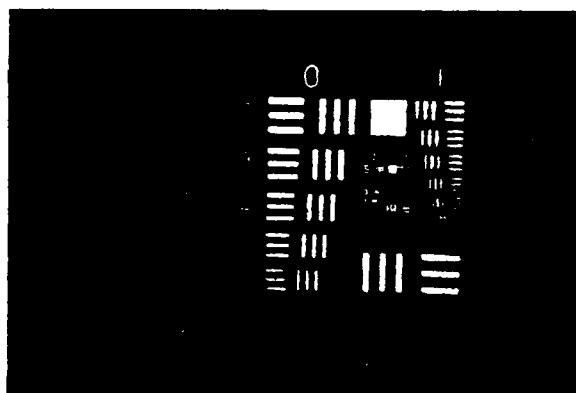


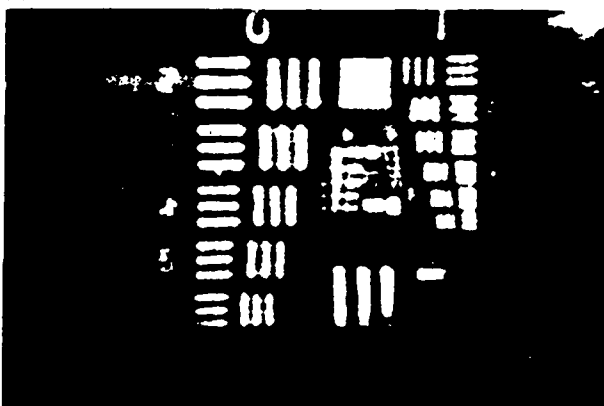
FIG. 3. Photograph of the SBN:75 phase conjugate mirror in operation.

constructed with cerium-doped strontium barium niobate. Phase conjugate reflectivities of 25 and 12%, not corrected for Fresnel reflections, were measured with Ce-doped SBN:75 and SBN:60, respectively. The imaging and distortion correcting properties of the SBN phase conjugator were also demonstrated.

This research was supported by Rockwell International Corporation, the U. S. Air Force Office of Scientific Research, and the U. S. Army Research Office.



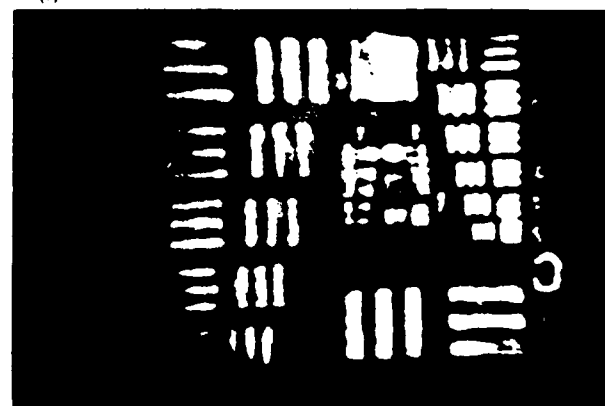
(a)



(b)



(c)



(d)

FIG. 4. (a) Air Force resolution chart. (b) Phase conjugate image of the resolution chart. (c) Image of the resolution chart with distortion. (d) Phase conjugate image of the resolution chart with distortion.

- ¹J. O. White, M. Cronin-Golomb, B. Fischer, and A. Yariv, Appl. Phys. Lett. **40**, 450 (1982).
- ²M. Cronin-Golomb, B. Fischer, J. O. White, and A. Yariv, Appl. Phys. Lett. **41**, 689 (1982).
- ³M. Cronin-Golomb, B. Fischer, J. O. White, and A. Yariv, Appl. Phys. Lett. **42**, 919 (1983).
- ⁴J. Feinberg, Opt. Lett. **7**, 486 (1982).
- ⁵K. R. MacDonald and J. Feinberg, J. Opt. Soc. Am. **73**, 548 (1983).
- ⁶J. Feinberg, Opt. Lett. **8**, 480 (1983).
- ⁷P. B. Jamieson, S. C. Abrahams, and J. L. Bernstein, J. Chem. Phys. **48**, 5048 (1968).
- ⁸K. Megumi, H. Kozuka, M. Kobayashi, and Y. Furuhashi, Appl. Phys. Lett. **30**, 631 (1977).
- ⁹G. A. Rakuljic, A. Yariv, and R. R. Neurgaonkar, Proc. SPIE **613**, 110 (1986).
- ¹⁰G. A. Rakuljic, A. Yariv, and R. Neurgaonkar, Opt. Eng. **25**, 1212 (1986).



Rockwell International
Science Center

SC5441.FTR

PHOTOREFRACTIVE PROPERTIES OF UNDOPED AND Ce-DOPED, AND Fe-DOPED
SBN:60 SINGLE CRYSTALS

Photorefractive properties of undoped, cerium-doped, and iron-doped single-crystal $\text{Sr}_{0.6}\text{Ba}_{0.4}\text{Nb}_2\text{O}_6$

George A. Rakuljic

Amnon Yariv

California Institute of Technology
Department of Applied Physics
Pasadena, California 91125

Ratnakar Neurgaonkar

Rockwell International Corporation
Science Center
Thousand Oaks, California 91360

Abstract. We present the results of our theoretical and experimental studies of the photorefractive effect in single-crystal SBN:60, SBN:Ce, and SBN:Fe. The two-beam coupling coefficients, response times, and absorption coefficients of these materials are given.

Subject terms: photorefractive materials; nonlinear optical materials; optical phase conjugation; image processing; optical signal processing.

Optical Engineering 25(11), 1212-1216 (November 1986)

CONTENTS

1. Introduction
2. Material properties
3. Photorefractive properties
4. Summary of results
5. Conclusion
6. Acknowledgments
7. References

1. INTRODUCTION

A given photorefractive material is considered useful for optical processing applications such as phase conjugate optics if it possesses three important features: low response time, large coupling coefficient, and high optical quality. Speed is necessary if the crystal is to be used in real-time applications, and a large photorefractive coupling coefficient is required for the construction of efficient devices. Regardless of its speed and gain, however, a crystal with poor optical quality is of little practical importance. Although a material is yet to be found that completely satisfies all three requirements, here we show how well SBN:60 approximates them.

2. MATERIAL PROPERTIES

Strontium barium niobate (SBN) belongs to a class of tungsten bronze ferroelectrics that are pulled from a solid solution of alkaline earth niobates. The crystal is transparent and can be grown with a variety of ferroelectric and electro-optic properties, depending on the specific cation ratios introduced into the structure. In SBN the unit cell contains 10 NbO_6 octahedra, with only five alkaline earth cations to fill 10 interstitial sites.¹⁻³ The structure is thus incompletely filled, which permits the addition of a wide range of dopants into the host crystal. The general formula for SBN is $\text{Sr}_x\text{Ba}_{1-x}\text{Nb}_2\text{O}_6$, so SBN:60 represents $\text{Sr}_{0.6}\text{Ba}_{0.4}\text{Nb}_2\text{O}_6$.

The point group symmetry of SBN is 4 mm, which implies that its electro-optic tensor is nonzero. The dominant electro-optic coefficient is r_{33} , which ranges from 100 pm/V in SBN:25 to 1400 pm/V in SBN:75. In order to realize the large values of electro-optic coefficients in SBN crystals, they must, in practice, be poled by first being heated to above their Curie points and then being cooled to room temperature with an applied dc electric field of 5 to 8 kV/cm.

3. PHOTOREFRACTIVE PROPERTIES

Single crystals of SBN:60, SBN:Ce ($\text{Sr}_{0.6}\text{Ba}_{0.4}\text{Nb}_2\text{O}_6:\text{Ce}$), and SBN:Fe ($\text{Sr}_{0.6}\text{Ba}_{0.4}\text{Nb}_2\text{O}_6:\text{Fe}$) grown at Rockwell International Corporation were studied using the two-wave mixing experiment shown in Fig. 1 to determine their effectiveness as photorefractive media. In Fig. 1 beams 1 and 2 are plane waves that intersect in the crystal and thus form an intensity interference pattern. Charge is excited by this periodic intensity distribution into the conduction band, where it migrates under the influence of diffusion and drift in the internal electric field and then preferentially recombines with traps in regions of low irradiance. A periodic space charge is thus created that modulates the refractive index by means of the electro-optic effect. This index grating, being out of phase with the intensity distribution, introduces an asymmetry that allows one beam to be amplified by constructive interference with light scattered by the grating while the other beam is attenuated by destructive interference with diffracted light. This process is shown graphically in Fig. 2. Although it is implicitly assumed here that the only photocarriers in SBN:60 are electrons, it is acknowledged that holes may also participate in the photorefractive effect. Experiments are currently under way to resolve this issue.

Mathematically, this two-beam coupling may be described in the steady state as follows:

$$\frac{dI_1}{d\xi} = -\Gamma \frac{I_1 I_2}{I_1 + I_2} - \alpha I_1 \quad (1)$$

$$\frac{dI_2}{d\xi} = \Gamma \frac{I_1 I_2}{I_1 + I_2} - \alpha I_2 \quad (2)$$

Paper 2182 received Aug. 13, 1985; revised manuscript received July 16, 1986; accepted for publication July 18, 1986; received by Managing Editor July 29, 1986. This paper is a revision of Paper 567-04 which was presented at the SPIE conference on Advances in Materials for Active Optics, Aug. 22-23, 1985, San Diego, Calif. The paper presented there appears (unrefereed) in SPIE Proceedings Vol. 567.

© 1986 Society of Photo-Optical Instrumentation Engineers.

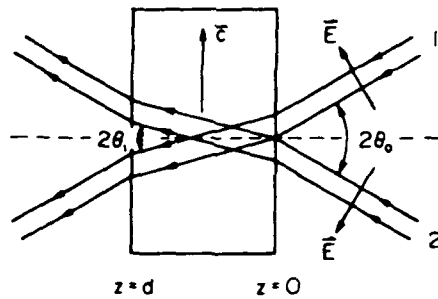


Fig. 1. Experimental setup for two-beam coupling experiments.

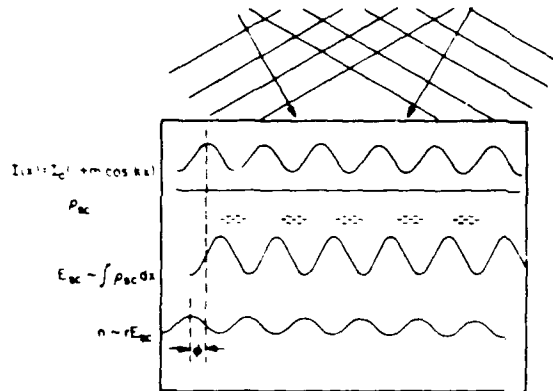


Fig. 2. The photorefractive mechanism. Two laser beams intersect, forming an interference pattern. Charge is excited where the intensity is large and migrates to regions of low intensity. The electric field associated with the resultant space charge operates through the electro-optic coefficients to produce a refractive index grating.

where I_1 and I_2 are the intensities of beams 1 and 2 inside the crystal, respectively. Γ is the two-beam coupling coefficient, α is the absorption coefficient, and $\xi = z \cos \theta$, where $0 \leq \xi \leq l = d \cos \theta$. The transient behavior is approximated by

$$I_i(\xi, t) = (1 - e^{-t/\tau})I_i(\xi, t \rightarrow \infty) + e^{-t/\tau}I_i(\xi, t = 0), \quad (3)$$

where τ is a characteristic time constant and

$$I_i(\xi, t \rightarrow \infty) = I_i(\xi). \quad (4)$$

The solutions of the above coupled-wave equations are

$$I_1(t) = \frac{[I_1(0) + I_2(0)]e^{-\alpha t}}{1 + \frac{I_2(0)}{I_1(0)} e^{\Gamma t}}, \quad (5)$$

$$I_2(t) = \frac{[I_1(0) + I_2(0)]e^{-\alpha t}}{1 + \frac{I_1(0)}{I_2(0)} e^{-\Gamma t}}. \quad (6)$$

By measurement of the four intensities $I_1(0)$, $I_2(0)$, $I_1(t)$, and $I_2(t)$, both in the steady state and as a function of time, the two-beam coupling coefficient Γ and the response time τ can

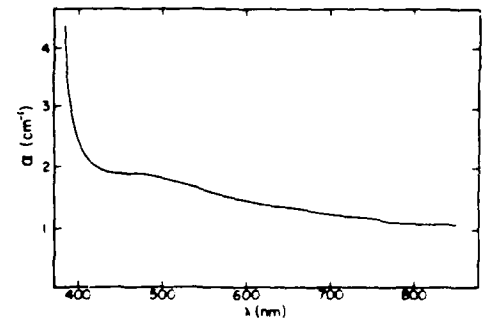


Fig. 3. Absorption spectrum of SBN:Ce.

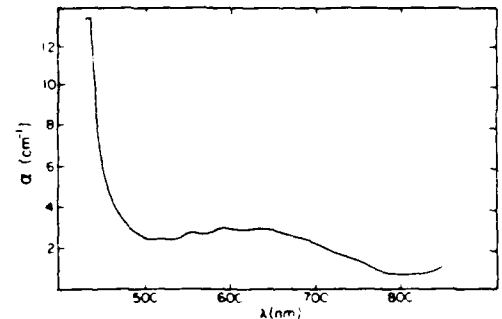


Fig. 4. Absorption spectrum of SBN:Fe.

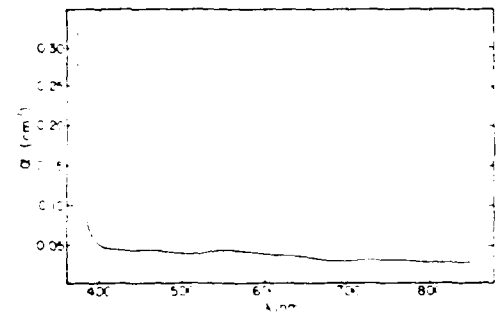


Fig. 5. Absorption spectrum of SBN:60.

be obtained from the above equations. It is important to note that although the above description of the transient behavior is not strictly correct,⁴ it does indeed approximate the temporal response of the two-wave mixing process in SBN very well since the measured waveforms can be accurately described by simple exponentials.

Maximum coupling will result in crystals with large Γ but small α . However, α and Γ are not independent. In fact, since charge must be excited into a conduction band by the intensity interference pattern in order to start the photorefractive process, some absorption is necessary. This is precisely where the role of the dopant enters. If impurities are purposely introduced into the crystal, donor sites are created that become the absorption centers. It must be noted, however, that any absorption that does not contribute to the photorefractive mechanism is undesirable.

Figures 3 and 4 show the effect of cerium and iron impurities on the absorption spectrum of undoped SBN, which is given in Fig. 5. Several interesting observations can be made. First, the band edge shifts from 400 nm in SBN:60 to 430 nm in SBN:Ce and 500 nm in SBN:Fe. Second, although the

SBN:60 was not intentionally doped, deep-level impurities are evidenced by perturbations in the spectrum near 550 nm. Finally, the effects of Ce and Fe in SBN:60 are seen to be significantly different. While the spectrum of SBN:Ce is rather featureless, with a broad deep level centered at 480 nm, the spectrum of SBN:Fe displays a structured but broad absorption extending from 500 to 700 nm, with characteristic peaks at 550 nm and 590 nm. Future investigation of these lines will indicate whether or not they contribute to the photorefractive effect.

First principle calculations using the band transport model⁵ can be used to derive expressions for Γ and τ . Solutions to the photorefractive equations developed most fully by Kukhta-rev⁶⁻⁸ show that Γ and τ can be represented functionally as

$$\Gamma = \Gamma(d_g, E_0, \lambda, T, \tau, N_D, N_A, \epsilon, n), \quad (7)$$

$$\tau = \tau(d_g, E_0, \lambda, T, I_0, s, \gamma_R, \mu, N_D, N_A, \epsilon), \quad (8)$$

where the experimentally controlled variables are

d_g = grating period

E_0 = applied field (normal to grating planes)

λ = wavelength of incident light

T = temperature

I_0 = total irradiance

and the material parameters are

r = effective electro-optic coefficient

s = photoionization cross section

γ_r = two-body recombination rate

μ = mobility

N_D = number of donors under dark conditions

N_A = number of traps under dark conditions

ϵ = static dielectric constant

n = background refractive index

These equations were applied to cerium-doped SBN. Specifically, the sample contained 10^{18} to 10^{19} cm⁻³ cerium atoms, which resulted in an as-grown crystal with $\Gamma = 11$ cm⁻¹, $\tau = 0.10$ s, and $\alpha = 1.8$ cm⁻¹ at $I_0 = 1$ W/cm², $T = 298$ K, $\lambda = 0.5145$ μ m, $E_0 = 0$ V/cm, and $d_g = 5$ μ m.

Variations in Γ and τ about this "operating point" are shown in Figs. 6 through 13, along with the experimentally obtained values of the two-beam coupling coefficient and response times for SBN:60 and SBN:Ce. Data for SBN:Fe are not shown since striations in the crystal so affected the optical quality of the crystal that no reliable experimental values could be measured. Although the SBN:60 and SBN:Ce samples were striation free and displayed good optical quality, to date all of the SBN:Fe crystals, regardless of their Fe concentration, have been severely marked with striations. We believe that better control of the melt temperature will eliminate this problem.

With no applied field, Fig. 7 indicates that Γ should be greater than 1 cm⁻¹ for all practical values of d_g , while the application of an electric field of 2 kV/cm ought to increase the coupling coefficient to 35 cm⁻¹ at $d_g = 5$ μ m, as shown in Fig. 8. Such a large response would then make even very thin samples of SBN:Ce useful photorefractive media. However, in practice, these large values of Γ are not easily obtainable. As an electric field is applied to the crystal, induced stresses deform the material and the incident beams are distorted. Therefore, we conclude that the application of an electric field to the crystal to control its two-beam coupling coefficient is of

limited use.

Another way Γ can be modified was suggested in Ref. 9. By varying the trap density N_A with reduction and oxidation treatments, one should be able to control Γ , as shown in Fig. 9. Although the exact number density of traps is difficult to measure, we have indeed been able to change the two-beam coupling coefficient from less than 0.1 cm⁻¹ to 15 cm⁻¹ by heating the crystal in atmospheres with different oxygen partial pressures.

The predicted variation of response time with trap density, which is shown in Fig. 10, has yet to be observed in SBN:Ce. Although Γ decreases as expected when the crystal is heated in a reducing atmosphere, the time constant remains unchanged at a typical value of 100 ms at 1 W/cm² irradiance. This unexpected and currently unexplained result has complicated our effort to produce a cerium-doped SBN photorefractive crystal with 1 ms response time, since heat treatment was proposed as a method of achieving this goal.⁹ Therefore, other techniques may need to be invoked to obtain the desired speed of response.

Figures 11, 12, and 13 show how the response time τ is affected by changes in the mobility μ , the two-body recombination rate γ_R , and the photoionization cross section s , respectively. Since μ is predominantly an intrinsic quantity of the host crystal, little can be done to increase its value. However, s and γ_R are extrinsic parameters that can be varied by the selection of different dopants. If the dopant chosen has either a larger photoionization cross section or a smaller two-body recombination rate coefficient than is presently obtained with cerium, the resulting doped sample of SBN should have a shorter response time. The selection of such a dopant, unfortunately, is a nontrivial task.

Table I shows the results of an elemental analysis by nuclear activation of undoped and cerium-doped SBN. Since undoped SBN is photorefractive while containing only trace quantities of cerium, we must conclude that cerium is not the only photorefractive species for SBN. In fact, Table I indicates that there are significant amounts of Fe, Ni, Mo, and Ta impurities in the undoped SBN crystal, and Fe and Ni, for example, are known to be effective photorefractive centers in LiNbO₃.¹⁰ Although iron has already been used as a dopant for SBN, the resulting crystals were optically imperfect. Therefore, we suggest that not only should the study of iron- and cerium-doped SBN continue, but crystals doped with other impurities, which may prove to have better values of γ_R and s , should also be investigated.

4. SUMMARY OF RESULTS

A major goal of our work has been the growth of high optical quality photorefractive SBN crystals. This was accomplished in part by growing striation-free SBN:60 and SBN:Ce. In fact, optically excellent crystals of SBN:60 and SBN:Ce can now be had as cubes approaching 1 cm on a side. SBN:Fe, unfortunately, has yet to be grown without striations. As was indicated earlier, better control of the melt temperature may be necessary to eliminate this problem.

Large two-beam coupling was observed in both SBN:60 and SBN:Ce. Values of Γ ranged from 2 cm⁻¹ in SBN:60 to greater than 10 cm⁻¹ in SBN:Ce. Such response was large enough to permit the use of these crystals in the construction of the ring¹¹ and semilinear¹² passive phase conjugate mirrors, for example. It was also found that oxidation and reduction techniques served as effective methods for varying the value of

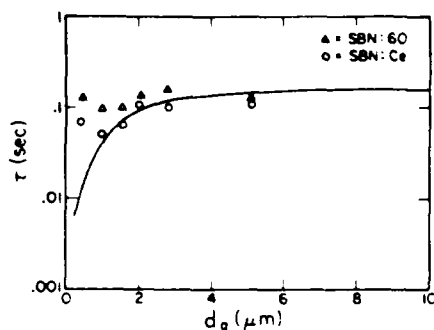


Fig. 6. Response time versus grating period at $I_0 = 1 \text{ W/cm}^2$ for $E_0 = 0 \text{ V/cm}$.

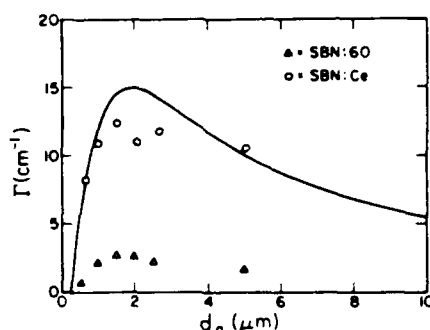


Fig. 7. Coupling coefficient versus grating period for $E_0 = 0 \text{ V/cm}$.

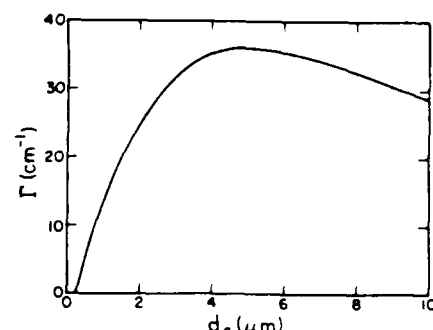


Fig. 8. Coupling coefficient versus grating period for $E_0 = 2 \text{ kV/cm}$.

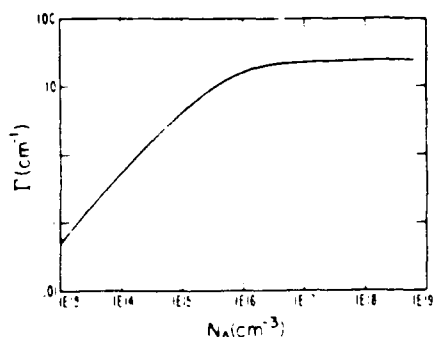


Fig. 9. Coupling coefficient versus trap density for $E_0 = 0 \text{ V/cm}$ and $d_g = 5 \text{ micrometers}$.

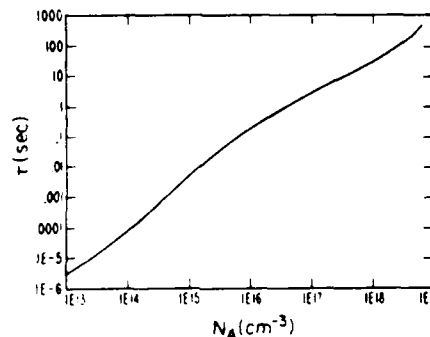


Fig. 10. Response time versus trap density at $I_0 = 1 \text{ W/cm}^2$, assuming $\mu = 0.1 \text{ cm}^2/\text{V}\cdot\text{s}$, $\gamma_R = 5 \times 10^{-8} \text{ cm}^3/\text{s}$, $s = 1.6 \times 10^{-19} \text{ cm}^2$, $N_D = 10^{19} \text{ cm}^{-3}$, and $d_g = 5 \text{ micrometers}$.

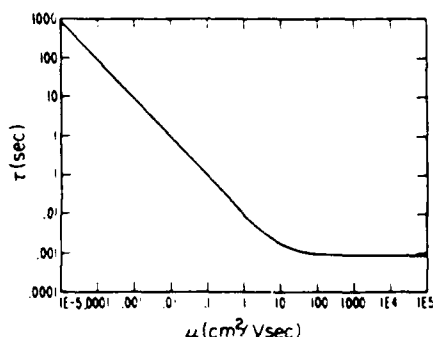


Fig. 11. Response time versus mobility at $I_0 = 1 \text{ W/cm}^2$, assuming $N_A = 10^{16} \text{ cm}^{-3}$, $\gamma_R = 5 \times 10^{-8} \text{ cm}^3/\text{s}$, $s = 1.6 \times 10^{-19} \text{ cm}^2$, $N_D = 10^{19} \text{ cm}^{-3}$, and $d_g = 5 \text{ micrometers}$.

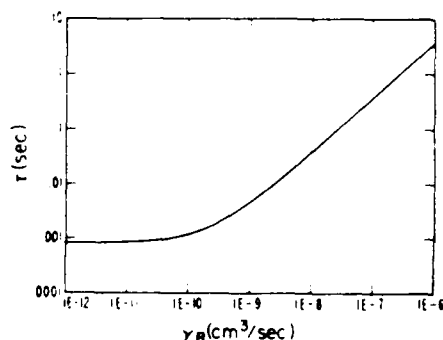


Fig. 12. Response time versus two-body recombination rate coefficient at $I_0 = 1 \text{ W/cm}^2$, assuming $N_A = 10^{16} \text{ cm}^{-3}$, $\mu = 0.1 \text{ cm}^2/\text{V}\cdot\text{s}$, $s = 1.6 \times 10^{-19} \text{ cm}^2$, $N_D = 10^{19} \text{ cm}^{-3}$, and $d_g = 5 \text{ micrometers}$.

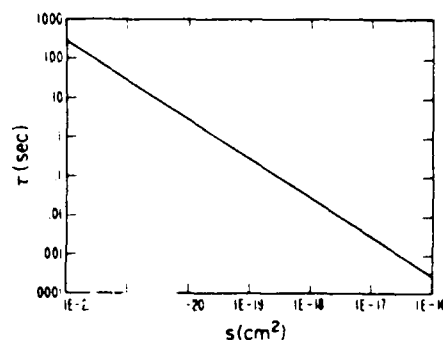


Fig. 13. Response time versus photoionization cross section at $I_0 = 1 \text{ W/cm}^2$, assuming $N_A = 10^{16} \text{ cm}^{-3}$, $\mu = 0.1 \text{ cm}^2/\text{V}\cdot\text{s}$, $\gamma_R = 5 \times 10^{-8} \text{ cm}^3/\text{s}$, $N_D = 10^{19} \text{ cm}^{-3}$, and $d_g = 5 \text{ micrometers}$.

Γ in these crystals. However, the application of an external electric field to the crystals tended to degrade their optical quality rather than improve the value of their coupling coefficients.

The response times of the SBN crystals we tested averaged about 100 ms for an incident irradiance of 1 W/cm^2 . In general, SBN:Ce responded quicker than SBN:60, with times approaching 50 ms at 1 W/cm^2 . Since the two-beam coupling coefficient of SBN:Ce is so large, the time required to reach a given diffraction efficiency with SBN:Ce will be much shorter than that needed with SBN:60. Although the response time of SBN:Fe has yet to be reliably determined, we believe that its speed will not differ significantly from that of the other two crystals.

5. CONCLUSIONS

High optical quality undoped and doped single-crystal SBN:60 has been grown and proved to be photorefractive. This effect was quantified by measuring the coupling coefficients and response times of several samples using the method of two-wave mixing. The results of this work indicate that the introduction of dopants into SBN:60 produces crystals with an even greater photorefractive effect than that of undoped SBN:60.

6. ACKNOWLEDGMENTS

This research was supported by grants from Rockwell International Corporation, the U.S. Air Force Office of Scientific Research, and the U.S. Army Research Office.

TABLE I. Elemental analysis by weight of SBN:60 and SBN:Ce.

Elements & Units	SBN:60	SBN:Ce
U PPM	< 0.1	< 0.1
TH PPM	< 0.3	< 0.2
NA PPM	30.0	<30.0
SC PPM	0.04	0.04
CR PPM	< 5.0	< 5.0
FE %	0.129	0.014
CO PPM	0.3	0.3
NI PPM	50.0	50.0
ZN PPM	7.0	5.0
AS PPM	< 1.0	< 1.0
SE PPM	< 5.0	< 5.0
BR PPM	< 0.5	< 0.5
MO PPM	11.0	4.0
SB PPM	0.5	0.5
CS PPM	< 0.2	< 0.2
BA PPM	160000.0	150000.0
LA PPM	0.2	1.0
HF PPM	< 0.2	< 0.2
TA PPM	12.0	13.0
W PPM	< 3.0	1.0
AU PPM	< 5.0	5.0
CE PPM	< 1.0	47.0
ND PPM	Interfer	Interfer
SM PPM	0.01	0.32
EU PPM	0.07	0.10
TB PPM	< 0.1	< 0.1
YB PPM	< 0.05	0.05
LU PPM	< 0.01	< 0.01
SR PPM	148000.0	135000.0
RB PPM	< 5.0	< 5.0

7. REFERENCES

1. P. B. Jamieson, S. C. Abrahams, and J. L. Bernstein, "Ferroelectric tungsten bronze-type crystal structures. I. Barium strontium niobate $\text{Ba}_{1-x}\text{Sr}_x\text{Nb}_2\text{O}_{10}$," *J. Chem. Phys.* 48, 5048 (1968).
2. P. B. Jamieson, S. C. Abrahams, and J. L. Bernstein, "Ferroelectric tungsten bronze-type crystal structures. II. Barium sodium niobate $\text{Ba}_{1-x}\text{Na}_x\text{Nb}_2\text{O}_{10}$," *J. Chem. Phys.* 50, 4352 (1969).
3. S. C. Abrahams, P. B. Jamieson, and J. L. Bernstein, "Ferroelectric tungsten bronze-type crystal structures. III. Potassium lithium niobate $\text{K}_{1-x}\text{Li}_x\text{Nb}_2\text{O}_{10}$," *J. Chem. Phys.* 54, 2355 (1971).
4. J. M. Heaton and L. Solymar, "Transient energy transfer during hologram formation in photorefractive crystals," *Opt. Acta* 32(4), 397 (1985).
5. G. C. Valley and M. B. Klein, "Optical properties of photorefractive materials for optical data processing," *Opt. Eng.* 22(6), 704-711 (1983).
6. N. V. Kukhtarev, V. B. Markov, and S. G. Odulov, "Transient energy transfer during hologram formation in LiNbO_3 in external electric field," *Opt. Commun.* 23, 338 (1977).
7. N. V. Kukhtarev, V. B. Markov, S. G. Odulov, M. S. Soskin, and V. L. Vinetski, "Holographic storage in electrooptic crystals. I. Steady state," *Ferroelectrics* 22, 949 (1979).
8. N. V. Kukhtarev, "Kinetics of hologram recording and erasure in electrooptic crystals," *Sov. Tech. Phys. Lett.* 2, 438 (1976).
9. G. A. Rakuljic, A. Yariv, and R. R. Neurgaonkar, "Photorefractive properties of ferroelectric BaTiO_3 and SBN:60," in *Nonlinear Optics and Applications*, P. Yeh, ed., Proc. SPIE 613, 110-118 (1986).
10. W. Phillips, J. J. Amodel, and D. L. Staebler, "Optical and holographic storage properties of transition metal doped lithium niobate," *RCA Rev.* 33, 94 (1972).
11. M. Cronin-Golomb, B. Fischer, J. O. White, and A. Yariv, "Passive phase conjugate mirror based on self-induced oscillation in an optical ring cavity," *Appl. Phys. Lett.* 42, 919 (1983).
12. M. Cronin-Golomb, B. Fischer, J. O. White, and A. Yariv, "Passive (self-pumped) phase conjugate mirror: theoretical and experimental investigation," *Appl. Phys. Lett.* 41, 689 (1982).



George A. Rakuljic was born in Chicago, Ill., on Sept. 1, 1961. After three years of undergraduate study at the University of California, Los Angeles, he received the M.S. degree in electrical engineering from the California Institute of Technology, Pasadena, in 1983, where he is currently pursuing the Ph.D. degree in electrical engineering.

His current research interests are photorefractive materials, phase conjugate optics, and optical information processing.



Amnon Yariv, a native of Israel, obtained the B.S. degree in 1954, the M.S. degree in 1956, and the Ph.D. degree in 1958 in electrical engineering from the University of California in Berkeley.

He went to the Bell Telephone Laboratories, Murray Hill, N.J., in 1959, joining the early stages of the laser effort. He joined the California Institute of Technology in 1964 as an associate professor of electrical engineering, becoming a professor in 1966. In 1980 he

became the Thomas G. Myers Professor of Electrical Engineering and Applied Physics.

On the technical side, he took part (with various coworkers) in the discovery of a number of early solid-state laser systems, in the formulation of the theory of parametric quantum noise and the prediction of parametric fluorescence, in the invention of the technique of mode-locked ultrashort-pulse lasers and FM lasers, in the introduction of GaAs and CdTe as infrared electro-optic and window materials, in proposing and demonstrating semiconductor-based integrated optics technology, and in pioneering the field of phase conjugate optics.

His present research efforts are in the areas of nonlinear optics, semiconductor lasers, and integrated optics, especially the problem of monolithic integration of transistors, injection lasers, and detectors for high frequency applications and ultrafast (10^{-12} s) semiconductor devices and phenomena.

Professor Yariv has published widely in the laser and optics fields (some 300 papers) and has written a number of basic texts in quantum electronics, optics, and quantum mechanics. He is an associate editor of *Optics Communications* and was previously associate editor of the *Journal of Quantum Electronics* and the *Journal of Applied Physics*. He is a member of the American Physical Society, Phi Beta Kappa, the American Academy of Arts and Sciences, and the National Academy of Engineering and a Fellow of the IEEE and OSA. He received the 1980 Quantum Electronics Award of the IEEE, the 1985 University of Pennsylvania Pender Award, and the 1986 OSA Ives Medal. He is a founder and chairman of the board of ORTEL Corp.



Ratnaker R. Neurgaonkar is manager of the Ferroelectric Materials Department at the Rockwell International Science Center. He received the B.Sc. degree with honors in 1962, the M.Sc. degree in 1963, and the Ph.D. degree in 1967 in solid-state chemistry from Poona University, India. At Rockwell, Dr. Neurgaonkar has been directing the ferroelectric materials research and development program for various device applications, including electro-optic, photorefractive, pyroelectric imagers,

surface acoustic wave, millimeter wave, and piezoelectric transducers. He and a coworker have developed various growth techniques for ferroelectric crystals/films and recently successfully demonstrated the growth of optical-quality doped and undoped $\text{Sr}_{1-x}\text{Ba}_x\text{Nb}_2\text{O}_6$ and BSKNN single crystals using the Czochralski technique. Besides ferroelectric materials, Dr. Neurgaonkar has been interested in magnetism, luminescence, and laser crystal development work. He is a member of various professional societies, including the American Ceramic Society, the Electrochemical Society, and the American Association for Crystal Growth. He is the author or coauthor of more than 70 research publications.



Rockwell International

Science Center

SC5441.FTR

PHOTOREFRACTIVE PROPERTIES OF STRONTIUM BARIUM NIOBATE

Photorefractive properties of strontium-barium niobate

M. D. Ewbank, R. R. Neurgaonkar, and W. K. Cory

Rockwell International Science Center, Thousand Oaks, California 91360

Jack Feinberg

Department of Physics, University of Southern California, Los Angeles, California 90089-0484

(Received 16 December 1986; accepted for publication 10 March 1987)

We have grown and optically characterized strontium-barium niobate crystals, including both undoped and cerium-doped crystals having two different Sr/Ba ratios (61/39 and 75/25). By measuring the coupling of two optical beams in the crystals, we have determined the following photorefractive properties: the effective density, sign, and spectral response of the dominant charge carrier, the grating formation rate, dark conductivity, and carrier diffusion length. We find that electrons are the dominant photorefractive charge carriers in all of our samples; the typical density of photorefractive charges is $\sim 1 \times 10^{16} \text{ cm}^{-3}$ in the undoped samples. The grating formation rate increases with intensity, with a slope of $\sim 0.3 \text{ cm}^2/(\text{W s})$ over an intensity range of $\sim 1\text{--}15 \text{ W/cm}^2$ in undoped samples. Cerium doping improves both the charge density (increased by a factor of ~ 3) and the response rate per unit intensity (~ 5 times faster).

I. INTRODUCTION

Photorefractive crystals¹ have been used to demonstrate a wide range of nonlinear optical applications,² including phase conjugation,³⁻⁵ image amplification,^{3,6-8} information processing,⁹⁻¹³ optical computing,¹²⁻¹⁴ optical resonators,^{3,15-16} inertial navigation devices,²⁰⁻²² associative memories,²³⁻²⁵ etc. Most of the above demonstrations were performed using barium titanate (BaTiO_3), because it has the largest optical nonlinearity of any commercially available²⁶ photorefractive material, and also because its photorefractive properties have been well characterized.²⁷⁻³²

Both nominally undoped strontium-barium niobate ($\text{Sr}_x\text{Ba}_{1-x}\text{Nb}_2\text{O}_6$ or SBN)³³⁻³⁷ and cerium-doped SBN^{34,38} are photorefractive (efficient internal self-pumped phase conjugation⁴⁰ has been recently observed in SBN⁴¹), but these crystals have not been as extensively characterized. The purpose of this work is to measure the optical absorption and some important photorefractive properties of these crystals, including their gain, wavelength sensitivity, charge density, and response time. We also discuss the dependence of these properties on crystal doping and on the Sr/Ba ratio.

II. OPTICAL QUALITY SBN

$\text{Sr}_x\text{Ba}_{1-x}\text{Nb}_2\text{O}_6$, $x = 0.61$, (or SBN:61) is relatively easy to grow compared to other photorefractive ferroelectric oxides, because it mixes congruently at $T \sim 1510^\circ\text{C}$.⁴² A typical Ce-doped SBN:61 crystal grown along the c axis is shown in Fig. 1(a). These crystals exhibit 24 well-defined natural facets, as illustrated in Fig. 1(b).

Single-crystalline boules with diameter of $\sim 2\text{--}3 \text{ cm}$ were grown by the Czochralski method at a rate of $\sim 8\text{--}10 \text{ mm/h}$.³⁶ From these boules, individual samples were cut and optically polished with rectangular faces $\sim 2\text{--}7 \text{ mm}$ on a side. The samples were electrically poled into a single ferroelectric domain by heating the samples to $\sim 10\text{--}15^\circ\text{C}$ above the Curie temperature T_C , applying an electric field of $\sim 8\text{--}$

10 kV/cm along the c axis of the sample, and slowly cooling the sample back to room temperature (at a rate of $\sim 1^\circ/\text{min}$ until $\sim 20^\circ\text{C}$ below T_C) before removing the electric field.

The optical quality of SBN crystals depends on the purity of the starting materials and on controlling the growth temperature to $\pm 0.10^\circ\text{C}$ while near the solid-liquid interface. In doped SBN, the optical quality is also influenced by the type of dopant, its location in the crystal structure, and the oxidizing or reducing atmosphere surrounding the melt. In our cerium-doped SBN samples, 0.1 wt. % of CeO_2 was added to the starting materials, and the crystals were grown in air (i.e., an oxidizing atmosphere).

III. COMPARISON OF SBN AND BaTiO_3

Table I compares some of the properties of $\text{Sr}_x\text{Ba}_{1-x}\text{Nb}_2\text{O}_6$ and the more familiar photorefractive material BaTiO_3 . Both materials are ferroelectric oxides with tetragonal symmetry (point group $4mm$) at room temperature. They also have similar refractive indices and birefringence. However, there are important differences between these two materials.

First, BaTiO_3 has a fixed composition, so that the temperature of its cubic-to-tetragonal phase transition is fixed⁴³ at $T_C \approx 128^\circ\text{C}$. For $\text{Sr}_x\text{Ba}_{1-x}\text{Nb}_2\text{O}_6$, the Sr-Ba ratio is variable between $0.2 < x < 0.8$, and the temperature of the cubic-to-tetragonal phase transition changes approximately linearly in x (e.g., T_C increases from $T_C \approx 57^\circ\text{C}$ at $x = 0.75$ to $T_C \approx 247^\circ\text{C}$ at $x = 0.25$ ⁴⁴). By choosing the Sr-Ba ratio so that the phase transition is slightly above room temperature, the SBN crystal lattice is highly polarizable in the z direction, causing the room-temperature dielectric constant ϵ_3 and the Pockels coefficients r_{13} and r_{33} to become quite large.

A second difference between the two crystals is the presence of a tetragonal-to-orthorhombic phase transition in BaTiO_3 at about 10°C , which, at room temperature, causes a softening of a lattice vibrational mode in directions perpendicular to z and produces a marked anisotropy in the dielec-

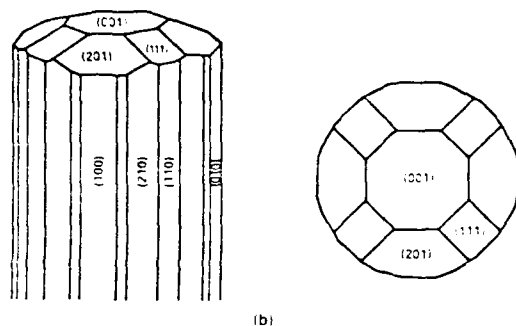
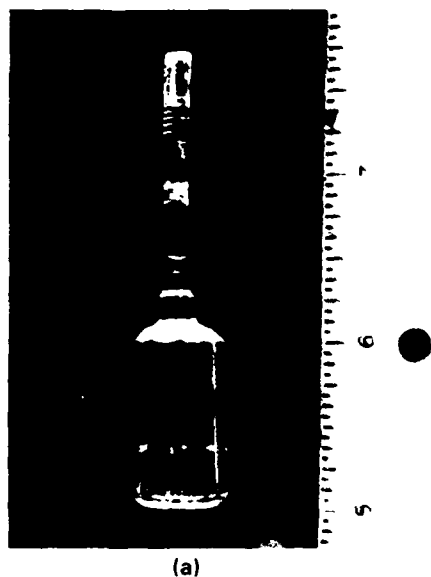


FIG. 1. $\text{Sr}_{0.4}\text{Ba}_{0.6}\text{Nb}_2\text{O}_6$ crystals. (a) boule of cerium-doped SBN grown at Rockwell Science Center. (b) crystallographic orientations of a few of the 24 natural facets on a boule of SBN.

tric constants of BaTiO_3 ($\epsilon_1/\epsilon_3 = 0.04$ in BaTiO_3 compared to $\epsilon_1/\epsilon_3 = 2$ in SBN:61). This phase transition is not observed in SBN for temperatures as low as -150°C , and so the electro-optic properties of SBN are less anisotropic.

Third, as a consequence of proximity of the different phase transitions to room temperature for the two crystals, the largest Pockels coefficient in SBN is r_{33} whereas the largest Pockels coefficient in BaTiO_3 is r_{42} . This distinction is important in photorefractive applications, because these coefficients dictate the optimal light polarizations and optimal orientation of the photorefractive grating.

The crystal structures of the two materials also differ. SBN has an open tungsten-bronze structure with vacant lattice sites, as shown in Fig. 2. The vacant C lattice sites can be intentionally filled by doping the crystal with impurity atoms. In contrast, BaTiO_3 has a completely filled crystal structure, so that doping requires substitution. (Of course, doping by substitution can also occur in SBN.)

TABLE 1. Comparison of materials properties for photorefractive $\text{Sr}_{0.4}\text{Ba}_{0.6}\text{Nb}_2\text{O}_6$ and BaTiO_3 .

T_c ($^\circ\text{C}$)	BaTiO_3 128 ^a	$\text{SBN}(x=0.61)$ 75 ^b	$\text{SBN}(x=0.75)$ 56 ^c
Index (5145 Å)	$n = 2.43^d$ $\Delta n = -0.07^d$	$n = 2.33^d$ $\Delta n = -0.03^d$	$n = 2.35^d$ $\Delta n = -0.02^d$
Dielectric constant	$\epsilon_1 = 3600^d$ $\epsilon_3 = 135^d$	$\epsilon_1 = 470^b$ $\epsilon_3 = 880^b$	$\epsilon_1 = 3400^c$
Electro-optic coefficient (pm/V)	$r_{11} = 19.5^e$ $r_{13} = 97^e$ $r_{42} = 1640^e$	$r_{11} = 47^f$ $r_{13} = 235^f$	$r_{11} = 67^g$ $r_{13} = 1340^g$ $r_{42} = 42^g$

^aReference 44, p. 452.

^bReference 36.

^cReference 44, p. 509.

^dE. L. Venturini, E. G. Spencer, P. V. Lenzo, and A. A. Ballman, *J. Appl. Phys.* **39**, 343 (1968).

^eS. Ducharme, J. Feinberg, and R. R. Neurgaonkar, to be published in *IEEE J. Quantum Electron.*

Finally, the optical absorption spectra of BaTiO_3 and the various SBN crystals studied here are qualitatively different. The spectral absorption curves for the SBN samples, shown in Fig. 3, have been obtained from optical transmission measurements using a dual-beam spectrophotometer (Perkin-Elmer model 330). Cerium-doped crystals of SBN grown with Ce in the 12-fold coordinated site (samples *D*, *E*, and *G*) are pink in color and they exhibit a broadband extrinsic absorption over the range from $\sim 0.6\mu\text{m}$ to the interband transition (i.e. optical band gap) near $0.4\mu\text{m}$, as shown in Fig. 3. [Note that sample *D* is not included in Fig. 3 because it was so thin (1.7 mm) that its transmission spectrum was dominated by surface losses.] In contrast, when Ce is forced into the nine-fold coordinated site, as in SBN:61 sample *F*, the color is greenish-yellow. The absorption in the visible for this crystal is higher and it extends farther into the near infrared, similar to commercially available²⁶ crystals of nominally undoped BaTiO_3 , which typically have absorption coefficients³² of $\sim 0.5\text{--}3.0\text{ cm}^{-1}$ over this spectral range. In comparison, the absorption coefficients of the three nominally undoped SBN:61 samples *A*, *B*, and *C* are substantially lower over the same spectral range (see Fig. 3).

IV. TWO-WAVE MIXING IN SBN: THEORY

The photorefractive properties of SBN can be measured using two-wave mixing.¹ As illustrated in Fig. 4, if two coherent light beams intersect in a photorefractive crystal, beam coupling occurs, causing one beam to gain intensity at the expense of the other beam. Let a "pump" beam and a "probe" beam of the same frequency enter the same face of the crystal with external angles $\pm\theta$ to the face normal. These two beams produce a sinusoidal interference pattern of intensity with a fringe separation Λ_g given by

$$\Lambda_g = 2\pi/K = \lambda/2 \sin \theta, \quad (1)$$

where λ is the wavelength of the light in air and K is the magnitude of the grating wave vector. The interference pattern causes migration of charge inside the crystal. The resulting space-charge field produces a photorefractive index grat-

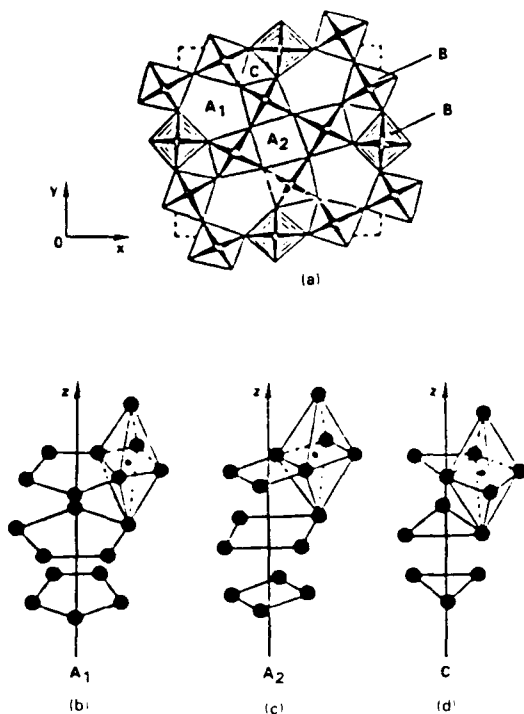


FIG. 2. Crystal structure of $\text{Sr}_x\text{Ba}_{1-x}\text{Nb}_2\text{O}_6$ where Sr and Ba occupy either of the lattice sites A_1 or A_2 in a variable composition. Nb resides at the six-fold-coordinated B lattice site, the C sites are vacant, and the oxygens form a octahedral cage surrounding each Nb. (a) Projection of the tetragonal tungsten-bronze structure into the x - y plane, (b) the A_1 atom (Sr or Ba) is surrounded by 15 nearest-neighbor oxygens (15-fold coordination), (c) the A_2 atom (Sr or Ba) is surrounded by 12 nearest-neighbor oxygens (12-fold coordination), and (d) the vacant C lattice site is surrounded by 9 nearest-neighbor oxygens (nine-fold coordination).

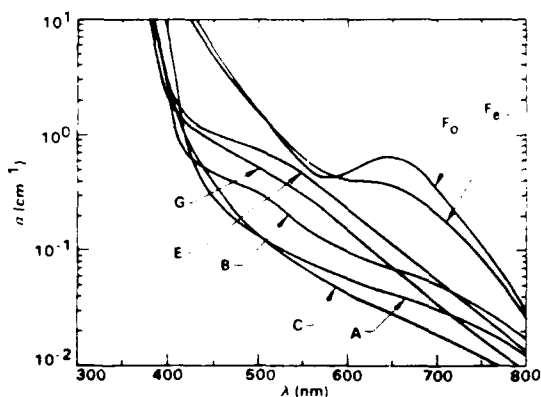


FIG. 3. Spectral dependence of the absorption coefficient α in nominally undoped SBN:61 (samples A-C), cerium-doped SBN:61 (samples E and F), and cerium-doped SBN:75 (sample G). Note the extrinsic broadband absorption in the cerium-doped SBN samples, extending from near the interband transition throughout most of the visible spectrum. These spectra were nearly independent of the light polarization, with the exception of sample F for which two absorption curves are shown (F_o for extraordinary and F_e for ordinary). In samples A, B, C, E, and G, the band edge of each ordinary absorption spectrum was shifted (~ 5 – 10 nm) toward shorter wavelength, compared to the extraordinary absorption spectra shown.

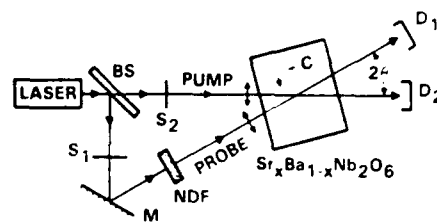


FIG. 4. Experimental setup for measuring the two-wave mixing gain coefficient in SBN for various external crossing angles 2θ of the optical beams. The most efficient beam coupling occurs when the incident beams are polarized extraordinary and the photorefractive space-charge field is parallel to the crystal c axis thereby using the largest electro-optic coefficient r_{33} . The neutral density filter (NDF) is used to adjust the incident pump/probe beam intensity ratio to minimize the effects of pump depletion and beam fanning during two-beam coupling. Shutters S_1 and S_2 permit the transmitted intensities to be measured both with and without coupling at detectors D_1 and D_2 .

ing, which couples the two beams with a two-wave mixing gain coefficient Γ (i.e., an exponential gain per unit length) defined by

$$\Gamma = (1/L) \times \ln(I_1 I_2 / I_1 I_2), \quad (2)$$

where L is the interaction length, I_1 (I_2) is the transmitted "probe" beam intensity with (without) coupling, and I_1 (I_2) is the transmitted "pump" beam intensity with (without) coupling. By using the transmitted intensities in Eq. (2), the absorption and Fresnel reflection losses do not appear in the expression for Γ in Eq. (2). Also note that for negligible pump depletion (i.e., $I_1 \approx I_2$), the two-wave mixing gain coefficient Γ becomes independent of the pump beam intensity.

The two-wave mixing gain coefficient Γ is related to the photorefractive index grating amplitude δn (defined as one-half the peak-to-peak value) by^{1,45}

$$\Gamma = 4\pi \delta n \sin \phi / m \lambda \cos \theta_i, \quad (3)$$

where θ_i is the half angle between the beams inside the crystal, ϕ is the phase shift between the optical interference pattern and the photorefractive index grating, and m is the modulation depth of the incident optical interference pattern [$m = 2\sqrt{I_1 I_2} / (I_1 + I_2)$]. The phase shift ϕ is $\sim \pi/2$ when the photorefractive process is dominated by diffusion, as it is in SBN.⁴⁶ The photorefractive index modulation δn is given by

$$\delta n = n^3 r_{\text{eff}} E_{\text{sc}} / 2, \quad (4)$$

E_{sc} is the space-charge electric field and n is the effective refractive index ($n = n_e n_o / \sqrt{n_e^2 \sin^2 \theta_i + n_o^2 \cos^2 \theta_i}$, with n_e and n_o being the extraordinary and ordinary refractive indices, respectively). For the configuration shown in Fig. 4, in which the grating wave vector is aligned along the c axis of the crystal and the optical beams are both extraordinary rays (while assuming a small birefringence $\Delta n = n_e - n_o$), the effective electro-optic coefficient r_{eff} is²

$$r_{\text{eff}} = r_{33} \cos^2 \theta_i - r_{13} \sin^2 \theta_i + (\Delta n / n_e) (r_{33} + r_{13}) \sin^2 2\theta_i. \quad (5)$$

The photorefractive space-charge field E_{sc} is given by⁴⁷

$$E_{\infty} = m(k_B T/e) [K/(1 + (K/K_0)^2)] \zeta(K) \cos 2\theta_i, \quad (6)$$

where $2\theta_i$ is the internal full crossing angle of the optical beams and $k_B T/e$ is the thermal energy per charge. The factor $\zeta(K)$ takes into account competition between holes and electrons.^{47,48}

An important parameter in Eq. (6) is the inverse Debye screening length K_0 ,

$$K_0^2 = e^2 N_{\text{eff}} / (\epsilon \epsilon_0 k_B T), \quad (7)$$

which depends on the effective density of photorefractive charge N_{eff} and the dc dielectric constant $\epsilon \epsilon_0$ along the direction of the grating wave vector K .

V. TWO-WAVE MIXING IN SBN: EXPERIMENTS

The two-wave mixing gain coefficient Γ was measured in a number of undoped and Ce-doped SBN crystals in an attempt to determine the effective density of photorefractive charge N_{eff} and the effective Pockels coefficient r_{eff} . As shown in Fig. 4, the single-longitudinal-mode output from a cw laser (an argon ion laser or a ring dye laser with R6G dye) was separated into two beams which intersect in the SBN sample at an external angle of 2θ .

Because r_{33} is the largest electro-optic coefficient in SBN, the two-wave mixing gain coefficient Γ is maximized by choosing extraordinary polarization and aligning the c axis of the crystal parallel to the K vector of the photorefractive grating (i.e., the bisector of the two incident light beams is aligned perpendicular to the c axis). Unfortunately, this choice of light polarization and crystal orientation increases the amount of extraneous light scattered into the direction of the transmitted probe beam by stimulated scattering and beam fanning of the pump beam. Nevertheless, because most photorefractive applications require a large coupling strength, we chose to measure Γ using the above geometry.

The transmitted powers of both the weak probe beam and the strong pump beam were measured with and without coupling. All of our two-wave mixing experiments were performed with an argon ion laser at 514.5 nm (except for the experiments in Sec. V C), and with both beams having the same $1/e^2$ diameter of 2.95 mm. Using equal-size beams was advantageous because any pump depletion was easily detected. (If the pump-beam diameter was much larger than the probe beam diameter, then a small localized area of the pump beam could have been severely depleted by the probe beam without noticeably affecting the pump beam's total power.) The beam diameters were sufficiently large so that the interaction length L of the two beams was limited by the physical length of the sample in all of our experiments (except for one data point at $2\theta = 60^\circ$ with the dye laser, for which the effective interaction length was computed from the beam diameters). The pump/probe intensity ratio was adjusted in the range of 10^3 – 10^5 . This range was a compromise that would minimize pump depletion yet insure that the amplified probe was much more intense than the background scattered light from beam fanning of the pump beam.

A. Intensity dependent two-wave mixing

Figure 5 shows the dependence of the steady-state two-wave mixing gain coefficient Γ on total optical intensity for a

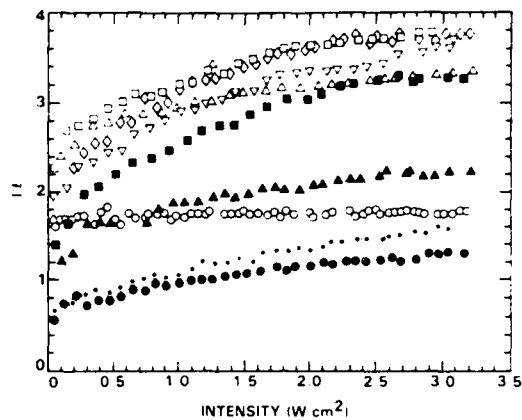


FIG. 5. The measured two-wave mixing gain ΓL vs incident optical intensity of the pump beam in nominally undoped SBN:61 sample C for beam crossing angles $2\theta = 3.2^\circ$ (\circ), 7.8° (Δ), 10.0° (\square), 12.6° (\diamond), 16.5° (∇), 21.5° (\blacksquare), 34.7° (\blacktriangle), 42.5° (\odot), and 60.0° (\bullet). For low-intensity levels, the two-beam coupling efficiency is decreased from its high-intensity value due to the nonzero dark erasure rate of the crystal.

number of different beam crossing angles in nominally undoped SBN sample C. The gain coefficient Γ saturates at large optical power, and is reduced at small optical power by the finite dark conductivity [$\sigma_d = 0.7 \times 10^{-10} (\Omega \text{ cm})^{-1}$] of this sample. (This dark conductivity was obtained from transient two-wave mixing measurements, described below.)

B. Optimal grating spacing for two-wave mixing in SBN

Combining Eqs. (1)–(6), the gain coefficient Γ can be written in the form

$$\Gamma = [A \sin \theta / (1 + B^{-1} \sin^2 \theta)] (\cos 2\theta / \cos \theta_i), \quad (8)$$

where θ is the external half angle and θ_i the internal half angle between the two incident laser beams. [Over the range of external crossing angles 2θ used here ($0 < 2\theta < 60^\circ$), the internal crossing angle $2\theta_i$ was always less than 25° , and the factor $(\cos 2\theta_i / \cos \theta_i)$ in Eq. (8) varied by less than 7% from unity.] In Eq. (8) we have assumed that the hole-electron competition factor^{47,48} $\zeta(K)$ is constant with K in order to simplify the data analysis.

Figure 6 shows the measured two-wave mixing gain coefficient Γ as a function of crossing angle of the optical beams [or grating spacing, i.e., see Eq. (1)] in various Ce-doped and undoped SBN samples at a $\lambda = 514.5$ nm. The gain increases linearly with θ for small crossing angles, reaching a maximum at $\theta = \theta_{\text{peak}}$, and then decreases for larger crossing angles, as predicted by Eq. (8). All data points were taken at sufficiently large optical intensity such that the gain was independent of intensity. The solid curves are a best fit to Eq. (8), and yield values for the parameters A and B , which relate to the photorefractive properties as follows.

The parameter A is proportional to the effective Pockels coefficient r_{eff} :

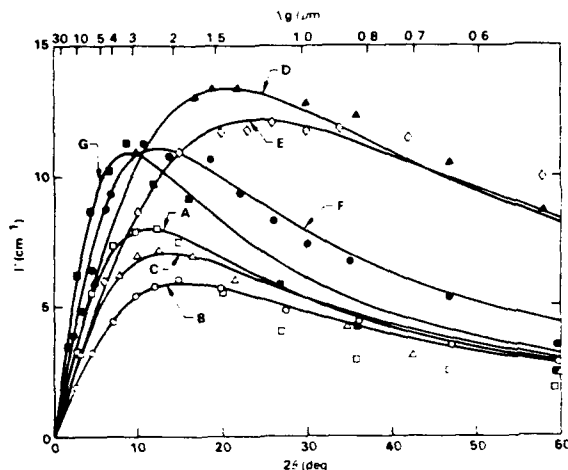


FIG. 6 The two-wave mixing gain coefficient Γ as a function of full external crossing angle 2θ in nominally undoped SBN:61 samples A-C, cerium-doped SBN:61 samples D-F, and cerium-doped SBN:75 sample G. The solid curves are best fits to the expression in Eq. (8). Note that cerium doping enhances the photorefractive coupling efficiency.

$$A = r_{\text{eff}} \zeta(K) \frac{8\pi^2 n^2 k_B T}{c \lambda^2} = \frac{\delta \Gamma}{\delta \theta} \quad (9)$$

and is determined by the slope of the plot of Γ vs 2θ near $\theta = 0$. The parameter B is related to the effective photorefractive charge density N_{eff} :

$$B = \frac{\lambda K_{\text{eff}}}{4\pi} = \frac{e \lambda}{4\pi} \sqrt{\frac{N_{\text{eff}}}{\epsilon \epsilon_0 k_B T}} \approx \sin \theta_{\text{peak}} \quad (10)$$

and is determined by $2\theta_{\text{peak}}$, the crossing angle at which the gain $\Gamma(2\theta)$ reaches its maximum value.

Comparing the curves for the undoped and doped SBN:61 samples in Fig. 6, it is apparent that cerium doping the SBN:61 samples causes an increase in the peak-gain crossing angle θ_{peak} . According to Eq. (10), this indicates that cerium doping increases the effective density of photorefractive charges N_{eff} . In addition, the slope of each curve near the origin is related to the product $r_{\text{eff}} \zeta(K)$ [see Eq. (9)]. The initial slope of the SBN:75 sample is noticeably

larger, as expected, due to its larger electro-optic coefficient. Note also that electron and hole competition^{47,48} appears to be important, as seen by the varying product $r_{\text{eff}} \zeta(K)$ in the various samples. The fitted values for $r_{\text{eff}} \zeta(K)$ and N_{eff} , corresponding to each curve in Fig. 6, are listed in Table II. The fact that cerium doping does not cause a systematic change in $r_{\text{eff}} \zeta(K)$ implies that the presence of cerium primarily alters the photorefractive charge density N_{eff} and not the competition of electrons and holes.

C. Wavelength dependence of the two-wave mixing gain in undoped SBN

Figure 7 shows the wavelength dependence of Γ vs Λ_K^{-1} for nominally undoped SBN:61 sample C. Here, the solid curves are the best fit of the data to Eq. (8) with the $(\cos 2\theta_i / \cos \theta_i)$ factor taken to be unity and the beam crossing angle 2θ converted to inverse grating spacing Λ_K^{-1} via Eq. (1). The gain of the nominally undoped SBN increases at shorter wavelengths and approaches that of cerium-doped SBN, indicating an increase in the effective number of photorefractive charges N_{eff} in this sample at short wavelengths. Figure 8 compares the wavelength dependence of the effective number of photorefractive charges N_{eff} with the absorption coefficient α for SBN sample C over the visible wavelength range. In this SBN sample, N_{eff} is approximately a linearly decreasing function of wavelength:

$$N_{\text{eff}} = [-0.0139 \times \lambda(\text{nm}) + 8.4] \times 10^{16} \text{ cm}^{-3}.$$

In contrast, the wavelength dependence of N_{eff} in BaTiO₃ was $\sim \lambda^{-2}$ in one sample²⁷ and N_{eff} was the same at 457.9 and 514.5 nm in another sample.²⁸

D. Sign of the effective photorefractive charge carriers in SBN

The sign of the dominant photorefractive charge carrier in SBN was determined by comparing the direction of two-beam coupling to the direction of the positive c axis of the crystal. The c -axis direction was verified experimentally, subsequent to poling, by observing the sign of a compressionally induced piezoelectric voltage. Comparing this piezoelectric voltage to the direction of beam coupling in each SBN sample indicated that the sign of the dominant photorefrac-

TABLE II Identification (note that these same ID's are used in Figs. 3, 6, and 9), composition x , dopant, and thickness L for seven samples of $\text{Sr}_{1-x}\text{Ba}_x\text{Nb}_2\text{O}_6$. The characterization parameters, including the effective photorefractive charge density N_{eff} , the product of the effective electro-optic coefficient r_{eff} and the hole/electron competition factor $\zeta(K)$, the grating formation rate per unit intensity, the dark conductivity σ_d , the mobility/recombination-time product $\mu\tau_R$, and the diffusion length L_d were obtained from the data in Figs. 6 and 9 at $\lambda = 514.5$ nm using Eqs. (9)–(12).

ID	x (%)	Dop	L (mm)	$N_{\text{eff}} (\times 10^{16})$ (cm ⁻³)	$r_{\text{eff}} \zeta(K)$ (pm/V)	Rate/int (cm ² /W s)	$\sigma_d (\times 10^{-10})$ ($\Omega \text{ cm}$) ⁻¹	$\mu\tau_R (\times 10^{-10})$ (cm ² /V)	L_d (Å)
A	61	---	5.3	0.7	170	0.27	0.92	4.2	330
B	61	---	7.1	1.3	90	0.17	2.65	1.2	170
C	61	---	5.5	1.1	120	0.35	0.69	5.6	380
D	61	Ce	1.7	2.5	150	1.85	0.30	3.5	300
E	61	Ce	4.2	3.4	120	1.05	0.23	2.9	270
F	61	Ce	4.9	1.8	210	1.67	0.20	2.4	250
G	75	Ce	6.0	0.9	280	0.10	0.14	1.7	210

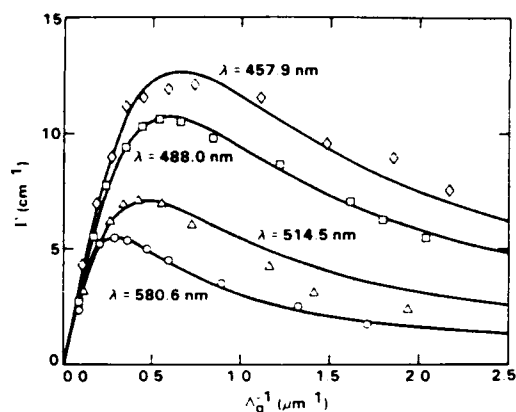


FIG. 7. The wavelength dependence of the two-wave mixing gain coefficient Γ vs inverse grating spacing Λ_g^{-1} in nominally undoped SBN:61 sample C. More impurity states become accessible at shorter optical wavelengths, contributing to a large photorefractive coupling efficiency.

tive charge carrier is negative in all of the SBN samples examined thus far, so that the direction of two-wave mixing gain (and the direction of beam fanning) is toward the positive poling electrode *c* face, in contrast to commercially available²⁰ BaTiO₃.

E. Photorefractive response time of SBN

The photorefractive response time of SBN was determined by measuring the rate of grating formation as a function of the total optical intensity incident on the crystal. Traditionally, one studies grating erasure²⁷⁻²⁸ rather than grating formation, since the former has a simple exponential time dependence while the latter does not.⁴¹ However, the grating formation rates are of more practical importance, and here they are arbitrarily defined to be the inverse of the time for the amplified beam in two-wave mixing to reach $(1 - e^{-1})$ of its steady-state value.

In general, the grating formation rate in SBN increased sublinearly with intensity. Figure 9 shows the measured grating formation rate at 514.5 nm in seven different SBN crystals over the intensity range of ~ 1 –15 W/cm². Over this

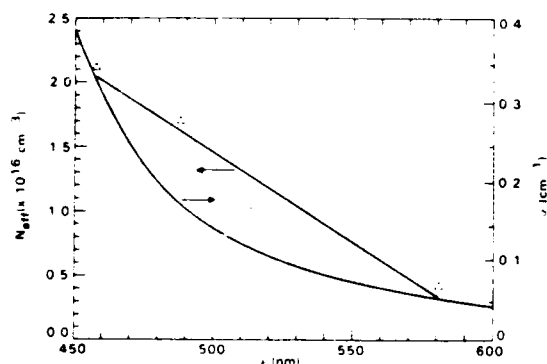


FIG. 8. Comparison of the spectral dependence of the effective photorefractive charge density N_{eff} (left) and the absorption coefficient α (right) in nominally undoped SBN:61 sample C. The straight line is a linear least-square fit to N_{eff} vs λ .

limited intensity range, the rate was approximately linear with an intensity of 1 W/cm² producing a photorefractive grating in ~ 1 s. Note that cerium doping in SBN:61 increases the grating formation rate per unit intensity (slope of the lines in Fig. 9) by a factor of ~ 5 .

The data in Fig. 9 can be used to compute the dark conductivity σ_d and the product of the mobility μ and recombination time τ_R . With no externally applied electric field, and in the limit that the grating spacing is much greater than the diffusion length⁵⁰ (i.e., $\Lambda_g^2 \gg 4\pi^2 \mu \tau_R k_B T / e$), the photorefractive time response τ_{PR} is given by the inverse of the dielectric relaxation rate^{1,50} and can be written as

$$(\tau_{PR})^{-1} = 4\pi(\sigma_d + e\lambda\alpha\mu\tau_R/hc)/\epsilon, \quad (11)$$

where (hc/λ) is the photon energy. Furthermore, the effective mean-free path or diffusion length L_d of the photorefractive charge carrier can simply be estimated as⁵¹

$$L_d = \sqrt{\mu\tau_R k_B T / e}. \quad (12)$$

The fitted values for σ_d and $(\mu\tau_R)$ are obtained from the intercept and slope, respectively, of each line in Fig. 9 for every SBN sample. These values, along with the corresponding L_d , are listed in Table II. Note that the values obtained for $(\mu\tau_R)$ are self-consistent with the assumption⁵⁰ $\Lambda_g \gg 2\pi L_d$. Cerium doping of SBN:61 increases the rate of response and reduces the dark conductivity. The cerium-doped SBN:75 sample also shows a reduced dark conductivity, although this crystal's overall response is relatively slow compared to SBN:61 due to the increase of its dielectric constant ϵ .

In a direct comparison between SBN and BaTiO₃, we found that the erasure and formation rates of a BaTiO₃ crystal obtained from Sanders²⁰ were a factor of 2 faster than the corresponding rates in the undoped SBN sample C, and were approximately one-third of the rates of the Ce-doped SBN sample D.

VI. CONCLUSIONS

In summary, Sr_{1-x}Ba_xNb₂O₆(SBN) can be grown with sufficient size, optical quality, and extrinsic dopants to be suitable for photorefractive applications. Small signal two-wave mixing gains (e^{rL}) exceeding 1000 have been observed in both nominally undoped SBN and cerium-doped SBN. The nominally undoped SBN:61 has an effective photorefractive charge density of $\sim 1 \times 10^{16}$ cm⁻³ and a photorefractive grating formation rate per unit intensity of ~ 0.3 cm²/W s over the intensity range of ~ 1 –15 W/cm² at 514.5 nm. Cerium doping SBN:61 increases the charge density by a factor of ~ 3 and increases the formation rate by a factor of ~ 5 .

SBN potentially exhibits a greater flexibility for doping than other photorefractive materials such as BaTiO₃, due to its open crystal structure containing vacant lattice sites. Currently, effort is underway to optimize the photorefractive response of cerium-doped SBN in the infrared by changing the crystallographic site occupied by the dopant from twelve- to nine- or sixfold coordination. Although the photorefractive efficiency and formation rate are enhanced by cerium doping, the identification of the valence states of ceri-

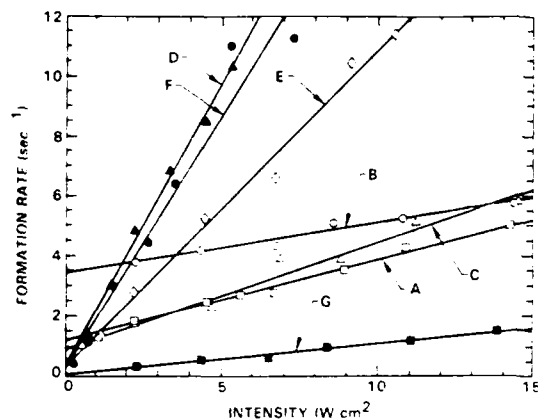


FIG. 9 The rate of photorefractive grating formation during two-wave mixing in nominally undoped SBN 61 samples 4–C, cerium-doped SBN 61 samples D–F and cerium-doped SBN 75 sample G as a function of incident intensity, for $\lambda = 514.5$ nm and $\lambda_c = 2$ μ m. Cerium doping enhances the photorefractive formation rate.

um (e.g., Ce^{3+} or Ce^{4+}) and their role in the photorefractive process remains to be determined.

ACKNOWLEDGMENTS

This work has, in part, been supported by contracts from DARPA and DARPA/AFWAL/Materials Laboratory. The authors appreciate discussions with A. Chiou, M. Khoshnevisan, J. Oliver, and P. Yeh from Rockwell International Science Center, and thank the referee for helpful suggestions.

- ¹N. V. Kukhtarev, V. B. Markov, S. G. Odulov, M. S. Soskin, and V. I. Vinetski, *Ferroelectrics* **22**, 949 (1979); P. Gunter, *Phys. Rep.* **93**, 197 (1982).
- ²P. Yeh, *Proc. Soc. Photo-Opt. Instrum. Eng.* **613** (1986).
- ³J. Feinberg and R. W. Hellwarth, *Opt. Lett.* **5**, 519 (1980); **6**, 257 (E) (1981).
- ⁴J. O. White, M. Cronin-Golomb, B. Fischer, and A. Yariv, *Appl. Phys. Lett.* **40**, 450 (1982).
- ⁵B. Fischer, editor, *Optical Phase Conjugation* (Academic, New York, 1983).
- ⁶J. P. Huignard and A. Marrakchi, *Opt. Commun.* **38**, 249 (1981).
- ⁷F. Laeri, T. Tschudi, and J. Albers, *Opt. Commun.* **47**, 387 (1983).
- ⁸Y. Fainman, E. Klancnik, and S. H. Lee, *Opt. Eng.* **25**, 228 (1986).
- ⁹J. O. White and A. Yariv, *Appl. Phys. Lett.* **37**, 5 (1980).
- ¹⁰J. Feinberg, *Opt. Lett.* **5**, 330 (1980).
- ¹¹E. Ochoa, J. W. Goodman, and L. Hesselink, *Opt. Lett.* **10**, 430 (1985).
- ¹²S.-K. Kwong, G. A. Rakuljic, and A. Yariv, *Appl. Phys. Lett.* **48**, 201 (1986).
- ¹³A. E. Chiou and P. Yeh, *Opt. Lett.* **11**, 306 (1986).

- ¹⁴Y. Fainman, C. C. Guest, and S. H. Lee, *Appl. Opt.* **25**, 1598 (1986).
- ¹⁵M. Cronin-Golomb, B. Fischer, J. Nilsen, J. O. White, and A. Yariv, *Appl. Phys. Lett.* **41**, 219 (1982).
- ¹⁶R. A. McFarlane and D. G. Steel, *Opt. Lett.* **8**, 208 (1983).
- ¹⁷M. D. Ewbank, P. Yeh, M. Khoshnevisan, and J. Feinberg, *Opt. Lett.* **10**, 282 (1985).
- ¹⁸P. Pellat-Finiet and J.-L. De Bougrenet De La Toynaye, *Opt. Commun.* **55**, 305 (1985).
- ¹⁹M. D. Ewbank and P. Yeh, *Opt. Lett.* **10**, 496 (1985).
- ²⁰J.-C. Diels and I. C. McMichael, *Opt. Lett.* **6**, 219 (1981).
- ²¹P. Yeh, M. Khoshnevisan, M. D. Ewbank, and J. Tracy, *Opt. Commun.* **57**, 387 (1986).
- ²²P. Yeh, I. C. McMichael, and M. Khoshnevisan, *Appl. Opt.* **25**, 1029 (1986).
- ²³D. Anderson, *Opt. Lett.* **11**, 56 (1986).
- ²⁴B. H. Soffer, G. J. Dunning, Y. Owechko, and E. Marom, *Opt. Lett.* **11**, 118 (1986).
- ²⁵A. Yariv and S.-K. Kwong, *Opt. Lett.* **11**, 186 (1986).
- ²⁶Sanders Associates, 95 Canal Street, Nashua, NH 03061.
- ²⁷J. Feinberg, D. Heiman, A. R. Tanguay, Jr., and R. W. Hellwarth, *J. Appl. Phys.* **51**, 1297 (1980); **52**, 537 (E) (1981).
- ²⁸S. Ducharme and J. Feinberg, *J. Appl. Phys.* **56**, 839 (1984).
- ²⁹D. Rak, I. Ledoux, and J. P. Huignard, *Opt. Commun.* **49**, 302 (1984).
- ³⁰M. B. Klein and G. C. Valley, *J. Appl. Phys.* **57**, 4901 (1985).
- ³¹S. Ducharme and J. Feinberg, *J. Opt. Soc. Am. B* **3**, 283 (1986).
- ³²M. B. Klein and R. N. Schwartz, *J. Opt. Soc. Am. B* **3**, 293 (1986); M. B. Klein, *Proc. Soc. Photo-Opt. Instrum. Eng.* **519**, 136 (1984).
- ³³J. B. Thaxter and M. Kestigian, *Appl. Opt.* **13**, 913 (1974).
- ³⁴I. R. Dorosh, Y. S. Kuzminov, N. M. Polozkov, A. M. Prokhorov, V. V. Osiko, N. V. Tkachenko, V. V. Voronov, and D. K. Nurligareev, *Phys. Status Solidi A* **65**, 513 (1981).
- ³⁵B. Fischer, M. Cronin-Golomb, J. O. White, A. Yariv, and R. R. Neurgaonkar, *Appl. Phys. Lett.* **40**, 863 (1982).
- ³⁶R. R. Neurgaonkar and W. K. Cory, *J. Opt. Soc. Am. B* **3**, 274 (1986).
- ³⁷G. A. Rakuljic, A. Yariv, and R. R. Neurgaonkar, *Proc. Soc. Photo-Opt. Instrum. Eng.* **613**, 110 (1986); G. A. Rakuljic, A. Yariv, and R. R. Neurgaonkar, *Opt. Eng.* **25**, 1212 (1986).
- ³⁸K. Megumi, H. Kozuka, M. Kobayashi, and Y. Furuhashi, *Appl. Phys. Lett.* **30**, 631 (1977).
- ³⁹V. V. Voronov, I. R. Dorosh, Yu. S. Kuz'minov, and N. V. Tkachenko, *Sov. J. Quantum Electron.* **10**, 1346 (1980).
- ⁴⁰J. Feinberg, *Opt. Lett.* **7**, 486 (1982).
- ⁴¹G. Salame, M. J. Miller, W. W. Clark, G. I. Wood, and E. J. Sharp, *Opt. Commun.* **59**, 417 (1986).
- ⁴²K. Megumi, N. Nagatsuma, Y. Kashiwada, and Y. Furuhashi, *J. Mater. Sci.* **11**, 1583 (1976).
- ⁴³The precise transition temperature in BaTiO_3 from Sanders Associates depends on the impurity level and the oxidation state of the crystal. See Ref. 31.
- ⁴⁴R. J. Pressley, editor, *Handbook of Lasers* (Chemical Rubber, Cleveland, 1971), p. 452.
- ⁴⁵P. Yeh, *J. Opt. Soc. Am. B* **2**, 1924 (1985).
- ⁴⁶I. McMichael and P. Yeh, *Opt. Lett.* **12**, 48 (1987).
- ⁴⁷F. P. Strohkendl, J. M. C. Jonathan, and R. W. Hellwarth, *Opt. Lett.* **11**, 312 (1986).
- ⁴⁸G. C. Valley, *J. Appl. Phys.* **59**, 3363 (1986).
- ⁴⁹L. Solymar and J. M. Heaton, *Opt. Commun.* **51**, 76 (1984).
- ⁵⁰M. B. Klein, *Opt. Lett.* **9**, 350 (1984).
- ⁵¹R. A. Mullen and R. W. Hellwarth, *J. Appl. Phys.* **58**, 40 (1985).



Rockwell International
Science Center SC5441.FTR

SBN AS A BROADBAND SELF-PUMPED PHASE CONJUGATE MIRROR

SBN AS A BROADBAND SELF-PUMPED PHASE CONJUGATE MIRROR

by

Edward J. Sharp, Mary J. Miller, Gary L. Wood,
and William W. Clark, III,
Night Vision and Electro-Optics Center
Fort Belvoir, VA 22060-5677

Gregory J. Salamo
Physics Department
University of Arkansas
Fayetteville, AR 72701

Ratnakar R. Neurgaonkar
Rockwell International Science Center
Thousand Oaks, CA 91360

ABSTRACT

The first observation of self-pumped phase conjugation using total internal reflection in cerium doped strontium barium niobate was described earlier for 442nm radiation [1]. We report here on an expansion of the frequency range from 458nm to 633nm which includes seven argon laser lines and one helium neon laser line. The self-pumped phase conjugate reflectivities for milliwatt beams at near normal incidence to the crystalline c-axis have been measured. Based on these measurements the importance of linear absorption in the operational bandwidth of the phase conjugate mirror is discussed. Applications include low power optical storage devices and optical diodes.

INTRODUCTION

Self-pumped phase conjugation using total internal reflection was first observed in a crystal of BaTiO_3 [2] and later in strontium barium niobate (SBN) [1] and barium strontium potassium sodium niobate (BSKNN) [3]. These self-pumped phase conjugate mirrors (SPPCMs) are completely self-contained and require no external mirrors, pumping beams, or applied electric fields. In addition, such devices are self-starting, self-aligning and require only milliwatt incident beams to produce a phase conjugate.

In a SPPCM the phase conjugate beam is produced by four-wave mixing. However, the two pumping beams that are normally required for four-wave mixing are self-generated within the crystal from the incident beam itself via beam fanning [4]. Light that is asymmetrically defocused by way of the photorefractive effect is internally reflected from faces adjacent to an edge of the crystal thereby forming a two-way loop as shown in Figure 1. This retroreflection of light from the incident beam within the crystal produces the pump beams and leads to the self-alignment and self-starting of the phase conjugate mirror.

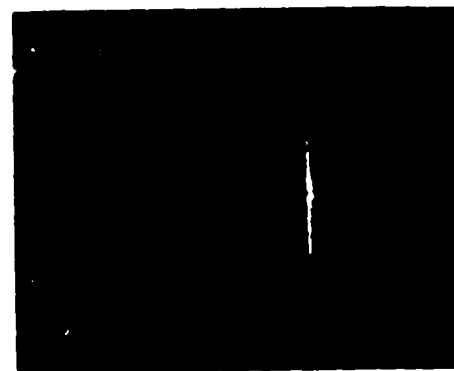


FIGURE 1 Self-pumping corner loop in a 6mm crystal cube of Ce-doped SBN:60.

The ferroelectric crystal $\text{Sr}_{0.6}\text{Ba}_{0.4}\text{Nb}_2\text{O}_6$ (SBN:60) belongs to the tungsten-bronze structural family and has received considerable attention recently due to its attractiveness for electro-optic, photorefractive, pyroelectric and millimeter wave applications [5,6,7]. The first use of SBN:60 as an efficient photorefractive four-wave mixing medium resulted in phase conjugate reflectivities exceeding unity in an undoped crystal [8]. This was quickly followed by a demonstration of passive phase conjugation in undoped SBN:60 based on a self-induced oscillation in an optical ring cavity [9]. The observation of a SPPCM in SBN:60 crystals has yielded phase conjugate reflectivities of 60% in undoped SBN:60 and 30% in Ce-doped SBN:60 at 442nm. These materials have recently been discussed [1] for applications as optical beam deamplifiers [10].

In this paper we report on an expansion of the wavelength range for Ce-doped SBN:60 as a SPPCM and discuss the importance of linear absorption on measured values of the reflectivity.

GROWTH OF DOPED SBN:60 SINGLE CRYSTALS

A comprehensive review of the status of the growth and applications of the tungsten-bronze family crystals, with emphasis on the $\text{Sr}_{1-x}\text{Ba}_x\text{Nb}_2\text{O}_6$ solid solution system, can be found in the paper and references therein by Neurgaonkar and Cory [11]. Of particular interest in this class of materials is SBN:60 since it is the only congruent melting composition in the SrNb_2O_6 - BaNb_2O_6 system [12]. Concentrated crystal growth efforts on this composition has resulted in good optical quality doped and undoped crystals. Boules as large as 2 to 2.5 cm in diameter are now routinely grown.

TABLE I
PHOTOREFRACTIVE PROPERTIES OF
TUNGSTEN BRONZE SBN:60 CRYSTALS

PROPERTY	SBN:60	SBN:60- 0.05% Ce	SBN:60- 0.1% Ce
DIELECTRIC CONSTANT	$\epsilon_{11} = 400$ $\epsilon_{33} = 900$	$\epsilon_{11} = \dots$ $\epsilon_{33} = 1000$	$\epsilon_{11} = \dots$ $\epsilon_{33} = 1100$
ELECTRO-OPTIC COEFFICIENT $\times 10^{12}$ m/V	$r_{22} = 420$	$r_{22} > 420$	$r_{22} > 420$
T_c (C°)	78	75	72
PHOTOREFRACTIVE SENSITIVITY (cm^2/J)	3.5×10^{-4}	8.5×10^{-4}	6.5×10^{-4}
RESPONSE TIME (ms)	1000	80	80
GROWTH TEMPERATURE (C°)	1500	1490	1485
GROWTH DIRECTION	[001]	[001]	[001]
COLOR OF CRYSTAL	PALE CREAM	PINK	PINK

These large optical-quality crystals of both Ce-doped and undoped SBN:60 have been grown by suppressing the problems associated with coring and striation. To date, attempts to suppress striations in Fe-doped SBN:60 have been unsuccessful. In the tungsten-bronze structure, Ce^{3+} and Ce^{4+} are expected to occupy 9 and 12-fold sites, while Fe^{2+} and Fe^{3+} ions are expected to occupy 6-fold coordinated sites. This suggests that the existence of striations in SBN:60 crystals depends strongly on the type of dopant and its location in the structure [11]. Table I summarizes the growth conditions and the physical properties of Ce-doped and undoped SBN:60 crystals which were cut into approximately 6x6x6mm cubes, optically polished, and poled to a single domain for photorefractive and SPPCM studies.

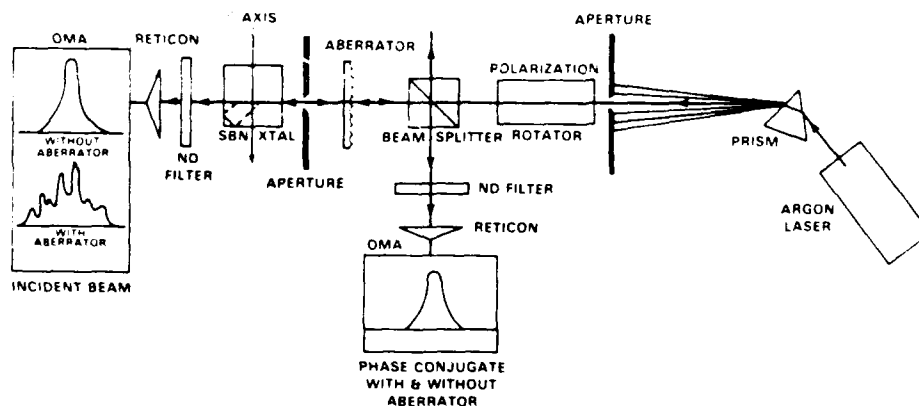


FIGURE 2 Experimental arrangement for measuring phase conjugate reflectivities.

EXPERIMENT

The experimental apparatus used for the self-pumped phase conjugate reflectivity measurements is shown in Figure 2. Phase conjugate reflectivities were measured at 442nm (He/Cd), seven argon-ion laser lines from 458nm to 515nm, and at 632.8nm (He/Ne). When the He/Cd and He/Ne lasers were used the beams were inserted directly into the polarization rotator. All beams were incident on the crystal unfocused and polarized extraordinary to take advantage of the large r_{33} ($>420 \times 10^{-12}$ m/V) electro-optic coefficient in SBN:60. The aperture directly in front of the crystal was intended to verify that the beams were incident at the same point on the front face and at the same angle. The laser output powers ranged from 0.2mW at 472nm to 15mW at 488nm. Beam diameters at the $1/e$ points of the peak-on-axis intensity ranged from 1.05mm to 2.2mm.

Extraordinary polarized light was used to write gratings while ordinary polarized light was used to erase the gratings. Although detailed data is not yet available, we have observed dark-storage times for gratings in Ce-doped SBN:60 in excess of four days. The beamsplitter was used to extract a calibrated fraction of the phase conjugate intensity. Both the input and the output intensities were monitored using an optical multi-channel analyzer (OMA) or photodiodes. The OMA was particularly useful in allowing comparisons of peak

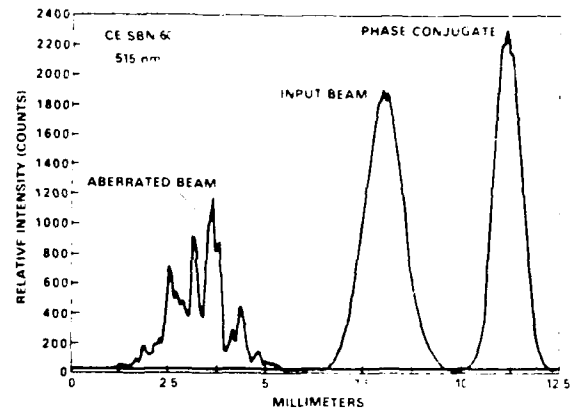


FIGURE 3 A comparison of spatial beam profiles to verify phase conjugation. Relative peak intensities are arbitrary.

intensities, beam shape, and testing for phase conjugation. For example, when an input Gaussian beam was propagated through a phase aberrator, the aberrated, input and phase conjugated beams could be observed on the OMA (Figure 3). This made it possible to verify that the distortion introduced by the aberrator was indeed reversed via phase conjugation by the SPPCM. All values of the phase conjugate reflectivity are for steady state and are shown in Figure 4 as a function of

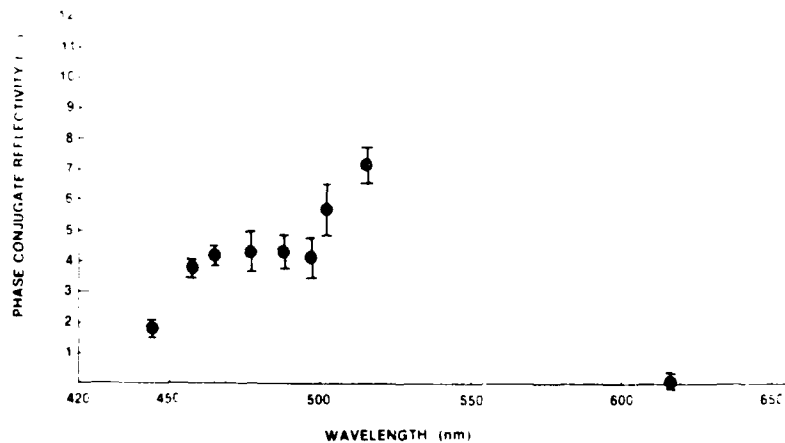


FIGURE 4 The phase conjugate reflectivity of the Ce-doped SBN:60 self-pumped phase conjugate mirror as a function of wavelength.

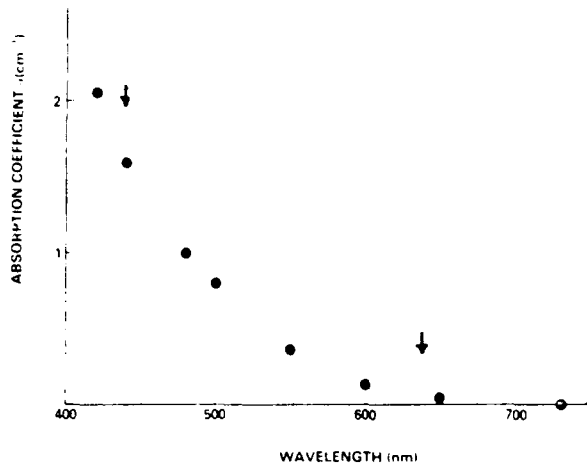


FIGURE 5 The absorption coefficient for SBN as a function of wavelength.

The wavelength dependence of the absorption coefficient for ordinary polarized light in our Ce-doped SBN:60 sample is shown in Figure 5. The limits of the wavelength region used in the SPPCM study of the Ce-doped material is indicated by the tick marks which correspond to 442nm and 632.8nm. The total transmission of the sample (~5mm thick) changed approximately 40% in this wavelength range due to the introduction of cerium ions into the SBN:60 crystal lattice.

RESULTS AND DISCUSSION

In order to gain an understanding of the importance of such strong absorption on the phase conjugate reflectivity in these doped samples a pumping geometry was selected to minimize changes in the beam coupling strength. In particular, we selected the near normal pumping geometry as shown in Figure 6 which served to fix the two pump beams within the crystal at angles $\alpha_1 \approx 90^\circ$ and $\alpha_2 \approx 80^\circ$ with respect to the crystal c-axis. This pumping geometry approximately corresponds to the optimized value of the coupling coefficient in SBN:60 [1]. Under these conditions we can write the coupling coefficient γ , as [2],[13]:

$$\gamma = \frac{r_{\text{eff}} E}{2nc \cos((\alpha_1 - \alpha_2)/2)}$$

where the electric field is:

$$E = \frac{K_B T}{e} \frac{k}{1 + (k/k_0)^2}$$

and $K_B = (Nq^2 / \epsilon_0 \epsilon_r) / (k_B T)$, $N = 10^{21} \text{ cm}^{-3}$ is the number density of charges available for grating formation which originate from

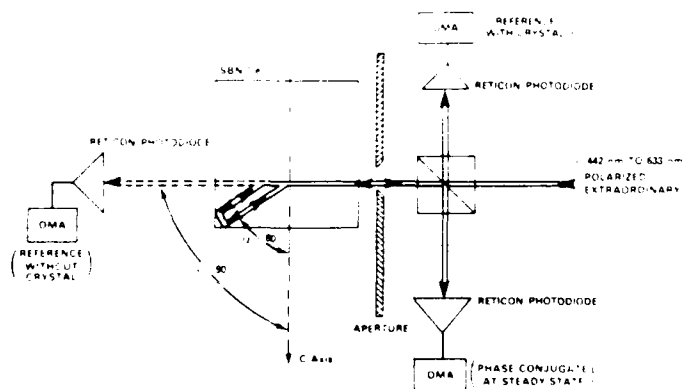


FIGURE 6 Details of pumping geometry used to analyze λ -dependence of Ce-doped SBN:60 SPPCM.

traps of unknown depth and which decrease with increasing wavelength, $\omega = 2\pi c/n\lambda$ is the optical frequency, $n=n(\lambda)$ is the refractive index which is λ -dependent due to the strong absorption in the region of interest, $k_B T/q$ is the thermal energy per charge, $\epsilon\epsilon_0$ is the dielectric constant in the grating direction, and $k = 2(n\lambda/c)\sin[(\alpha_1 - \alpha_2)/2]$ is the magnitude of the grating wave vector k . SBN:60 belongs to the 4mm symmetry point group so that for extraordinary rays r_{eff} is given by [13],[14]:

$$r_{eff} = [n_o^4 r_{13} \cos\alpha_1 \cos\alpha_2 + \frac{n_o^2 n_e^2}{n_o^2 - n_e^2} r_{42} \sin\alpha_1 \sin\alpha_2 + \frac{n_o^2 n_e^2}{n_o^2 - n_e^2} r_{33} \sin\alpha_1 \sin\alpha_2 \sin[(\alpha_1 + \alpha_2)/2]]$$

Note that r_{eff} is a complicated function of λ , explicitly through α_1 and α_2 and implicitly through $N(\lambda)$ and $n(\lambda)$. Using the near constancy of $(\alpha_1 - \alpha_2)$ and putting only the explicit wavelength dependence occurring through α_1 in these expressions we can write r_{eff} as:

$$r_{eff} = \frac{r_{13} \cos\alpha_1}{\cos\alpha_2} \approx r_{13} \cos\alpha_1$$

In Figure 7, the explicit wavelength dependence of the coupling coefficient at normal incidence for Ce-doped SBN:60 is given by the solid curve. When the implicit λ -dependence of both the dispersion in the index of refraction [15] and the charge carrier density $N(\lambda)$ is

also considered, the coupling coefficient is given by the dashed curve. Here we have assumed a $1/\lambda^2$ dependence on N [13]. This is a reasonable assumption since our data was taken on the high wavelength side of the impurity-related absorption profile [16]. It should be noted that the strong wavelength dependence of $r_{eff}(\lambda)$ is not evident in the measured phase conjugate reflectivity data of Figure 4. On the contrary, the phase conjugate reflectivity is seen to increase with λ until at least a value of 515nm. We suggest that the effects of linear absorption in the wavelength region of our measurements is responsible for this surprising behavior. Of course, the reflectivity must eventually fall to zero due to its threshold behavior as a function of the coupling strength, r_{eff} [17].

As can be seen in the absorption coefficient data, shown in Figure 5, the intensity loss by a pumping beam as it reflects from one interaction region into the other (Figure 1) is also heavily dependent on wavelength. As first pointed out in a paper by MacDonald and Feinberg [17], the rather large coupling losses will substantially diminish the reflectivity of the SPPCM. As a result, the reflectivity is predicted to decrease with increasing wavelength, due to the decrease in the coupling coefficient r_{eff} , but simultaneously predicted to increase due to the lower coupling loss. These two opposing effects lead to the data in Figure 4. In this case, therefore, absorption plays a significant role in determining the reflectivity of SBN as a self-pumped phase conjugate mirror.

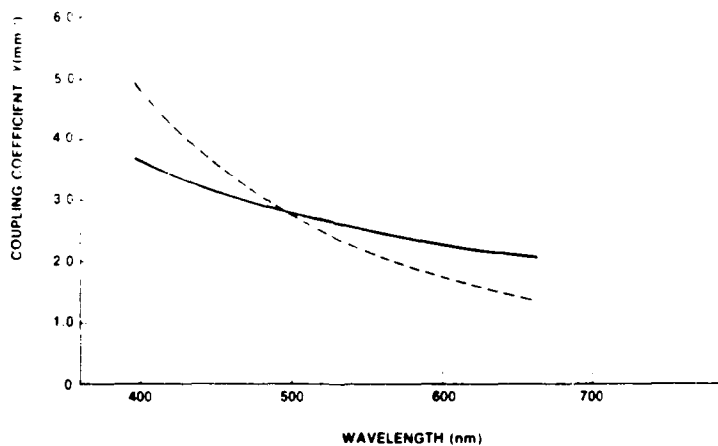


FIGURE 7 The steady-state coupling strength per unit length as a function of wavelength.

REFERENCES

- [1] G. Salamo, M.J. Miller, W.W. Clark, III, G.L. Wood and E.J. Sharp, "SBN as a Self-Pumped Phase Conjugator," Opt. Comm. (to be published) 1986.
- [2] J. Feinberg, "Self-Pumped, Continuous-Wave, Phase Conjugator Using Internal Reflection," Opt. Lett., Vol. 7, pp. 486-488, 1982.
- [3] We have observed self-pumped phase conjugation in BSKNN over the same wavelength range reported here. Details of these measurements are being prepared for publication.
- [4] J. Feinberg, "Asymmetric Self-Defocusing of an Optical Beam from the Photorefractive Effect," J. Opt. Soc. Am., Vol. 72, pp. 46-51, 1981.
- [5] O. Eknoyan, C.H. Bulmer, H.F. Taylor, W.K. Burns, A.S. Greenblatt, L.A. Beach and R.R. Neurgaonkar, "Vapor Diffused Optical Waveguides in Strontium Barium Niobate (SBN:60)," Appl. Phys. Lett., Vol. 98, pp. 13-18, 1986.
- [6] A.M. Glass, "Investigations of the Electrical Properties of $\text{Sr}_{1-x}\text{Ba}_x\text{Nb}_2\text{O}_6$ with Special Reference to Pyroelectric Detectors," J. Appl. Phys., Vol. 40, pp. 4699-4713, 1968.
- [7] W.W. Ho, W.F. Hall and R.R. Neurgaonkar, "Dielectric Properties of Ferroelectric Tungsten Bronze $\text{Ba}_{2-x}\text{Sr}_x\text{K}_{1-x}\text{Nb}_5\text{O}_{15}$ Crystals at RF and Millimeter Wave Frequencies," Ferroelec., Vol. 50, pp. 325-330, 1983.
- [8] B. Fischer, M. Cronin-Golomb, J.O. White, A. Yariv and R.R. Neurgaonkar, "Amplifying Continuous-Wave Phase Conjugate Mirror with Strontium Barium Niobate," Appl. Phys. Lett., Vol. 40, pp. 863-865, 1982.
- [9] M. Cronin-Golomb, B. Fischer, J.O. White and A. Yariv, "Passive Phase Conjugate Mirror Based on Self-Induced Oscillation in an Optical Ring Cavity," Appl. Phys. Lett., Vol. 42, pp. 919-921, 1983.
- [10] M. Cronin-Golomb and A. Yariv, "Optical Limiters Using Photorefractive Nonlinearities," J. Appl. Phys., Vol. 57, pp. 4906-4910, 1985.
- [11] R.R. Neurgaonkar and W.K. Cory, "Progress in Photorefractive Tungsten Bronze Crystals," J. Opt. Soc. Am., Vol. 3, pp. 274-282, 1986.
- [12] K. Megumi, N. Nagatsuma, K. Kashiwada and Y. Furuhashi, "Congruent Melting Compositions of SBN," Mat. Sci., Vol. 11, pp. 1583-1592, 1976.
- [13] J. Feinberg, D. Heiman, A.R. Tanguay, Jr. and R.W. Hellwarth, "Photorefractive Effects and Light-Induced Charge Migration in Barium Titanate," J. Appl. Phys., Vol. 51, pp. 1297-1305, 1980.
- [14] J. Feinberg and R.W. Hellwarth, "Phase-Conjugating Mirror with Continuous Wave Gain," Opt. Lett., Vol. 5, pp. 519-521, 1980.
- [15] The dispersion in the extraordinary index of refraction for the Ce-doped SBN:60 has been measured from 400 to 750nm with values of 2.460 to 2.260, respectively. Details are being prepared for publication.
- [16] Measurement of the transmission spectrum of both a doped and undoped SBN sample show a peak in the impurity-related absorption profile to occur near 420nm and fall to zero near 750nm.
- [17] K.R. MacDonald and J. Feinberg, "Theory of a Self-Pumped Phase Conjugator with Two Coupled Interaction Regions," J. Opt. Soc. Am., Vol. 73, pp. 548-553, 1983.



Rockwell International

Science Center SC5441.FTR

BROADBAND PHOTOREFRACTIVE PROPERTIES AND SELF-PUMPED PHASE
CONJUGATION IN Ce-DOPED SBN:60

Broadband Photorefractive Properties and Self-Pumped Phase Conjugation in Ce-SBN: 60

**Gary L. Wood
William W. Clark III
Mary J. Miller
Edward J. Sharp
Gregory J. Salamo
Ratnakar R. Neurgaonkar**

**Reprinted from
IEEE JOURNAL OF QUANTUM ELECTRONICS
Vol. QE-23, No. 12, December 1987**

Broadband Photorefractive Properties and Self-Pumped Phase Conjugation in Ce-SBN:60

GARY L. WOOD, WILLIAM W. CLARK III, MARY J. MILLER, MEMBER, IEEE, EDWARD J. SHARP, GREGORY J. SALAMO, AND RATNAKAR R. NEURGAONKAR

Abstract—The first use of cerium-doped $\text{Sr}_{0.6}\text{Ba}_{0.4}\text{Nb}_2\text{O}_6$ as a broadband self-pumped phase-conjugate mirror using internal reflection is reported. The phase-conjugate reflectivity at normal incidence ranged from two percent at 442 nm to seven percent at 515 nm and was zero at 633 nm. The electron-hole competition was found to be significant and had a wavelength dependence in one sample but not the other. The charge carrier density was $\sim 7 \times 10^{16} \text{ cm}^{-3}$ and was wavelength independent. The absorption coefficient ranged from 2 cm^{-1} at the shorter wavelengths to zero at longer wavelengths. The dispersion in the indexes of refraction was measured and the birefringence was -0.036 . The sign of the dominant charge carriers was determined to be negative and the sign of the electrooptic coefficient, r_{33} , was positive. Using the above values, a wavelength dependent coupling coefficient has been determined. The experimental results indicate that the phase-conjugate reflectivity decreases at shorter wavelengths due to increased absorptive losses and experiences a threshold effect at longer wavelengths.

INTRODUCTION

THE ferroelectric crystal $\text{Sr}_{0.6}\text{Ba}_{0.4}\text{Nb}_2\text{O}_6$ (SBN:60) belongs to the tungsten-bronze structural family and has received considerable attention recently due to its attractiveness for electrooptic, photorefractive, pyroelectric, and millimeter wave applications [1]–[3]. It was shown to be an efficient two-beam mixing material by Megumi *et al.* [4] after the introduction of Ce-ions as impurity dopants. The first use of undoped SBN:60 as a photorefractive four-wave mixing medium employed external pumping beams and resulted in phase-conjugate reflectivities exceeding unity [5]. This was quickly followed by a demonstration of passive phase conjugation in undoped SBN:60 based on self-induced oscillation in an optical ring cavity [6]. The first use of SBN:60 as a self-pumped phase-conjugate mirror (SPPCM) requiring no external mirrors or pumping beams, yielded phase-conjugate reflectivities of 60 percent in undoped crystals and 30 percent in Ce-doped crystals at 442 nm [7]. To date only three crystals have demonstrated self-pumped phase conjugation: BaTiO_3 [8], SBN [7], [9], and BSKNN [10].

In this paper, we present our experimental data characterizing Ce-doped SBN:60 as a broadband photorefrac-

tive material. Specifically, we demonstrate for the first time self-pumped phase conjugation in this material over a broad spectral range in the visible. We have determined the charge carrier density, the electron-hole competition, and the gain coupling coefficient through two-beam coupling measurements at 488 nm and 633 nm. In addition, we have measured the refractive indexes, the absorption coefficient, and the poling factor. By taking the dispersion of these measured parameters into account, we provide a calculation of the wavelength dependence of the coupling coefficient and explain the relationship of absorption to self-pumped phase conjugation.

GROWTH OF DOPED SBN:60 SINGLE CRYSTALS

A comprehensive review of the status of the growth and applications of the tungsten-bronze family crystals, with emphasis on the $\text{Sr}_{1-x}\text{Ba}_x\text{Nb}_2\text{O}_6$ solid-solution system, can be found in the paper and references therein by Neurgaonkar and Cory [11]. Of particular interest in this class of materials is SBN:60 since it is the only congruent melting composition in the SrNb_2O_6 – BaNb_2O_6 system [12]. Concentrated crystal growth efforts on this composition have resulted in good optical-quality doped and undoped crystals. Boules as large as 2 to 2.5 cm in diameter are now routinely grown and allow the fabrication of photorefractive crystal cubes approaching 2 cm on a side (see Fig. 1).

These large optical-quality crystals of both Ce-doped and undoped SBN:60 have been grown by suppressing the problems associated with coring and striation. The addition of cerium produces a broadband absorption in the visible which enhances the photorefractive effect considerably in this crystal [4], [13]. In the tungsten-bronze structure, Ce^{3+} and Ce^{4+} ions are expected to occupy 9- and 12-fold sites, while Fe^{2+} and Fe^{3+} ions are expected to occupy 6-fold coordinated sites. To date, attempts to suppress striations in Fe-doped SBN:60 have been unsuccessful. This suggests that the existence of striations in SBN:60 crystals depends strongly on the type of dopant and its location in the structure [11]. Table I summarizes the growth conditions and typical physical properties of Ce-doped and undoped SBN:60 crystals.

For our photorefractive and SPPCM studies, high optical-quality SBN:60 samples, both undoped and nominally-doped with cerium, were cut from different boules, optically polished, and poled to a single domain. In all,

Manuscript received March 9, 1987; revised June 12, 1987.

G. L. Wood, W. W. Clark III, M. J. Miller, and E. J. Sharp are with the Center for Night Vision and Electro-Optics, Fort Belvoir, VA 22060.

G. J. Salamo is with the Department of Physics, University of Arkansas, Fayetteville, AR 72701.

R. R. Neurgaonkar is with the Rockwell International Science Center, Thousand Oaks, CA 91360.

IEEE Log Number 8717189.

CE-DOPED SBN:60 CRYSTAL
GROWTH DIRECTION, [001]

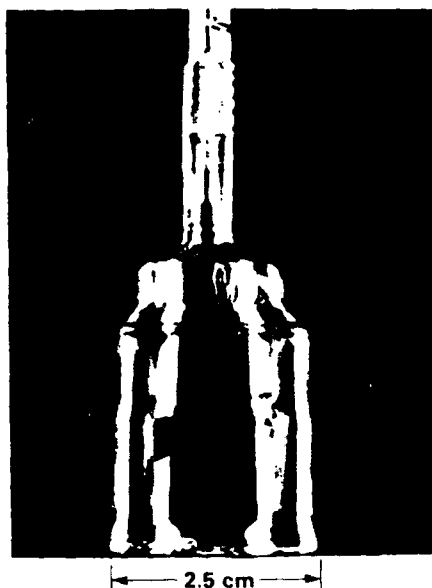


Fig. 1. A photograph of an as-grown boule of Ce-doped SBN:60. The long dimension of the boule defines the growth direction [001] and the crystal *c* axis.

TABLE I
PHOTOREFRACTIVE PROPERTIES OF TUNGSTEN-BRONZE SBN:60 CRYSTALS

PROPERTY	SBN:60	Ce-SBN:60
DIELECTRIC CONSTANT	$\epsilon_{11} = 470^a$ $\epsilon_{33} = 880^a$	$\epsilon_{11} = 470^a$ $\epsilon_{33} = 1100^a$
ELECTRO OPTIC COEFFICIENT $\times 10^{-12}$ m/V	$r_{13} = 55^b$ $r_{33} = 224^b$ $r_{42} = 80$	$r_{13} = 55^b$ $r_{33} = 224^b$ $r_{42} = 80$
REFRACTIVE INDEX (514.5 nm)	$n_o = 2.367^c$ $n_e = 2.337^c$	$n_o = 2.346^e$ $n_e = 2.310^e$
BIREFRINGENCE $\Delta n = n_e - n_o$	$\Delta n = -0.03^c$	$\Delta n = -0.036^e$
T_c (°C)	75°	72°
PHOTOREFRACTIVE SENSITIVITY (Cm^2/J)	$3.2 \times 10^{-5}^d$	$6.5 \times 10^{-3}^d$
RESPONSE TIME (ms)	1000°	80°
GROWTH TEMPERATURE (°C)	1500°	1485°
GROWTH DIRECTION	[001] ^d	[001] ^d
COLOR OF CRYSTAL	PALE CREAM ^d	PINK ^d

^aReference [11]

^bReference [21]

^cReference [33]

^dReference [34]

^eThis paper

measurements were carried out on four different samples. Crystal #1 was a Ce-doped wedge-shaped sample (23° apex angle) used to measure the indexes of refraction. Crystal #2 was an undoped 6 × 5 × 5 mm sample used for comparative purposes. Crystals #3 (6.5 mm cube) and 4 (3.5 × 6.5 × 9.0 mm slab) were both cerium-doped and were used for photorefractive measurements.

EXPERIMENTAL RESULTS

Material Properties

The total transmission of our Ce-doped and undoped SBN:60 samples can be seen in Fig. 2, showing that the doped SBN:60 crystals will be particularly sensitive in the blue-green region due to the introduction of cerium

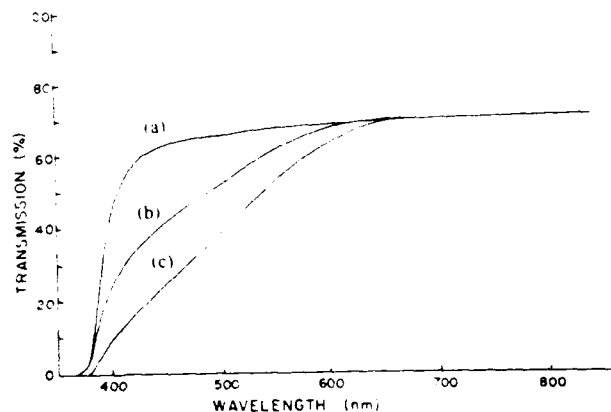


Fig. 2. The transmission spectra of SBN:60 (a) Crystal #2 (undoped), thickness = 5.0 mm. (b) Crystal #4 (Ce-doped), thickness = 3.5 mm. (c) Crystal #3 (Ce-doped), thickness = 6.5 mm.

ions into the 12-fold coordinated sites of the SBN:60 crystal lattice. The wavelength dependence of the absorption coefficient for ordinary polarized light in crystal #4 is shown in Fig. 3.

The strong absorption in the ultraviolet is mainly responsible for the dispersion in the index of refraction. The ordinary and extraordinary indexes of refraction were measured as a function of wavelength and are shown in Fig. 4. These values (points) were obtained using the minimum angle of deviation technique on a poled 23° wedge of Ce-doped SBN:60 (crystal #1). The dispersion relationships are

$$n_o = A_o \lambda^2 + B_o \lambda + C_o$$

and

$$n_e = A_e \lambda^2 + B_e \lambda + C_e$$

(1)

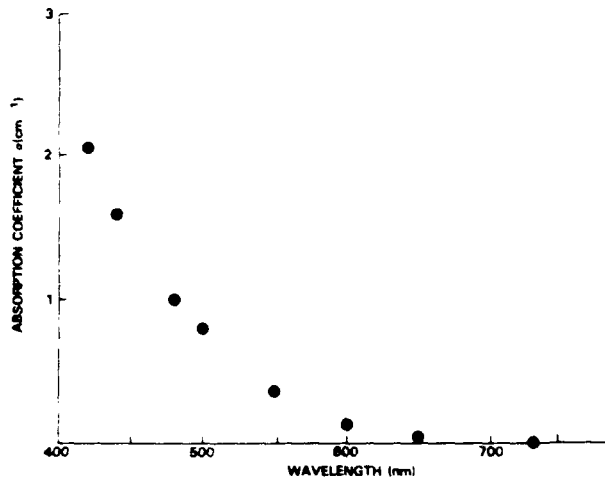


Fig. 3. The absorption coefficient for Ce-doped SBN:60 as a function of wavelength (crystal #4).

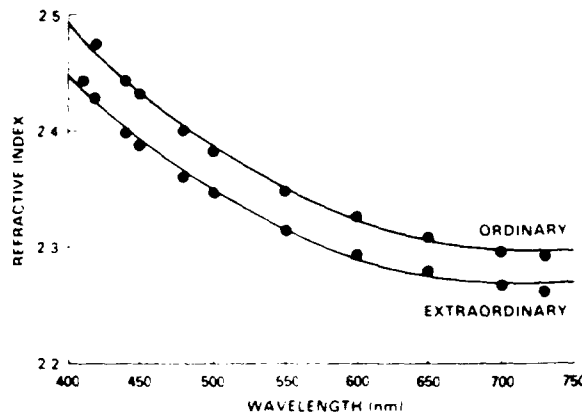


Fig. 4. Measured refractive index for Ce-doped SBN:60 as a function of wavelength (crystal #1).

where $A_0 = 1.877 \times 10^{-6}/\text{nm}^2$, $B_0 = -2.708 \times 10^{-3}/\text{nm}$, $C_0 = 3.272$, $A_e = 1.826 \times 10^{-6}/\text{nm}^2$, $B_e = -2.608 \times 10^{-3}/\text{nm}$, and $C_e = 3.197$. These relationships represent the best fit to the measured data (normalized rms deviation of fit ~ 0.2 percent). We can estimate the birefringence from these curves to be $\Delta n = (n_e - n_o) \sim -0.036$.

The sign of the largest electrooptic coefficient r_{33} was determined to be positive for all samples by use of a calibrated compensator [14]. This fact, coupled with the observation that extraordinary light fans toward the electrode held positive during poling, gives a negative sign for the photorefractive charge carriers, as similarly found in BSKNN [10]. By comparison, under normal growth conditions the charge carriers in BaTiO_3 are positive and extraordinary light fans toward the negative poling electrode [14], [15].

Two-Beam Coupling

Steady-state two-beam coupling measurements were made on crystals #3 and 4 at 488 and 633 nm. The mea-

surements were made using ordinary polarized light after the technique described by Ducharme and Feinberg [15]. A beam splitter was used to direct coherent Gaussian beams through the crystals such that the grating wave vector, k_g , was parallel to the c axis direction. The beam intensities were chosen so that $I_{01} \ll I_{02}$ and were introduced into the crystal such that the weaker beam, I_1 , experienced gain. The two beams were incident in a plane normal to the crystal at an external crossing angle 2θ , where θ defines the angle between the incident beam and a normal to the c axis of the crystal. For these conditions $k_g = 2(\omega/c) \sin \theta$. The transmitted intensity of the weak beam was monitored with and without coupling, I_{1c} and I_1 , respectively. Intensity ratios of $m = I_{01}/I_{02} = 1/85$ for 633 nm and $m = 1/106$ for 488 nm were used to permit theoretical modeling [14], [16]. Under these conditions, the weak beam, I_1 , experiences an increase in intensity along its direction of propagation given by [17]

$$\frac{I_{1c}}{I_1} = \frac{(1 + m) \exp(\gamma L_{\text{eff}})}{1 + m \exp(\gamma L_{\text{eff}})} \quad (2)$$

where for small m

$$I_{1c}/I_1 \sim \exp(\gamma L_{\text{eff}}) \quad (3)$$

In the above equations, L_{eff} is the interaction length and γ is the two-beam energy-coupling gain coefficient. The beam crossing angles were selected such that the overlap region of the input beams extended the entire thickness of the crystal making $L_{\text{eff}} = 6.5$ mm for crystal #3 and 3.5 mm for crystal #4. The coupling coefficient is given by [15], [18], [19]

$$\gamma = \frac{R 2 \pi r_{\text{eff}} k_B T k_g}{\lambda n \cos \theta q [1 + (k_g/k_0)^2]} \quad (4)$$

where $k_0^2 = q^2 N_{\text{eff}}/k_B T \epsilon \epsilon_0$, $k_B T/q$ is the thermal energy per charge, $\epsilon \epsilon_0$ is the dielectric constant in the grating direction, and $N_{\text{eff}} = N_A(1 - N_A/N_D)$ is the effective density of photorefractive charges. Here, N_D is the number of donor sites and N_A is the number of trap sites under dark conditions and $N_D > N_A$. The parameter R gives a measure of the electron-hole competition in the formation of the space-charge field. The values of R range from -1 to $+1$ where ± 1 indicates no competition and a zero value indicates equal competition. $r_{\text{eff}} = R_{\text{eff}} \times F$ is an effective electrooptic coefficient which depends on the polarization state of the crossing beams, the crystal symmetry and the fractional poling factor F [18]. SBN:60 belongs to the 4 mm symmetry point group so that for extraordinary rays R_{eff} is given by

$$R_{\text{eff}} = n_e^4 r_{33} \cos^2 \theta - n_o^4 r_{13} \sin^2 \theta \quad (5)$$

and for ordinary rays, R_{eff} is given by

$$R_{\text{eff}} = n_o^4 r_{13} \quad (6)$$

The fractional poling factor is included in r_{eff} to account for the 180° domains which could exist if the sample is not completely poled. The poling factor for crystal #3 was

measured to be 0.94 [20]. The poling factor for crystal #4 will be assumed to be 1.0.

Our two-beam coupling data was taken with a total input intensity ($I_{01} + I_{02}$) of 15 mW/cm². The results were found to be intensity independent above a total input intensity of 1.5 mW/cm². This indicates that the dark conductivity was small compared to the photoconductivity over the regime of our measurements; thus R and γ were independent of intensity. In addition, the dark decay time of these crystals was on the order of a few days, which indicates a dark conductivity of approximately 1×10^{-15} ($\Omega \text{ cm}$)⁻¹.

The ratio of I_{lc}/I_l (ordinary light) was measured as a function of the external angle θ . The data was taken on a chart recorder to ensure that a steady state was reached. The normalized experimental points are shown in the plot of k_g/γ versus k_g^2 in Fig. 5. By plotting the data in this way, a straight line fit is obtained from (4). A deviation from a straight line fit in crystal #4 [Fig. 5(a)] for the normalized $k_g^2 > 0.1$ indicates a slight dependence of R on k_g which becomes apparent at larger crossing angles. This dependence was further evidenced by measuring the coupling at the $\sim 180^\circ$ crossing angle, which yielded a value of k_g/γ that was larger than the straight line fit by a factor of three.

The y-intercept of the fitted lines in Fig. 5 determines $r_{eff}R$ and the slope determines N_{eff} . With ordinary light, $r_{eff}R$ can be written as $Rn_0^2r_{13}F$. If the value of 55 pm/V is assumed for the r_{13} electrooptic coefficient [21] and the value of F is as given earlier, then R and N_{eff} can be found. This procedure gave a value of N_{eff} for crystals #3 and 4 which changed very little from 488 to 633 nm; $N_{eff} \sim 7 \pm 0.5 \times 10^{16} \text{ cm}^{-3}$. In crystal #3, R was found to vary only slightly, from 0.58 at 488 nm to 0.62 at 633 nm. Crystal #4, by contrast, varied from $R = 0.32$ at the 488 nm line to $R = 0.45$ at the 633 nm line. These values indicate significant electron-hole competition in both crystals and show that the electron-hole competition can be wavelength dependent. Using the values of N_{eff} and R above, γ is plotted versus external angle in Fig. 6.

Other samples of SBN, both cerium-doped and undoped, were studied recently by Ewbank *et al.* [22] and found to have a smaller N_{eff} than our crystals. In addition, N_{eff} was found to vary with wavelength in an undoped sample. Another difference involved the dark decay time which was on the order of seconds for their samples compared to days for ours. The observed differences in these parameters are related to the dopant concentration which can be controlled during crystal growth.

Self-Pumped Phase Conjugation

The self-pumped phase-conjugate mirrors (SPPCM's) discussed here are completely self-contained and require no external mirrors [23], [24], pumping beams [25], or applied electric fields. In addition, such devices are self-starting, self-aligning, and require only milliwatt incident beams to produce a phase-conjugate. In an SPPCM, the phase-conjugate beam is produced by four-wave mixing.

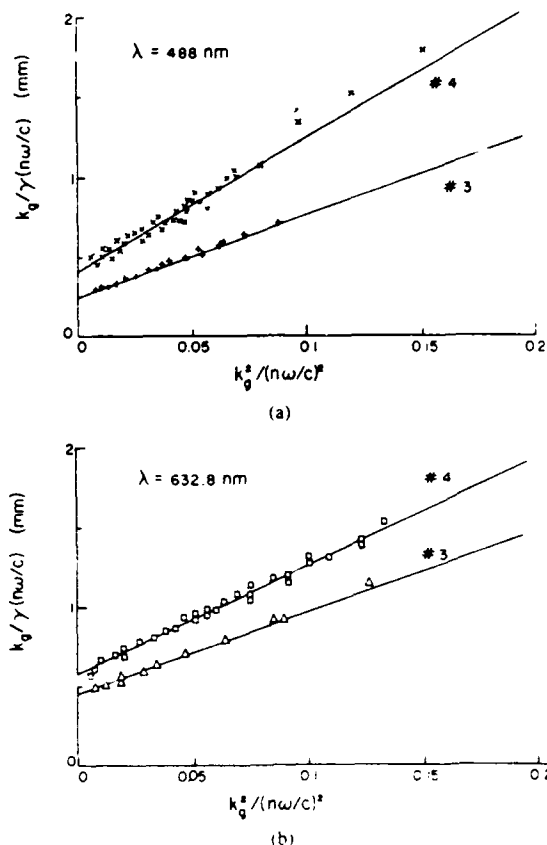


Fig. 5. Normalized plots of the inverse of the coupling coefficient γ times the grating period k_g as a function of k_g^2 for Ce-doped SBN 60 crystals #3 and 4. The fitted lines determine the values of N_{eff} and R . (a) 488 nm—#3, $R = 0.58$, $N_{eff} = 7.0 \times 10^{16} \text{ (cm)}^{-3}$, #4, $R = 0.32$, $N_{eff} = 7.0 \times 10^{16} \text{ (cm)}^{-3}$. (b) 633 nm—#3, $R = 0.62$, $N_{eff} = 7.0 \times 10^{16} \text{ (cm)}^{-3}$, #4, $R = 0.45$, $N_{eff} = 6.6 \times 10^{16} \text{ (cm)}^{-3}$.

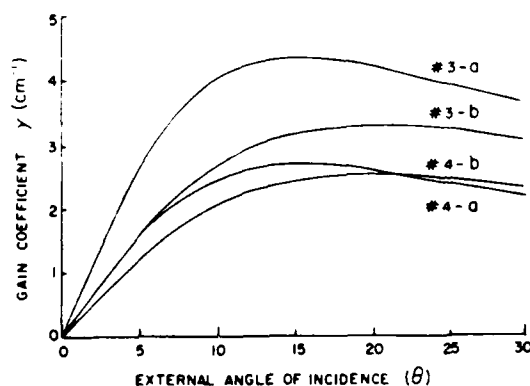


Fig. 6. The coupling coefficient γ as a function of the external angle of incidence, θ , for Ce-doped SBN 60 crystals #3 and 4. These curves were drawn using the R 's and N_{eff} 's determined in Fig. 5. (a) 488 nm. (b) 633 nm.

However, the two pumping beams that are normally required for four-wave mixing are self-generated within the crystal from the incident beam via stimulated scattering (beam fanning) [26]. Light that is "fanned" via the photorefractive effect is internally reflected from faces adja-

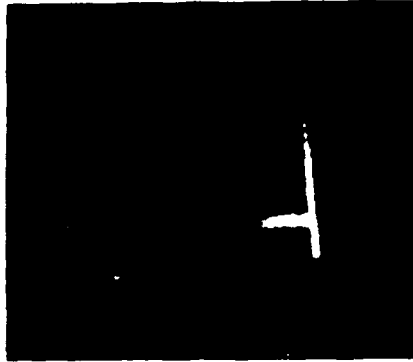


Fig. 7. A photograph of a Ce-doped SBN:60 crystal taken while the crystal was self-pumping. The c -axis of the crystal is directed from the bottom to the top of the photograph and the extraordinary polarized beam at 442 nm is propagating from right to left, entering the crystal with a positive angle of incidence. That is, the incident beam was heading in the general direction of the top left corner and then curved down to the bottom left corner of the crystal.

cent to an edge of the crystal thereby forming a two-way corner loop [8]. This retroreflection of light within the crystal provides feedback for the four-wave mixing process leading to the self-alignment and self-starting of the phase-conjugate mirror. Fig. 7 is a photograph showing the top view of a Ce-doped SBN:60 crystal while the crystal is self-pumping in the steady state for an incident beam angle of 50° . The crystal is in air and is being pumped with the 442 nm line of a HeCd laser [7]. The illuminated front face of the crystal is due to imperfections in the polished surface.

The experimental apparatus used for the self-pumped phase-conjugate reflectivity measurements is shown in Fig. 8. Phase-conjugate reflectivities were measured at seven argon-ion laser lines; 458, 465, 477, 488, 497, 502, and 515 nm; at 442 (HeCd) and at 633 nm (HeNe). The laser output intensities ranged from ~ 50 mW/cm² to 1 W/cm². Beam diameters at the $1/e^2$ points of the peak-on-axis intensity ranged from 1.05 to 2.2 mm. The coherence length of these multilongitudinal mode lasers was on the order of a few centimeters.

When the HeCd and HeNe lasers were employed, the prism shown in Fig. 8 was not used. All beams were unfocused, at normal incidence, and polarized extraordinary to take advantage of the r_{33} electrooptic coefficient [21] (~ 224 pm/V). The aperture directly in front of the crystal was used to ensure that the beams were incident at the same point on the front face. After a measurement, ordinary polarized light was used to erase the gratings. Erasure was necessary because of the long dark decay times. The beam splitter was used to extract a measured fraction of the phase-conjugate intensity. Both the input and the output intensities were monitored using photodiodes or an optical multichannel analyzer (OMA).

The OMA was particularly useful in allowing comparisons of peak intensities, beam shape, and testing for phase conjugation. Phase conjugation was demonstrated by allowing an input Gaussian beam to propagate through

a phase aberrator. The spatial beam profiles of the aberrated, input, and phase-conjugated beams were recorded with the OMA at the positions shown in Fig. 8. Fig. 9 shows a comparison of these spatial beam profiles which verify that the phase distortion introduced by the aberrator was indeed reversed via phase conjugation by the SPPCM.

The self-pumped phase-conjugate reflectivity data taken on crystal #3 is shown in Fig. 10. These reflectivity values would be larger if Fresnel reflection losses were eliminated. Note that the value at 497 nm does not fit the general upward trend at shorter wavelengths. This is presently unexplained but a similar result was also noted by Jahoda *et al.* [27] in BaTiO₃ around 615 nm. Our data was recorded with the pumping geometry as shown in Fig. 11. This pumping geometry served to fix the two pump beams within the crystal at angles $\alpha_1 \approx 90^\circ$ and $\alpha_2 \approx 72^\circ \pm 5^\circ$ with respect to the crystal c axis, as measured from photographs. The beam entered the crystal at normal incidence ~ 2 mm from the edge indicated. A beam fan would appear and subsequently collapse into two strong beams bent into the corner, as shown in Fig. 7. The appearance of the phase conjugate coincided with the collapse of the beam fan. The time response for the formation of the phase conjugate is intensity dependent and two to three orders of magnitude longer than that of beam fanning [7], [28]. The HeNe line at 633 nm would not self-pump with this geometry, although it fanned considerably. The beam had to be sent directly into the corner at a minimum angle of 3° (the data point in Fig. 10 was recorded at this angle). It should be noted that the optimum reflectivities for these wavelengths were observed with different pumping geometries, in particular, at larger angles [7].

DISCUSSION

The pumping geometry of Fig. 11 approximately corresponds to the optimized value of the coupling coefficient in SBN:60 as seen in Fig. 12; where we show the complete angular dependence of the coupling coefficient for Ce-doped SBN:60 at 488 nm. Note that α_1 was fixed by the incident angle (90°) and α_2 was free to form at whichever angle corresponded to the maximum value of the coupling coefficient. The coupling coefficient is given by [8], [29]

$$\gamma = \frac{\omega r_{eff} E}{2\pi c \cos[(\alpha_1 - \alpha_2)/2]} \quad (7)$$

where the electric field is

$$E = R \frac{k_B T k_g \cos(\alpha_1 - \alpha_2)}{q [1 + (k_g/k_0)^2]} \quad (8)$$

$\omega = 2\pi c/\lambda$, λ is the vacuum wavelength, $n = n(\lambda)$ is the refractive index which is wavelength dependent in the region of interest, and $k_g = 2(n\omega/c) \times \sin[(\alpha_1 - \alpha_2)/2]$ is the magnitude of the grating wave vector. r_{eff}

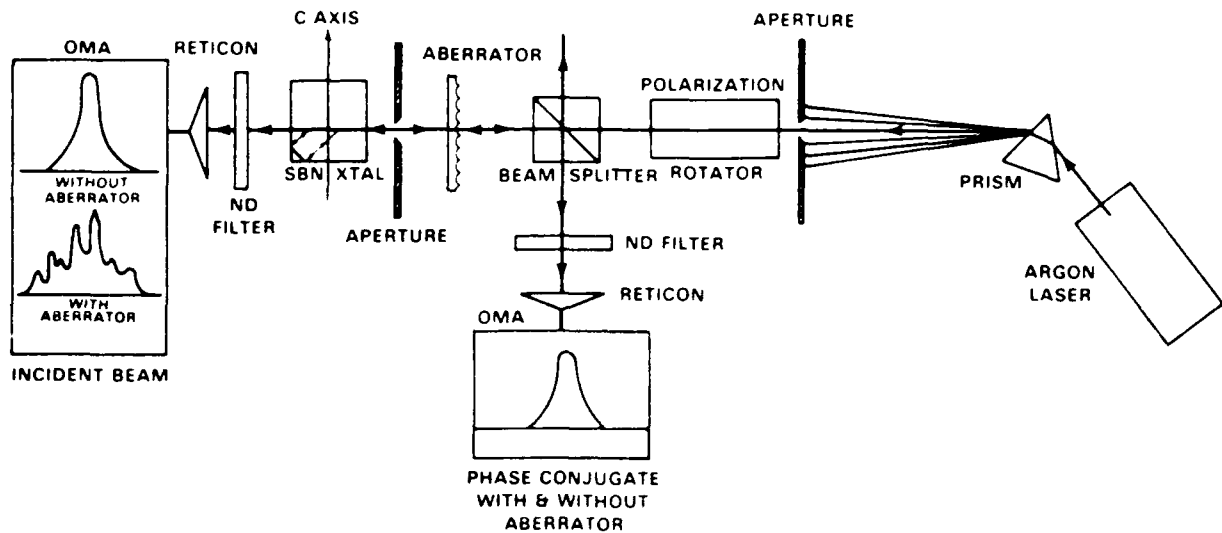


Fig. 8 Experimental arrangement for measuring phase-conjugate reflectivities and for testing the phase-correcting ability of the phase-conjugate wave.

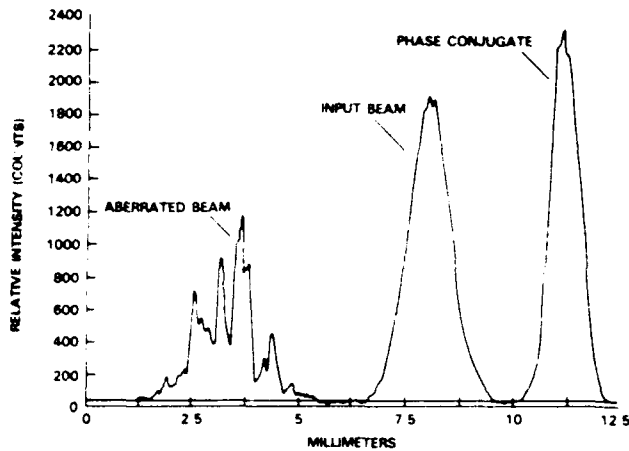


Fig. 9. A comparison of spatial beam profiles to verify phase conjugation. Relative peak intensities are arbitrary.

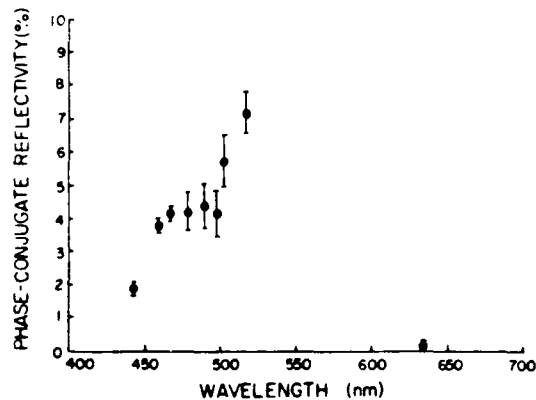


Fig. 10. The steady-state phase-conjugate reflectivity of the Ce-doped SBN:60 self-pumped phase-conjugate mirror (crystal #3) for a normally incident beam as a function of wavelength. The data has not been corrected for Fresnel losses.

$= R_{eff} \times F$ and R_{eff} is given as

$$R_{eff} = [n_0^4 r_{13} \cos \alpha_1 \cos \alpha_2 + 2n_0^2 n_0^2 r_{42} \cdot \cos^2 \{(\alpha_1 + \alpha_2)/2\} + n_0^4 r_{33} \sin \alpha_1 \cdot \sin \alpha_2] \sin \{(\alpha_1 + \alpha_2)/2\} \quad (9)$$

for extraordinary light and

$$R_{eff} = n_0^4 r_{13} \sin \{(\alpha_1 + \alpha_2)/2\} \quad (10)$$

for ordinary light. It should be noted that this γ , which relates electric-field amplitudes, is one half the value of the γ denoted in (4) for the two-beam coupling, which related beam intensities.

The wavelength dependence of the coupling coefficient can be written as

$\gamma =$

$$\frac{R(\lambda) 4\pi^2 k_B T r_{eff}(\lambda) \sin [(\alpha_1 - \alpha_2)/2] \cos (\alpha_1 - \alpha_2)}{q \lambda^2 \cos [(\alpha_1 - \alpha_2)/2] [1 + (4\pi n(\lambda) \cdot \sin [(\alpha_1 - \alpha_2)/2] / \lambda k_0(\lambda))^2]} \quad (11)$$

where all the wavelength dependent terms have been denoted. We assume that the electrooptic coefficients, r_{13} , r_{42} , and r_{33} , are wavelength independent over the visible spectrum and, hence, the wavelength dependence of r_{eff} is solely due to the dispersion in the indexes of refraction. γ is plotted, in Fig. 13, as a function of wavelength for steady-state coupling for beams at normal incidence. For these curves, a constant value for N_{eff} was used as determined from two-beam coupling experiments done on crystals #3 and 4. This wavelength independent behavior for N_{eff} is in agreement with the single species model of Kukhtarev *et al.* [30] in the region of $N_D > N_A$. The data for Fig. 13 was extracted from curves similar to those in Fig. 12, where we used the maximum of the $\alpha_1 = 90^\circ$ curves (steady-state coupling) for each wavelength. In

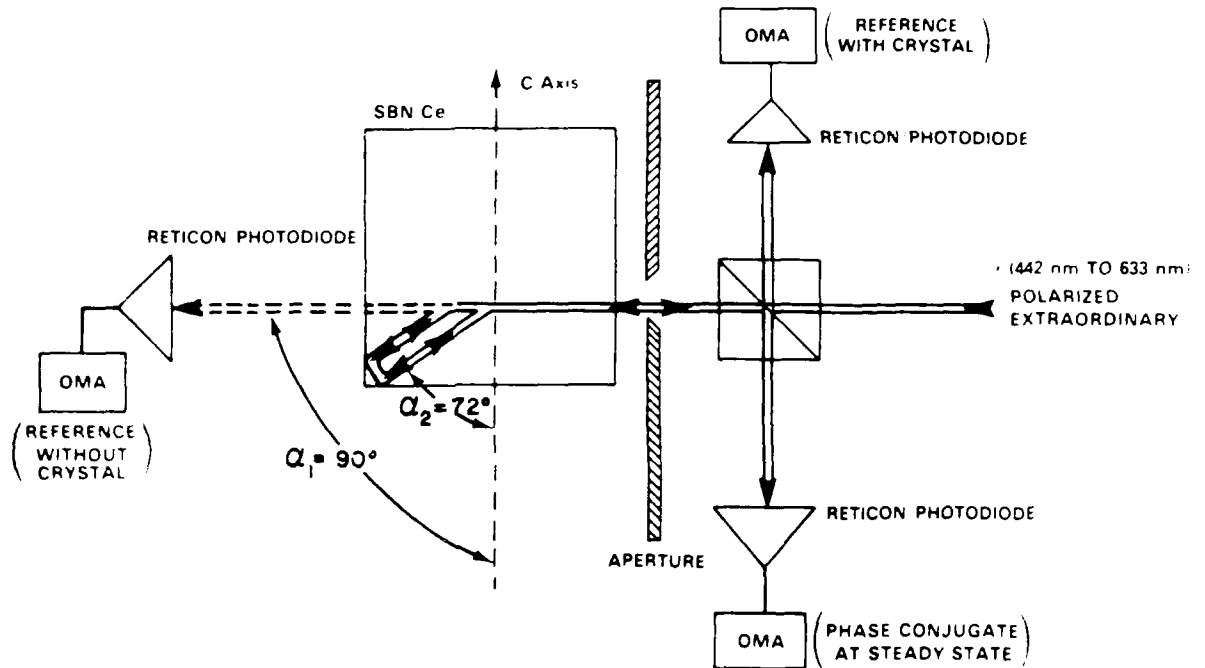


Fig. 11. Details of pumping geometry used to measure the phase-conjugate reflectivity and to analyze the wavelength dependence of the Ce-doped SBN:60 SPPCM.

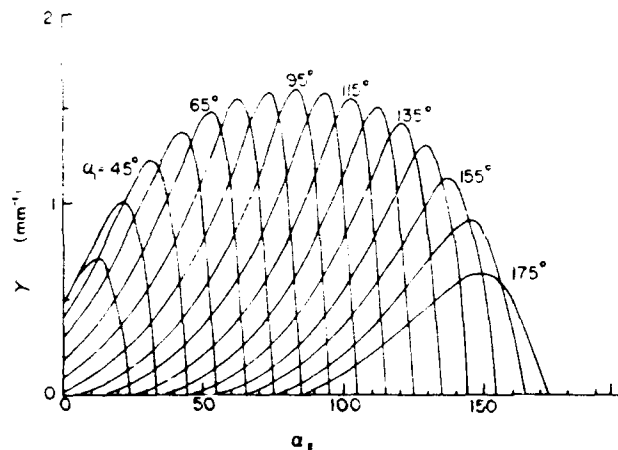


Fig. 12. Plot of the coupling constant γ versus α_2 for various α_1 (as defined in Fig. 11) for 488 nm extraordinary polarized light. These curves are based on a measured effective number density of photorefractive charges $N_{eh} = 7 \times 10^{16} \text{ cm}^{-3}$ and the assumption that there is no electron-hole competition in the formation of the space-charge field, i.e., $R = 1$. The other parameters used in this computation are: the poling factor $F = 1$, the dielectric constants $\epsilon_e = 400$ and $\epsilon_o = 1100$, the index of refraction $n_o = 2.40$ and $n_e = 2.36$, and the electrooptic coefficients from Table I, $r_{11} = 55 \times 10^{-12} \text{ V/m}$, $r_{12} = 80 \times 10^{-12} \text{ V/m}$, and $r_{33} = 224 \times 10^{-12} \text{ V/m}$.

curve *a*, R and n are held constant, thus only the explicit $1/\lambda^2$ -dependence is evident. Curves *b* and *c* show the dependence of γ on λ when the measured dispersion in the index of refraction is included but R is held constant. In curve *b*, $R = 1$ and in curve *c*, $R = 0.5$. In curves *d* and *e*, the dispersion in the index of refraction, as well as a

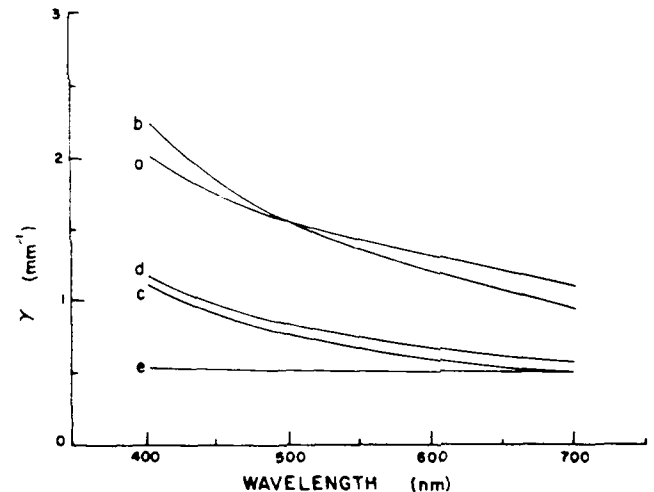


Fig. 13. Computed coupling coefficient at normal incidence. Each curve uses the material parameters of Fig. 12, except for R and n . Curve *a*: $R = 1$, $n_o = 2.40$, $n_e = 2.36$. Curve *b*: $R = 1$, $n = n(\lambda)$. Curve *c*: $R = 0.5$, $n = n(\lambda)$. Curve *d*: $R = R(\lambda)$, $n = n(\lambda)$ in crystal #3. Curve *e*: $R = R(\lambda)$, $n = n(\lambda)$ in crystal #4. For curve *d*, the poling factor used was 0.94. For curves *d* and *e*, R was assumed to have a linear wavelength dependence through measured points.

linear relationship for the competition factor are considered; thus, these curves represent the complete wavelength dependence for crystals #3 and 4. In crystal #4 the implicit wavelength dependence almost exactly cancels the explicit wavelength dependence yielding a nearly constant coupling coefficient.

At present, there are several possible mechanisms that

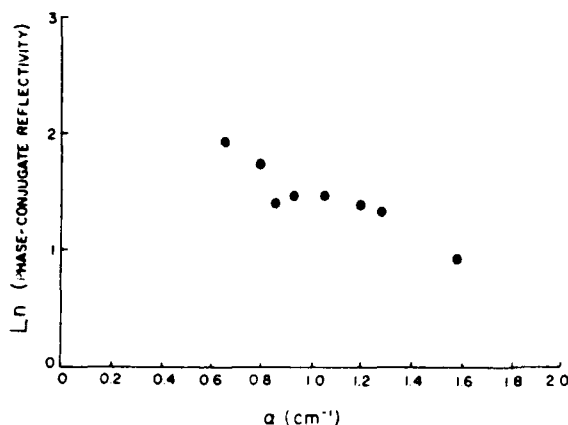


Fig. 14. The natural logarithm of the phase-conjugate reflectivity versus absorption coefficient. The points suggest a Beer's law relationship, $R_{pc} = R_0 e^{-\alpha l}$, where $R_0 = 0.11$ and $l = 1.0$ cm.

can lead to self-pumped phase-conjugation. In particular, there exists a resonator model [31], [32] and a four-wave mixing, two-interaction region model [29]. In the resonator model, the magnitude of the phase-conjugate reflectivity should be adversely affected if the crystal surfaces which do not form the loop are painted. Another feature of this model is that the phase-conjugate beam should be frequency shifted relative to the input beam. These effects were not observed in any of our SPPCM's. The other model, with two-interaction regions, contains a loss factor L , which is the fraction of intensity lost by the pumping beam as it propagates from one interaction region to the other. A loss factor greater than 60 percent is required to fit our experimental data. However, if we assume that L is a constant as a function of wavelength, then this model predicts that the phase-conjugate reflectivity will vary as the coupling coefficient which, for crystal #3, decreased with wavelength. As seen in Fig. 10, the measured phase-conjugate reflectivity generally increased with wavelength up to $\lambda = 515$ nm for the pumping geometry of Fig. 11. Therefore, neither the two-interaction region model nor the resonator model is appropriate for our results in the blue-green spectral region.

As seen in Fig. 3, absorption is significant in Ce-doped SBN:60 from 442 to 515 nm. Therefore, it is possible that absorption is a contributing factor to the phase-conjugate reflectivity in this region. Fig. 14, a plot of the natural log of the reflectivity versus absorption, supports this idea. The data suggest a straight line. This would imply a simple Beer's law relationship ($R_{pc} = R_0 \times e^{-\alpha l}$) with an effective length, $l = \sim 1.0$ cm, and an absorption-independent reflectivity value, $R_0 = \sim 11$ percent. This length is consistent with the crystal dimensions (6.5 mm cube). The two-interaction region model may have failed in this spectral region because it neglects absorption.

On the other hand, as the wavelength is increased to 633 nm, the reflectivity drops to zero for the geometry of Fig. 10. This would suggest a threshold somewhere between 515 and 633 nm. This behavior cannot be explained by absorption which decreases in this spectral region to

nearly zero. In addition, the effective charge carrier density and the electron-hole competition remain fairly constant as indicated by the two-beam coupling measurements. Notice, however, the coupling coefficient (Fig. 13, curve *d*) decreases in this spectral region due to the explicit wavelength dependence and the dispersion in the index of refraction.

The two-interaction region model may be appropriate here because of the low absorption. This model predicts a threshold behavior dependent on the coupling coefficient. Using the coupling coefficient for crystal #3, the two-interaction region model predicts an interaction length between 3.3 and 4.0 mm for a threshold between 515 and 633 nm. These interaction lengths are not unreasonable compared to the crystal dimension of 6.5 mm.

CONCLUSION

In this paper, we have reported on the experimental determination, for cerium-doped SBN:60, of the wavelength dependence of our self-pumped phase-conjugate mirrors. We have achieved the following results over the visible spectrum: the phase-conjugate reflectivity at normal incidence ranged from zero to seven percent, the electron-hole competition was found to be significant and had a wavelength dependence in one sample but not the other, the charge carrier density was $\sim 7 \times 10^{16}$ cm⁻³ and was wavelength independent, and the absorption coefficient ranged from 2 cm⁻¹ at the smaller wavelengths to zero at longer wavelengths. Using the above values, we have also determined a wavelength-dependent coupling coefficient.

Absorption can be directly and indirectly related to many of the above photorefractive properties. The strong absorption in the ultraviolet is mainly responsible for the dispersion in the index of refraction and does not directly contribute to the photorefractive process. The absorption in the visible is primarily dependent on the dopant levels and leads to the value of N_{eff} . This factor affects the value of the coupling coefficient and therefore, α and γ are not independent. Consequently, absorption plays a key role in phase conjugation and other photorefractive processes such as two-beam coupling, beam fanning, etc.

We have shown a relationship between absorption and the phase-conjugate reflectivity in the region where absorption is significant. If the crystals are doped with impurities having significant photoionization cross sections in the NIR and IR regions, self-pumped phase conjugation in these spectral regions may be possible. By controlling the dopant concentrations and their locations in the crystal structure, we may be able to tailor these crystals to obtain certain desired photorefractive properties.

ACKNOWLEDGMENT

We gratefully acknowledge the assistance of L. E. Cross in the determination of the poling factor used in this study for crystal #3. We would also like to thank G. C.

Valley for suggestions regarding the calculation of the coupling coefficient.

REFERENCES

- [1] O. Eknayan, C. H. Bulmer, H. F. Taylor, W. K. Burns, A. S. Greenblatt, L. A. Beach, and R. R. Neurgaonkar, "Vapor diffused optical waveguides in strontium barium niobate (SBN-60)," *Appl. Phys. Lett.*, vol. 48, pp. 13-18, 1986.
- [2] A. M. Glass, "Investigations of the electrical properties of $\text{Sr}_{1-x}\text{Ba}_x\text{Nb}_2\text{O}_6$ with special reference to pyroelectric detectors," *J. Appl. Phys.*, vol. 40, pp. 4699-4713, 1968.
- [3] M. Cronin-Golomb and A. Yariv, "Optical limiters using photorefractive nonlinearities," *J. Appl. Phys.*, vol. 57, pp. 4906-4910, 1985.
- [4] K. Megumi, H. Kozuka, M. Kobayashi, and Y. Furuhashi, "High-sensitive holographic storage in Ce-doped SBN," *Appl. Phys. Lett.*, vol. 30, pp. 631-633, 1977.
- [5] B. Fischer, M. Cronin-Golomb, J. O. White, A. Yariv, and R. R. Neurgaonkar, "Amplifying continuous-wave phase conjugate mirror with strontium barium niobate," *Appl. Phys. Lett.*, vol. 40, pp. 863-865, 1982.
- [6] M. Cronin-Golomb, B. Fischer, J. O. White, and A. Yariv, "Passive phase conjugate mirror based on self-induced oscillation in an optical ring cavity," *Appl. Phys. Lett.*, vol. 42, pp. 919-921, 1983.
- [7] G. Salamo, M. J. Miller, W. W. Clark, III, G. L. Wood, and E. J. Sharp, "SBN as a self-pumped phase conjugator," *Opt. Commun.*, vol. 59, pp. 417-422, 1986.
- [8] J. Feinberg, "Self-pumped, continuous-wave, phase conjugator using internal reflection," *Opt. Lett.*, vol. 7, pp. 486-488, 1982.
- [9] M. J. Miller, E. J. Sharp, G. L. Wood, W. W. Clark, III, G. J. Salamo, and R. R. Neurgaonkar, "Time response of a cerium-doped $\text{Sr}_{0.4}\text{Ba}_{0.6}\text{Nb}_2\text{O}_6$ self-pumped phase conjugate mirror," *Opt. Lett.*, vol. 12, pp. 340-342, 1987.
- [10] J. Rodriguez, A. Siahmakoun, G. Salamo, M. J. Miller, W. W. Clark, III, G. L. Wood, E. J. Sharp, and R. R. Neurgaonkar, "BSKNN as a self-pumped phase conjugator," *Appl. Opt.*, vol. 26, pp. 1732-1736, 1987.
- [11] R. R. Neurgaonkar and W. K. Cory, "Progress in photorefractive tungsten-bronze crystals," *J. Opt. Soc. Amer. B*, vol. 3, pp. 274-282, 1986.
- [12] K. Megumi, N. Nagatsuma, K. Kashiwada, and Y. Furuhashi, "Congruent melting compositions of SBN," *Mat. Sci.*, vol. 11, pp. 1583-1592, 1976.
- [13] G. Rakuljic, A. Yariv, and R. R. Neurgaonkar, "Photorefractive properties of undoped, cerium-doped, and iron-doped single-crystal $\text{Sr}_{0.4}\text{Ba}_{0.6}\text{Nb}_2\text{O}_6$," *Opt. Eng.*, vol. 25, pp. 1212-1216, 1986.
- [14] J. Feinberg, D. Heiman, A. R. Tanguay, Jr., and R. W. Hellwarth, "Photorefractive effects and light-induced charge migration in barium titanate," *J. Appl. Phys.*, vol. 51, pp. 1297-1305, 1980.
- [15] S. Ducharme and J. Feinberg, "Altering the photorefractive properties of BaTiO_3 by reduction and oxidation at 650°C," *J. Opt. Soc. Amer. B*, vol. 3, pp. 283-292, 1986.
- [16] G. C. Valley and M. B. Klein, "Optimal properties of photorefractive materials for optical data processing," *Opt. Eng.*, vol. 22, pp. 704-711, 1983.
- [17] J. P. Huignard and A. Marrakchi, "Coherent signal beam amplification in two-wave mixing experiments with photorefractive $\text{Bi}_{12}\text{SiO}_{20}$ crystals," *Opt. Commun.*, vol. 38, pp. 249-254, 1981.
- [18] M. Klein, "Physics of the photorefractive effect in BaTiO_3 ," in *Electro-Optic and Photorefractive Materials*, Springer Proceedings in Physics, P. Gunter, Ed., New York: Springer-Verlag, 1987.
- [19] F. P. Strohkendl, J. M. C. Jonathan, and R. W. Hellwarth, "Hole-electron competition in photorefractive gratings," *Opt. Lett.*, vol. 11, pp. 312-314, 1986.
- [20] The spontaneous polarization changed only slightly from $30 \mu\text{C}/\text{cm}^2$ in the "as measured" crystal to $32 \mu\text{C}/\text{cm}^2$ after the crystal was re-poled. The fact that the dielectric permittivity increased after the sample was re-poled and that the spontaneous polarization changed only slightly indicates that the depoling is due to localized partial domain reversal rather than a formation of micro-domains.
- [21] S. Ducharme, J. Feinberg, and R. R. Neurgaonkar, "Electrooptic and pyroelectric measurements in photorefractive materials," *J. Opt. Soc. Amer. A*, vol. 3, p. 25, 1986.
- [22] M. D. Ewbank, R. R. Neurgaonkar, W. K. Cory, and J. Feinberg, "Photorefractive properties of strontium barium niobate," *J. Appl. Phys.*, vol. 62, pp. 374-380, 1987.
- [23] J. O. White, M. Cronin-Golomb, B. Fischer, and A. Yariv, "Coherent oscillation by self-induced gratings in the photorefractive crystal BaTiO_3 ," *Appl. Phys. Lett.*, vol. 40, pp. 450-452, 1982.
- [24] M. Cronin-Golomb, B. Fischer, J. O. White, and A. Yariv, "Passive (self-pumped) phase conjugate mirror: Theoretical and experimental investigation," *Appl. Phys. Lett.*, vol. 41, pp. 689-691, 1982.
- [25] J. Feinberg and R. W. Hellwarth, "Phase-conjugating mirror with continuous wave gain," *Opt. Lett.*, vol. 5, pp. 519-521, 1980.
- [26] J. Feinberg, "Asymmetric self-defocusing of an optical beam from the photorefractive effect," *J. Opt. Soc. Amer.*, vol. 72, pp. 46-51, 1981.
- [27] F. C. Jahoda, P. G. Weber, and J. Feinberg, "Optical feedback, wavelength response, and interference effects of self-pumped phase conjugation in BaTiO_3 ," *Opt. Lett.*, vol. 9, pp. 362-364, 1984.
- [28] G. A. Rakuljic, K. Sayano, A. Yariv, and R. R. Neurgaonkar, "Self-starting passive phase conjugate mirror with Ce-doped strontium barium niobate," *Appl. Phys. Lett.*, vol. 50, pp. 10-12, 1987.
- [29] K. R. MacDonald and J. Feinberg, "Theory of a self-pumped phase conjugator with two coupled interaction regions," *J. Opt. Soc. Amer.*, vol. 73, pp. 548-553, 1983.
- [30] N. V. Kukhtarev, V. B. Markov, S. G. Odulov, M. S. Soskin, and V. L. Vinetski, "Holographic storage in electrooptic crystals. I. Steady state," *Ferroelec.*, vol. 22, pp. 949-960, 1979.
- [31] M. Ewbank and P. Yeh, "Photorefractive resonators," *J. Opt. Soc. Amer. A*, vol. 2, p. 76, 1985; "Fidelity of passive phase conjugators," *SPIE*, vol. 613, 1986; "Frequency shift of self-pumped phase conjugators," *SPIE*, vol. 613, 1986.
- [32] S. Kwong, M. Cronin-Golomb, and A. Yariv, "Oscillation with photorefractive gain," *IEEE J. Quantum Electron.*, vol. QE-22, pp. 1508-1523, 1986.
- [33] E. L. Venturini, E. G. Spencer, P. V. Lenzo, and A. A. Ballman, "Refractive indices of strontium barium niobate," *J. Appl. Phys.*, vol. 39, pp. 343-344, 1968.
- [34] E. J. Sharp, M. J. Miller, G. L. Wood, W. W. Clark, III, G. J. Salamo, and R. R. Neurgaonkar, in *Proc. 6th IEEE Int. Symp. Appl. Ferroelec. (ISAF'86)*, 1986, p. 51.



Mr. Wood is a member of the Optical Society of America.

Gary L. Wood was born in Woodbury, NJ, in 1957. He received the B.S. and M.S. degrees in physics from Drexel University, Philadelphia, PA, in 1980 and 1982, respectively.

From 1978 to 1980 he investigated optically-pumped millimeter-wave sources at Harry Diamond Labs, Adelphi, MD. In 1982 he joined the Center for Night Vision and Electro-Optics, Fort Belvoir, VA, where he has been conducting research on self-induced nonlinear optical processes.



William W. Clark III was born in Boca Raton, FL, on March 3, 1947. He received the B.S. degree in physics from Davidson College, Davidson, NC, in 1969, and the Ph.D. degree in physics from Duke University, Durham, NC, in 1976. His dissertation was in the area of rotational molecular spectroscopy under the direction of Dr. W. Gordy.

From 1976 to 1979 he served as a research associate at Duke, continuing his spectroscopic investigations. Since 1979 he has been a Research Physicist with the U.S. Army Center for Night Vision and Electro-Optics, Fort Belvoir, VA, where he has been involved in work on millimeter and infrared detectors and related devices. His current work is in the field of nonlinear optics, with emphasis on interactions in photorefractive media.

Dr. Clark is a member of Sigma Xi.



Mary Jo Miller (S'83-M'84) was born in Eugene, OR, on July 29, 1962. She received the B.S. degree in electrical engineering from the University of Washington, Seattle, in 1984.

She is currently working towards the M.S. degree in electrical engineering at George Washington University, Washington, DC.

Since receiving the B.S. degree, Mrs. Miller has been working as an electronics engineer with the Center for Night Vision and Electro-Optics, Fort Belvoir, VA. Her major areas of interest include electrooptic processes and photorefractive effects in tungsten-bronze materials.

Ms. Miller is a member of the Optical Society of America.



Edward J. Sharp was born in Uniontown, PA, on September 26, 1939. He received the B.S. degree in physics from Wheeling College, Wheeling, WV, in 1961, the M.S. degree in physics from John Carroll University, Cleveland, OH, in 1963, and the Ph.D. degree in physics from Texas A&M University, College Station, in 1966.

He has been working as a Research Physicist at the Center for Night Vision and Electro-Optics, Fort Belvoir, VA. His major areas of interest have included laser crystal physics, thermal imaging

materials, electrooptic and nonlinear optical processes in organic materials, beam control devices, and photorefractive effects in ferroelectric materials.

Dr. Sharp is a member of the Optical Society of America.



Gregory J. Salamo was born in Brooklyn, NY, on September 19, 1944. He received the B.S. degree in physics from Brooklyn College, Brooklyn, NY, in 1966, the M.S. degree in physics from Purdue University, West Lafayette, IN, in 1968, and the Ph.D. degree in physics from the City University of New York, New York, in 1973. His dissertation work was carried out at Bell Laboratories, Murray Hill, NJ.

After receiving the Ph.D. degree, he performed postdoctoral work in physics at the University of Rochester, Rochester, NY, before joining the University of Arkansas, Fayetteville, in 1975, where he is now a Full Professor with the Department of Physics. He has carried out research in the areas of short-pulse propagation, quantum optics, photoacoustics, two-photon absorption, dye lasers, image processing, and photorefractive. He has also developed a laser education laboratory at the University of Arkansas.

Ratnakar R. Neurgaonkar, for a photograph and biography, see this issue, p. 2121.



Rockwell International

Science Center

SC5441.FTR

BSKNN AS A SELF-PUMPED PHASE CONJUGATOR

BSKNN as a self-pumped phase conjugator

Juan Rodriguez, Azad Siahmakoun, Gregory Salamo, Mary J. Miller, William W. Clark III, Gary L. Wood, Edward J. Sharp, and Ratnakar R. Neurgaonkar

Self-pumping has been observed in a cerium-doped $\text{Ba}_{2-x}\text{Sr}_x\text{K}_{1-x}\text{Na}_x\text{Nb}_5\text{O}_{15}$ (BSKNN) crystal at four argon-ion laser wavelengths. Phase-conjugate reflectivities as high as 30% were measured with response times inversely proportional to the 0.5 power of the input intensity. The response time for beam fanning in the crystal was determined to be inversely proportional to the 0.82 power of the input intensity.

1. Introduction

Many different nonlinear phenomena and techniques have been used to produce phase-conjugate beams.¹ Until recently, however, only barium titanate^{2,3} (BaTiO_3) and Ce-doped strontium barium niobate⁴ (SBN) have been successfully demonstrated as broadband self-pumped phase-conjugate mirrors using milliwatt beams. Self-pumped phase conjugation, as reported here, is completely self-contained and requires no external mirrors,^{5,6} pumping beams,⁷ or applied electric fields. In our experiments, the incident beam is directed into a crystal corner via asymmetrical self-defocusing⁸ where retroreflection provides the pump beams for the four-wave mixing process and the subsequent phase conjugate build-up.

Currently, both BaTiO_3 and SBN crystals are leading candidates for applications in many areas, including electrooptics, photorefractive, and millimeter waves. Both of the above crystals are tetragonal at room temperature with a 4-mm point group symmetry; however, BaTiO_3 exhibits a strong longitudinal electrooptic coefficient (r_{51}) while tungsten-bronze SBN:60 exhibits a strong transverse electrooptic coefficient (r_{33}). At this point in time, the use of BaTiO_3 is somewhat limited due to the extreme difficulty in growing doped crystals of adequate size and quality for a number of applications. For this reason, Neurgaon-

kar *et al.* introduced the tungsten-bronze $\text{Ba}_{2-x}\text{Sr}_x\text{K}_{1-x}\text{Na}_x\text{Nb}_5\text{O}_{15}$ (BSKNN) solid solution system⁹ and has since grown optical quality, twin-free, doped and undoped BSKNN crystals.

Specifically, $\text{Ba}_{1.5}\text{Sr}_{0.5}\text{K}_{0.75}\text{Na}_{0.25}\text{Nb}_5\text{O}_{15}$ (BSKNN-1) and $\text{Ba}_{0.5}\text{Sr}_{1.5}\text{K}_{0.5}\text{Na}_{0.5}\text{Nb}_5\text{O}_{15}$ (BSKNN-2) have been grown using an automatic, diameter-controlled Czochralski pulling technique. The growth of BSKNN-1 crystals is much more difficult than that of BSKNN-2 which indicates that BSKNN-2 is closer to the congruent melting composition in this solid solution system. These crystals resemble both SBN and BaTiO_3 in many respects, i.e., point group symmetry, optical properties, and ferroelectric properties. The electrooptic effect in BSKNN-2 is strongly longitudinal as in BaTiO_3 .

In this paper we confine our photorefractive phase conjugation experiments to the BSKNN-2 composition. BSKNN-2 is characterized by a sharp anomaly in the polar-axis dielectric constant at the ferroelectric phase-transition temperature occurring between 170 and 178°C. The room temperature dielectric constants, $\epsilon_{\parallel} = 170$ and $\epsilon_{\perp} = 750$, have been measured for poled samples at 10 kHz.⁹ For crystals poled to a single ferroelectric domain, the dielectric dispersion has been found to be minimal over the range of 100 Hz to 100 kHz.⁹

The sign of the electrooptic coefficient, r_{33} , has been determined to be positive by use of a calibrated compensator. This fact, coupled with the observation that extraordinary light fans toward the electrode held positive during poling, gives a negative sign for the photorefractive charge carriers, as similarly found in SBN. By comparison, the charge carriers in BaTiO_3 are positive and extraordinary light fans toward the negative poling electrode.¹⁰ The transmission spectra for our BSKNN-2 samples, both doped and undoped, are shown in Fig. 1, curves *a* and *b*, respectively.

Ratnakar Neurgaonkar is with Rockwell International Science Center, Thousand Oaks, California 91360; J. Rodriguez, A. Siahmakoun, and G. Salamo are with University of Arkansas, Physics Department, Fayetteville, Arkansas 72701; the other authors are with Center for Night Vision and Electro-Optics, Fort Belvoir, Virginia 22060-5677.

Received 29 October 1986.

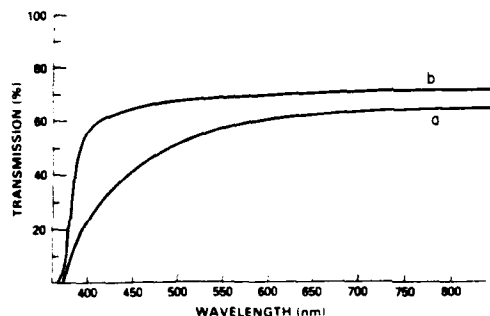


Fig. 1. Transmission curves for typical doped (curve a) and undoped (curve b) samples of BSKNN. These curves were recorded for 6 and 5 mm thicknesses, respectively, and have not been corrected for Fresnel losses.

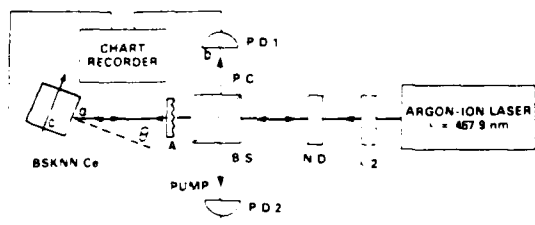


Fig. 2. Apparatus used in the measurement of phase-conjugate reflectivity and the phase-conjugate response time. In this diagram $\lambda/2$ is a polarization rotator, N.D. is a neutral density filter, B.S. is a beam splitter, A is an aberrator, θ is the angle of the incident beam with respect to the normal of the c axis, and P.D. 1 and 2 are matched photodiodes.

In this paper we report the first observation of self-pumping in the photorefractive crystal barium strontium potassium sodium niobate (BSKNN-2). The phase-conjugate reflectivities measured on a 6 mm cube of BSKNN-2 are comparable with those previously reported for BaTiO_3 (Ref. 2) and SBN.^{4,11,12} In addition to the BSKNN behavior as a self-pumped phase conjugator, we also report the time required for the onset of the phase-conjugate beam¹³ and the time required for asymmetrical self-defocusing (beam fanning). Both of these characteristic times were measured as a function of pump intensity.

II. Experimental Arrangement for Self-Pumping

The experimental arrangement used for the self-pumped phase-conjugate reflectivity measurements is shown in Fig. 2. The laser output was kept in a single transverse mode although several longitudinal modes were oscillating. A polarization rotation device was used directly at the output of the laser to provide the flexibility of either ordinary or extraordinary light. Extraordinary polarized light was used to write gratings while ordinary polarized light was used to erase gratings. This was necessary since the observed dark storage time in these BSKNN crystals was at least a few days. The beam splitter was used to separate the phase conjugate from the input, as well as split off a measured fraction of the input for normalization of the

Table I. Reflectivity Measurements as a Function of Wavelength

Wavelength (nm)	Input intensity at the crystal (W/cm^2)	Average reflectivity (%)
457.9	0.19	27.5
476.5	0.21	18.0
496.5	0.24	18.0
514.5	3.82	16.5

phase-conjugate intensity. The input beam and the phase-conjugate beam were monitored with matching photodiodes. The experimental measurements were taken using four spectral lines (see Table I) subject to the stringent requirement of high laser stability in both mode structure and intensity. The unfocused beam diameter ($1/e^2$ point) was ~ 2.1 mm at the crystal face. Neutral density filters were used to vary the input intensity of the beam from several W/cm^2 to a few mW/cm^2 and to limit phase-conjugate feedback into the argon laser. It was determined that neither the input intensity nor the phase-conjugate feedback affected the reflectivity measurements reported here.

III. Experimental Results for Self-Pumping

Although self-pumping was observed for incident input angles between $\theta = \pm 45^\circ$ with respect to the normal, the measurements of the phase-conjugate intensity were taken as a function of wavelength at a constant input angle of $\theta = +20^\circ$. As can be seen from the results shown in Table I, the phase-conjugate reflectivity increases as the wavelength shifts toward the blue. For longer wavelengths, such as 514.5 nm, a much larger pump power was required to initiate self-pumping. The minimum intensity for observing a phase-conjugate signal was determined to be ~ 100 mW/cm^2 for the 457.9 nm line at an incident angle of $\theta = +20^\circ$. The minimum intensity was observed to increase nonlinearly with wavelength.

When the crystal was self-pumping, we observed that the extraordinary polarized beam entering the crystal was fanned into a corner where two beams appeared to be retroreflected back toward the incident beam. Figure 3 is a photograph showing the top view of a Ce-doped BSKNN-2 crystal (10 \times) while the crystal is self-pumping. The crystal is in air and being pumped with the 457.9 nm line of the argon-ion laser. The c axis of the crystal is directed from bottom to top and the incident Gaussian beam is extraordinary polarized and propagates from right to left entering the crystal with a positive angle θ as defined in Fig. 4. The illuminated portions of the crystal at the entrance and exit faces are due to light scattered from the natural facets on the crystal corners parallel to the crystal growth direction (c axis) which remained after the entrance and exit windows were cut and polished. The unusually large separation of the two beams forming the loop is due to the chamfered edge of the crystal corner containing the loop. In crystals having sharp edges on the corners, the observed separation between the beams in the loop is much less.

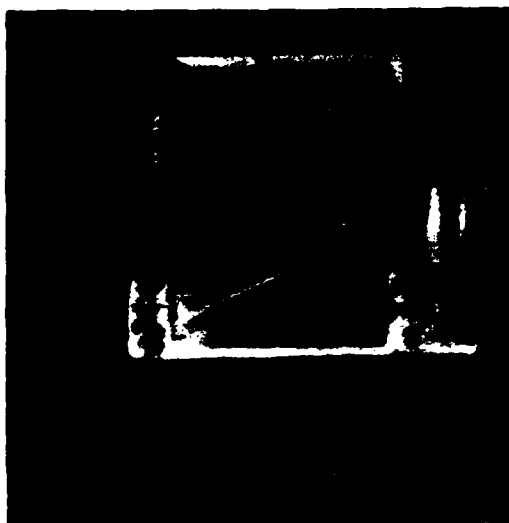


Fig. 3. Photograph of a BSKNN-2 crystal (10X) taken perpendicular to the c axis and to the direction of propagation while the crystal is self-pumping. The c axis of the crystal is directed from the bottom to the top and the extraordinary polarized beam at 457.9 nm is propagating from right to left, entering the crystal at an angle $\theta = 30^\circ$. The angular relationship of the beams within the crystal shown in this photograph is sketched in Fig. 4.

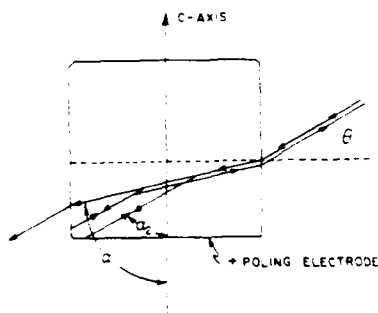


Fig. 4. Sketch of the BSKNN-2 crystal showing the angular relationship of the beams within the crystal while it is self-pumping. This sketch is based on the visual observation of the location of the beams in the photograph of Fig. 3. The angular relationship between (α_1) and (α_2) is in good agreement with the computed angular dependence of the coupling coefficient γ in Fig. 6.

That the backscattered wave was in fact a phase-conjugate beam was verified by inserting a phase aberrator in the beam as shown in Fig. 2. The beam's spatial characteristics were subsequently monitored with an optical multichannel analyzer (OMA). Its profile was recorded with the OMA for the following conditions: with and without the aberrator at position (a) and after reversing its path through the aberrator at position (b). These profiles are compared in Fig. 5. The spatial profile of the beam recorded at position (b) is that of a Gaussian, as would be expected of a true conjugate beam. In addition, it should be noted that the beamwidth at the $1/e^2$ points of these beams is different. This is due to the fact that the incident

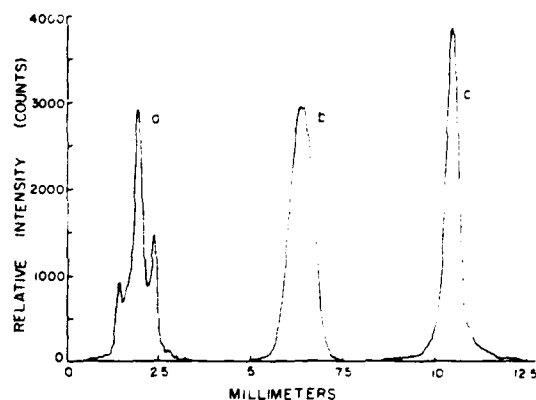


Fig. 5. Comparison of spatial beams profiles to verify phase conjugation in cerium-doped BSKNN-2 where (a) is the aberrated beam, (b) is the input beam, and (c) is the phase-conjugate beam. The relative peak intensities are arbitrary.

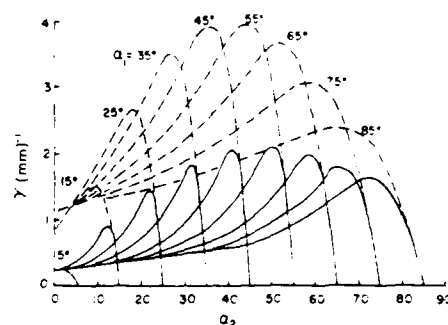


Fig. 6. Coupling constant γ vs α_2 for various values of α_1 . α_2 is the angle formed by the loop direction and the c axis and α_1 is the angle formed by the input beam direction and the c axis. BaTiO_3 is represented by the solid lines and BSKNN is represented by the dashed lines. The curves are for 457.9-nm radiation and are based on the same estimated values of the number density of charges $N \sim 2 \times 10^{16} \text{ cm}^{-3}$; and the following values: BaTiO_3 : $\epsilon = 106$, $\epsilon_\infty = 4300$, $n_o = 2.488$, $n_e = 2.424$, $r_{13} = 33 \times 10^{-12} \text{ m/V}$, $r_{42} = 820 \times 10^{-12} \text{ m/V}$, and $r_{33} = 120 \times 10^{-12} \text{ m/V}$; BSKNN: $\epsilon = 170$, $\epsilon_\infty = 750$, $n_o = 2.35$, $n_e = 2.27$, $r_{13} = 50 \times 10^{-12} \text{ m/V}$, $r_{42} = 820 \times 10^{-12} \text{ m/V}$, and $r_{33} = 200 \times 10^{-12} \text{ m/V}$.

Gaussian beam and the aberrated beam recorded at position (a) are diverging beams, while the phase-conjugate beam recorded at position (b) is a converging beam.

The computed coupling coefficient γ , as a function of the angle of the loop with respect to the c axis (α_2) for various incident angles (α_1), is shown in Fig. 6 for BaTiO_3 (Ref. 2) and BSKNN, where (α_1) and (α_2) are defined in Fig. 4. The set of curves for BaTiO_3 is not identical to that computed by Feinberg in Ref. 2 since we use 457.9 nm for the wavelength and more recent values of the r_{13} and r_{33} electrooptic coefficients.¹⁴ The newer electrooptic coefficients produce a slight increase in the coupling strength for BaTiO_3 as the pumping beam approaches normal incidence. The values of the electrooptic coefficients and dielectric constants used in the calculation of γ for BSKNN were

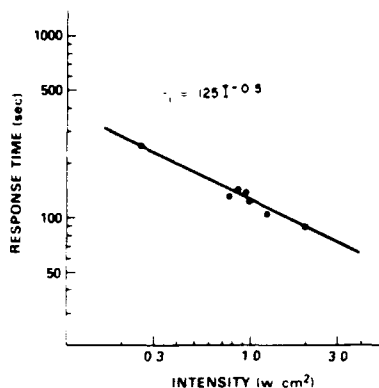


Fig. 7. Phase-conjugate formation time vs input intensity. τ_i is the time required for the phase-conjugate reflectivity to reach $1/e$ of its equilibrium value.

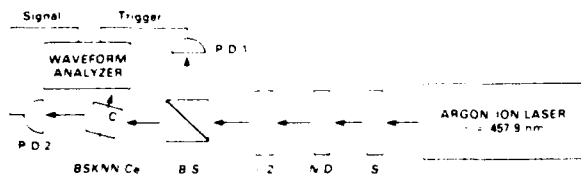


Fig. 8. Apparatus used to measure the beam fanning response time. In this diagram S is a shutter, N.D. is a neutral density filter, A is a polarization rotator, B.S. is a beam splitter, and P.D. 1 and 2 are photodiodes.

extracted from Ref. 9. These calculations indicate that for an extraordinary beam and the same charge carrier density, the coupling within BSKNN is approximately a factor of 2 stronger than that in BaTiO₃.

IV. Time Response

In these experiments, we measured both the time required for the initiation of the phase-conjugate beam¹³ and the time required for beam fanning to reach $1/e$ of its equilibrium value.^{11,15} All these measurements were taken using the 457.9 nm line of the argon-ion laser because of increased photorefractive sensitivity to that wavelength, as illustrated in Table I.

The same apparatus (Fig. 2) used to obtain the phase-conjugate reflectivity measurements was used to obtain the phase-conjugate formation time. These measurements were taken at an angle of $\theta = +10^\circ$, using the 457.9 nm blue line of the argon laser. The phase-conjugate formation time as a function of intensity is shown in Fig. 7. The points represent the time required for the phase-conjugate reflectivity to reach $1/e$ of its final value. The analytical expression representing the best fit to the data is $\tau_i = 125 I^{-0.50}$. In this expression τ_i is in seconds while I is given in W/cm².

The experimental arrangement used for the measurement of beam fanning response time is shown in Fig. 8. In this experiment, opening the shutter caused detector 1 to trigger a waveform analyzer that monitored and stored the transient response seen by detec-

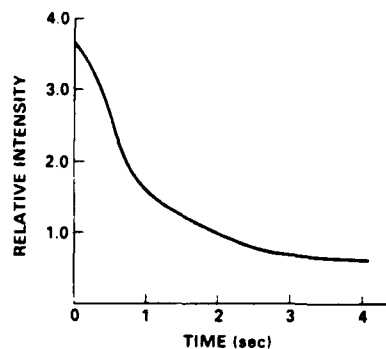


Fig. 9. Typical trace showing the nonexponential decay of the intensity of the transmitted beam due to beam fanning.

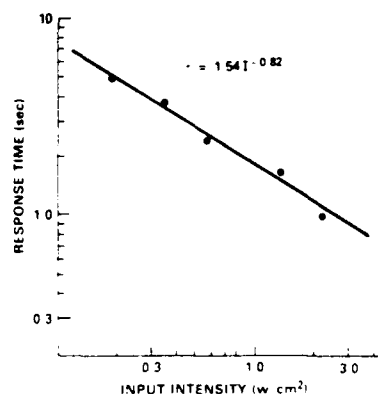


Fig. 10. Beam fanning response time τ vs input intensity I is the time required for the transmitted beam to decay to $1/e$ of the difference between the initial and final intensity.

tor 2. The output from detector 2 was then plotted using a chart recorder. A typical trace is shown in Fig. 9. As seen in the figure, the decay of the transmitted beam is nonexponential with an unusually slow start. The response time was chosen as the time for the transmitted beam to reach $1/e$ of the difference between the initial and equilibrium intensities. The incident input angle (θ) was held fixed at $+10^\circ$ with respect to the normal during these measurements. Figure 10 shows the response time τ as a function of the input intensity I . The curve fits the expression $\tau = 1.54 I^{-0.82}$, where τ is in seconds and I is in W/cm².

V. Conclusion

In summary, we have observed for the first time self-pumping in a new photorefractive material, BSKNN, and have also reported on the phase-conjugate reflectivity of the crystal as a function of wavelength. In addition, we have determined the characteristic response times of the crystal.

References

1. See, for example, R. A. Fisher, Ed. *Optical Phase Conjugation* (Academic, New York, 1983).
2. J. Feinberg, "Self-Pumped, Continuous-Wave Phase Conjugator Using Internal Reflection," *Opt. Lett.* 7, 486 (1982).

3. F. C. Jahoda, P. G. Weber, and J. Feinberg, "Optical Feedback, Wavelength Response, and Interference Effects of Self-Pumped Phase Conjugation in BaTiO₃," *Opt. Lett.* **9**, 362 (1984).
4. E. J. Sharp, M. J. Miller, G. L. Wood, W. W. Clark III, G. J. Salamo, and R. R. Neurgaonkar, "SBN as a Broadband Self-Pumped Phase Conjugate Mirror," *ISAF '86—Proc. of the Sixth IEEE Int. Symp. on Appl. of Ferro.*, page 51 (1986). (volume # unknown)
5. J. O. White, M. Cronin-Golomb, B. Fischer, and A. Yariv, "Coherent Oscillation by Self-Induced Gratings in the Photorefractive Crystal BaTiO₃," *Appl. Phys. Lett.* **40**, 450 (1982).
6. M. Cronin-Golomb, B. Fischer, J. O. White, and A. Yariv, "Passive (Self-Pumped) Phase Conjugate Mirror: Theoretical and Experimental Investigation," *Appl. Phys. Lett.* **41**, 689 (1982).
7. J. Feinberg and R. W. Hellwarth, "Phase-Conjugating Mirror with Continuous-Wave Gain," *Opt. Lett.* **5**, 519 (1980).
8. J. Feinberg, "Asymmetric Self-Defocusing of an Optical Beam from the Photorefractive Effect," *J. Opt. Soc. Am.* **72**, 46 (1982).
9. R. R. Neurgaonkar, W. K. Cory, J. R. Oliver, W. W. Clark III, G. L. Wood, M. J. Miller and E. J. Sharp, "Growth of Ferroelectric Tungsten Bronze Ba_{1-x}Sr_xK_{1-y}Na_yNb₅O₁₅ (BSKNN) Composition Crystals," *J. Cryst. Growth*, accepted for publication May 1987. (volume & page # unknown)
10. J. Feinberg, D. Heiman, A. R. Tanguay, Jr. and R. W. Hellwarth, "Photorefractive Effects and Light-Induced Charge Migration in Barium Titanate," *J. Appl. Phys.* **51**, 1297 (1980).
11. G. J. Salamo, M. J. Miller, W. W. Clark III, G. L. Wood, and E. J. Sharp, "SBN as a Self-Pumped Phase Conjugator," *Opt. Commun.* **59**, 417 (1986).
12. M. J. Miller, E. J. Sharp, G. L. Wood, W. W. Clark III, G. J. Salamo, and R. R. Neurgaonkar, "Time Response of a Cerium-Doped Sr_{0.75}Ba_{0.25}Nb₂O₆ Self-Pumped Phase Conjugate Mirror," *Opt. Lett.* **12**, (1987) accepted for May 1987.
13. B. T. Anderson, P. R. Forman, and F. C. Jahoda, "Self-Pumped Phase Conjugation in BaTiO₃ at 1.06 μ m," *Opt. Lett.* **10**, 627 (1985).
14. S. Ducharme, J. Feinberg, and R. R. Neurgaonkar, "Electrooptic and Piezoelectric Measurements in Photorefractive Materials," *J. Opt. Soc. Am. A* **3**(13), P25 (1986).
15. M. Cronin-Golomb and A. Yariv, "Optical Limiters Using Photorefractive Nonlinearities," *J. Appl. Phys.* **56**, 4906 (1985). The time response reported in this reference should not be directly compared to our results since they measured the time required for beam fanning to reach 90% of its equilibrium value.



Rockwell International
Science Center

SC5441.FTR

TIME RESPONSE OF A Ce-DOPED SBN:75 SELF-PUMPED
PHASE CONJUGATE MIRROR

Time response of a cerium-doped $\text{Sr}_{0.75}\text{Ba}_{0.25}\text{Nb}_2\text{O}_6$ self-pumped phase-conjugate mirror

Mary J. Miller, Edward J. Sharp, Gary L. Wood, and William W. Clark III

Center for Night Vision & Electro-Optics, Fort Belvoir, Virginia 22060-5677

Gregory J. Salamo

University of Arkansas, Fayetteville, Arkansas 72701

Ratnakar R. Neurgaonkar

Rockwell International Science Center, Thousand Oaks, California 91360

Received December 1, 1986; accepted February 5, 1987

Self-pumping in cerium-doped strontium barium niobate has been observed with phase-conjugate reflectivities near 6% and a formation time of 8 sec for a 200-mW/cm^2 beam at 442 nm. The time response for asymmetrical self-defocusing was also measured, and the observed transmissions through the crystal at normal incidence were limited to about 1.5% of the incident radiation.

A great deal of attention has been given to self-pumped photorefractive phase-conjugate mirrors for a wide variety of applications.¹⁻³ These mirrors exhibit a number of attractive features, including high reflectivity, a modest wavelength range of operation, and only milliwatt beam-power requirements for start-up. Self-pumped phase conjugation,⁴ as reported here, operates on internal reflection and is completely self-contained, requiring no external mirrors,⁵ pumping beams,⁶ or applied electric fields. The only known demonstrations of self-pumping using internal reflection have been in BaTiO_3 ,^{4,7} undoped and cerium-doped strontium barium niobate (SBN),⁹ and cerium-doped barium strontium potassium niobate (BSKNN).¹⁰

In this Letter we report on self-pumped phase conjugation in a single crystal of cerium-doped $\text{Sr}_{1-x}\text{Ba}_x\text{Nb}_2\text{O}_6$, $x = 0.75$ (SBN:75). The addition of cerium produces a broad absorption in the visible, which enhances the photorefractive effect considerably in this crystal.^{11,12} The 0.05 wt. % cerium-doped SBN:75 crystal used in this study was an approximately $5\text{ mm} \times 5\text{ mm} \times 5\text{ mm}$ cube, poled at 8 kV/cm at a temperature well above the Curie temperature of 56°C .¹³ SBN:75 is tetragonal, has a 4-mm point group symmetry, and possesses a strong transverse electro-optic coefficient, r_{33} , as do other SBN compositions. By contrast, BSKNN and BaTiO_3 exhibit a strong longitudinal electro-optic coefficient, r_{51} . The phase-conjugate reflectivity of SBN:75 measured at 442 nm is similar to that previously reported for BaTiO_3 ,⁷ BSKNN,¹⁰ and SBN:60.^{8,9} In addition to the behavior of SBN:75 as a self-pumped phase-conjugate mirror, we also report on the time required for the onset of the phase-conjugate beam^{14,15} and the time needed to deamplify the beam through asymmetrical self-defocusing (beam fanning).^{8,16,17} These characteristic times were measured as a function of the pump intensity for a fixed spot size.

The phase-conjugate reflectivity and response-time

measurements were recorded using the experimental arrangement depicted in Fig. 1. A He-Cd laser provided an extraordinary polarized beam at 442 nm. The incident beam was 2.5 mW , with a $1/e^2$ beam diameter of 1.8 mm at the crystal. Neutral-density filters (ND's) were used to vary the input intensity of the beam from 200 mW/cm^2 to a few milliwatts per square centimeter. The beam was incident upon the crystal at an angle of $\theta = -50^\circ$ to the normal of the c axis, so that it was directed toward a crystal corner where retroreflection provided feedback for the four-wave mixing process and the subsequent phase-conjugate beam buildup. The phase-conjugate beam intensity was determined as a function of time at detector D1 (see Fig. 2). As can be seen from the data, the temporal buildup of the phase-conjugate intensity for the self-pumping configuration is nonexponential, as would be expected of a phenomenon that is a stimulat-

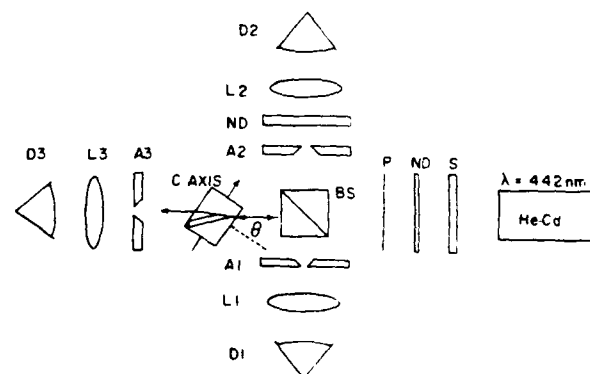


Fig. 1. Diagram of the experimental apparatus used to measure the phase-conjugate reflectivity and characteristic response times of the cerium-doped SBN:75 crystal. P, polarizer; L1, L2, lenses.

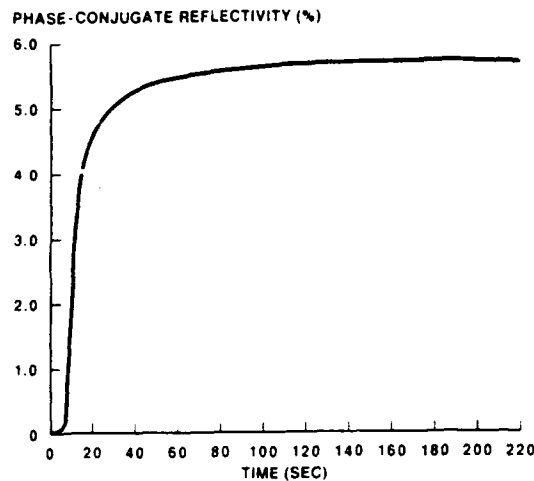


Fig. 2. Typical plot of phase-conjugate reflectivity for cerium-doped SBN:75 as a function of time for an incident intensity of 191 mW/cm².

ed effect depending on feedback and arising from noise.

The steady-state phase-conjugate reflectivity for SBN:75 as a function of incident intensity is presented in Fig. 3. The data indicate that the phase-conjugate reflectivity (R) remains constant as a function of input intensities above values of ~ 100 mW/cm²; however, there is a noticeable falloff in R for input intensities below this value. One explanation for this behavior is that the dark conductivity becomes insignificant compared with the total photoconductivity for input intensities greater than 100 mW/cm². This results in a saturation or constant value of the crystal diffraction efficiency.¹⁸ This explanation is consistent with the observed response-time and beam-fanning behavior described below and with a similar observation in BaTiO₃.¹⁹

The results of the phase-conjugate formation time, or initiation time (τ_i), as a function of the incident intensity are given in Fig. 4. In order to permit a comparison of this response time with those of other materials, we present the time for the phase-conjugate beam to reach the 90% point (curve a) and the e^{-1} point (curve b) of the steady-state reflectivity. The data for these curves show a departure from log-log linearity for input beam intensities below ~ 100 mW/cm². This observation is consistent with the assumption¹⁸ that the equilibrium diffraction efficiency of the grating formed during self-pumping saturates or becomes constant only for values of the input intensity above 100 mW/cm². The response times at the higher intensities are compared with those of other materials in Table 1 for similar pumping conditions. Input intensities of 0.2 and 2 W/cm² are used for comparison.

For the beam-fanning measurements, an extraordinary beam from the He-Cd laser was incident upon the crystal normal to the c axis. Radiation from the beam fanned toward the crystal face that was held positive during poling, that is, in a direction opposite the c -axis direction.²⁰ The drop in power through aperture A3 (see Fig. 1) was measured by detector D3

and recorded on a fast storage scope, which was triggered by D2 after a shutter (S) was opened. The final, steady-state power transmission as a function of incident intensity is shown in Fig. 5. The data show a decrease in percent transmission with increasing input intensity. This observation is consistent with the argument that the diffraction efficiency of any self-generated gratings is intensity dependent for the range of input intensities used in our experiment. As can be seen, the final transmission was less than 3% for even the weakest beam used in our measurements. This is comparable with the results obtained with BaTiO₃, for which a higher intensity (~ 30 W/cm²) was used.¹⁷

The intensity dependence of the time response for

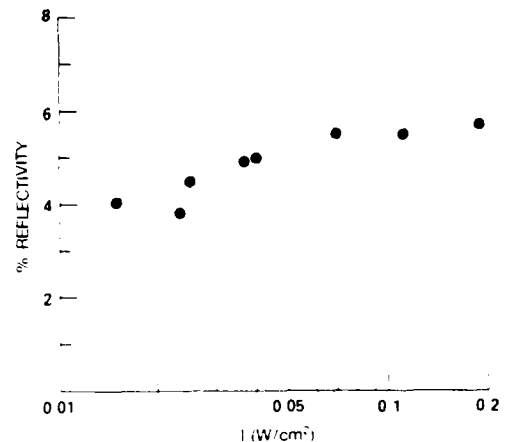


Fig. 3. Steady-state phase-conjugate reflectivity of cerium-doped SBN:75 as a function of intensity at 442 nm.

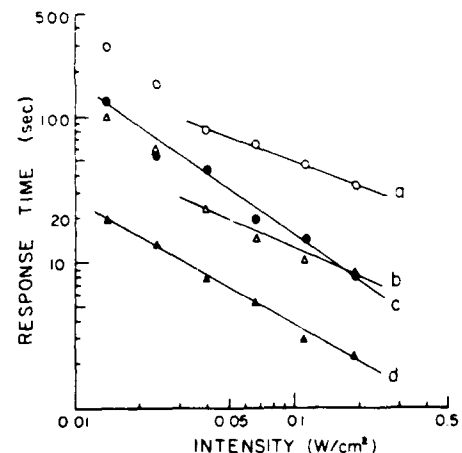


Fig. 4. Characteristic response times of cerium-doped SBN:75 as a function of intensity. Plots a and b are the phase-conjugate formation times measured at the 90% point and the e^{-1} point, respectively, of the steady-state reflectivity. Plots c and d are beam-fanning response times measured at the points where 90 and 63.2% ($1 - e^{-1}$) of $T(\text{initial}) - T(\text{final})$ is diverted, respectively (where T is the transmissivity). The analytical expressions for the best fit of this data (straight lines) are given in Table 1.

Table 1. Time Response of Self-Pumped Photorefractive Materials^a

Material	Time(s) versus I (W/cm ²) Relationship	Response Time(s) (W/cm ²)		Wavelength (nm)	Point of Measurement
		0.2	2		
Phase-conjugate initiation time					
Ce-SBN:75	$\tau_i = 12.5 I^{-0.50}$	32	8.3 ^b	442	90°
Ce-SBN:75	$\tau_i = 2.6 I^{-0.68}$	7.7	1.6 ^b	442	e^{-1}
BaTiO ₃ ^c	$\tau_i = 5 I^{-1.0}$	25 ^b	2.5 ^b	514.5	90°
Ce-BSKNN ^d	$\tau_i = 125 I^{-0.50}$	279	88	457.9	e^{-1}
Beam-fanning response time					
Ce-SBN:75	$\tau = 1.3 I^{-1.06}$	7.2	0.6 ^b	442	90°
Ce-SBN:75	$\tau = 0.47 I^{-0.88}$	2.0	0.25 ^b	442	e^{-1}
Ce-SBN:60 ^e	$\tau = 0.11 I^{-1.1}$	0.6	0.05 ^b	442	e^{-1}
BaTiO ₃ ^f	$\tau = 1.1 I^{-0.91}$	4.8 ^b	0.6 ^b	488	90°
Ce-BSKNN ^g	$\tau = 1.54 I^{-0.82}$	5.8	0.9	457.9	e^{-1}

^a All data are for self-pumping via internal reflection except the initiation time for BaTiO₃, which is for a ring-passive phase-conjugate mirror.

^b Extrapolated data.

^c Ref. 19.

^d Ref. 10.

^e Ref. 8.

^f Ref. 17.

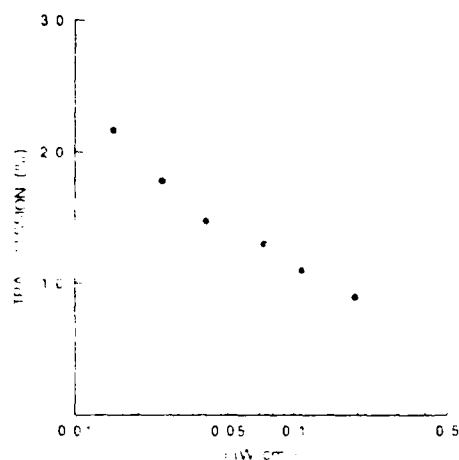


Fig. 5. The transmission through a SBN:75 crystal as a function of the incident intensity for steady-state beam fanning.

beam fanning is plotted in Fig. 4. The data indicate that the slope of the time-versus-intensity curves for beam fanning is not the same as the corresponding slope for self-pumping. This observation is consistent with earlier arguments regarding the saturation of the grating diffraction efficiency. That is, the input beam intensity for which saturation occurs would be expected to be lower for the self-pumping configuration than for the beam-fanning configuration because of the noticeably higher intensities that form in the corner loop during self-pumping. The beam-fanning response times are compared in Table 1 with those of other materials for two different intensities.

In summary, we report on the beam-fanning properties of SBN:75 and its behavior as a self-pumped phase-conjugate mirror. In addition, we report on the measured time response for these effects and compare the results with those obtained in other photorefractive crystals for similar pumping conditions and intensities.

References

1. J. Feinberg, *Optical Phase Conjugation*, R. A. Fisher, ed. (Academic, New York, 1983), p. 417.
2. G. C. Valley and M. B. Klein, *Opt. Eng.* **22**, 704 (1983).
3. S. Sternklar, S. Weiss, M. Segev, and B. Fischer, *Opt. Lett.* **11**, 528 (1986).
4. J. Feinberg, *Opt. Lett.* **7**, 486 (1982).
5. J. O. White, M. Cronin-Golomb, B. Fischer, and A. Yariv, *Appl. Phys. Lett.* **40**, 450 (1982).
6. J. Feinberg and R. W. Hellwarth, *Opt. Lett.* **5**, 519 (1980).
7. F. C. Jahoda, P. G. Weber, and J. Feinberg, *Opt. Lett.* **9**, 362 (1984).
8. G. Salamo, M. J. Miller, W. W. Clark III, G. L. Wood, and E. J. Sharp, *Opt. Commun.* **59**, 417 (1986).
9. E. J. Sharp, M. J. Miller, G. L. Wood, W. W. Clark III, G. J. Salamo, and R. R. Neurgaonkar, *Ferroelectrics Suppl., Proceedings of Sixth IEEE International Symposium on Applications of Ferroelectrics* (1986), p. 51.
10. J. Rodriguez, A. Siahmakoun, G. J. Salamo, M. J. Miller, W. W. Clark III, G. L. Wood, E. J. Sharp, and R. R. Neurgaonkar, "Self-pumped phase conjugation in photorefractive Ba_{1-x}Sr_xK_{1-x}Na_{1-x}Nb_{1-x}O₃," submitted to *Appl. Opt.*
11. K. Megumi, H. Kozuka, M. Kobayashi, and Y. Furuhashi, *Appl. Phys. Lett.* **30**, 631 (1977).
12. G. Rakuljic, A. Yariv, and R. Neurgaonkar, *Opt. Eng.* **25**, 1212 (1986).
13. R. R. Neurgaonkar and W. K. Cory, *J. Opt. Soc. Am.* **3**, 274 (1986).
14. B. T. Anderson, P. R. Foreman, and F. C. Jahoda, *Opt. Lett.* **10**, 627 (1985).
15. D. Pepper, *Appl. Phys. Lett.* **49**, 1001 (1986).
16. J. Feinberg, *J. Opt. Soc. Am.* **72**, 46 (1982).
17. M. Cronin-Golomb and A. Yariv, *J. Appl. Phys.* **57**, 4906 (1985).
18. P. Gunter, *Phys. Rep.* **93**, 199 (1982).
19. M. Cronin-Golomb, K. Y. Lau, and A. Yariv, *Appl. Phys. Lett.* **47**, 567 (1985).
20. We determined that the sign of the electro-optic coefficient, r_{33} , is positive by the use of a calibrated compensator. This fact, coupled with the observation that extraordinary light fans toward the electrode held positive during poling, gives a negative sign for the photorefractive charge carriers.



Rockwell International
Science Center

SC5441.FTR

FERROELECTRIC PROPERTIES OF La-MODIFIED SBN:60 SINGLE CRYSTALS

FERROELECTRIC PROPERTIES OF LANTHANUM-MODIFIED $\text{Sr}_{0.6}\text{Ba}_{0.4}\text{Nb}_2\text{O}_6$ SINGLE CRYSTALS

R.R. NEURGAONKAR, J.R. OLIVER and W.K. CORY

Rockwell International Science Center, Thousand Oaks, California 91360, USA

and

L.E. CROSS

Materials Research Laboratory, The Pennsylvania State University, University Park, Pennsylvania 16802, USA

Received 20 October 1987; manuscript received in final form 22 January 1988

The role of La^{3+} in tungsten bronze $\text{Sr}_{0.6}\text{Ba}_{0.4}\text{Nb}_2\text{O}_6$ (SBN:60) ferroelectric crystals has been studied with respect to Czochralski crystal growth parameters and fundamental ferroelectric properties. Direct substitution of La^{3+} for Sr^{2+} or Ba^{2+} results in a significant decrease of the ferroelectric phase transition temperature and, consequently, dramatic increases in the room temperature dielectric constant and pyroelectric coefficient along the polar axis. Although La-modified SBN:60 is more difficult to grow, it was possible to grow defect-free crystal boules up to 2 cm diameter with optical quality. Striation-free crystals found for lanthanum modifications up to 1.0 mol%

1. Introduction

Tungsten bronze solid solution crystals such as $\text{Sr}_{1-x}\text{Ba}_x\text{Nb}_2\text{O}_6$ (SBN), either doped or undoped, have proven to be excellent materials for various applications such as guided wave optics [1], photorefractive [2-7], millimeter wave [8-10] and pyroelectric [11,12] device applications. Tetragonal (4mm) bronze crystals, such as SBN, exhibit excellent transverse ferroelectric and optical properties in contrast to perovskite BaTiO_3 crystals which show strong longitudinal optical properties. Fig. 1 shows the classification of the various types of tungsten bronze crystals based on their crystal structure and ferroelectric and optical properties. Included among these are important bronzes such as SBN, BSKNN, KLN, SKN, morphotropic PBN, SNN and SCNN [13,14] all of which have potential utility in millimeter wave and optical applications, although high-quality crystal growth has proven to be difficult in some instances.

The present paper focused on modified versions of the congruently melting [15] $\text{Sr}_{0.6}\text{Ba}_{0.4}$

Nb_2O_6 (SBN:60) crystal composition with La^{3+} substituting for Sr^{2+} or Ba^{2+} in the crystal lattice. Previous work by Liu and Maciolek [11] has shown that rare-earth-modified $\text{Sr}_{0.6}\text{Ba}_{0.4}\text{Nb}_2\text{O}_6$ (SBN:50) results in a lowered ferroelectric phase transition temperature and thereby improved pyroelectric properties. However, SBN:50 is an incongruently melting bronze composition which is difficult to grow in bulk single crystal form, particularly with good optical quality. SBN:60, on the other hand, can be grown with excellent optical quality [14] and therefore presents the opportunity to grow modified crystals of comparable high quality for potential millimeter wave, optical and pyroelectric applications.

2. Experimental

2.1. The SBN:60- $M^{3+}\text{NbO}_4$ system

Modified forms of SBN were initially studied using sintered ceramic samples. For convenience,

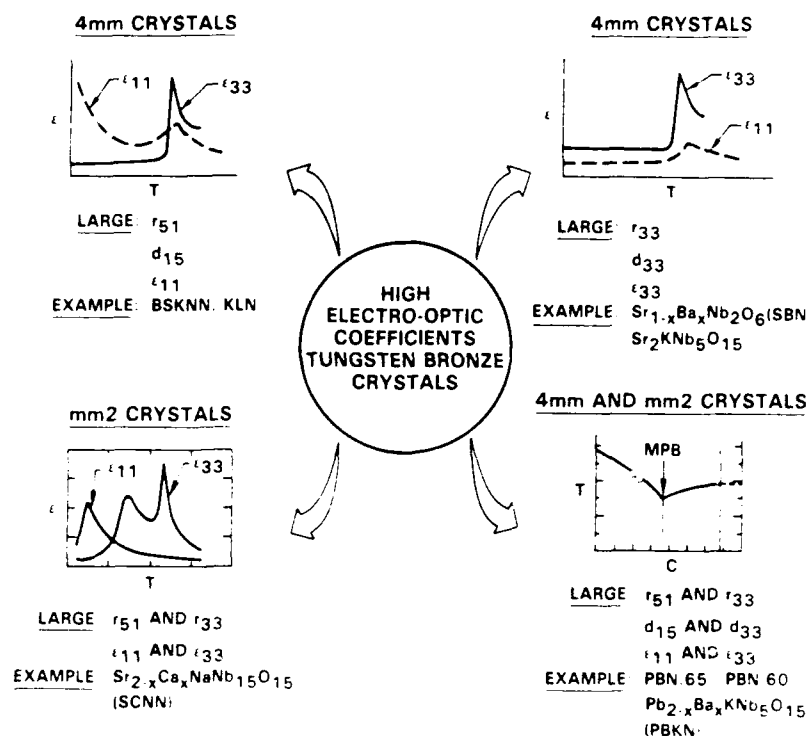


Fig. 1. Classification of tungsten bronze ferroelectric crystals.

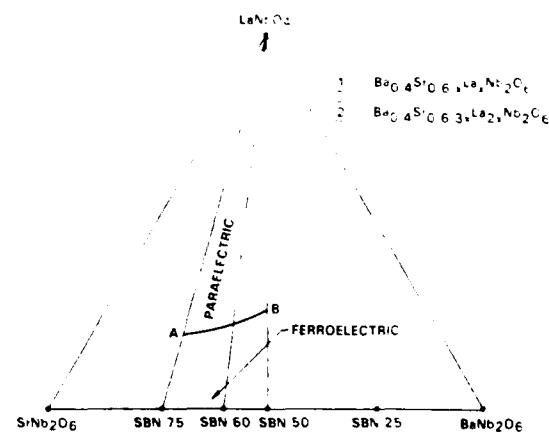
modifications of the composition SBN:50 were examined because of its higher phase transition temperature (~ 120 versus 75°C for SBN:60). Reagent grade BaCO_3 , SrCO_3 , Nb_2O_5 and La_2O_3 or Y_2O_3 oxide powders were used for these ceramics, with the thoroughly mixed materials calcined at 1000°C , ball-milled in acetone, and then cold-pressed and sintered at 1350°C for 4 h. Rare earth modifications of $\text{Sr}_{0.75}\text{Ba}_{0.25}\text{Nb}_2\text{O}_6$ (SBN:75) and SBN:60 ceramic compositions were also checked for solid solubility and structure using X-ray diffraction measurements.

Since lanthanum and yttrium exist in trivalent states, modifications of SBN:50 were attempted in the following manner:

- (1) $\text{Sr}_{0.5-x}\text{M}_x^{3+}\text{Ba}_{0.5}\text{Nb}_2\text{O}_6$,
 - (2) $\text{Sr}_{0.5-x}\text{La}_{2x}\square_x\text{Ba}_{0.5}\text{Nb}_2\text{O}_6$,
- $\text{M} = \text{La or Y}$,

where \square represents a lattice site vacancy.

Equivalent substitutions for Ba^{2+} were also examined. The phase diagram for La-modification is illustrated in fig. 2; X-ray analysis showed that the

Fig. 2. Ternary phase diagram for the BaNb_2O_6 - SrNb_2O_6 - LaNbO_4 solid solution system.

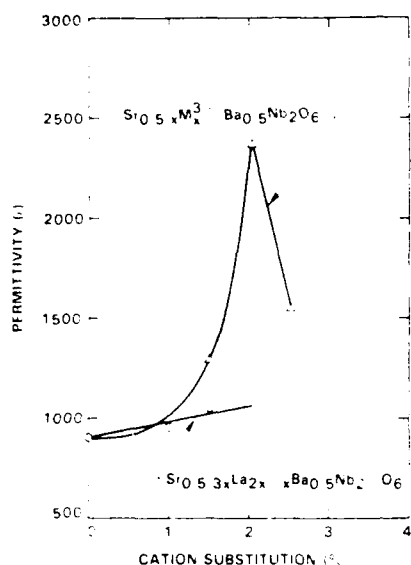


Fig. 3. Room temperature dielectric constant for La-modified SBN:50 ceramics.

solubility limit for these modifications of SBN is upwards of 20 mol%.

Fig. 3 shows the room temperature dielectric constant at 1 kHz for two types of SBN:50 ceramic modifications using La^{3+} ; similar results were obtained for Y^{3+} modifications. Only the type $\text{Sr}_{0.5-x}(\text{La}, \text{Ba})_{3x}\text{Nb}_2\text{O}_6$ modification resulted in significant changes in the dielectric constant with increasing La^{3+} or Y^{3+} substitution, this being a consequence of a lower ferroelectric phase transition temperature. Equivalent results were also obtained with rare earth substitutions for Ba^{2+} . Hence, only type 1 modifications were used in subsequent crystal growth work with SBN:60. Since Sr^{2+} and La^{3+} have similar cationic sizes, Czochralski crystal growth was attempted for La-modified SBN:60 to avoid potential growth problems which might arise from dissimilar size cations in the same crystallographic site.

2.2 Growth of La-modified SBN:60 single crystals

Because of extensive prior experience in the Czochralski crystal growth of congruently melting

SBN:60 [16], the growth of La-modified SBN:60 proceeded without undue difficulty. A $\text{Sr}_{0.5-x}\text{La}_x\text{Ba}_{0.5}\text{Nb}_2\text{O}_6$ substitution of La^{3+} for Sr^{2+} was used (type 1 modification), with concentrations varying from 0.5 to 2.0 mol%. High purity starting materials were used exclusively for these growths with the calcined materials thoroughly ball-milled in acetone prior to melting in a 5 cm diameter, 5 cm height platinum crucible. All crystal growths were performed in an RF induction heated furnace operating at 370 kHz.

The incorporation of La^{3+} in the SBN crystal lattice did not cause major changes in the growth conditions. Czochralski growth was performed along the c -axis ($\langle 001 \rangle$) using an automatic diameter control system (proven mandatory for high-quality tungsten bronze crystal growth) and an after-heater geometry. Initially, c -axis SBN:60 crystal seeds were used until La-modified crystals became adequate for use in subsequent growths. Bulk fracture was an early problem in these growths, probably as a result of the multiple site preference of La^{3+} in the 15-, 12- and 9-fold coordinated oxygen octahedra sites of the SBN lattice. This problem was overcome in part by maintaining strictly constant cooling rates after crystal growth.

Fig. 4 shows examples of unmodified and La-modified SBN:60 crystal boules. Modified crystals were successfully grown up to 2 cm in diameter. A striking feature of these crystals, common to other tungsten bronzes, is the presence of large natural facets. La-modified SBN:60 boules grow with 24 natural facets, similar to unmodified crystals, with the crystal cross-section becoming more rectangular with increasing lanthanum modification and featuring large $\langle 100 \rangle$ and $\langle 010 \rangle$ facets, as seen in fig. 4. A rectangular growth habit is not uncommon to crystals in the tungsten bronze family; for example, larger unit cell bronzes such as $\text{Ba}_{2-x}\text{Sr}_x\text{K}_{1-x}\text{Na}_x\text{Nb}_5\text{O}_{15}$ (BSKNN) and KLN typically grow in a rectangular shape with 8 well-defined facets [14]. What is unusual about La-modified SBN:60 crystals is that the crystal unit cell does not change markedly with increasing lanthanum content; for example, a 1.0 mol% La-modified crystal has unit cell dimensions of $a = b = 12.466 \text{ \AA}$, $c = 3.930 \text{ \AA}$ compared to $a = b =$



Fig. 4. La-modified (left) and unmodified (right) SBN:60 crystal boules grown by the Czochralski technique. Marker represent 2 cm

12.465 Å, $c = 3.935$ Å for unmodified SBN:60. Hence, the gradual change in growth habit from a circular to a more rectangular shape with La modification may be a result of the partial occupancy of the otherwise empty 9-fold coordinated lattice site.

Table 1 summarizes the major crystal growth parameters and physical properties of these crystals. Crystal growth beyond 2 mol% modification was not attempted since we wished to maintain a ferroelectric phase at room temperature. Furthermore, the more heavily modified compositions showed major optical striations and were very difficult to grow. Nevertheless, it would be interesting to examine crystals with heavier La modifications since such paraelectric (4/mm) crystals should have large quadratic electro-optical and possibly large electrostrictive properties.

2.3. Ferroelectric properties

The polar c -axis dielectric properties for a poled, 1 mol% La-modified SBN:60 crystal are shown as a function of temperature in fig. 5. Like unmodified SBN crystals, the polar axis dielectric constant is characterized by a large dielectric anomaly at the ferroelectric phase transition temperature (Curie point), above which the dielectric constant follows a Curie-Weiss law.

$$\epsilon_{33} = C_3(T - \Theta_3), \quad (1)$$

where $C_3 = 4.3 \times 10^5$ and $\Theta_3 = 38^\circ\text{C}$. The Curie constant, C_3 , remains remarkably unchanged with La substitution up to 2 mol%, with the only change occurring in the Curie temperature, Θ_3 , which is 75°C in unmodified SBN:60. The drop in Θ_3 with La substitution is nearly at approximately 36°C/mol\% , so that for a 1.5 mol% substitution, Θ_3 occurs at room temperature.

As evident in fig. 5, SBN:60/La shows a strong frequency dependence for the polar axis dielectric

Table 1
Growth conditions and properties for pure and La^{3+} modified SBN:60 crystals

	SBN:60	SBN:60/La (1 mol% La)	SBN:60/La (1.5 mol% La)
Crystal symmetric at 20°C	4mm	4mm	4mm
Growth temperature ($^\circ\text{C}$)	1480 $^\circ\text{C}$	1480 $^\circ\text{C}$	1475 $^\circ\text{C}$
Pulling rate (mm/h)	10	9	6-7
Interface	Smooth and flat	Rough but nearly flat	Rough and concave
Quality	Optical	Optical	Weak striations
Growth habit	Circular	Near-circular	Squarish
Number of facets	24 Facets	24 Facets, (100) prominent	24 Facets (100) prominent
Color	Pale cream	Pale cream	Pale cream

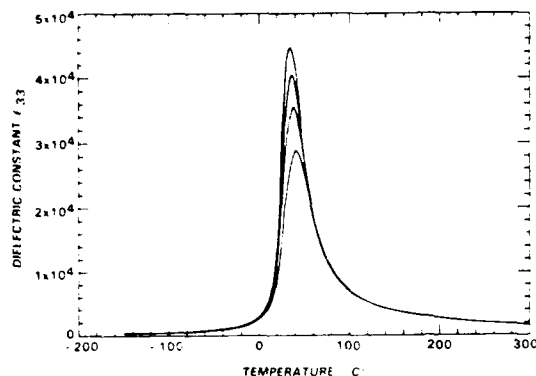


Fig. 5. Polar axis dielectric constant for a poled, 1.0 mol% La-modified SBN:60 crystal at 100 Hz (upper curve), 1.0 kHz and 10 kHz (lower curve).

constant near the phase transition. Because of this relaxor behavior, the temperature of the dielectric maximum, T_c , varies with frequency from 34 to 42 °C over a 100 Hz to 100 kHz range, for a 1 mol% La substitution, so that the specification of T_c loses some of its meaning. Relaxor behavior has also been found in unmodified SBN:60 [10] but the effects are much less pronounced than those in fig. 5. This behavior in SBN:60 is felt to arise from the lattice site uncertainty of the Sr^{2+} and Ba^{2+} ions between the 15- and 12-fold coordinated oxygen octahedral sites of the partially empty lattice, leading to a distribution of phase transition temperatures in the crystal bulk. In the present case of La substitution, this site uncertainty extends to the 9-fold coordinated site as well, so that more pronounced relaxor effects would be expected.

Because of the lowered phase transition temperature and increased relaxor effects, the room temperature polar axis dielectric constant for 1 mol% La-substituted SBN:60 is very large at 9600–7000, depending on frequency. These values are roughly an order of magnitude large than the nearly dispersionless value of 920 for unmodified crystals. The corresponding room temperature dielectric loss tangent varies from 0.01 to 0.07 in poled crystals, about a factor of five greater than for unmodified SBN:60 but still reasonable in light of the close proximity of the phase transition

temperature. For 1.5 mol% La substitution, the relaxor effects become very pronounced, with $\epsilon_{33} = 36000$ –21000 and $\tan \delta = 0.05$ –0.28.

Crystal poling was found to be straightforward, with a 5 kV/cm DC poling field being sufficient to pole the crystals at room temperature to a single ferroelectric domain. No advantages were found by poling from the phase transition temperature down to room temperature. The coercive field necessary to initiate ferroelectric domain reversal at room temperature was relatively low at 1–2 kV/cm, a factor for consideration in potential device applications.

The nonpolar *a*-axis dielectric constant, ϵ_{11} , for a 1 mol% La-modified SBN:60 crystal is shown as a function of temperature in fig. 6. The dielectric anomaly near 40 °C is typical of SBN:60 crystals and arises from the onset of nonzero spontaneous polarization along the *c*-axis [14]. As a result, some frequency dispersion is observed near the peak, but the effect is generally minimal. The *a*-axis constant follows a Curie-Weiss law above the phase transition temperature, with $C_1 = 2.1 \times 10^7$ and $\theta_1 = -265 \pm 20$ °C. As in the *c*-axis case, C_1 is essentially the same as for unmodified SBN:60, with only θ_1 varying downward from -245 °C with increasing La substitution. At room temperature, $\Theta = 640$ for 1 mol% La modification, increasing to 700 for 1.5 mol% crystals. The corresponding dielectric loss tangents are low (0.012 or less) and are nearly independent of frequency.

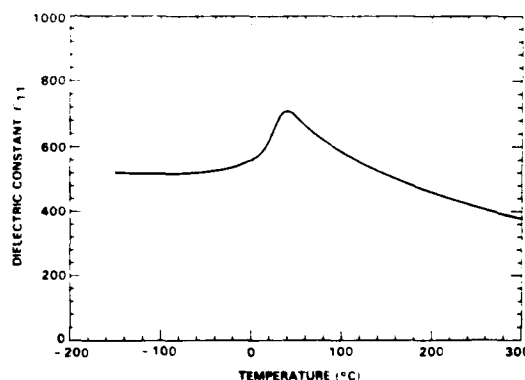


Fig. 6. Nonpolar *a*-axis dielectric constant for 1.0 mol% La-modified SBN:60 at 10 kHz. Data at other frequencies are substantially the same.

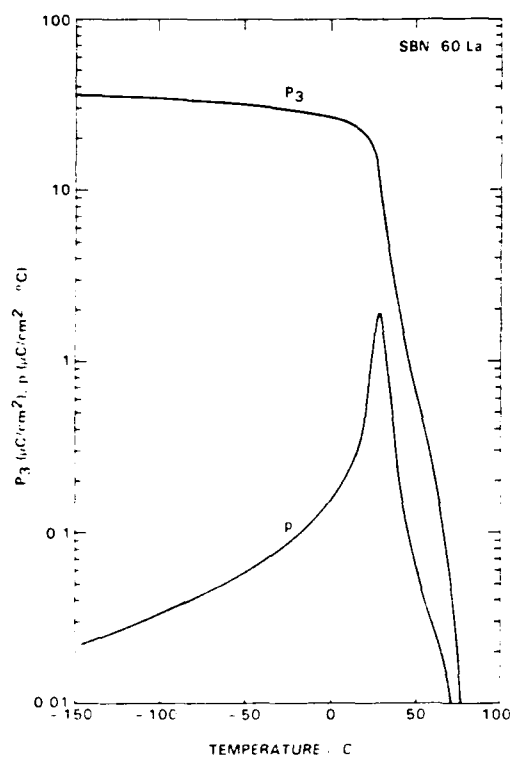


Fig. 7. Polarization, P_3 , and the pyroelectric coefficient, p , for 1.0 mol% La-modified SBN:60.

The net spontaneous polarization along the c -axis, P_3 , was measured by integrating the charge

released during warming at a uniform rate ($2^\circ\text{C}/\text{min}$) under zero bias conditions [12]. The results for 1 mol% La substituted SBN:60 are shown in fig. 7 along with the pyroelectric coefficient, $p = -dP_3/dT$. As in the case for the dielectric properties, the polarization and the pyroelectric coefficient behave in a manner similar to that for unmodified SBN:60, differing only in an overall temperature shift of the characteristics due to the change in Θ_3 and a slight broadening of the pyroelectric peak near the phase transition. The pyroelectric maximum occurs at 27°C , 11°C below Θ_3 , compared to the 8°C separation typical of unmodified SBN:60 crystals; this downward shift from Θ_3 is a consequence of the diffuse nature of the ferroelectric transition.

The room temperature values of the spontaneous polarization and the pyroelectric coefficient are summarized in table 2 along with other ferroelectric data for unmodified, 1 mol% and 1.5 mol% La-modified SBN:60 crystals. The changes in these parameters with composition, as well as the changes in the dielectric properties, are essentially reflections of the changes in the Curie temperature. For example, in the particular case of 1.5 mol% La modification, the very low polarization and large ϵ_{33} are due to the occurrence of the phase transition close to room temperature; consequently, these parameters are also extremely sensitive to small temperature changes.

Table 2
Ferroelectrical properties^a

	SBN:60	SBN:60-La (1.0 mol% La)	SBN:60-La (1.5 mol% La)
Curie point, T_C ^b ($^\circ\text{C}$)	73–76	34–42	17–28
Θ_3 ($^\circ\text{C}$)	75	38	22
C_3 ($^\circ\text{C}$)	4.1×10^5	4.3×10^5	4.3×10^5
Θ_1 ($^\circ\text{C}$)	$-245 \pm 20^\circ$	$-265 \pm 20^\circ$	$-275 \pm 20^\circ$
C_1 ($^\circ\text{C}$)	2.04×10^5	2.1×10^5	2.1×10^5
ϵ_{33} (at 1 kHz)	920	8800	30,000 ^c
ϵ_{11} (at 1 kHz)	485	640	700
P_3 ($\mu\text{C}/\text{cm}^2$)	28.5	21.1	3.4
p ($\mu\text{C}/\text{cm}^2 \cdot ^\circ\text{C}$)	0.097	0.62	0.95
E-O coefficient, r_{33} ^c (10^{-12} m/V)	460	3290	1800

^a All values are at 20°C , unless otherwise indicated.

^b Over range 100 Hz to 100 kHz.

^c Calculated values (see text).

3. Discussion

It is worthwhile to examine the potential utility of La-modified SBN:60 crystals in potential device applications. For pyroelectric detector considerations, the decrease of the phase transition temperature with La-modification crystal necessarily increases both the polar axis dielectric constant and the pyroelectric coefficient at room temperature, as shown in table 2, so that the longitudinal pyroelectric device figure-of-merit, p/ϵ_{33} , actually declines with increasing La substitution. However, in transverse pyroelectric detector configurations where a low detector impedance (high capacitance) is desirable, La-modified SBN:60 is clearly superior to unmodified SBN:60 because of the higher dielectric constant and pyroelectric coefficient available.

The large increase in the room temperature dielectric constant over unmodified SBN:60 is also significant for electro-optical or nonlinear optical applications. From the phenomenology developed for tetragonal tungsten bronze ferroelectrics [17], the linear electro-optic coefficient, r_{33} , is given by

$$r_{33} = 2g_{33}P_3/\epsilon_0\epsilon_{33}, \quad (2)$$

where g_{33} is the quadratic electro-optic coefficient and ϵ_0 is the permittivity of free space. In the particular case of La-modified SBN:60, the enhancement of r_{33} due to the dramatic increase of ϵ_{33} at room temperature is partially offset by a corresponding decrease in the spontaneous polarization. Nevertheless, the calculated r_{33} for 1.0 mol% La modification, using $g_{33} = 0.10 \text{ m}^4/\text{C}^2$ typical of bronze ferroelectrics, is $3290 \times 10^{-12} \text{ m/V}$ at 1 kHz compared to $460 \times 10^{-12} \text{ m/V}$ (470×10^{-12} , measured) for unmodified SBN:60. The lower value of $1800 \times 10^{-12} \text{ m/V}$ for 1.5 mol% modification in table 2 results from the substantial decline in the spontaneous polarization at the room temperature ferroelectric phase transition. In this case, it is also difficult to maintain a single ferroelectric domain unless a dc bias field is maintained on the crystal; this would also serve to substantially increase P_3 , and therefore, r_{33} .

The large pyroelectric and electro-optic coefficients for La-modified SBN:60 crystals make these very attractive materials for infrared focal plane array, millimeter wave, electro-optic and nonlinear optical applications. Although heavily modified crystals ($\geq 1.5 \text{ mol\%}$) have prominent optical striations, more lightly modified crystals have excellent optical quality and can maintain a single ferroelectric domain, after poling, for an indefinite period of time below 35°C . Lanthanum modifications greater than 1.5 mol% result in crystal which are paraelectric at room temperature, which may be of interest for very low loss, biased pyroelectric detectors or for electrostrictive applications; quadratic electro-optic applications, however, would necessarily require further improvements in crystal optical quality.

These very attractive materials for infrared focal plane array, millimeter wave, electro-optic and nonlinear optical applications. Although heavily modified crystals ($\geq 1.5 \text{ mol\%}$) have prominent optical striations, more lightly modified crystals have excellent optical quality and can maintain a single ferroelectric domain, after poling, for an indefinite period of time below 35°C . Lanthanum modifications greater than 1.5 mol% result in crystal which are paraelectric at room temperature, which may be of interest for very low loss, biased pyroelectric detectors or for electrostrictive applications; quadratic electro-optic applications, however, would necessarily require further improvements in crystal optical quality.

Acknowledgements

This work was supported by DARPA (Contract No. N00014-82-C-2246) and by the Office of Naval Research (Contract No. N00014-81-C-0463).

References

- [1] O. Etkovyan, C.H. Bulmer, H.F. Taylor, W.K. Burns, A.S. Greenblatt, L.A. Beach and R.R. Neurgaonkar, *Appl. Phys. Letters* 48 (1986) 13.
- [2] G.J. Salamo, M.J. Miller, E.J. Sharp, G.L. Wood and W.W. Clark III, *Opt. Commun.* 59 (1986) 417.
- [3] E.J. Sharp, M.J. Miller, G.L. Wood, W.K. Clark III, G.J. Salamo and R.R. Neurgaonkar, in: *Proc. 6th IEEE Intern. Symp. on Applications of Ferroelectrics (ISAF)*, 1986, p. 51.
- [4] G.E. Rakuljic, A. Yaniv and R.R. Neurgaonkar, *Appl. Phys. Letters* 50 (1987) 10.
- [5] M.J. Miller, E.J. Sharp, G.L. Wood, W.W. Clark III, G.J. Salamo and R.R. Neurgaonkar, *Opt. Letters* 12 (1987) 340.
- [6] J. Rodriguez, A. Siahmakoun, G. Salamo, M.J. Miller, W.W. Clark III, G.L. Wood, E.J. Sharp and R.R. Neurgaonkar, *Appl. Opt.* 26 (1987) 1732.]
- [7] M.D. Ewbank, R.R. Neurgaonkar, W.K. Cory and J. Feinberg, *Appl. Phys. Letters* 62 (1987) 374.
- [8] B. Bobbs, M. Matloubin, H.R. Fetterman, R.R. Neurgaonkar and W.K. Cory, *Appl. Phys. Letters* 48 (1986) 1642.
- [9] W.W. Ho, W.F. Hall and R.R. Neurgaonkar, *Ferroelectrics* 56 (1984) 230.

- [10] R.R. Neurgaonkar, W.W. Ho, W.K. Cory, W.F. Hall and L.E. Cross, *Ferroelectrics* 51 (1984) 185.
- [11] S.T. Liu and R.B. Macielek, *J. Electron. Mater.* 4 (1975) 91.
- [12] A.M. Glass, *J. Appl. Phys.* 40 (1969) 4699.
- [13] J.R. Oliver, G. Shoop and R.R. Neurgaonkar, in: *Proc. 6th IEEE Intern. Symp. on Applications of Ferroelectrics (ISAF)*, 1987, p. 485.
- [14] R.R. Neurgaonkar and W.K. Cory, *J. Opt. Soc. Am. B3* (1986) 274.
- [15] K. Megumi, N. Nagatsuma, K. Kashiwada and Y. Furuhata, *Mater. Sci.* 11 (1976) 1583.
- [16] R.R. Neurgaonkar, W.K. Cory and J.R. Oliver, *Ferroelectrics* 35 (1983) 301.
- [17] M. DiDomenico and S.H. Wemple, *J. Appl. Phys.* 40 (1969) 720.



Rockwell International

Science Center

SC5441.FTR

VAPOR DIFFUSED OPTICAL WAVEGUIDES IN SBN:60

Vapor diffused optical waveguides in strontium barium niobate (SBN: 60)

O. Eknayan,^{a)} C. H. Bulmer, H. F. Taylor, W. K. Burns, A. S. Greenblatt, and L. A. Beach
Naval Research Laboratory, Washington, D.C. 20375-5000

R. R. Neurgaonkar

Rockwell International Science Center, Thousand Oaks, California 91360

(Received 22 August 1985; accepted for publication 22 October 1985)

Single mode planar and channel waveguides have been produced in $\text{Sr}_{0.6}\text{Ba}_{0.4}\text{Nb}_2\text{O}_6$ (tungsten bronze structure) by sulfur diffusion in a sealed ampule, followed by oxidation in an open tube. Losses in channel waveguides were $\sim 15\text{--}20\text{ dB/cm}$ for TM polarization and $\sim 27\text{--}32\text{ dB/cm}$ for the TE polarization in z-cut substrates. Electro-optic modulation was observed after poling of the substrate. The experimentally determined value of the effective electro-optic coefficient was slightly greater than reported earlier for bulk samples of SBN:60, and about 15 times greater than for LiNbO_3 . Based on measurements with the S_{35} radioisotope, the average atomic sulfur concentration was estimated to be about $4 \times 10^{17}/\text{cm}^3$ in the region extending from the surface to a depth of $2.5\text{ }\mu\text{m}$, and a significant background concentration ($\sim 5 \times 10^{16}/\text{cm}^3$) was present to depths in excess of $20\text{ }\mu\text{m}$.

Metal diffusion in LiNbO_3 and LiTaO_3 is the most commonly used technique for fabricating waveguides for integrated optics.^{1,2} There has, however, been a continuing interest in producing waveguides and modulators in other ferroelectric materials with higher electro-optic coefficients. One particularly attractive candidate is $\text{Sr}_{0.6}\text{Ba}_{0.4}\text{Nb}_2\text{O}_6$ (SBN:60), in which recent improvements in growth techniques have led to the production of large ($\sim 1\text{-in.}$ dimension) crystals of excellent optical quality. The r_{33} electro-optic coefficient of $\text{Sr}_{0.6}\text{Ba}_{0.4}\text{Nb}_2\text{O}_6$ at room temperature³ is more than an order of magnitude greater than that for LiNbO_3 and LiTaO_3 .⁴ However, previous efforts to produce suitable waveguides in SBN:60 by metal diffusion in this laboratory and elsewhere have been unsuccessful. This letter reports the use of vapor diffusion to fabricate planar and channel waveguides in SBN:60. This represents the first use of gaseous diffusion to fabricate waveguides in any ferroelectric material, and the first fabrication of waveguides in any material with such a high electro-optic coefficient. Electro-optic modulation has been demonstrated in channel waveguides, and a radioisotope technique has been used to characterize the sulfur diffusion process.

The waveguides were produced by indiffusion of sulfur followed by oxidation. The indiffusion process is very similar to that used to produce waveguides in CdS by Se indiffusion.⁵ Initially, a substrate was loaded with sulfur powder in a quartz ampule which was evacuated with a diffusion pump and sealed at a gauge pressure of about 10^{-7} Torr. The ampule was then heated in a tube furnace for several hours. The best waveguides for which the data below are reported, were obtained for diffusion at 800°C for 6 h, although waveguiding was observed for diffusion temperatures as high as 900°C . After the ampule was removed from the furnace and broken to remove the crystal, it was treated with flowing oxygen in an open-tube furnace at 600°C for 24 h. The oxidation produced a clear (transparent) band $\sim 2\text{ mm}$ wide

around the periphery of the crystal, which was totally opaque in appearance after the sulfur diffusion.

In order to determine whether the presence of sulfur is necessary for waveguide formation, the procedure described above was followed except that no sulfur was added to the ampule containing the crystal. No waveguiding was observed in this sample. Another as-polished crystal was run through the oxidation step only, with similarly negative results. It was concluded that the sulfur diffusion is necessary for waveguide formation.

The substrates were cut from single-crystal boules grown by Czochralski technique from a platinum crucible at the congruent melt composition $\text{Sr}_{0.6}\text{Ba}_{0.4}\text{Nb}_2\text{O}_6$ ($T_c = 78^\circ\text{C}$). Careful temperature control of the melt virtually eliminated striations which had been observed in SBN:60 grown earlier.^{6,7} Both z-cut and y-cut substrates were utilized, and typical dimensions were $\sim 0.5\text{--}1.0\text{ cm}$ in length per side and 1 mm thick. The large-area surfaces were polished prior to diffusion, and the ends were polished after diffusion. To make channel waveguides, the appropriate photolithographically defined pattern was etched in a 3000-\AA -thick layer of SiO_2 which had been sputtered on the surface of the substrate.

Optical evaluation was carried out with a $0.63\text{-}\mu\text{m}$ HeNe laser using both end-fire and prism coupling. Measurements on planar waveguide in z-cut substrates indicated an effective mode refractive index change in the range of $0.001\text{--}0.0025$ for both polarizations. Optical insertion losses were measured in channel waveguides in z-cut substrates after polishing. In these samples, a 500-\AA -thick sputtered SiO_2 buffer layer and a gold electrode had been deposited on top of waveguides. Insertion losses for the TM mode in a 5-mm -long sample ranged from 15 dB for a waveguide produced from a $20\text{-}\mu\text{m}$ -wide mask to 12.5 dB for a $2\text{-}\mu\text{m}$ width. Insertion losses for the TE mode were consistently about 6 dB greater for these channels. Applying a correction estimated at 5 dB for Fresnel and mode-mismatch losses leads to waveguide attenuation figures of $15\text{--}20\text{ dB/cm}$ for the TM mode and $27\text{--}32\text{ dB/cm}$ for the TE mode. Near-field profiles

^a Visiting scientist from Texas A&M University, Electrical Engineering Department, College Station, TX 77843-3128

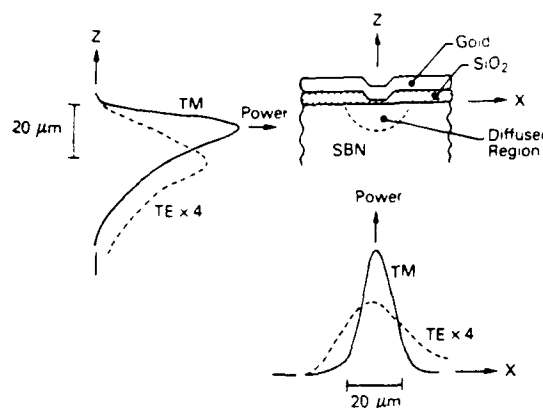


FIG. 1. Near-field patterns for waveguide produced with 8- μ m-wide channel mask (resolution $\sim 0.2 \mu$ m). The plots were obtained by scanning a photodetector with a narrow slit in front of it across an image of the waveguide aperture.

for a single mode waveguide diffused through an 8- μ m channel mask are given in Fig. 1.

Electro-optic modulation was observed in the channel waveguides with the input light polarized at 45° to the crystal axes and the output analyzer also oriented at 45° . Peak to peak voltages as high as 300 V were applied along the c axis across the 1-mm substrate thickness to the 4.3-mm-long top electrode. A typical intensity modulation behavior is shown in Fig. 2. A value of the effective electro-optic coefficient $r_{33} = n_1^3 r_{13}/n_3^3$ was determined to be $3.3 \pm 0.2 \times 10^{-10}$ m/V over the frequency range from 100 Hz to 1 MHz from these measurements. This is about 20% greater than values of this same quantity determined previously from measurements on bulk samples of SBN:60,⁴ and about 15 times greater than for LiNbO₃.⁸

To investigate the diffusion process, a radioactive tracer technique⁹ employing the low-energy (167.4 keV) β^- emitter S₃₅ was used. The normal diffusion process was followed, except that a measured quantity of the radioisotope was added

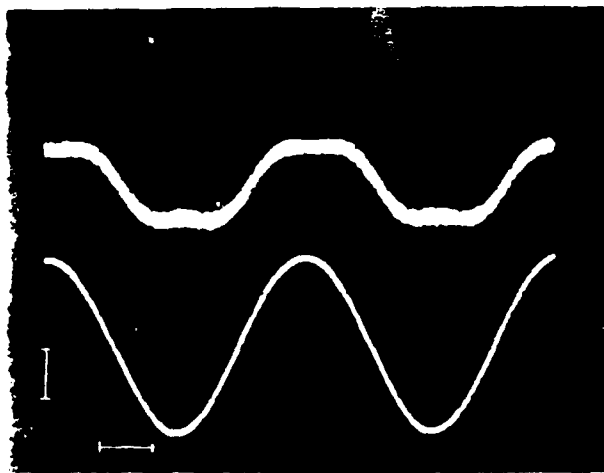


FIG. 2. Observed intensity modulation behavior. Top trace: photodetector signal (2 mV/div), bottom trace: modulating voltage (20 V/div), frequency = 1 kHz.

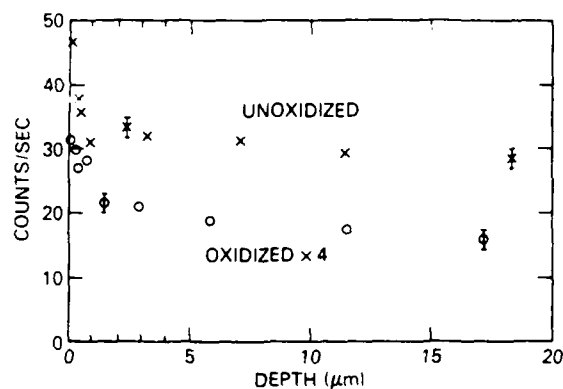


FIG. 3. Profiles of radioisotope activity as a function of depth for one sample immediately after sulfur diffusion and another which was oxidized after diffusion.

ed to the ampule prior to diffusion. The β^- activity of substrates both after diffusion and after oxidation was then evaluated by placing the sample in contact with a plastic scintillator which was attached to the face of a photomultiplier tube. The photomultiplier pulse-height distribution was analyzed and plotted by a computer system to give an indication of the energy spectrum of the β^- particles entering the scintillator. By repetitively polishing and weighing the samples, it was possible to determine the activity as a function of depth, as illustrated in Fig. 3. Only events with energy above 50 keV are counted to eliminate background counts attributable to photomultiplier dark current. The effective depth for the β^- radiation in this experiment is estimated to be $\sim 30 \mu$ m, so that the count rate in effect measures the total sulfur concentration integrated over that depth. It is evident from that figure that the sulfur concentration drops rapidly in the first 1–2 μ m beneath the surface, and that a substantial background level remains at depths greater than 20 μ m. The profiles for the unoxidized and oxidized samples were similar, but the sulfur concentration is lower by about a factor of 6 in the oxidized sample. Finally, data on the activity of the crystals were compared with those from a calibrated carbon-14 β^- source to give a quantitative indication of the sulfur concentration in the samples. From the data of Fig. 3 and the known value of the activity per unit weight of the sulfur in the ampule, it was possible to estimate the concentration of sulfur in different depth regimes, as indicated in Table I.

In conclusion, waveguides have been produced by vapor diffusion of sulfur into SBN:60 substrates and electro-optic modulation has been demonstrated in these waveguides. The relatively high losses in the waveguides could be related to

TABLE I. Estimated average sulfur ($\times 10^{16}/\text{cm}^3$) concentration in diffused SBN:60 samples.

Depth (μ m)	Before oxidation	After oxidation
0–2.5	220	37
2.5–20	48	8
> 20	38	5

incomplete oxidation after diffusion and might be corrected by lower diffusion temperatures or longer oxidation times. The high electro-optic coefficient of the SBN:60 can lead to a substantial reduction in the voltage-length product for guided wave modulators and switches for communications and signal processing applications. From the radioisotope measurements the concentration of sulfur in the samples is found to be greatest near the surface, with a substantial background level present deep in the crystal. The vapor diffusion process is quite simple, and may be applicable to other ferroelectric materials and gaseous diffusants as well.

The authors would like to acknowledge the assistance of E. J. West for his efforts in the ampule diffusion process.

- ¹R. V. Schmidt and I. P. Kaminow, *Appl. Phys. Lett.* **25**, 458 (1974).
- ²R. C. Alferness, *IEEE J. Quantum Electron.* **QE-17**, 946 (1981).
- ³R. R. Neurgaonkar, J. R. Oliver, and L. E. Cross, *Ferroelectrics* **56**, 31 (1984).
- ⁴S. Nomura, H. Kojima, Y. Hattoni, and H. Kotsuka, *Jpn. J. Appl. Phys.* **13**, 1185 (1974).
- ⁵H. F. Taylor, W. E. Martin, D. B. Hall, and V. N. Smiley, *Appl. Phys. Lett.* **21**, 95 (1972).
- ⁶R. R. Neurgaonkar, M. H. Kalisher, T. C. Lim, E. J. Staples, and K. L. Keester, *Mater. Res. Bull.* **15**, 1235 (1980).
- ⁷R. R. Neurgaonkar, W. K. Cory, and J. R. Oliver, *Ferroelectrics* **51**, 3 (1983).
- ⁸E. H. Turner, *Appl. Phys. Lett.* **8**, 303 (1966).
- ⁹*Radiation Dosimetry*, G. J. Hines and G. L. Brownell, eds. (Academic, New York, 1956), Chaps. 6 and 16.



Rockwell International
Science Center

SC5441.FTR

EPITAXIAL GROWTH OF FERROELECTRIC TUNGSTEN BRONZE $\text{Sr}_{1-x}\text{Ba}_x\text{Nb}_2\text{O}_6$
FILMS FOR OPTOELECTRONIC APPLICATIONS

EPITAXIAL GROWTH OF FERROELECTRIC T.B. $\text{Sr}_{1-x}\text{Ba}_x\text{Nb}_2\text{O}_6$ FILMS
FOR OPTOELECTRONIC APPLICATIONS

Ratnakar R. Neurgaonkar and Edward T. Wu
Rockwell International Science Center
Thousand Oaks, CA 91360

(Received April 13, 1987; Communicated by W.B. White)



Pergamon Journals

New York • Oxford • Beijing • Frankfurt • São Paulo • Sydney • Tokyo • Toronto

EPITAXIAL GROWTH OF FERROELECTRIC T.B. $\text{Sr}_{1-x}\text{Ba}_x\text{Nb}_2\text{O}_6$ FILMS
FOR OPTOELECTRONIC APPLICATIONS

Ratnakar R. Neurgaonkar and Edward T. Wu
Rockwell International Science Center
Thousand Oaks, CA 91360

(Received April 13, 1987; Communicated by W.B. White)

ABSTRACT

This paper reports preliminary results of epitaxial growth of tetragonal ferroelectric $\text{Sr}_{1-x}\text{Ba}_x\text{Nb}_2\text{O}_6$ (SBN) thin films by the liquid phase epitaxial (LPE) technique. Several V^{5+} -containing flux systems were investigated; however, the BaV_2O_6 flux was found to be the most effective in producing SBN solid-solution films. Although the film growth rate was much faster on the (001) direction, film quality was best on the (100) and (110) directions with thickness in the range 5 to 20 μm . Lattice constant measurements indicate that the films are Ba^{2+} -rich, with compositions close to $\text{Sr}_{0.46}\text{Ba}_{0.54}\text{Nb}_2\text{O}_6$ and $\text{Sr}_{0.4}\text{Ba}_{0.6}\text{Nb}_2\text{O}_6$. This technique offers a unique opportunity to develop simple or complex bronze films of superior quality for several optoelectronic device applications.

MATERIALS INDEX: tungsten bronze films, niobates, barium, strontium

Introduction

The need for active materials for various optoelectronic devices, including electro-optic (1,2), spatial light modulators, pyroelectric detectors (3), surface acoustic wave (SAW) (4,5) and many others has stimulated recent work on the growth of ferroelectric tungsten bronze films. The bronze composition $\text{Sr}_{1-x}\text{Ba}_x\text{Nb}_2\text{O}_6$ (SBN), $0.75 \leq x \leq 0.25$, is very attractive and possesses electro-optic and pyroelectric coefficients higher than any other well-behaved ferroelectric material (6,7). Although the growth of optical-quality bulk crystals of $\text{Sr}_{0.6}\text{Ba}_{0.4}\text{Nb}_2\text{O}_6$ (SBN:60) has been shown to be successful by Neurgaonkar and Cory (8-11), there is great promise for other compositions within this solid-solution system; hence, the LPE technique has been established for their growth. Furthermore, the lattice match between SBN:60 and other compositions is excellent, and SBN:60 crystals are now available for use as substrate material. The present paper reports the epitaxial growth of SBN compositions using vanadium-containing flux systems for various device applications.

Experimental Procedure

The partial phase diagrams for the $M^{2+}V_2O_6$ -SBN and M^+VO_3 -SBN systems, $M^{2+} = Ba$ or Sr , and $M^+ = K$, Na and Li , were established with respect to composition and temperatures up to $1300^\circ C$. Reagent-grade carbonates or oxides of 99.9% purity were used as starting materials for this investigation. X-ray and DTA techniques were used to identify the solid solubility range of the tungsten bronze structure, lattice constants, solidus-liquidus temperature and eutectic compositions.

SBN:60 single crystals were grown by the rf Czochralski technique, and crystals as large as 2 to 3 cm in diameter and 4 to 6 cm long were available for use as substrate material. The (001), (100) and (110) substrates were cut from air-grown crystals and their top surfaces were optically polished. Substrate surfaces were cleaned using organic solvents, dilute acids, and then water to remove any dust particles, oils, etc. before use in LPE film growth.

Results and Discussion

Solvent for Tungsten Bronze Family Compositions

Crucial to the success of isothermal LPE growth is an ability to supercool the solution without the occurrence of spontaneous nucleation. Therefore, before LPE can be performed, a suitable flux system for the SBN solid-solution system must be found. Although a large number of solvents have been identified for this family, the present work was restricted to only the vanadium-containing solvents. Based on current research on ferroelectric $LiNbO_3$ thin-film growth (12-16), the vanadium-containing solvents have been found useful for SBN and the bronze compositions because of the following important reasons:

1. V^{5+} cation has strong preference for the four-fold coordinated site; hence, no vanadium inclusion in the bronze film is expected.
2. Supercooling range for the V^{5+} -containing solvents is reasonably high, of the order of 20 to $30^\circ C$.
3. V^{5+} -containing solvents melt at significantly low temperature, and thus allow LPE growth at much lower temperatures.
4. V^{5+} -containing solvents are remarkably stable at elevated temperatures (up to $1100^\circ C$).
5. All V^{5+} -containing solvents dissolve in dilute acids.

Table 1 summarizes a number of flux systems used in the present study for the SBN solid-solution systems. Since this system contains five or more components, the determination of a complete phase diagram is impractical. As described by Roy and White (17), such systems can be treated as pseudo-binary, with the phase to be crystallized as one component (solute) and the flux (solvent) as the other. Using this concept, as summarized in Table 1, several flux systems have been investigated for the SBN solid-solution system.

The determination of the phase diagrams BaV_2O_6 -SBN and BaB_6O_{13} -SBN, as shown in Figs. 1a and 1b, indicate that the ferroelectric tetragonal SBN phase exists over a wide range of temperature and compositional conditions. X-ray measurements of these systems indicated that the crystallized compositions are Ba^{2+} -rich with $0.54 \leq x \leq 0.62$. In the third system, SrV_2O_6 -SBN, $SrNb_2O_6$ was a major phase and extended over a wide

Table 1
Flux Systems for Tungsten Bronze Compositions

System	Melting Temperature of Flux (°C)	Eutectic Temperature (°C)**	Main Phase	Remarks
BaV ₂ O ₆ -SBN	720	68*	SBN (0.46 ≤ x ≤ 0.38)	Useful range for LPE work
BaB ₂ O ₇ -SBN	890	800	SBN	Useful range for LPE work
SrV ₂ O ₆ -SBN	760	710	SrNb ₂ O ₆	Not suitable
KVO ₃ -SBN	520	490	Sr ₂ KNb ₅ O ₁₅ **	Useful range for LPE work
NaVO ₃ -SBN	630	570	Sr ₂ NaNb ₅ O ₁₅	Useful range for LPE work
LiVO ₃ -SBN	700	630	LiNbO ₃ + SBN	Not suitable
Li ₂ WO ₄ -SBN	900	830	LiNbO ₃	Not suitable

* Phase relation was studied up to 1300°C

** belongs to tungsten bronze family

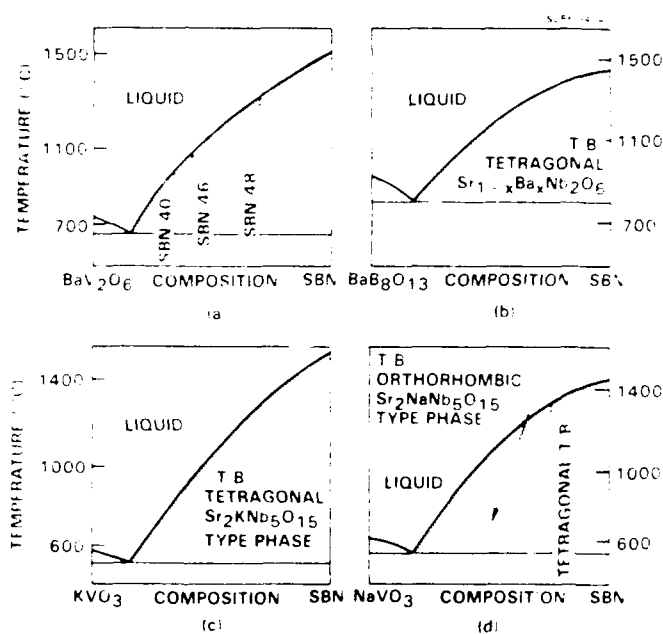


Fig. 1. Partial phase diagram for M^{2+} -V₂O₆-SBN and M^{2+} VO₃-SBN systems.

compositional range. This system was found to be unsuitable for bronze compositions. In two other systems, KVO₃-SBN and NaVO₃-SBN, although the tungsten bronze phase crystallized over a wide compositional range, the composition of the phases in each system was different; e.g., Sr₂KNb₅O₁₅ (tetragonal) and Sr₂NaNb₅O₁₅ (orthorhombic) in the latter system, respectively (18,19). Since compositions from both systems exhibit

excellent dielectric, pyroelectric and electro-optic properties, these systems will be considered for future growth work.

The remaining two flux systems, LiVO_3 -SBN and Li_2WO_4 -SBN (nonvanadium system) did not produce tungsten bronze compositions of SBN until 75 mole% or more of SBN was in the mixture, and also required a dipping temperature of at least 1300°C. LiNbO_3 was found to be a more stable phase in these systems instead of bronze SBN.

Since the SBN solid solution is stable in only two systems, BaV_2O_6 -SBN and BaB_2O_7 -SBN, the choice of solvents is very limited. Furthermore, since the tetragonal ferroelectric phase exists over a wide compositional range for SBN, $0.75 \leq x \leq 0.25$, the Sr:Ba ratio must be established in each composition before any film growth experiments are conducted.

Since SBN, $0.75 \leq x \leq 0.25$ is a solid-solution system, the Sr:Ba ratio must be established to check lattice compatibility with SBN:60 substrates. For this reason, we studied the join BaV_2O_6 - $\text{Sr}_{0.5}\text{Ba}_{0.5}\text{Nb}_2\text{O}_6$ in detail using x-ray diffraction and DTA techniques. Based on lattice constant measurements, the compositions along this line are predominantly Ba^{2+} -rich and varied from $\text{Sr}_{0.4}\text{Ba}_{0.6}\text{Nb}_2\text{O}_6$ (SBN:40) to $\text{Sr}_{0.46}\text{Ba}_{0.54}\text{Nb}_2\text{O}_6$ (SBN:46) with increasing SBN:50 concentration in the system. The DTA results indicate that a pseudo-eutectic occurs at 15 mole% of SBN:50, with a eutectic temperature of approximately 685°C. The supercooling range for this system is reasonably large at an estimated 25°C, which is suitable for film growth experiments.

LPE Growth of SBN Thin Films

The compositions SBN:40 and SBN:46, which correspond to the batch mixtures of 60 mole% BaV_2O_6 -40 mole% SBN:50 and 70 mole% BaV_2O_6 -30 mole% SBN:50, respectively, were selected for epitaxial growth studies. The lattice constants, ferroelectric and electro-optic properties for these SBN compositions and for LiNbO_3 are given in Table 2. An important consideration for the growth of SBN:40 and SBN:46 on SBN:60 substrates is a sufficiently close lattice match between films and substrate. As given in Table 2, the lattice match for these compositions with SBN:60 is fairly close, on the order of 0.6% or less on the (001) and 0.3% or less on the (100) and (110) oriented faces.

Table 2
Structural and Optical Properties of Bronze Compositions

Property	SBN:60	SBN:40	SBN:46	LiNbO_3
Lattice Constants	$a = 12.462\text{\AA}$ $c = 3.932\text{\AA}$	$a = 12.473\text{\AA}$ $c = 3.933\text{\AA}$	$a = 12.478\text{\AA}$ $c = 3.935\text{\AA}$	$a = 5.145\text{\AA}$ $c = 13.76\text{\AA}$
Lattice Mismatch*		(001) = 0.38% (100) = 0.13% (110) = 0.20%	(001) = 0.42% (100) = 0.16% (110) = 0.19%	
LPE Growth Temperature		1040-1050°C	920-930°C	
Growth Rate ($\mu\text{m/hr}$)		(001) = 1-2 μm (100) = 0.5 μm (110) = 0.5 μm	(001) = 1-2 μm (100) = 0.5 μm (110) = 0.5 μm	
T_c (°C)	78	135	160	1150
Electro-Optic Coeff. ($\times 10^{-12} \text{ m/V}$)	$r_{33} = 42$ $r_{31} = 6$	$r_{33} = 18$ $r_{31} = 3$	$r_{33} = 11$ $r_{31} = 2$	$r_{33} = 3$ $r_{31} = 8.6$
SAW Coupling Constant	(001) = 180×10^{-6}	(001) = 100×10^{-6}	—	(100) = 420×10^{-6}
Poling Field	(001) = 7 kV/cm (100) = 10 kV/cm (110) = 10 kV/cm	(001) = 8 kV/cm (100) = 10 kV/cm (110) = 10 kV/cm	(001) = 8 kV/cm (100) = 10 kV/cm (110) = 10 kV/cm	

* - with respect to SBN:60

Initially, efforts concentrated on the growth of the SBN:46 composition, since it has a closer lattice match to SBN:60. The calcined mixture was melted in a 100 cc platinum crucible and then placed in the growth furnace, as shown in Fig. 2. The growth apparatus consisted of a vertical tube furnace whose temperature was controlled with an accuracy of $\pm 1^\circ\text{C}$. The mixture was held overnight at approximately 100°C above its melting temperature. After achieving complete homogeneity, the molten solution was slowly cooled to the growth temperature at the rate of $10^\circ\text{C}/\text{h}$. An oriented SBN:60 substrate, positioned slightly above the melt to equilibrate with the solution temperature, was then dipped into the melt. Table 2 summarizes the substrate orientations, dipping temperature range, lattice constants and film compositions. After the required growth time had elapsed, the sample was withdrawn from the melt and cooled very slowly to room temperature. The adhering flux was removed by dipping the film/substrate in dilute HCl acid. This is the first time such ferroelectric SBN films have been grown by this technique, however, the growth of other tetragonal bronze compositions by the sputtering and LPE techniques has also been reported (20,21).

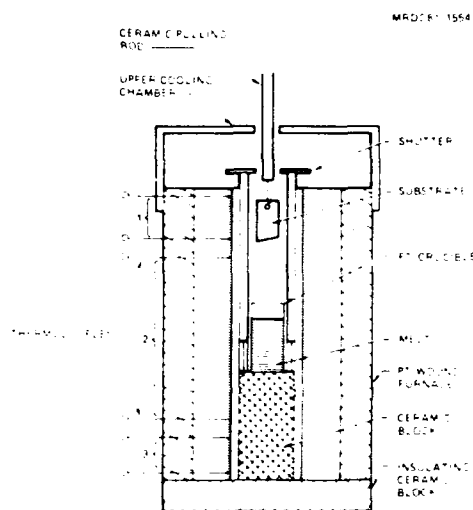


Fig. 2 Growth furnace.

The success of thin-film growth is due, in part, to the availability of large, high-quality SBN:60 substrates (1,2). Since SBN:60 bulk crystals exhibit 24 well-defined facets (22), the maintenance of precise substrate orientations was a relatively easy task. The films were developed on three different orientations, specifically, (001), (100) and (110), and the LPE growth process was studied with respect to growth temperature, orientation and lattice match. Film quality and thickness were found to depend strongly on the substrate orientation and the rate of crystallization. For example, growth was approximately three to four times faster on the (001) direction as compared to the (100) and (110) directions. This is consistent with our observations on bulk single crystal growth of SBN compositions by the Czochralski technique, where the growth rate is considerably greater along the (001) direction, whereas growth along other orientations has been found to be most difficult and, in some instances, impossible.

Figure 3 shows a typical cross section for a thin film grown on a (001)-oriented SBN:60 substrate. The growth rate was typically 1 to $2\ \mu\text{m}/\text{min}$ on the (001) direction, while under the same conditions the rate was $0.5\ \mu\text{m}$ or less on the (100) and (110) direc-

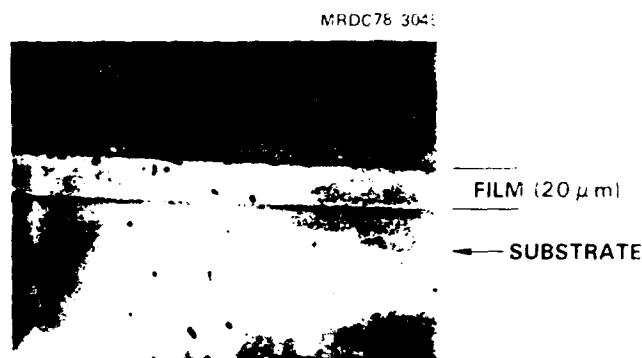


Fig. 3 Cross section of 20 μm SBN:46 film on the (001)-oriented SBN:60 substrate.

tions. However, because of the lower growth rates on the latter directions, the film quality was superior and films as thick as 5 to 25 μm were grown without compromising quality or ferroelectric properties.

The quality of the (001)-oriented films was studied with respect to growth temperature for both batch mixtures, and was found to improve considerably with increasing growth temperatures from 1040-1050°C and 920-930°C, respectively. However, the film quality gradually degraded for the composition corresponding to SBN:40 (Batch I), probably because of the increased lattice mismatch for (001)-oriented films. These films also showed a tendency to crack. However, for the (100) and (110)-oriented substrates, film quality was excellent for both mixtures.

The tetragonal SBN, $0.75 \times a \times 0.25$, solid solution extends over a wide compositional range, and the change in the c lattice constant is more pronounced as compared to a with respect to changes in the Br/Ba ratio. Our results suggest that for the successful epitaxial growth of these bronze compositions, it is important to maintain an 0.3% or less lattice mismatch between the film and substrate along the growth direction. Recent work by Achari et al. (20,21) also demonstrated the growth of excellent quality bronze $\text{K}_2\text{Li}_2\text{Nb}_2\text{O}_7$ films on $\text{K}_2\text{BrNb}_2\text{O}_7$ substrates using the LPE and sputtering techniques. Clearly, to generalize these results, further work is necessary to establish the tolerance factors for allowable lattice mismatch in the growth of bronze composition films.

Characterization

To confirm single phase film growth and to accurately determine composition, the a and c lattice constants for both film and substrate were measured using the x-ray diffraction technique. Figure 4a and 4b shows x-ray reflections for films grown from the batch mixture 60 mole% BaV_2O_6 -40 mole% SBN:40. The composition for the film was established by measuring the difference between the substrate and film lattice constants. This technique was previously successful in our work to establish the dopant concentration in LiNbO_3 films (12,15,16). As shown in Fig. 4a and 4b, two reflections corresponding to (003) and (004) for the c axis, and (10,00) and (12,00) for the a axis were studied for both film and substrate. Since the lattice constant changes for the a axis are small compared to the c axis, it was necessary to select higher angle reflections to get adequate separation between the film and substrate peaks. Further, when scanning the reflections at $1/8$ 2 θ /min, the separation was even wider, as shown in Fig. 5, to estimate their lattice constants. Using these reflection values, the lattice constants a and c were determined for both film compositions as follows:

SBN:46 $a = 12.476\text{\AA}$, $c = 3.956\text{\AA}$
 SBN:40 $a = 12.482\text{\AA}$, $c = 3.961\text{\AA}$

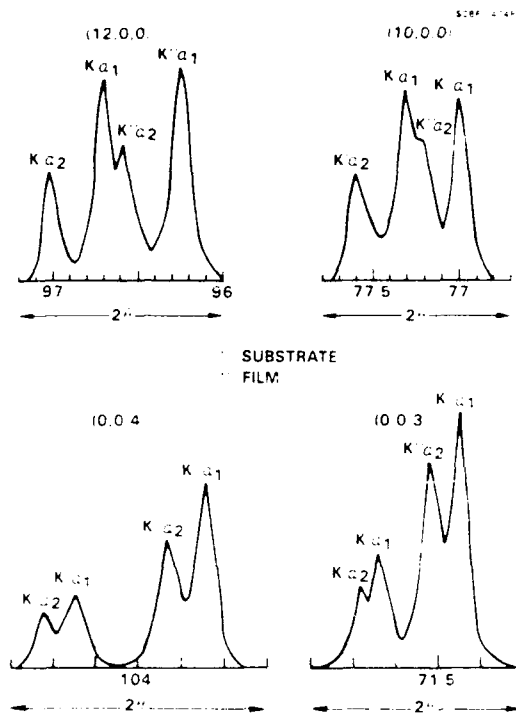


Fig. 4 X-ray reflections for films grown from 60 mole% BaV_2O_6 -40 mole% SBN:50.

These films exhibited unchanging lattice parameters with variations of growth process parameters until vanadium loss due to volatilization became significant. These constants are reasonably close to the values reported for SBN:46 and SBN:40 in Table 2 and, based on these results, the growth of uniform compositions seems possible. Also clear from these experiments is that the films are Ba^{2+} -rich over a wide range of compositions in the BaV_2O_6 -SBN:50 system. At higher concentrations of Sr^{2+} , the major phase formed is nonferroelectric SrNb_2O_6 , which is of no interest in the present work.

The SAW electromechanical coupling constant (K^2) for SBN:46 films was measured on poled (001) plates propagating in the (100) direction using the method described by Staples (23). The films were poled in all configurations, but the poling of (100) and (110)-oriented films was more difficult as compared to films grown in the (001) direction. Although the quality of the (001)-oriented films is not as good as that achieved for the other orientations, the coupling constant for these films could still be evaluated. The coupling constant for SBN:46 is approximately 100×10^{-4} , which is smaller than the current best SBN:60 crystals (180×10^{-4} (5)). These films were also tested for optical waveguide applications using a He-Ne laser operating at 6328\AA , and the quality of the (100) and (110) films was quite reasonable, whereas the (001)-oriented films were unsuitable. Although the electro-optic (r_{33}) and pyroelectric coefficients for SBN:46 are not as large as SBN:60, r_{33} is at least five times better than that of LiNbO_3 crystals. The composi-

tion SBN:50 is now being studied in our laboratory for pyroelectric detection because of its excellent pyroelectric figure-of-merit. Therefore, the development of these better quality films is expected to significantly impact ongoing research programs in optical waveguides and pyroelectric thermal detectors.

Conclusions

The LPE technique appears to be suitable for the tungsten bronze family compositions, provided the lattice mismatch between the film and substrate is sufficiently small (0.3% or less). In a forthcoming paper, we will describe the extension of this technique to another important tungsten bronze, $\text{Sr}_2\text{KNb}_5\text{O}_{15}$, using the SBN:60 substrate. Such films should have a significant impact on various device applications, including optical waveguides, switches, pyroelectric detectors and SAW.

Acknowledgements

This research work was supported by DARPA (Contract No. N00014-82-C-2466). The authors are grateful for discussions on this research with L.E. Cross, W.F. Hall, J.R. Oliver and E.J. Staples.

References

1. R.R. Neurgaonkar, W.K. Cory and J.R. Oliver, *Ferroelectrics* 15, 3 (1983).
2. R.R. Neurgaonkar, J.R. Oliver and L.E. Cross, *Ferroelectrics* 56, 31 (1984).
3. A.M. Glass, *J. Appl. Phys.* 40, 4699 (1969).
4. S.T. Liu and R.B. MacIsaac, *J. Electron. Mat.* 4, 91 (1975).
5. R.R. Neurgaonkar and L.E. Cross, *Mat. Res. Bull.* 21, 893 (1986).
6. F.V. Lanzo, E.G. Spencer and A.A. Ballman, *Appl. Phys. Lett.* 11, 23 (1967).
7. J.B. Thaxter, *Appl. Lett.* 15, 210 (1969).
8. R.R. Neurgaonkar, M.H. Kalisher, T.C. Lim, E.J. Staples and K.K. Keester, *Mat. Res. Bull.* 15, 1235 (1980).
9. R.R. Neurgaonkar and W.K. Cory, *J. Opt. Soc. America* 3 (2), 232 (1986).
10. R.R. Neurgaonkar, *Proc. SPIE* 465, 97 (1984).
11. R.R. Neurgaonkar, T.C. Lim, E.J. Staples and L.E. Cross, *Proc. Ultrasonic Symp.*, 410 (1980).
12. R.R. Neurgaonkar, M.H. Kalisher, E.J. Staples and T.C. Lim, *Appl. Phys. Lett.* 35 (8), 606 (1979).
13. E.J. Staples, R.R. Neurgaonkar and T.C. Lim, *Appl. Phys. Lett.* 32, 197 (1978).
14. A. Baudrant, H. Vial and J. Daval, *Mat. Res. Bull.* 10, 1373 (1975).
15. R.R. Neurgaonkar and E.J. Staples, *J. Cryst. Growth* 54, 572 (1981).
16. R.R. Neurgaonkar, Semi-Annual Technical Report No. 4, DARPA, Contract No. N00014-82-C-2466.
17. R. Roy and W.B. White, *J. Cryst. Growth* 33, 314 (1968).
18. G. Burns, E.A. Giess, D.F. O'Kane, B.A. Scott and S.W. Smith, *J. Phys. Soc. Jpn.* 28, 153 (1970).
19. T. Ohta and R.A. Watanate, *Jap. J. Appl. Phys.* 9, 721 (1970).
20. M. Adachi, T. Shiosaki and A. Kawabata, *Jap. J. Appl. Phys.* 18, 1637 (1979).
21. M. Adachi, M. Hori, T. Shiosaki and A. Kawabata, *Jap. J. Appl. Phys.* 17, 2053 (1978).
22. O.F. Dudnik, A.K. Gromov, V.B. Kravchenko, Y.L. Kipylov and G.F. Kunznetsov, *Sov. Phys. Crystograph.* 15, 330 (1970).
23. E.J. Staples, *Proc. 28th Annual Frequency Control Symp.*, 280 (1974).



Rockwell International
Science Center

SC5441.FTP

LPE GROWTH OF FERROELECTRIC TUNGSTEN BRONZE $\text{Sr}_2\text{KNb}_5\text{O}_{15}$
THIN FILMS

LPE Growth of Ferroelectric Tungsten Bronze $\text{Sr}_2\text{KNb}_5\text{O}_{15}$ Thin Films

R.R. Neurgaonkar and J.R. Oliver
Rockwell International Science Center
Thousand Oaks, CA 91360 USA

and

L.E. Cross
Materials Research Laboratory
The Pennsylvania State University
University Park, PA 16802 USA

Abstract

Ferroelectric tungsten bronze $\text{Sr}_2\text{KNb}_5\text{O}_{15}$ (SKN) thin films have been grown by liquid phase epitaxy on (100), (110) and (001) orientations of tungsten bronze $\text{Sr}_{0.6}\text{Ba}_{0.4}\text{Nb}_2\text{O}_6$ (SBN:60) substrates using vanadium-containing solvents. Single crystal film growths of up to 25 μm thickness were achieved with very good film quality in all growth directions, due in part to the excellent lattice match with SBN:60. Surface acoustic wave (SAW) measurements show electro-mechanical coupling of up to 130×10^{-4} , comparable to values measured in other tungsten bronze ferroelectrics. The high dielectric constants available in these films also indicate potentially very large linear electro-optic effects which are roughly an order of magnitude greater than for LiNbO_3 .

Introduction

The solid solution $\text{Sr}_2\text{KNb}_5\text{O}_{15}$ (SKN) is a tetragonal (4 mm) tungsten bronze ferroelectric which exists in the SrNb_2O_6 - KNbO_3 pseudobinary system.¹⁻³ SKN has been of practical interest for several device applications because of its potentially large electro-optic and electro-mechanical properties.⁴⁻⁷ In particular, extensive efforts have been made to grow SKN in bulk single crystal form for surface acoustic wave (SAW), electro-optic and millimeter wave device applications. Although we have been able to grow small crystals of reasonable quality by the Czochralski technique in our own work, improvements in homogeneity, optical quality and crystal size have been hampered by the K^+ volatility at the growth temperature and by bulk crystal fracture during cooldown.

An alternative growth method for this ferroelectric bronze is liquid phase epitaxy (LPE) which has been successfully utilized to grow tungsten bronze $\text{Sr}_{0.5}\text{Ba}_{0.5}\text{Nb}_2\text{O}_6$ (SBN:50), ilmenite LiNbO_3 and LiTaO_3 thin films for SAW evaluation.⁸⁻¹¹ In this paper, we report the LPE growth of SKN thin films on $\text{Sr}_{0.6}\text{Ba}_{0.4}\text{Nb}_2\text{O}_6$ (SBN:60) substrates, the latter being chosen because of its close lattice match to SKN.

LPE Flux Systems

The successful LPE growth of volatile solid solutions such as SKN requires the development of an appropriate flux system permitting relatively low-temperature growths without the occurrence of spontaneous nucleation during supercooling. Based on our prior work on the LPE growth of tungsten bronze SBN compositions,⁸ KVO_3 solvents appear to have the best potential for SKN film growth since V^{5+} does not incorporate into the tungsten bronze lattice. In particular, the flux system KVO_3 - SBN was found to form tetragonal SKN over a wide compositional range due to the exchange of Ba for K and the

formation of BaV_2O_6 and SKN.⁸ The phase diagram for this system, with KVO_3 and SBN:50 as end members, was established by DTA measurements and x-ray diffraction analysis to determine the structure and lattice constants of the major phases, and is shown in Fig. 1. Additional dielectric measurements were carried out on sintered ceramics obtained from several flux compositions to determine the composition of the major phase, i.e. either SBN or SKN, the latter having a typically large room temperature dielectric constant and high Curie point ($> 150^\circ\text{C}$). For the KVO_3 - SBN:50 system, single phase SKN was found over a wide compositional range up to 60 mole% SBN:50 (Fig. 1a), with ceramic samples showing a ferroelectric transition temperature of $T_C = 154 - 156^\circ\text{C}$ and large room-temperature dielectric constants of approximately 1300, ruling out SBN as a possible phase. In the compositional range of 60 - 90 mole% SBN:50, mixed phases of SKN and SBN were found, and above 90 mole% SBN:50, only SBN compositions were found with very high melting temperatures.

The flux system $\text{K}_5\text{V}_5\text{O}_{15}$ - $\text{Sr}_2\text{KNb}_5\text{O}_{15}$ was also examined for possible use in LPE film growth. Because of the absence of Ba^{2+} in this system, single phase bronze SKN was found in the entire compositional region above 13 mole% SKN concentration, as shown in the phase diagram of Fig. 1b. As in the case of the previous flux system, ceramics derived from the $\text{K}_5\text{V}_5\text{O}_{15}$ - SKN system showed a high transition temperature of $T_C = 162^\circ\text{C}$ and large room temperature dielectric constants of approximately 1100. However, the overall melting temperatures were somewhat lower in this flux system, as can be seen in Fig. 1.

LPE Thin Film Growth

Since both the KVO_3 - SBN:50 and $\text{K}_5\text{V}_5\text{O}_{15}$ - SKN flux systems show the formation of single phase SKN compositions at suitably low melting temperatures, both systems

were used for the LPE growth of SKN thin films. The particular flux compositions (0.75) KVO_3 - (0.25) SBN:50 and (0.80) $\text{K}_5\text{V}_5\text{O}_{15}$ - (0.20) SKN were chosen for film growth based on their low melting temperatures and the close lattice match of the resulting crystals to stoichiometric $\text{Sr}_2\text{KNb}_5\text{O}_{15}$. The measured crystal lattice constants in these cases were $a, b = 12.469 \text{ \AA}$, $c = 3.943 \text{ \AA}$ for the (0.75) KVO_3 - (0.25) SBN:50 flux system and $a, b = 12.473 \text{ \AA}$, $c = 3.943 \text{ \AA}$ for (0.80) $\text{K}_5\text{V}_5\text{O}_{15}$ - (0.20) SKN. These values compare very closely with $a, b = 12.471 \text{ \AA}$, $c = 3.942 \text{ \AA}$ for stoichiometric SKN.

Reagent grade carbonates and oxides of 99.95% purity were used as starting materials, with film growths performed in a vertical tube furnace controllable to within $\pm 1^\circ\text{C}$. In each case, the calcined flux was melted in a 100 cc platinum crucible and held overnight at approximately 100°C above the melting temperature to achieve complete homogeneity. The molten solution was then cooled at a rate of $10^\circ\text{C}/\text{h}$ back down to the melting temperature where it was allowed to equilibrate. Finally, oriented substrates were then individually dipped into the melt for LPE film growth; after the required growth time had elapsed, the substrates were removed from the melt and then slowly cooled to room temperature. Adhering flux was removed using dilute HCl followed by water rinsing. Further details may be found in earlier papers.⁸⁻¹²

Essential to the successful growth of high-quality epitaxial thin films is the use of closely lattice-matched substrates. In the case of SKN, a close lattice match exists with tungsten bronze SBN:60 along both (100) ($a, b = 12.468 \text{ \AA}$) and (001) ($c = 3.938 \text{ \AA}$) orientations. SBN:60 is a congruently melting bronze solid solution which can be grown in exceptionally high quality by the Czochralski technique in crystal boules up to 3 cm diameter.¹³⁻¹⁵ Therefore, SBN:60 is particularly suited for the LPE growth of SKN thin films of the highest possible quality.

SBN:60 substrate wafers with $\langle 100 \rangle$, $\langle 110 \rangle$ and $\langle 001 \rangle$ orientations were used to evaluate film growth rates and film quality. After cutting with diamond saw, each crystal wafer was lapped and then optically polished on one surface, followed by cleaning in dilute acid. LPE growth of SKN films was found to be faster along $\langle 001 \rangle$ for both flux systems, with a growth rate of typically 1-2 $\mu\text{m}/\text{min}$ compared to 0.5 $\mu\text{m}/\text{min}$ or less for $\langle 100 \rangle$ or $\langle 110 \rangle$. This is consistent with our observations on Czochralski bulk single crystal growth of tungsten bronze ferroelectrics where $\langle 001 \rangle$ is the preferred growth direction.¹³⁻¹⁵ However, optical and x-ray diffraction evaluations of these films showed somewhat better film quality for the $\langle 100 \rangle$ and $\langle 110 \rangle$ orientations because of their slower growth rates. Nevertheless, all of these SKN thin films were found generally superior to previous SBN:50 growths on SBN:60 substrates⁸ due to the improved lattice match between SKN and SBN:60, with SKN films of up to 15 - 25 μm thickness showing no significant compromise of film quality. This result reflects the general observation that the lattice mismatch tolerance factor for good quality tungsten bronze films appears to be relatively low at 0.3% or less.

The crystallinity, phase purity and lattice constants of the SKN films were evaluated by x-ray diffraction measurements. Since SKN and SBN:60 have nearly the same lattice constants, it is necessary to use very slow scanning rates (1/8 to 1/4°/min) to separate the diffraction peaks arising from the SKN film and the underlying substrate. Figure 2 shows the relative intensity of the Cu $K\alpha_1$ and $K\alpha_2$ diffraction peaks for the (800) reflection in films of successively greater thickness. In the figure, the primed lines indicate diffraction due to the SKN film, and the unprimed lines due to the underlying substrate. The latter are seen to disappear for film thicknesses greater than 10 μm . Film crystallinity was generally very good, as indicated by the sharpness of the film diffraction peaks in Fig. 2.

Table I summarizes the growth conditions and major physical properties for the SKN films grown from each flux system. The film lattice constants were established from the (400), (600) and (800) x-ray reflections from (100)-oriented films and the (001), (002) and (004) reflections from (001)-oriented films. The measured constants are in excellent agreement with the values obtained from stoichiometric $\text{Sr}_2\text{KNb}_5\text{O}_{15}$ ceramics. The SAW electromechanical coupling constants, K^2 , were measured on poled $\langle 001 \rangle$ SKN thin films using the method by Staples.¹⁶ Poling to a single ferroelectric domain was accomplished by cooling from the SKN transition temperature with a 6 kV/cm field applied across the substrate/film combination. The measured SAW coupling constants at room temperature for acoustic propagation along $\langle 100 \rangle$ were $110\text{--}130 \times 10^{-4}$, depending primarily on the flux used for growth (Table I). Although these values are smaller than for SBN:60 (180×10^{-4}) and $\text{Pb}_2\text{KNb}_5\text{O}_{15}$ (188×10^{-4}),^{17,18} it may be possible to increase SAW coupling in SKN by altering the Sr:K ratio, although such compositional changes have not yet been explored.

The linear electro-optic effect in SKN is anticipated to be large because of the high dielectric constants found along both polar and nonpolar directions. From the phenomenology for tetragonal bronze ferroelectrics,¹⁹ the electro-optic coefficients, r_{ij} , are given by

$$r_{33} = 2g_{33}P_3\epsilon_0\epsilon_{33}$$

$$r_{51} = 2g_{44}P_3\epsilon_0\epsilon_{11}$$

where ϵ_0 is the permittivity of free space, P_3 is the spontaneous polarization and g is the quadratic electro-optic coefficient. From dielectric measurements on small Czochralski-grown SKN single crystals, $\epsilon_{11} = 1000$ and $\epsilon_{33} = 1200$ at room temperature. Dielectric

measurements on SKN thin films using a close-spaced surface electrode geometry were necessarily influenced by geometric factors and possible substrate contributions, but in general showed semi-quantitative agreement with the bulk crystal values. Using $P_3 = 0.30$ C/m² and $g_{33} = 0.09$, $g_{44} = 0.04$ m⁴/C² typical of tetragonal bronze ferroelectrics, the anticipated linear electro-optic coefficients for these films are roughly $r_{33} = 550 \times 10^{-12}$ m/V and $r_{51} = 200 \times 10^{-12}$ m/V, values substantially larger than those encountered in tungsten bronze SBN:60 (470×10^{-12} and $80-90 \times 10^{-12}$ m/V, respectively) and more than an order of magnitude better than r_{33} for LiNbO₃ (31×10^{-12} m/V).²⁰ Hence, these SKN thin films could prove to be especially important for electro-optic device applications. Although the optical quality of the current films is still not sufficient for detailed electro-optical and optical waveguide characterization, this appears to be largely a consequence of substrate surface preparation (and substrate quality) rather than an inherent problem in the grown films.

Conclusions

Tungsten bronze SKN thin films grown by the LPE technique appear to be suitable for SAW device applications upon further evolutionary improvements in thin film quality. Increased SAW electromechanical coupling may also be possible through alteration of the Sr:K ratio, although such compositional changes should not be so large that the advantages of substrate lattice matching are lost. Perhaps one of the greatest advantages of these films is the high ferroelectric transition temperature (155°C) which permits the application of relatively large applied voltages and usage over a wide temperature range without ferroelectric domain reversal or depoling. With improvements in film quality, these SKN films could also have a significant impact on optical and possibly pyroelectric applications as well.

Acknowledgements

The authors wish to thank W.K. Cory for his insights and discussions on this work, and E.J. Staples for the initial SAW measurements. This research was supported by DARPA (Contract No. N00014-82-C-2466) and by the Office of Naval Research (Contract No. N00014-81-C-0463).

References

1. E.A. Giess, B.A. Scott, G. Burns, D.F. O'Kane and A. Segmuller, J. Am. Cer. Soc. 58, 276 (1968).
2. B.A. Scott, E.A. Giess, D.F. O'Kane and G. Burns, J. Am. Cer. Soc. 53, 106 (1969).
3. F.W. Ainger, J.A. Beswick and S.G. Porter, Ferroelectrics 3, 321 (1972).
4. E.A. Giess, G. Burns, D.F. O'Kane and A.W. Smith, Appl. Phys. Lett. 11, 233 (1967).
5. R. Clarke and F.W. Ainger, Ferroelectrics 7, 101 (1974).
6. G. Burns, E.A. Giess, D.F. O'Kane, B.A. Scott and A.W. Smith, J. Phys. Soc. Japan 28(Suppl.), 153 (1970).
7. R.R. Neurgaonkar, W.W. Ho, W.K. Cory, W.F. Hall and L.E. Cross, Ferroelectrics 51, 185 (1984).

8. R.R. Neurgaonkar and E.T. Wu, Mat. Res. Bull. 22, 1095 (1987).
9. E.J. Staples, R.R. Neurgaonkar and T.C. Lim, Appl. Phys. Lett. 32, 197 (1978).
10. R.R. Neurgaonkar, M.H. Kalisher, E.J. Staples and T.C. Lim, Appl. Phys. Lett. 35(8), 606 (1979).
11. R.R. Neurgaonkar, T.C. Lim, E.J. Staples and L.E. Cross, Ferroelectrics 27, 63 (1980).
12. R.R. Neurgaonkar and E.J. Staples, J. Cryst. Growth 27, 352 (1981).
13. R.R. Neurgaonkar, M.H. Kalisher, T.C. Lim, E.J. Staples and K.L. Keester, Mat. Res. Bull. 15, 1305 (1980).
14. R.R. Neurgaonkar and W.K. Cory, J. Opt. Soc. Am. B 3, 276 (1986).
15. R.R. Neurgaonkar, W.K. Cory, J.R. Oliver, M.D. Ewbank and W.F. Hall, Opt. Eng. 26(5), 392 (1987).
16. E.J. Staples, Proc. 28th Ann. Freq. Control Symp., 280 (1974).
17. R.R. Neurgaonkar and L.E. Cross, Mat. Res. Bull. 21, 893 (1986).
18. P.H. Carr, Proc. IEEE Ultrasonics Symp., 286 (1974).

19. M. DiDomenico and S.H. Wemple, J. Appl. Phys. 40(2), 720 (1969).
20. K.-H. Hellwege, ed., Landolt-Bornstein New Series, Group III, Vol. 11 (Springer-Verlag, Berlin, 1979).

Figure Captions

Fig. 1 LPE flux systems for tungsten bronze SKN film growth: (a) KVO_3 - SBN:50; (b) $\text{K}_5\text{V}_5\text{O}_{15}$ - SKN.

Fig. 2 Cu $\text{K}\alpha_1$ and $\text{K}\alpha_2$ x-ray diffraction peaks for the (800) line as a function of SKN film thickness. The unprimed peaks are due to the SBN:60 substrate material.

Table I
Physical Properties of SKN Films Grown by LPE

	Substrate	SKN Films	
	SBN:60	(0.75) KVO ₃ -(0.25) SBN:50	(0.80) K ₅ V ₅ O ₁₅ -(0.20) SKN
Growth Temperature	--	920-925°C	880-890°C
Growth Rate:			
<001>	--	1-2 μm/min	1-2 μm/min
<100> or <110>	--	≥ 0.5 μm/min	≥ 0.5 μm/min
Lattice Constants and Substrate Mismatch:			
a, b	12.465 Å	12.469 Å (0.032%)	12.473 Å (0.064%)
c	3.938 Å	3.943 Å (0.127%)	3.943 Å (0.127%)
Curie Point	75°C	153°C	162°C
Dielectric Constant at 20°C:			
ε ₁₁	475	~ 1000	~ 1000
ε ₃₃	920	~ 1200	~ 1200
SAW Coupling, K ² (<100>)	180 × 10 ⁻⁴	130 × 10 ⁻⁴	110 × 10 ⁻⁴
Electro-optic Coefficient (10 ⁻¹² m/V):*			
r ₃₃	470	~ 550	~ 550
r ₅₁	80 - 90	~ 200	~ 200

*Calculated values for SKN.